



**HAL**  
open science

# Gulf of Mexico ocean dynamics and its modulation by air-sea interactions

Marco Larranaga

► **To cite this version:**

Marco Larranaga. Gulf of Mexico ocean dynamics and its modulation by air-sea interactions. Climatology. Université Paul Sabatier - Toulouse III, 2023. English. NNT : 2023TOU30080 . tel-04297850

**HAL Id: tel-04297850**

**<https://theses.hal.science/tel-04297850>**

Submitted on 21 Nov 2023

**HAL** is a multi-disciplinary open access archive for the deposit and dissemination of scientific research documents, whether they are published or not. The documents may come from teaching and research institutions in France or abroad, or from public or private research centers.

L'archive ouverte pluridisciplinaire **HAL**, est destinée au dépôt et à la diffusion de documents scientifiques de niveau recherche, publiés ou non, émanant des établissements d'enseignement et de recherche français ou étrangers, des laboratoires publics ou privés.



# THÈSE

En vue de l'obtention du

**DOCTORAT DE L'UNIVERSITÉ DE TOULOUSE**

Délivré par : *l'Université Toulouse 3 Paul Sabatier (UT3 Paul Sabatier)*

---

---

Présentée et soutenue le 24/02/2023 par :

**Marco LARRAÑAGA**

**Gulf of Mexico ocean dynamics and its modulation by air-sea interactions**

---

---

## JURY

SÉBASTIEN MASSON	Directeur de recherche (LOCEAN, Paris)	Rapporteur
JULIO SHEINBAUM	Professeure (CICESE, México)	Rapporteur
MATTHIEU LE HÉNAFF	Associate Professor (MU, Miami)	Examinateur
PAULA PÉREZ BRUNIUS	Professeure (CICESE, México)	Examinatrice
YVES MOREL	Directeur de recherche (LEGOS, Toulouse)	Examinateur
JULIEN JOUANNO	Directeur de recherche (LEGOS, Toulouse)	Directeur de thèse
LIONEL RENAULT	Chargé de recherche (LEGOS, Toulouse)	Co-directeur de thèse

---

**École doctorale et spécialité :**

*SDU2E : Océan, Atmosphère, Climat*

**Unité de Recherche :**

*LEGOS (UMR 5566)*

**Directeur(s) de Thèse :**

*Julien JOUANNO et Lionel RENAULT*

**Rapporteurs :**

*Sébastien MASSON et Julio SHEINBAUM*



---

**Résumé** — À l'échelle des bassins océaniques, il est reconnu depuis plusieurs décennies que les interactions entre l'océan et l'atmosphère ont une grande influence sur le climat de la Terre. Cependant, les biais persistants des modèles globaux, par exemple en température de surface de la mer, ont mis en exergue les limites d'une approche globale à relativement basse résolution spatiale. Il en a ainsi découlé une nouvelle ligne de recherche basée sur une approche régionale de la dynamique océanique et des interactions entre l'océan et l'atmosphère. Cette thèse s'inscrit dans cette approche en se focalisant sur le Golfe du Mexique (GdM).

Le GdM fait partie du système de courants de bord ouest de l'Atlantique Nord. Il s'agit d'un système complexe où les activités humaines, telles que l'extraction pétrolière et la pêche, interagissent largement avec l'environnement océanique et les écosystèmes biogéochimiques. La dynamique du GoM est dominée par l'emblématique Loop Current (LC), un courant anticyclonique intense qui apporte des eaux chaudes des Caraïbes dans le GoM. Le LC libère épisodiquement des tourbillons anticycloniques chauds qui se propagent vers l'ouest : les Loop Current Eddies (LCEs). Cependant, le GdM est confronté à des problèmes environnementaux croissants tels que les marées noires et les plastiques. La connaissance de la dynamique des océans est de la plus haute importance pour la compréhension et la surveillance de ces problèmes environnementaux et l'amélioration des activités économiques, telles que la navigation, la pêche, ou le développement et l'exploitation de structures offshore pour l'extraction d'énergie.

L'augmentation de la résolution spatiale dans les modèles régionaux a permis de résoudre la mésoéchelle océanique ( $O(100\text{km})$ ), ce qui a contribué notamment à largement améliorer la représentation de la dynamique du GdM. Cependant, des biais persistent dans nos modèles, comme par exemple, un LC qui ne pénètre pas assez dans le GdM ainsi qu'une énergie tourbillonnaire trop importante. Les deux dernières décennies ont été marquées par l'avènement de nouveaux satellites et le développement de modèles régionaux couplés océan-atmosphère. Cela a permis l'émergence d'études portant sur les interactions entre l'Océan et l'Atmosphère à fine-échelle. Dans un premier temps, les efforts de la communauté scientifique se sont principalement focalisés sur l'interaction thermique entre l'océan et l'atmosphère. Plus récemment, de nombreuses études ont démontré que la prise en compte de l'interaction mécanique entre les courants de surface et l'atmosphère (Current FeedBack en anglais, CFB) corrigeait des biais persistants dans la représentation de la dynamique océanique en fournissant un puit d'énergie de l'Océan vers l'Atmosphère. Cependant, l'effet du CFB sur la dynamique du GdM est méconnu. Le principal but de cette thèse est d'étudier son impact sur la dynamique du GdM avec une attention particulière sur les caractéristiques du LC et des tourbillons libérés par le LC.

Pour ce faire, une double approche est proposée. Elle se base sur l'utilisation de données satellites et de simulations jumelles couplées océan-atmosphère riches en tourbillons, avec et sans CFB, qui ont été réalisées pour la période 1993-2016 sur le GdM. Je démontre dans un premier temps que le CFB induit un transfert de quantité de mouvement des courants de mésoéchelle vers l'atmosphère, ce qui entraîne *i.e.*, une réduction de l'activité de mésoéchelle (*eddy killing* dans la littérature), ici d'environ 20%. Je montre en outre la présence d'un

effet indirect du CFB : en réduisant l'activité à mésoéchelle, le CFB diminue les interactions d'échelles entre tourbillons et courants moyens, ce qui a pour effet de moduler les caractéristiques du LC, les libérations de tourbillons par ce dernier et les propriétés des jets frontaux présents le long du LC. Enfin, via une analyse basée sur des observations satellites sur une période de 24-ans, nous démontrons que les détachements de tourbillons survenant au nord de  $25^{\circ}\text{N}$  sont plus susceptibles de mener à une séparation définitive, tandis que les détachements survenant au sud de  $25^{\circ}\text{N}$  sont plus susceptibles de se rattacher. Les tourbillons cycloniques semblent aussi jouer un rôle important dans la séparation définitive des LCEs. Le CFB, en réduisant l'énergie tourbillonnaire, aurait ainsi un rôle déterminant à jouer dans cette dynamique. Je conclurai cette thèse en discutant des interactions des vagues avec l'Océan et l'Atmosphère qui sont, jusqu'à présent, largement ignorée dans la littérature.

**Mots clés :** *Golfe du Mexique ; interactions air-mer ; rétroaction des courants ; modélisation régionale couplée océan-atmosphère ; observations altimétriques ; dynamique du golfe du Mexique ; détachement des tourbillons*

---

---

**Abstract** — At basin-scale, it has been recognized for several decades that interactions between the ocean and the atmosphere have a major influence on the Earth’s climate. However, persistent biases in global models, for example in sea surface temperature, have highlighted the limitations of a global approach at relatively low spatial resolution. This led to a new line of research based on a regional approach to ocean dynamics and ocean-atmosphere interactions. This thesis is part of this approach by focusing on the Gulf of Mexico (GoM).

The GoM is located in the northwest region of the Atlantic Ocean. It represents a complex system where human activities, such as oil extraction and fishing, interact extensively with the ocean environment and biogeochemical ecosystems. The dynamics of the GoM are dominated by the emblematic Loop Current (LC), an intense anticyclonic current that brings warm Caribbean waters into the GoM. The LC episodically sheds warm core anticyclonic eddies that propagate westward: the Loop Current Eddies (LCEs). However, the GoM is facing increasing environmental problems such as oil spills and plastics. Knowledge of ocean dynamics is of utmost importance for understanding and monitoring these environmental problems and improving economic activities, such as shipping, fishing, or the development and exploitation of offshore structures for energy extraction.

The increase in spatial resolution in regional modeling allowed us to resolve the oceanic mesoscale activity  $O(100\text{km})$ , which has contributed to greatly improve the representation of the GoM dynamics. However, biases persist in our models, such as a LC that does not penetrate enough into the GoM and a too energetic mesoscale activity. The last two decades have been marked by the advent of new satellites and the development of coupled regional ocean-atmosphere models. It allowed the emergence of studies focusing on fine-scale interactions between the Ocean and the Atmosphere. Initially, the efforts of the scientific community were mainly focused on the thermal interaction between the ocean and the atmosphere. More recently, many studies have shown that ocean models, including the mechanical interaction between surface currents and the Atmosphere (the Current FeedBack, CFB), correct persistent biases in the representation of ocean dynamics by providing an energy sink from the Ocean to the Atmosphere. However, the effect of CFB on the dynamics of the GoM is poorly understood. The main goal of this thesis is to study its impact on the GoM dynamics with a particular focus on its impact on the characteristics of the LC and LCEs.

To do so, a double approach is proposed. It is based on the use of satellite data and coupled ocean-atmosphere eddy-rich twin simulations, with and without CFB, which were performed for the period 1993-2016 over the GoM. First, it is shown that CFB induces a transfer of momentum from mesoscale currents to the atmosphere, which leads to a reduction of the mesoscale activity (*aka eddy killing* in the literature), here, of about 20%. We also show the presence of an indirect impact of the CFB: by reducing the mesoscale activity, the CFB decreases the cross-scale interactions between eddies and mean currents, thus modulating the characteristics of the LC, the eddy-shedding, and the frontal jets present along the LC. Finally, via an analysis based on satellite observations over a 24-year period, we show that eddy detachments occurring north of  $25^\circ\text{N}$  are more likely to lead to definitive separation, while detachments occurring south of  $25^\circ\text{N}$  are more likely to reattach. Cyclonic eddies are

also shown to play an important role in the final separation of LCEs. The CFB, by reducing the eddy energy, would thus play a determining role in their dynamic. I will conclude this thesis by discussing the interactions of waves with the Ocean and the Atmosphere, which are, until now, largely ignored in the literature.

**Keywords:** *Air–sea interactions; current feedback; regional coupled ocean–atmosphere modeling; altimeter observations; Kinetic energy budget; Gulf of Mexico dynamics; Loop Current variability; Loop Current eddy detachments; frontal eddies*

---

# Acknowledgments

I would like to express my deep appreciation and gratitude to the individuals who have contributed significantly to the completion of my doctoral thesis. Their support, guidance, and encouragement have been invaluable throughout this research journey.

I am immensely grateful to my thesis supervisors, Julien Jouanno and Lionel Renault, for their exceptional mentorship, unwavering support, and expert guidance. Their extensive knowledge, insightful feedback, and dedication to academic excellence have been instrumental in shaping the direction and quality of my research. I am truly fortunate to have had the opportunity to work under their supervision.

I would like to extend my sincere thanks to Sébastien Masson, Julio Shienbaum, Matthieu Le Hénaff, Paula Pérez Brunius, and Yves Morel, who served as my thesis examiners. Their thorough evaluation, constructive criticism, and valuable suggestions have significantly enhanced the rigor and credibility of my work. I am grateful for their expertise and commitment to maintaining the highest academic standards.

My heartfelt appreciation goes to my colleagues in the PhD program, Gabriela, Manon, Pierre, Lisa, Adélaïde, Benjamin, Margot, Camille, Arne, Julia, Roberto, Carlos, and Marcela. Their intellectual contributions, engaging discussions, and mutual support have created a stimulating academic environment. The collaborative spirit and shared experiences within our group have been a source of inspiration and motivation throughout this journey.

I want to express my gratitude to my dear friends Guillaume Morvan, Ross Sosa, and Fernando Niño. Your unwavering friendship, support, and encouragement have been invaluable. The moments of camaraderie, shared experiences, and uplifting conversations have provided much-needed respite during the challenges of the research process. I am grateful for your presence in my life.

I sincerely thank the administrative team members, Brigitte, Agathe, Bertrand, Nicolas, and Catherine. Their efficient management, meticulous attention to detail, and willingness to assist have significantly facilitated the administrative aspects of my research. I appreciate their professionalism and dedication.

I would also like to acknowledge the contributions of Geoffray and Caroline from the computing team. Their technical expertise, guidance, and support in handling computational aspects have been instrumental in the execution of my research. I am grateful for their assis-

tance and collaboration.

To Geneviève Soucail and Adrien Bru, members of the doctoral school, I offer my heartfelt appreciation. Your guidance, administrative support, and responsiveness to my inquiries have been invaluable in navigating the academic processes. I am thankful for your assistance and commitment.

I want to express my deepest gratitude to my family in Mexico. Your unwavering love, encouragement, and belief in my abilities have been my driving force. Your constant support and sacrifices have provided me with the strength to overcome challenges and pursue my academic aspirations. I am forever grateful for your presence in my life.

Lastly, I would like to convey my heartfelt thanks to my wife Jessica and my son Marco. Your love, patience, and understanding have been my constant source of inspiration. Your unwavering support and sacrifices have enabled me to pursue this academic endeavor. I am deeply grateful for your presence, encouragement, and belief in me.



# Contents

<b>Acronyms</b>	<b>xiii</b>
<b>General introduction</b>	<b>1</b>
<b>Introduction générale</b>	<b>5</b>
<b>1 Background</b>	<b>9</b>
1.1 The Gulf of Mexico . . . . .	10
1.2 Mesoscale Air-Sea Interactions . . . . .	27
1.3 The thermal feedback . . . . .	32
1.4 The current feedback to the atmosphere . . . . .	36
1.5 The wave feedback to the atmosphere and the ocean . . . . .	42
<b>2 Materials and method</b>	<b>49</b>
2.1 Numerical simulations and observational datasets . . . . .	50
2.2 Methods . . . . .	53
<b>3 Long-term conditions over the Intra-Americas Sea and numerical validations</b>	<b>57</b>
3.1 Mean and eddy circulation . . . . .	58
3.2 Sea Surface Temperature and air-sea heat fluxes . . . . .	60
3.3 Wind stress and wind stress curl . . . . .	62
3.4 Sensitivity to the Current Feedback . . . . .	63
<b>4 Partial control of the Gulf of Mexico dynamics by the current feedback to the atmosphere</b>	<b>65</b>
4.1 Introduction . . . . .	66
4.2 Modulation of the kinetic energy and energy conversion by the current feedback	66

4.3	Discussion and conclusions . . . . .	80
<b>5</b>	<b>The role of cyclonic eddies in the detachment and separation of Loop Current eddies and clues of their modulation by the current feedback</b>	<b>83</b>
5.1	Introduction . . . . .	84
5.2	Preferential latitudes of detachments . . . . .	84
5.3	The role of cyclonic eddies in the detachment of Loop Current eddies . . . . .	85
5.4	Discussion and conclusions . . . . .	89
<b>6</b>	<b>Spatial scales of the eddy wind work over the Loop Current</b>	<b>93</b>
6.1	Introduction . . . . .	94
6.2	Methods . . . . .	94
6.3	Energy transfers . . . . .	95
6.4	Impact of the CFB on cyclonic eddies and frontal jets . . . . .	97
6.5	Unraveling the kinetic energy budget over the Loop Current region at 80 km scale . . . . .	102
6.6	Discussion and conclusions . . . . .	104
	<b>Conclusion and perspectives</b>	<b>107</b>
	<b>Bibliography</b>	<b>119</b>

# List of Figures

1.1	Main dynamical features of the GoM dynamics illustrated by a snapshot of AVISO sea surface height anomaly for March 5, 1998. The continuous contours highlight the Loop Current (LC) and LC eddies (LCE). The dashed contours highlight the LC frontal eddies. YC refers to Yucatan Channel, FS to Florida Straits, DT to Dry Tortugas islands, MF to Mississippi Fan, CS to the Caribbean Sea, FE to frontal eddy, CCE to Caribbean cyclonic eddy, TE to Tortugas eddy, and MARB to the Mississippi–Atchafalaya River Basin. The gray contours refer to the 200 m (continuous), 2500 m (dashed), and 3500 m (thin and continuous) depths. . . . .	10
1.2	Large-scale features of the GoM dynamics illustrated with the kinetic energy averaged over 29-year of altimeter data. The thick black line represents the LC, the thin black line the western gulf anticyclonic gyre (WGAG), and the segmented line represents the Bay of Campeche cyclonic gyre (BCCG). . . .	11
1.3	Temperature (top) and salinity (bottom) sections measured in the anticyclonic eddy Poseidon. The thick contour shows the 1025-isopycnal contour. The figure is taken from <a href="#">Meunier et al. (2021)</a> . . . . .	13
1.4	Production of barotropic (a) and baroclinic (b) instabilities from 14-year numerical simulations from <a href="#">Garcia-Jove (2016)</a> . . . . .	15
1.5	Relative vorticity ( $10^{-5} \text{ s}^{-1}$ ) evolution over 45 days. Black lines are the relative vorticity near the surface, while green lines in deeper regions. Solid lines represent positive values and dashed lines the negative ones. Letters from A to D indicate Loop Current frontal eddies. Subscript d indicates the deep part of cyclonic eddies. Figure taken from <a href="#">Le Hénaff et al. (2012)</a> . . . . .	17
1.6	Hovmöller diagram of sea surface height anomalies along the western Caribbean Sea and Campeche Bank. Segmented lines indicate LCEs detachments. Figure taken from <a href="#">Jouanno et al. (2016)</a> . . . . .	18
1.7	Time series of the sea level anomaly from altimeter along-tracks. Positive values depict the LC, whereas negative values represent the presence of cyclonic eddies. The occurrence of LCEs separation is shown with gray lines. Figure taken from <a href="#">Zavala-Hidalgo et al. (2006)</a> . . . . .	19
1.8	Example of frontal jets resulting from the interaction between the LC (black continuous contour) and frontal eddies (black segmented circles). . . . .	20

1.9	The LC in the presence of a weak (a) and intensified frontal eddy (b). The LC is represented by the black contour, a mooring array by the gray dots, and the transect from where the corresponding temperature profiles (c,d) are represented by the black line. Current speeds perpendicular to the transect are displayed by white lines, dotted lines for the southwestward component, and solid lines for the northwestward component. The figure is taken from <a href="#">Hiron et al. (2020)</a> . . . . .	21
1.10	Mean sea surface height averaged over the 2009–2011 period. The LC is represented by the black contour and the black exhibit the occurrence of frontal jets and intensified frontal eddies. The figure is taken from <a href="#">Hiron et al. (2020)</a> .	22
1.11	Wind speed seasonal climatology (from 1999 to 2009) inferred from SCOW (Scatterometer Climatology of Ocean Winds). . . . .	25
1.12	Seasonal climatologies (2001 to 2010) of significant wave heights for winter (a), spring (b), summer (c), and autumn (d). The mean wave direction is represented by the black arrows. The figure is taken from <a href="#">Abolfazli et al. (2020)</a> . . . . .	27
1.13	Lorenz diagram of main energy sources and conversion terms. Continuous lines represent the classic energy source and conversion terms, while dashed lines represent the energy sources and conversion terms when using coupled models that consider the feedbacks between the ocean, sea surface waves, and the atmosphere. MPE and EPE are the mean and eddy potential energy. MKE and EKE are the mean and eddy potential energy. $F_m P_m$ and $F_e P_e$ are the sources of potential energy related to buoyant fluxes, whereas $F_m K_m$ and $F_e K_e$ are the sources of kinetic energy related to the wind work. $P_m K_e$ is the conversion of MPE to MKE, $P_m P_e$ is the conversion of MPE to EPE, $K_m K_e$ is the conversion of MKE to EKE, and $P_e K_e$ is the conversion of EPE to EKE. DMPE, DEPE, DMKE, and DEKE represent the dissipation of MPE, EPE, MKE, and EKE, respectively. . . . .	32
1.14	Linear relationships between the sea surface temperature and the wind stress divergence and curl. $s$ corresponds to the linear regression slope. Figure taken from <a href="#">Chelton (2004)</a> . . . . .	33
1.15	Wind stress anomalies resulting from the winds blowing along or crossing sea surface temperature fronts. Figure taken from <a href="#">Chelton (2004)</a> . . . . .	34
1.16	Impact of warm-core (left) and cold-core (right) Southern Ocean mesoscale eddies on atmosphere properties. Div. refers to wind divergence and Conv. to wind convergence. Figure taken from <a href="#">Frenger et al. (2013)</a> . . . . .	35
1.17	Sources of potential energy at the large, seasonal, and turbulent scales. The figure is taken from <a href="#">Bishop et al. (2020)</a> . . . . .	36

1.18 Schematic representation of mechanical air-sea interactions when not considering (left) and considering (right) CFB on a uniform northward (upper) and southward (lower) wind blowing over a northward coastal current. MWW refers to the wind work. The red color refers to a positive wind work, *i.e.*, transfer of energy from the atmosphere to the ocean. The blue color refers to a negative wind work, *i.e.*, transfer of energy from the ocean to the atmosphere. Scheme modified from Renault et al. (2016a). . . . . 38

1.19 Schematic representation of mechanical air-sea interactions when considering (left) and not considering (right) CFB on a uniform southward wind blowing over an anticyclonic eddy. EWW refers to the eddy wind work. The red color refers to a positive wind work, *i.e.*, transfer of energy from the atmosphere to the ocean. The blue color refers to a negative wind work, *i.e.*, transfer of energy from the ocean to the atmosphere. Scheme modified from Renault et al. (2016a). . . . . 39

1.20 Coupling coefficient between the vorticity of surface geostrophic currents and the surface stress curl. Figure taken from Renault et al. (2019b). . . . . 40

1.21 Observed eddy wind work ( $1 \times 10^{-6} \text{ m}^3 \text{ s}^{-3}$ ) estimated from 9-year satellite measurements of surface stress and geostrophic currents. The figure is taken from Renault et al. (2017a). . . . . 40

1.22 Coupling coefficient between the vorticity of surface geostrophic currents and the surface winds from observations (a) and numerical simulations (b,c). The coupling coefficient  $s_w$  in b) is computed using the equivalent neutral winds relative to surface currents, whereas in c) is computed directly from the 10-m winds. Figure taken from Renault et al. (2019b). . . . . 41

1.23 Representation of the momentum balance and wave-induced mixing related to the wave breaking and vertical shear of Stokes drift.  $k$  represents the wave number. Foam and curved arrows on the free surface indicate wave breaking and related mixing. Scheme modified from Belcher et al. (2012). . . . . 42

1.24 Development of Langmuir cells. Wind-driven current perturbations are indicated by  $\hat{u}$ , their vorticity by  $\zeta$ , and the Stokes drift profile by  $U_s$ .  $vf$  is the vortex-force. Scheme modified from Leibovich (1983) and Sullivan et al. (2007). 43

1.25 Mean flow velocity is related to the full Ekman balance (thick line). Ekman (thin line) and Ekman-Stokes (segmented line) components are depicted with the thin and segmented lines, respectively. Dotted-dashed line is the Stokes drift components. All quantities are normalized with the friction velocity ( $u_*$ ). Scheme modified from Polton et al. (2005). . . . . 44

1.26 Mean differences in the wind stress computed with and without the influence of surface waves over 3-year numerical simulations. Figure taken from Chune and Aouf (2018). . . . . 46

1.27	Mean differences in the wind stress computed with and without the influence of surface waves over 3-year numerical simulations. The figure is taken from Couvelard et al. (2020). . . . .	47
1.28	Drag coefficient $C_{d_w}$ as a function of the wind speed ( $ U_a $ ). WS_CPL and NO_CPL refer to the numerical experiments with and without a Charnock parameter dependent on the sea state. The figure is taken from Couvelard et al. (2020). . . . .	47
2.1	Numerical domains of NEMO (black square) and WRF (gray square). . . . .	50
3.1	Polygons to delimit the Gulf of Mexico (GoM), Caribbean Sea (CS), and the northern and southern Atlantic (AtlN and AtlS) regions. . . . .	58
3.2	Geostrophic currents climatology and main dynamical features over the IAS from 1993 to 2016. . . . .	59
3.3	KE (first column), MKE (second column), and EKE (third column) climatologies over the IAS for AVISO (first row), CF (second row), and NOCF (third row). j-1) Spatially integrated energy over the regions comprising the IAS is shown in the bottom row. . . . .	60
3.4	Sea surface temperature climatology (1993 to 2016) computed from AVHRR and its difference with respect to CF (b) and NOCF (c). The occurrence of the 26 and 28 °C is delimited by the thin and thick contours, respectively. Differences of $-1^\circ\text{C}$ are shown with the segmented black line (b-c). . . . .	61
3.5	Net (first row), radiative (second row), and turbulent (third row) heat fluxes climatologies (1993 to 2016) for OAFLUX (first column) and their differences with respect to the numerical simulations CF (second column) and NOCF (third column). The thick and black contour in the first row depicts the 0 $\text{W}/\text{m}^2$ net heat flux. Thin continuous (segmented) contours in the second and third columns depict positive (negative) differences of 25 $\text{W}/\text{m}^2$ . . . . .	62
3.6	Wind stress (first row) and wind stress curl (second row) climatologies from 1993 to 2009. SCOW climatologies are shown in the first row, while climatologies from CF and NOCF experiments are shown in the second and third rows. . . . .	63
3.7	Differences between CF and NOCF with respect to the sea surface temperature (a), wind stress (b), and wind stress curl (c) climatologies. . . . .	64

4.1 Surface mean kinetic energy (first row) and eddy kinetic energy (second row) climatologies (1993–2016) from AVISO (first column), NOCF (second column), and CF (second column). The 17 cm contours of the climatological sea surface height anomaly of AVISO and the numerical experiments are represented by the thin segmented line and the continuous line, respectively. The thick segmented lines delimit the LC (east), center (GoMC), and west (GoMW) regions. GoM makes reference to the whole Gulf of Mexico. The light gray contours refer to the 200 (continuous) and 2500 m (segmented) depths. Spatially integrated values over regions are shown in the last row. . . . . 67

4.2 Difference between CF (a) and NOCF (b) EKE climatologies (1993–2016). The 17 cm contours of the climatological sea surface height anomaly of NOCF and CF experiments are represented by the black thin line and the black thick line, respectively. The thick segmented lines delimit the LC (east), center (GoMC), and west (GoMW) regions. GoM makes reference to the whole Gulf of Mexico. The light gray contours refer to the 200 (continuous) and 2500 m (segmented) depths. . . . . 68

4.3 Mean (solid lines) and standard deviation (shading area) of geostrophic currents along the Yucatan Channel. Segmented lines in NOCF and CF are associated with an error estimation of the mean current obtained by using a bootstrap method over 50,000 random samples. To more easily appreciate the bootstrap error bars, a zoom of the region with stronger currents in the numerical simulations is included in the upper right corner of the figure. . . . 69

4.4 Barotropic (top) and baroclinic (bottom) instabilities maps and spatially integrated values over regions (right) for the NOCF and CF experiments for the period 1993–2016. The segmented lines delimit the LC (east), center (GoMC), and west (GoMW) regions. GoM makes reference to the whole Gulf of Mexico. The light gray contours refer to the 200 (continuous) and 2500 m (segmented) depths. . . . . 70

4.5 Eddy (top) and mean (center) geostrophic wind work maps and spatially integrated values over regions (right) for the NOCF and CF experiments for the period 1993–2016. The segmented lines delimit the LC (east), center (GoMC), and west (GoMW) regions. GoM makes reference to the whole Gulf of Mexico. The light gray contours refer to the 200 (continuous) and 2500 m (segmented) depths. Spatially integrated energy budget terms over the LC region are shown in the last panel (g). . . . . 72

- 4.6 Probability density functions related to the occurrence of LC maximum latitudes and longitudes for the period 1993–2016 for AVISO (first column), NOCF (second column) and CF (third column), and associated average of spatially integrated KE. The thick, medium–thick, and thin–black contours represent examples of the retracted, canonical, and elongated LC forms, respectively. The light gray contours refer to the 200 (continuous) and 2500 m (segmented) depths. . . . . 74
- 4.7 Number of separated LCEs as a function of the number of days between separations. . . . . 76
- 4.8 Trajectories related to LCEs with a lifetime longer than 200 days for AVISO (a), NOCF (b), and CF (c). Gray squares represent the location of a LC eddy liberation, and gray circles the location where LCEs are no longer detected. The colormap refers to the corresponding climatology of EKE. The 17 cm contours of the climatological sea surface height anomaly of AVISO and the numerical experiments are represented by the black line. The light gray contours refer to the 200 (continuous) and 2500 m (segmented) depths. (d) Number of LCEs that cross the segmented thick line shown in panel a) as a function of the latitude. . . . . 77
- 4.9 LC most extended position (gray dots) after separation (first row) and reattachment (second row) events, for AVISO (first column), NOCF (second column), and CF (third column). The light gray contours refer to the 200 (continuous) and 2500 m (segmented) depths. PDFs related to the latitude of the LC most extended position after separation and reattachment events are shown in g) and h). . . . . 78
- 4.10 LC eddy composite of temperature (first column) and salinity (second column) and the relative vorticity ( $\zeta$ ) normalized with the Coriolis parameter ( $f$ ; third column) for CF (first row) and NOCF (second row). Black and thick contours indicate thermoclines at 26 and 220 m depth. Normalized relative vorticity contours of 0.05, 0.1, and 0.5 are shown using white lines. . . . . 80
- 5.1 a) LC outermost position after reattachment/separation events (orange/blue). b) Histogram related to the number of reattachment (orange) and separation (blue) events as a function of their latitude of occurrence. YC refers to Yucatan Channel, FS to Florida Straits, DT to Dry Tortugas islands, MF to Mississippi Fan, CBS to the Caribbean Sea, and CHB to Chinchorro Bank. Black dots are used to build the transects for the Hovmöller diagrams in figures 3 and 4. The light gray contours refer to the 200 m (continuous) and 2500 m (dashed) depths. . . . . 85

5.2 Rossby number composites during LCEs detachment that end in reattachments (first row) and separation (second row) for the *south* (first column), *center* (second column), *north* (third column), and *upper north* (fourth column) regions. Continued and discontinued black contours represent the LC (17 cm) and CEs (-18 cm). Gray circles represent the LC outermost position after detachment events used for the composites. The light gray contours refer to the 200 m (continuous) and 2500 m (dashed) depths. . . . . 86

5.3 Rossby number composites related to the evolution of reattachments (first row), and separations (third row) events for the *south* region. Continued and discontinued black lines represent the LC (17 cm contour of the SSHa) and CEs (-18 cm contour of the SSHa). Gray circles represent the LC outermost position after detachment events used for the composites (c and h). The light gray contours refer to the 200 m (continuous) and 2500 m (dashed) depths. Hovmöller diagrams the low-pass filtered (30 days) SSHa composites of reattachment and separation events are shown in the last column. The LC is represented by the black contour. . . . . 87

5.4 Rossby number composites related to the evolution of reattachments (first row), and separations (third row) events for the *north* region. Continued and discontinued black lines represent the LC (17 cm contour of the SSHa) and CEs (-18 cm contour of the SSHa). Gray circles represent the LC outermost position after detachment events used for the composites (c and h). The light gray contours refer to the 200 m (continuous) and 2500 m (dashed) depths. Hovmöller diagrams the low-pass filtered (30 days) SSHa composites of reattachment and separation events are shown in the last column. The LC is represented by the black contour. . . . . 89

5.5 Mean diameter (a) and KE (b) of LCEs after separation events. The standard deviation is represented by black lines. . . . . 91

6.1 Geostrophic eddy wind work  $FeK_{eg}$  for scales ranging from 16 km to 256 km and spatially integrated over the polygon delimited by the black segmented contours in Figure 6.2 and out of the shelf delimited by the 200 m depth contour. . . . . 95

6.2 10-years of averaged coarse-grained geostrophic eddy wind work (first column), baroclinic instability (second column), and barotropic instability (third column) for the NOCF (first row) and CF (second row) experiments. The 10-year LC mean position is represented by the 17 cm contour of the sea surface height anomaly. The thick segmented black lines delimit the LC region. The light gray contours refer to the 200 (continuous) and 2500 m (segmented) depths. Spatially integrated values over the LC region are shown in the last row. . . . . 96

6.3	Kinetic energy snapshots from CF every 7 days from February 7, 2006, to March 14, 2006. Black continuous contours denoted the LC and black segmented contours represent the cyclonic eddies. FE refers to frontal eddy and TE to Tortugas eddy. The light gray contours refer to the 200 m (continuous) and 2500 m (dashed) depths. . . . .	98
6.4	24-year statistics about the diameter (first row) and KE (second row) of cyclonic eddies (first column) and frontal jets (second column). The mean and standard deviation of cyclonic eddies and frontal jets properties are included on the top right corner. . . . .	99
6.5	Two-dimensional probability density function relating the diameter and KE of cyclonic eddies (first column) and frontal jets (second column) for the numerical simulations NOCF (first row) and CF (second row). The figures show the number of eddies and jets for the different classifications delimited by the segmented lines. The second line shows the percentage increase/decrease in the number of eddies and jets from NOCF to CF. . . . .	100
6.6	Probability of cyclonic eddies (first column) and frontal jets (third column) occurrence over the GoM over 24-years and associated kinetic energy (second and fourth columns) for AVISO (first row) and the numerical simulations NOCF (second row) and CF (third row). A thick contour represents the mean LC penetration into the GoM. The light gray contours refer to the 200 m (continuous) and 2500 m (dashed) depths. MF represents the Mississippi Fan and DT Dry Tortugas Islands. . . . .	101
6.7	Coarse-grained geostrophic eddy wind work (first row) and baroclinic (second row) and barotropic (third row) energy conversions decomposed into their low-frequency (first column), high-frequency (second column), and non-linear interaction components (third column). The thick segmented black lines delimit the LC region. The light gray contours refer to the 200 (continuous) and 2500 m (segmented) depths. . . . .	103
6.8	Spatially integrated coarse-grained EKE budget terms over 10-years for NOCF (orange) and CF (blue). Forward and inverse cascade energy fluxes are spatially integrated in a), whereas only Forward cascade energy fluxes are considered in b) and only inverse cascade energy fluxes in c). . . . .	104
6.9	EKE climatologies over the Intra-Americas Sea for AVISO (a), CF (b), and NOCF (c). Spatially integrated MKE (d) and EKE (e) over the regions comprising the IAS are shown in the bottom row. GoM refers to the Gulf of Mexico, CS to the Caribbean Sea, and ATLS to the south Atlantic region. . . . .	112

# List of Tables

1.1	Main characteristic of numerical simulations. Their performance related to the LC penetration into the GoM and separation of LCEs is evaluated in Table 1.2. RIF refers to reduced inflow. . . . .	23
1.2	Comparison of statistics related to the LC penetration into the GoM and the separation of LCEs between AVISO and different numerical simulations. AVISO statistics are computed over 24-years of daily data. RIF refers to reduced inflow, NSE to the number of separated eddies, and PBS to the period between separations. . . . .	24
1.3	Main characteristic of numerical simulations that include surface wave interactions with the ocean or atmosphere. OCE and ATM refer to the ocean and atmosphere models used in the numerical implementations. BS and NS refer to the Baltic Sea and North Sea, respectively. . . . .	45
1.4	Numerical simulations that include surface wave interactions with the ocean or atmosphere and their parametrizations. VF, SC, LT, and TKE refer to vortex-force, Stokes-Coriolis, Langmuir turbulence, and turbulent kinetic energy, respectively. The superscript (*) indicates that the variable has been computed in the wave model. . . . .	45
2.1	Main characteristic of numerical simulations. The Charnock parameter ( $\alpha$ ) in NOCF and CF experiments is equal to 0.0185, whereas in the WF experiment, $\alpha_w$ is estimated directly by WW3 and sent to WRF. . . . .	52
4.1	Statistics of Yucatan Channel current. The current width is computed as the distance between locations with velocities larger than $0.6 \text{ ms}^{-1}$ and the current speed rate of change from the maximum speed to the eastern region of the Yucatan Channel. . . . .	69
4.2	Statistics related to the LCEs shedding and their detection through the eddy detection method (EDM). A number of detached LCEs (first column). A number of LCEs that are not reabsorbed by the LC and travel to the west of the GoM (second column). A number of separated eddies detected by the eddy detection method (EDM; third column). A number of separated eddies detected by the eddy detection method (EDM) with a lifetime longer than 200 days (fourth column). . . . .	75
4.3	Statistics of LCEs properties with a lifetime longer than 200 days. . . . .	79



# Acronyms

<b>GoM</b>	<i>Gulf of Mexico</i>
<b>LC</b>	<i>Loop Current</i>
<b>LCE</b>	<i>Loop Current eddy</i>
<b>CFB</b>	<i>Current feedback</i>
<b>WF</b>	<i>Wave feedback</i>
<b>KE</b>	<i>Kinetic energy</i>
<b>MKE</b>	<i>Mean kinetic energy</i>
<b>EKE</b>	<i>Eddy kinetic energy</i>
<b>TKE</b>	<i>Turbulent kinetic energy</i>
<b>NEMO</b>	<i>Nucleus for European Modeling of the Ocean</i>
<b>WRF</b>	<i>Weather Research and Forecasting</i>
<b>WW3</b>	<i>WAVEWATCH III</i>
<b>AVHRR</b>	<i>Advanced Very High Resolution Radiometer</i>
<b>SCOW</b>	<i>Scatterometer Climatology of Ocean Winds (SCOW)</i>



# General introduction

The Gulf of Mexico (GoM) is located in the northwest region of the Atlantic Ocean. This region is a complex system where human activities, such as oil extraction and fisheries, largely interact with the ocean environment (*e.g.*, strong currents, river discharges, and atmospheric features such as storms or hurricanes) and biogeochemical ecosystems (McKinney et al., 2021). The GoM dynamics are dominated by the Loop Current (LC), an intense anticyclonic-shaped current that brings warm Caribbean water into the GoM. The LC episodically sheds long-living warm-core anticyclonic eddies that propagate westward: the so-called Loop Current Eddies (LCEs; Leben, 2005). However, the GoM is facing increasing environmental issues such as oil spills (White et al., 2012; Kostka et al., 2011; Michel et al., 2013) and plastics (Phillips and Bonner, 2015). The knowledge of ocean dynamics is of uppermost importance for the understanding and monitoring of these environmental issues and improving economic activities, such as navigation, fisheries, or the development and operation of offshore structures for energy extraction.

Early efforts to describe the dynamics of the GoM are related to hydrography campaigns (Ichiye, 1959; Cochrane, 1972; Elliott, 1982). Infrared satellite images capable of mapping LCEs arrived in 1973. These images allowed the identification of LCEs during winter through their thermal contrast with surrounding waters, which was not possible during the summer since the warming of surface waters largely reduces the thermal contrast between the dynamical features over the GoM (Cooper et al., 1990). The arrival of satellite-altimeters led to significant advances in our knowledge of the GoM dynamics, allowing us to quantify the LC variability in terms of its penetration into the GoM and LCEs detachment statistics (Leben, 2005). However, altimetry only allows detecting large structures in geostrophic balance, *i.e.*, large mesoscale eddies and western boundary currents, leaving aside small geostrophic structures and many ageostrophic processes such as unbalanced eddies and wind-driven currents (Chelton et al., 2011; Amores et al., 2018; Archer et al., 2020). Realistic numerical oceanic simulations are often used to go one step forward and overcome observational uncertainties, by allowing us to represent ocean dynamics with a finer temporal and spatial resolution, but also by providing information on currents and thermodynamic variables at depth.

Nevertheless, reproducing the GoM circulation remains a challenge for numerical modelers (Oey et al., 2005). Indeed, on the one hand, numerical models with a low spatial resolution ( $1^\circ$ ) tend to produce a nearly stationary LC that fails to extend into the GoM (*e.g.*, Putrasahan et al., 2017). On the other hand, eddy-rich simulations with a spatial resolution of about 10 km (or less) can reproduce the main GoM dynamics but are characterized by persistent biases in, *e.g.*, the LC penetration into the GoM and the LC eddy detachments (Le Hénaff et al., 2012; Garcia-Jove et al., 2016; Putrasahan et al., 2017). Eddy-rich coupled ocean-atmosphere simulations that consider the Thermal FeedBack (TFB), *i.e.*, the influence of sea surface temperature on the atmosphere, have been implemented in an attempt to better reproduce the GoM dynamics (Putrasahan et al., 2017). Although TFB improved numerical results by better resolving turbulent heat fluxes between the atmosphere and the ocean, biases

in the LC variability and LCEs detachment statistics remain (Putrasahan et al., 2017).

These biases could be related to the fact that forced eddy-rich simulations are characterized by high energy levels compared to observations. This has been shown by Jullien et al. (2020), who compared the eddy kinetic energy (EKE) of high and low-resolution simulations ( $1/12^\circ$  and  $1/4^\circ$ , respectively). The results show that high-resolution simulations have at least two times larger EKE in comparison with lower spatial resolution simulations ( $1/4^\circ$ ) and overestimate by over 30% the EKE in altimeter observations. However, it is well known that an optimal interpolation applied to altimetric products smooths and underestimates their EKE estimation (Chelton et al., 2011; Amores et al., 2018; Archer et al., 2020), so the bias between observations and forced eddy-rich simulations could be smaller. Nevertheless, the authors exhibit that high-resolution models need an energy sink to better represent the energy at the mesoscale. Chassignet and Xu (2017) suggest that this energy overestimation can be counteracted by increasing the model viscosity. Coupled ocean-atmosphere simulations considering the feedback of surface currents to the atmosphere, *i.e.*, the Current FeedBack (CFB), has been shown to better reproduce the energy at the (sub)mesoscale by inducing a sink of energy from the ocean to the atmosphere at both large-scale and fine-scale (Renault et al., 2016a,b, 2017b; Seo et al., 2017; Oerder et al., 2018; Jullien et al., 2020; Renault et al., 2021a). These studies have been mostly carried out in places characterized by western boundary currents and rich in mesoscale activity, *e.g.*, Gulf Stream and the Agulhas Current retroflection, but also in other regions with a large mesoscale activity such as the California Current, the Humboldt Current, and the Mediterranean Sea. CFB induces damping of the (sub)mesoscale activity by roughly 30% and better-representing large-scale currents, *e.g.*, Gulf Stream and Agulhas Current retroflection. Therefore, as the GoM is characterized by intense mesoscale dynamics, mesoscale air-sea interactions may play a key role in determining its dynamical equilibrium.

The surface gravity Wave FeedBacks (WFB) to the ocean and the atmosphere is a hot topic within the Earth Science community, as *e.g.*, illustrated by the recent launch of the CFOSAT (Chinese French Ocean SATellite) mission, which provides wave measurements of the directional spectra of sea surface waves (Hauser et al., 2021). Waves can have several impacts on momentum, heat, and freshwater fluxes through feedback loops between waves and the atmosphere (via a change in the roughness) and between waves and the ocean (via *e.g.*, wave-induced mixing). Several efforts have been made to assess the role of surface waves over the ocean and atmosphere by using global forced (atmosphere-waves or atmosphere) simulations, as well as coupled ocean-waves-atmosphere simulations (Breivik et al., 2015; Chune and Aouf, 2018; Pianezze et al., 2018; Wu et al., 2019b,a; Couvelard et al., 2020). Ocean models in these studies have different spatial resolutions, solving or not the full ocean mesoscale activity, most of them conclude that surface waves tend to better reproduce the sea surface temperature by increasing the vertical mixing, but also by better solving the momentum flux. Regarding the GoM, Abolfazli et al. (2020) have already studied the effect of surface currents over sea surface waves by means of ocean-waves coupled simulations, showing that currents can modify the significant wave height by about  $\pm 0.15$  m. However, so far, the role of CFB and WFB in modulating the GoM dynamics has not been studied.

---

This thesis aims to examine and quantify the extent to which CFB and WFB can control the dynamics of the GoM, focusing on the LC dynamics and the eddy shedding process. To that end, this study uses satellite observations and a set of 24-year coupled simulations carried out over the Western Tropical Atlantic, which only differs by the inclusion or not of CFB and WFB. The numerical implementations include the ocean model NEMO (Nucleus for European Modeling of the Ocean; Madec et al., 1997), the atmospheric model WRF (The Weather Research and Forecast; Skamarock et al., 2019), and the wave model WW3 (WAVEWATCH III; Tolman III). Model configurations and validations are shown in Chapters 2 and 3, respectively. The first objective was to evaluate the overall impact of the CFB on the dynamics of the Gulf of Mexico. Chapter 4 discusses how the CFB modifies the most relevant energy sources and eddy–mean conversion. It also reveals the large impact of the CFB on the LC variability, LC eddy–shedding statistics, and LCEs properties. These findings pointed to a sensitivity of the LCEs reattachment events to the CFB. This motivated us to further investigate in Chapter 5 the dynamical drivers of the detachments and reattachment/separation events by analyzing 24-year satellite–altimetry observations. Additionally, we analyze in a more profound way the energy pathways driving the EKE reduction at the scales where CFB is the most active in Chapter 6. Preliminary results about the role of WFB in modulating the Western Atlantic dynamics are presented in the Conclusion and perspectives.



# Introduction générale

Le Golfe du Mexique (GdM) fait partie du système de courants de bord ouest de l'Atlantique Nord (Schmitz and McCartney, 1993). Cette région est un système complexe où les activités humaines, telles que l'extraction pétrolière et la pêche, interagissent largement avec l'environnement océanique (par exemple, les courants forts, les rejets fluviaux et les caractéristiques atmosphériques telles que les tempêtes ou les ouragans) et les écosystèmes bio-géochimiques (McClean et al., 2011). La dynamique du GoM est dominée par le Loop Current (LC), un courant anticyclonique intense qui apporte l'eau chaude des Caraïbes dans le GoM. Le LC libère épisodiquement des tourbillons anticycloniques qui se propagent vers l'ouest du Golfe du Mexique : les " Loop Current Eddies " (LCE; Leben, 2005). Cependant, le GdM est confronté à des problèmes environnementaux croissants tels que les marées noires (White et al., 2012; Kostka et al., 2011; Michel et al., 2013) et les plastiques Phillips and Bonner (2015). La connaissance de la dynamique des océans est d'une importance capitale pour la compréhension et la surveillance de ces problèmes environnementaux et l'amélioration des activités économiques, telles que la navigation, la pêche, ou le développement et l'exploitation de structures offshore pour l'extraction d'énergie.

Les premiers efforts pour décrire la dynamique du GdM sont liés aux campagnes d'hydrographiques (Ichiye, 1959; Cochrane, 1972; Elliott, 1982). Les images satellites infrarouges capables de cartographier les LCE sont arrivées en 1973. Ces images ont permis d'identifier les LCE en hiver grâce à leur contraste thermique avec les eaux environnantes, ce qui n'était pas possible en été puisque le réchauffement des eaux de surface réduit largement le contraste thermique pour l'ensemble du GdM (Cooper et al., 1990). L'arrivée de l'altimétrie satellitaire a conduit à des avancées significatives dans notre connaissance de la dynamique du GdM, nous permettant de quantifier la variabilité du LC en termes de pénétration dans le GdM et de statistiques de détachement des LCEs (Leben, 2005). Cependant, si l'altimétrie permet de détecter que les grandes structures en équilibre géostrophique, c'est-à-dire les grands tourbillons de mésoéchelle et les courants de bord ouest, elle ne permet pas de détecter la dynamique ageostrophiques tels que les tourbillons de petite échelle ou les courants induits par le vent (Chelton et al., 2011; Amores et al., 2018; Archer et al., 2020). Ainsi, les simulations numériques océaniques réalistes sont souvent utilisées pour franchir une étape et surmonter les incertitudes liées aux observations, en permettant de représenter la dynamique océanique avec une résolution temporelle et spatiale plus fine, mais aussi en fournissant des informations sur les courants et les variables thermodynamiques en profondeur.

Néanmoins, la reproduction de la circulation du GdM reste un défi pour les modélisateurs de l'océan (Oey et al., 2005). En effet, d'une part, les modèles numériques à basse résolution spatiale ( $1^\circ$ ) ont tendance à produire un LC quasi stationnaire qui ne parvient pas à s'étendre dans le GoM (par exemple, Putrasahan et al., 2017) D'autre part, les simulations riches en tourbillons avec une résolution spatiale d'environ 10 km (ou moins) peuvent reproduire les principales caractéristiques du GdM, mais sont caractérisées par des biais persistants, qui concernent par exemple la pénétration du LC dans le GdM et les détachements des LCEs

(Le Hénaff et al., 2012; Garcia-Jove et al., 2016; Putrasahan et al., 2017). Des simulations couplées océan-atmosphère riches en tourbillons qui prennent en compte le Thermal FeedBack (TFB), c'est-à-dire l'influence de la température de surface de la mer sur l'atmosphère, ont été mises en œuvre pour tenter de mieux reproduire la dynamique du GdM (Putrasahan et al., 2017). Bien que TFB ait amélioré les résultats numériques en résolvant mieux les flux de chaleur turbulents entre l'atmosphère et l'océan, des biais dans les statistiques de variabilité de la LC et de détachement des LCE demeurent (Putrasahan et al., 2017).

Ces biais pourraient être liés au fait que les simulations riches en tourbillons sont caractérisées par des niveaux d'énergie élevés par rapport aux observations. C'est ce qu'ont montré Jullien et al. (2020), qui ont comparé l'énergie cinétique des tourbillons (EKE) de simulations à haute et basse résolution ( $1/12^\circ$  et  $1/4^\circ$ , respectivement). Les résultats montrent que les simulations à haute résolution ont une EKE au moins deux fois plus importante par rapport aux simulations à plus faible résolution spatiale ( $1/4^\circ$ ) et surestiment de plus de 30% l'EKE des observations altimétriques. Cependant, il est bien connu qu'une interpolation optimale appliquée aux produits altimétriques lisse et sous-estime leur estimation de l'EKE (Chelton et al., 2011; Amores et al., 2018; Archer et al., 2020), de sorte que le biais entre les observations et les simulations riches en tourbillons forcés pourrait être plus faible. Néanmoins, les auteurs exposent que les modèles à haute résolution ont besoin d'un puits d'énergie pour mieux représenter l'énergie à la mésoéchelle. Chassignet and Xu (2017) suggèrent que cette surestimation de l'énergie peut être contrecarrée en augmentant la viscosité du modèle. Cependant il a été démontré que les simulations couplées océan-atmosphère prenant en compte la rétroaction des courants de surface vers l'atmosphère, c'est-à-dire le Current Feed-Back (CFB), reproduisent mieux l'énergie à (sous-)mésoéchelle en induisant un puits d'énergie de l'océan vers l'atmosphère à la fois à grande et à fine échelle (Renault et al., 2016b,a, 2017b; Seo et al., 2017; Oerder et al., 2018; Jullien et al., 2020; Renault et al., 2021a). Ces études ont surtout été réalisées dans des endroits caractérisés par des courants de bord-ouest riches en activité de mésoéchelle, par exemple le Gulf stream, la rétroflexion du courant des Aiguilles, mais aussi dans d'autres régions à forte activité de mésoéchelle comme le courant de Californie, le courant de Humboldt et la mer Méditerranée. Le CFB induit un amortissement de l'activité de (sous-)mésoéchelle d'environ 30% et mène à une meilleure représentation des courants à grande échelle dans les modèles numériques, par exemple le Gulf Stream et la rétroflexion du courant des Aiguilles. Par conséquent, comme le GdM est caractérisé par une dynamique de mésoéchelle intense, les interactions air-mer à mésoéchelle peuvent jouer un rôle clé dans la détermination de son équilibre dynamique.

La rétroaction des vagues sur l'océan et l'atmosphère (WFB) est un sujet important au sein de la communauté des sciences de la Terre, comme l'illustre par exemple le lancement récent de la mission CFOSAT (Chinese French Ocean SATellite), qui fournit des mesures des spectres directionnels des ondes de surface de la mer (Hauser et al., 2021). Les vagues peuvent avoir plusieurs impacts sur les flux de quantité de mouvement, de chaleur et d'eau douce par le biais de boucles de rétroaction entre les vagues et l'atmosphère (via un changement de la rugosité) et entre les vagues et l'océan (via, par exemple, le mélange induit par les vagues). Plusieurs efforts ont été faits pour évaluer le rôle des vagues de surface sur l'océan et l'atmosphère en utilisant des simulations globales forcées (atmosphère-vagues ou atmosphère),

ainsi que des simulations couplées océan-vagues-atmosphère (Breivik et al., 2015; Chune and Aouf, 2018; Pianezze et al., 2018; Wu et al., 2019b,a; Couvelard et al., 2020). Les modèles océaniques de ces études ont des résolutions spatiales différentes, résolvant ou non l'ensemble de l'activité mésoéchelle de l'océan. La plupart d'entre eux concluent que les vagues de surface ont tendance à mieux reproduire la température de surface de la mer en augmentant le mélange vertical, mais aussi en résolvant mieux le flux de quantité de mouvement. En ce qui concerne le GoM, Abolfazli et al. (2020) ont déjà étudié l'effet des courants de surface sur les vagues de surface de la mer au moyen de simulations couplées océan-vagues, montrant que les courants peuvent modifier la hauteur significative des vagues d'environ  $\pm 0.15$  m. Cependant, jusqu'à présent, le rôle du CFB et du WFB dans la modulation de la dynamique du GdM n'a pas été étudié.

Cette thèse a pour but d'examiner et de quantifier dans quelle mesure le CFB et le WFB peuvent contrôler la dynamique du GoM, en se concentrant sur la dynamique du LC et le processus de libération de tourbillons. Pour cela, j'exploite des observations satellitaires et j'ai développé un ensemble de simulations couplées sur 24 ans sur l'Atlantique tropical ouest, qui ne diffèrent que par l'inclusion ou non de CFB et WFB. Le modèle couplé s'appuie sur le modèle océanique NEMO (Nucleus for European Modeling of the Ocean; Gurvan et al., 2022), le modèle atmosphérique WRF (The Weather Research and Forecast; Skamarock et al., 2019), et le modèle de vagues WW3 (WAVE-WATCH III; Tolman III). Les configurations et les validations du modèle sont présentées dans les Chapitres 2 et 3, respectivement. Le premier objectif était d'évaluer l'impact global du CFB sur la dynamique du Golfe du Mexique. Le Chapitre 4 traite de la façon dont le CFB modifie les sources d'énergie les plus pertinentes. Il révèle également l'impact important du CFB sur la variabilité du LC, les statistiques des tourbillons du GdM et en particulier des LCEs. Ces résultats indiquent une influence du CFB sur le processus de libération. Cela nous a motivé à étudier plus en profondeur dans le Chapitre 5 les facteurs dynamiques qui contrôlent les détachements et les événements de rattachement/séparation, d'abord en analysant les observations de 24 ans d'altimétrie par satellite. En outre, nous analysons plus en profondeur les voies d'énergie qui conduisent à la réduction de l'EKE aux échelles où la CFB est plus active dans le Chapitre 6.



# Background

## Contents

<b>1.1</b>	<b>The Gulf of Mexico</b>	<b>10</b>
1.1.1	Geography and background circulation in the Gulf of Mexico	10
1.1.2	The Loop Current Eddies	11
1.1.3	The Loop Current Eddy shedding process	13
1.1.4	Modeling the Gulf of Mexico	22
1.1.5	Air-sea interactions in the Gulf of Mexico	24
<b>1.2</b>	<b>Mesoscale Air-Sea Interactions</b>	<b>27</b>
1.2.1	Turbulent air-sea fluxes formulations	27
1.2.2	Main energy pathways	29
<b>1.3</b>	<b>The thermal feedback</b>	<b>32</b>
<b>1.4</b>	<b>The current feedback to the atmosphere</b>	<b>36</b>
<b>1.5</b>	<b>The wave feedback to the atmosphere and the ocean</b>	<b>42</b>

The objective of this chapter is to introduce the ocean dynamics of the Gulf of Mexico and to present the state of the art of numerical modeling of the region. In addition, the main coupling processes between the ocean, atmosphere, and waves, which are at the core of this thesis, will be introduced and placed within the Gulf of Mexico regional context.

## 1.1 The Gulf of Mexico

### 1.1.1 Geography and background circulation in the Gulf of Mexico

The Gulf of Mexico (GoM) is a semi-enclosed basin connected to the Caribbean Sea through the Yucatan Channel and the Atlantic Ocean through the Florida Straits (Figure 1.1). The Gulf reaches depths of 3500 m and has a shelf that is well identified by the 200-m depth isobath. The western shelf extends up to 80 km and decreases to about 30 km to the south. Louisiana–Texas Shelf is 210 km long, while the West Florida Shelf and Campeche Bank extend up to 200 and 250 km, respectively. The GoM receives important river discharges (González-Ramírez et al., 2019), the Mississippi–Atchafalaya River being the one with the most important annual runoff, with a long-term averaged annual discharge of about  $15,000 \text{ m}^3\text{s}^{-1}$  (Goolsby et al., 1999).

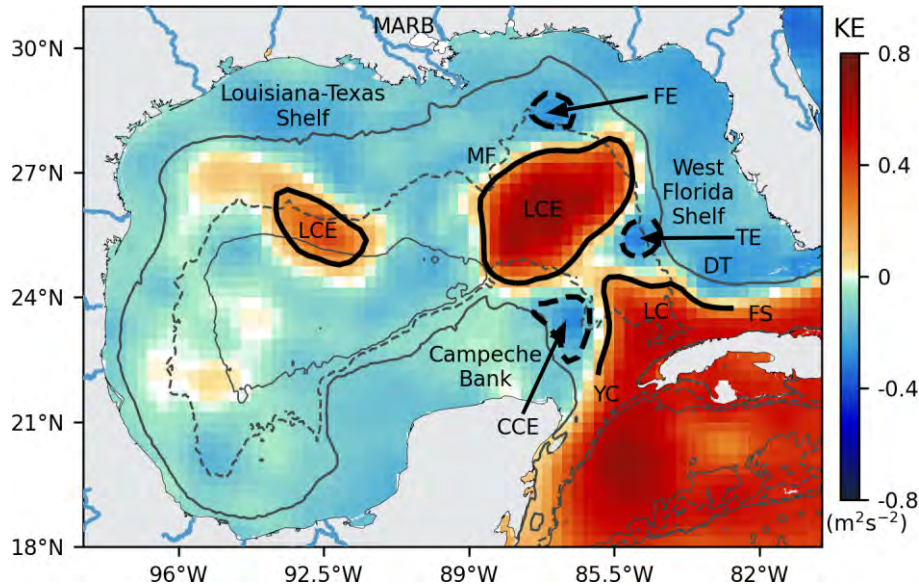


Figure 1.1: Main dynamical features of the GoM dynamics illustrated by a snapshot of AVISO sea surface height anomaly for March 5, 1998. The continuous contours highlight the Loop Current (LC) and LC eddies (LCE). The dashed contours highlight the LC frontal eddies. YC refers to Yucatan Channel, FS to Florida Straits, DT to Dry Tortugas islands, MF to Mississippi Fan, CS to the Caribbean Sea, FE to frontal eddy, CCE to Caribbean cyclonic eddy, TE to Tortugas eddy, and MARB to the Mississippi–Atchafalaya River Basin. The gray contours refer to the 200 m (continuous), 2500 m (dashed), and 3500 m (thin and continuous) depths.

The Loop Current (LC) is the more energetic feature of the GoM and behaves as an anticyclonic-shaped current that joins the Yucatan Current and the Florida Current (Figure 1.2). On average, the LC transports about  $27.6 \pm 11.4$  Sv ( $1 \text{ Sv} = 10^6 \text{ m}^3 \text{ s}^{-1}$ ; Athié et al., 2020; Candela et al., 2019). Its surface velocities can be larger than  $2 \text{ m s}^{-1}$  near the Yucatan coast (Coronado et al., 2007). The LC is characterized by a fluctuating northward extension (Hurlburt and Thompson, 1980) that can reach lengths up to 1,300 km and extends up to  $28.1^\circ\text{N}$  and  $85.8^\circ\text{W}$  (Leben, 2005). The LC penetration is generally described as a function of its extension and has been cataloged in two principal states, *i.e.*, retracted and extended (Garcia-Jove et al., 2016; Putrasahan et al., 2017). The retracted form is generally the result of a LC that has shed an eddy shortly before, while the extended form is representative of a LC that deeply penetrates into the GoM and is about to shed an eddy.

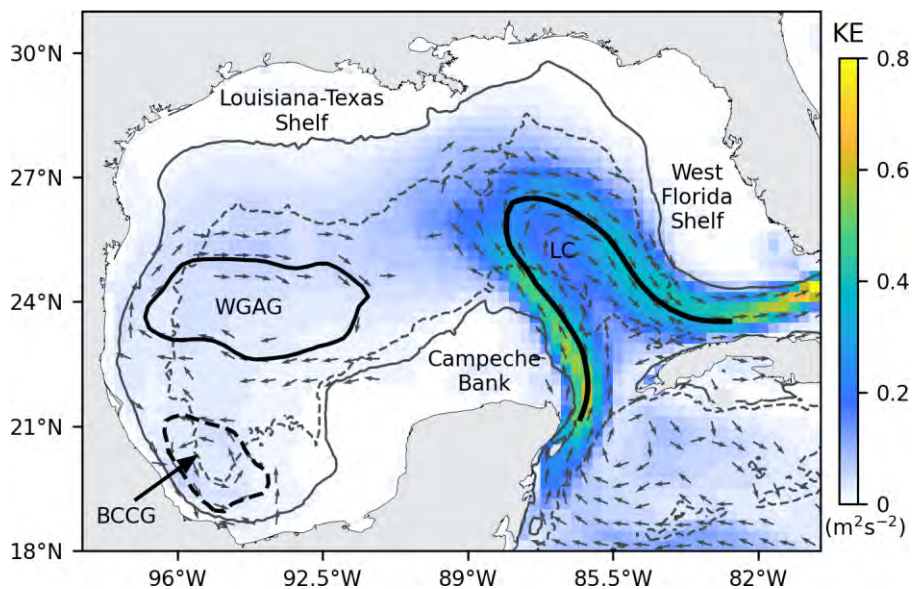


Figure 1.2: Large-scale features of the GoM dynamics illustrated with the kinetic energy averaged over 29-year of altimeter data. The thick black line represents the LC, the thin black line the western gulf anticyclonic gyre (WGAG), and the segmented line represents the Bay of Campeche cyclonic gyre (BCCG).

The long-term circulation of the GoM is depicted in Figure 1.2. It is composed of the long-term LC signature, a large anticyclonic gyre in the western Gulf (Sturges and Blaha, 1976), and the Bay of Campeche cyclonic gyre (Pérez-Brunius et al., 2013). The circulation on the shelves is mainly wind-driven (Zavala-Hidalgo et al., 2014).

### 1.1.2 The Loop Current Eddies

The Gulf circulation is particularly influenced by fluctuations of the LC and the anticyclonic eddies it liberates: the so-called Loop Current Eddies (LCEs). LCEs are large anticyclonic structures (200–400 km in diameter; Vukovich et al., 1979) that separate from the LC at

irregular intervals between 3 and 13 months. They can be reattached several times before their final separation (Sturges and Leben, 2000; Leben, 2005; Garcia-Jove et al., 2016). Long time series analysis of the LCEs detachment from Chang and Oey (2012, over 15 years) and Hall and Leben (2016 over, 37 years) suggest that LCEs separations are more likely to occur during summer and winter. These eddies propagate westward with a mean translation velocity of about 5 km/day (Vukovich and Crissman, 1986) and have a lifetime of about 1-year (Elliott, 1982). Through the analysis of 12 years (1973–1984) of satellite infrared data and ship–of–opportunity data, Vukovich and Crissman (1986) report that LCEs display three characteristic paths: a northern path, a mid–Gulf path, and a path that takes the eddies to the southwestern region of the GoM. However, the authors observe that all three paths converge at the northwestern region of the GoM. Vukovich and Crissman (1986) also show that LCEs decrease by about 45% of their initial size after 150 days of being detached and by about 79% of their initial size after 300 days. The authors also discuss that LCEs are commonly dissipated by erosion at the boundaries and by shedding smaller rings.

The LCEs are warm core eddies and bring important amounts of heat from the Caribbean to the western Gulf of Mexico (*e.g.*, Meunier et al., 2018, 2021). This has consequences on the regional heat budget, but also on the regional air–sea interactions. In particular, LCEs can drive hurricane or storm intensification by providing heat to these atmospheric features (Molina et al., 2016; Yablonsky and Ginis, 2012; Potter et al., 2021). An emblematic impact of this heat input is the intensification of Hurricane Katrina in August 2005 over the LC and a LCE about to be released (*e.g.*, Jaimes and Shay, 2009).

Historical observations from Elliott (1982), Cooper et al. (1990), and Forristall et al. (1992) show that measured LCEs have a salty core that reaches 200 m depth. Recent glider observations of the Poseidon LCE evolution (Meunier et al., 2018, 2021) reveals that LCEs exhibit a warm and homogeneous temperature core that extends from 50 to 200 m in depth (Figure 1.3). The LCEs also transport a subsurface high salinity maximum ( $\geq 36.9$  psu), which is generally located at the bottom of the eddy core, at a depth between 150 and 300 (Sosa-Gutiérrez et al., 2020; Meunier et al., 2022). Near the surface, the salinity is generally fresher, as a result of precipitations and river runoff.

The LCEs eddies also have important consequences on the biogeochemistry of the Gulf of Mexico. For example, Damien et al. (2021) show that LCEs enhance the phytoplankton biomass during winter. LCEs also have economic repercussions by inhibiting oil and gas extraction from unanchored drilling rigs (Kantha, 2014). They also may play a role in accumulating and transporting Sargassum (Andrade-Canto et al., 2022) which can end into the GoM coasts (Gower et al., 2006).

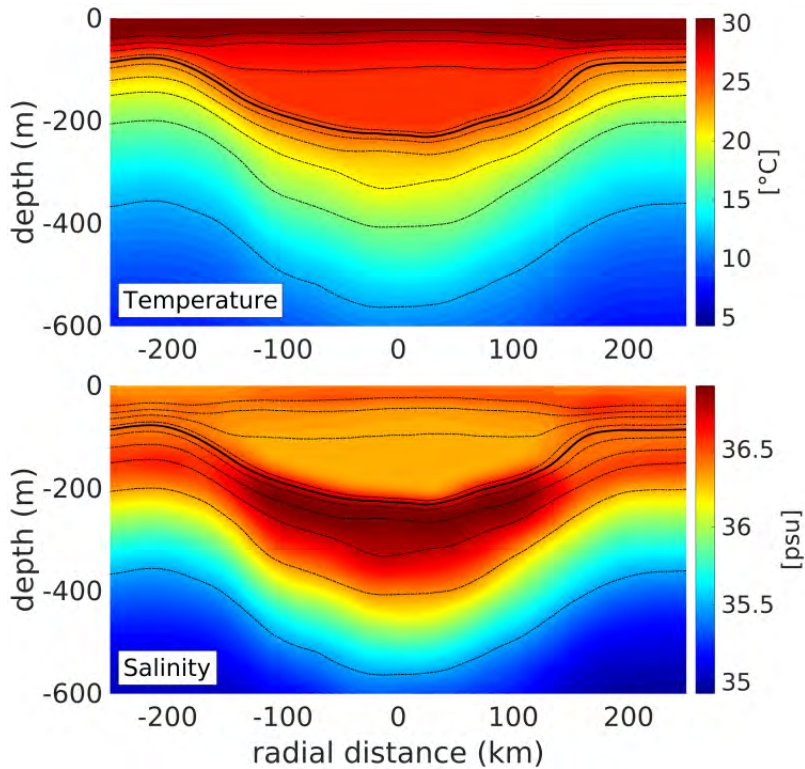


Figure 1.3: Temperature (top) and salinity (bottom) sections measured in the anticyclonic eddy Poseidon. The thick contour shows the 1025–isopycnal contour. The figure is taken from Meunier et al. (2021).

### 1.1.3 The Loop Current Eddy shedding process

Because of their essential role in the atmosphere and ocean dynamics of the GoM, the community has put a lot of effort to understand the processes related to the liberation of the LCEs, especially in the attempt to better predict them. However, as we will see below, there is no consensus on the processes triggering the LCEs shedding, and forecasting them still remains a challenge. Several theories have been developed to explain the mechanisms that drive LC eddy shedding.

Early studies have put forward the importance of differential rotation ( $\beta > 0$ ). This was identified by Hurlburt and Thompson (1980), who conclude from a reduced gravity model that differential rotation of the earth ( $\beta$ ) is essential for eddy shedding to occur realistically. This was later confirmed and rationalized by Pichevin and Nof (1997). The authors explain the detachment of eddies by the westward propagation of a long Rossby wave that exceeds the growth of the LC. This is the so-called Pichevin–Nof mechanism. However, this theory assumes that the LC returns to the same initial position after detachments, which is not the case. Leben (2005) show that the retreat latitude of the LC after separations is inversely correlated with the time between separations, suggesting that LCEs separations are more related to the LC state after the previous release.

The role of the current instabilities was also emphasized early on. [Hurlburt and Thompson \(1980\)](#) show that a reduced gravity model was the simplest model to simulate the eddy-shedding cycle. They concluded that baroclinic instability was not an essential element and pointed to the role of horizontal shear instabilities. Later [Hurlburt \(1986\)](#) found that the LC shedding process was connected with a mixed barotropic—baroclinic instability. From numerical simulations, [Chérubin et al. \(2006\)](#) confirm that the shedding events are driven by instabilities and also found that the instability is mixed, with baroclinic instability intensified in the deep layers of the Loop Current and barotropic instability intensified in the upper layers.

By means of 10-years of numerical simulation results, [Oey \(2008\)](#) shows that the LC retraction–expansion cycle is related to a larger transfer of eddy potential energy to mean potential energy in the north of Campeche Bank and west of the Florida Shelf. These results suggest that baroclinic instabilities can also modulate LCEs detachment.

[Garcia-Jove et al. \(2016\)](#) use numerical simulations to study the processes leading to the production of Eddy Kinetic Energy (EKE) over 14-years (1996 to 2009; Tables 1.1 and 1.2). Their results show that EKE is largely produced by the horizontal shear of currents (barotropic instabilities), principally between the Campeche Bank and the LC but also between the northeastern LC region and the Western Florida shelf, with larger values of about  $0.6 \times 10^{-4} \text{ kg m}^{-1} \text{ s}^{-3}$ . The production of EKE through baroclinic instabilities mostly occurs in the same regions, but with a smaller amplitude ( $\sim 0.2 \times 10^{-4} \text{ kg m}^{-1} \text{ s}^{-3}$ ). The authors conclude that LCEs separation is linked to instability processes. However, they also found a relationship between the period of time between separations and the latitude of occurrence: the farther south the LC retreats after a detachment, the longer the subsequent separation occurs. Based on this relationship, the authors suggest that the separation of LCEs is more related to the LC extension.

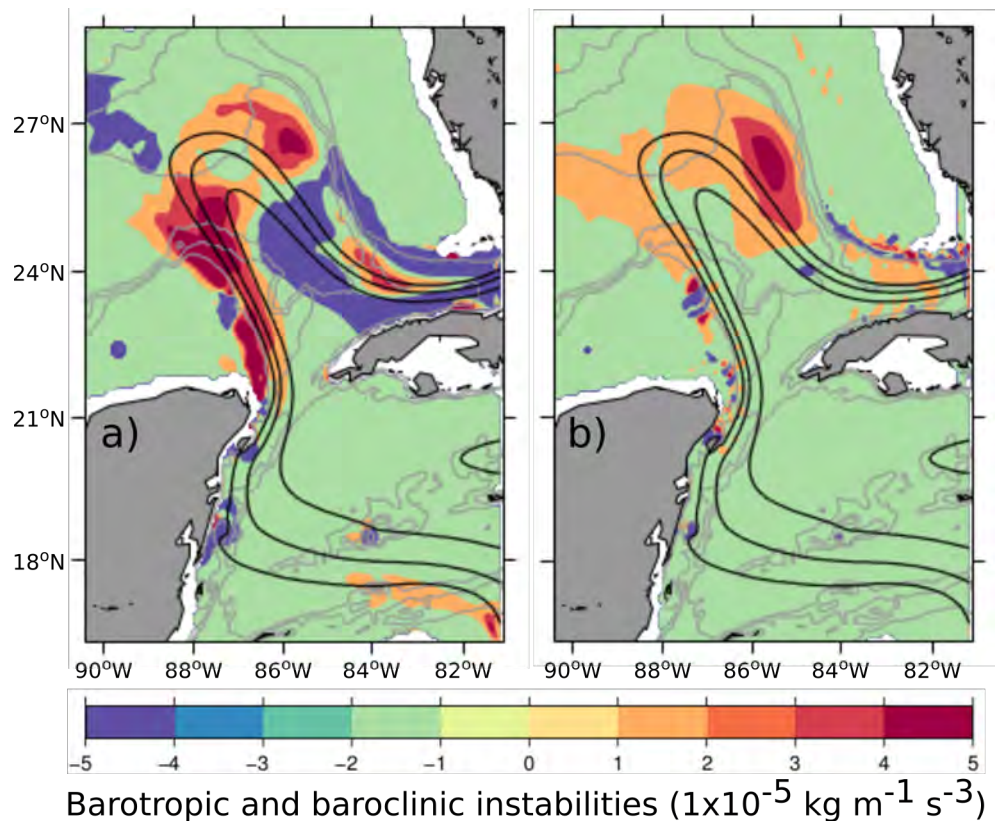


Figure 1.4: Production of barotropic (a) and baroclinic (b) instabilities from 14-year numerical simulations from Garcia-Jove (2016).

Donohue et al. (2016) study the separation of the LCEs Ekman, Franklin, and Hadal by using an array of moored current meters and bottom mounted pressure equipped inverted echo sounders located between the Campeche Bank, the Mississippi Fan, and the center of the West Florida Shelf. The authors found that LCEs detachments are related to an increase in deep EKE at the time when large-scale meander occurs in the northern and eastern regions of the LC. They conclude that the increase in EKE is related to an extraction of the available potential energy from the mean-field that is converted to EKE.

The LC is also surrounded by a variety of cyclonic eddies suspected to strongly interact with the LC and to play a crucial role in the shedding process (Cochrane, 1972; Vukovich and Maul, 1985; Chérubin et al., 2006; Le Hénaff et al., 2012). So far, three main kinds of cyclonic eddies have been identified and could be involved at different degrees in the shedding process by “pinching-off” the LC (Figure 1.1; Schmitz, 2005): (i) the LC frontal eddies, (ii) the Tortugas eddies, and (iii) the Caribbean cyclonic eddies.

i) The Loop Current frontal eddies (Figure 1.1) are principally generated east of the Campeche Bank and increase their energy and diameter as they travel along the LC (Oey, 2008; Jouanno et al., 2016; Hiron et al., 2020). These frontal eddies have diameters around 50 and 100 km, extend to more than 2000 m depth, and have swirl speeds of about  $0.3 \text{ m s}^{-1}$  (Oey, 2008;

Rudnick et al., 2015; Jouanno et al., 2016). Hénaff et al. (2014) show that these cyclonic eddies are in solid-body rotation and different authors report that they can be intensified through vortex-stretching next to Campeche Bank (Zavala-Hidalgo et al., 2003) and over the Mississippi Fan (Le Hénaff et al., 2012). Besides, vortex merging can also intensify frontal eddies at the northeast region of the LC (Zavala-Hidalgo et al., 2003; Le Hénaff et al., 2012). Hiron et al. (2020) show that these eddies can increase in size and energy when interacting with the LC, and their intensification is more related to their proximity to the LC.

Through numerical simulations and observations, Le Hénaff et al. (2012) assess case studies involving LCEs detachments in the presence of intensified frontal eddies. An example of a frontal eddy intensification process is depicted in Figure 1.5. By following a group of frontal eddies traveling around the LC (A, B, C, and D), the authors observe that eddy A remains stuck at the east of the LC while frontal eddy B continues its journey along the LC. Frontal eddy B reaches frontal eddy A, and both eddies merge into a large cyclonic eddy that drastically modifies the LC shape.

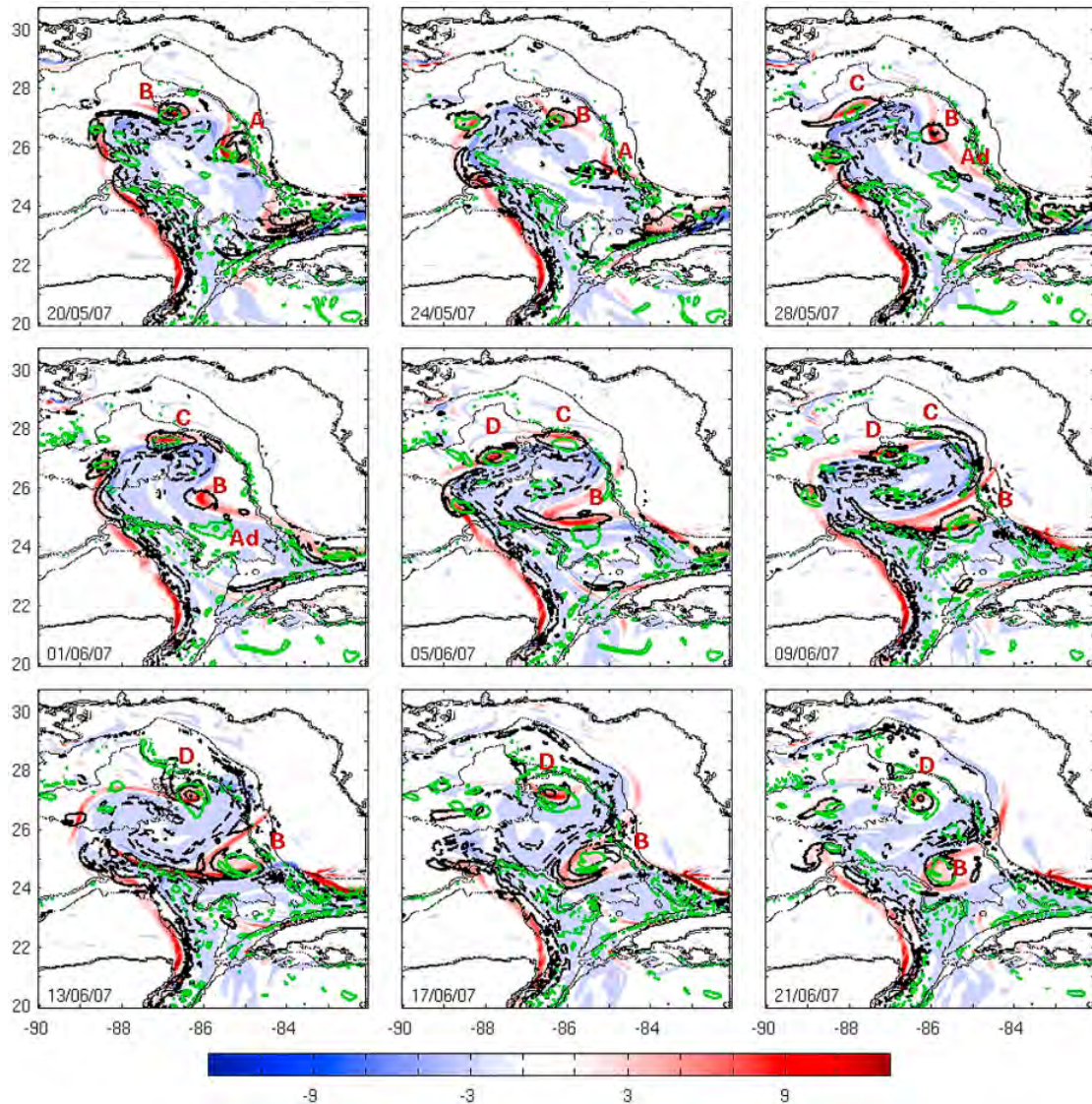


Figure 1.5: Relative vorticity ( $10^{-5} \text{ s}^{-1}$ ) evolution over 45 days. Black lines are the relative vorticity near the surface, while green lines in deeper regions. Solid lines represent positive values and dashed lines the negative ones. Letters from A to D indicate Loop Current frontal eddies. Subscript d indicates the deep part of cyclonic eddies. Figure taken from [Le Hénaff et al. \(2012\)](#).

ii) Tortugas eddies are larger cyclonic structures with a diameter between 100–200 km that are found in the southeastern region of the LC (Figs. 1.1; [Fratantoni et al., 1998](#)). These cyclonic eddies are referred to as Tortugas eddies since they are formed near Dry Tortugas Islands. [Fratantoni et al. \(1998\)](#) suggest that Tortugas eddies result from the merging of two or several frontal eddies, increasing their size and residence time, which can last more than 4 months. The authors report that during these periods, Tortugas eddies can favor LCEs detachments.

iii) The Caribbean cyclonic eddies have a characteristic radius of  $\sim 160$  km and an amplitude of 4 cm (López-Álzate et al., 2022). These eddies regularly flow into the GoM, as demonstrated by Athié et al. (2012) and Jouanno et al. (2016) by means of altimetry and numerical simulations, respectively (Figure 1.6). The authors show that many separations are related to the arrival of Caribbean cyclonic eddies into the GoM. This is depicted in Figure 1.6, where it can be seen that negative sea surface height anomalies related to Caribbean cyclonic eddies reach Campeche Bank at the time that LCEs detachments occur. The authors found some relationship between the incoming Caribbean eddies and the LCEs shedding, but could not explain the mechanisms at play.

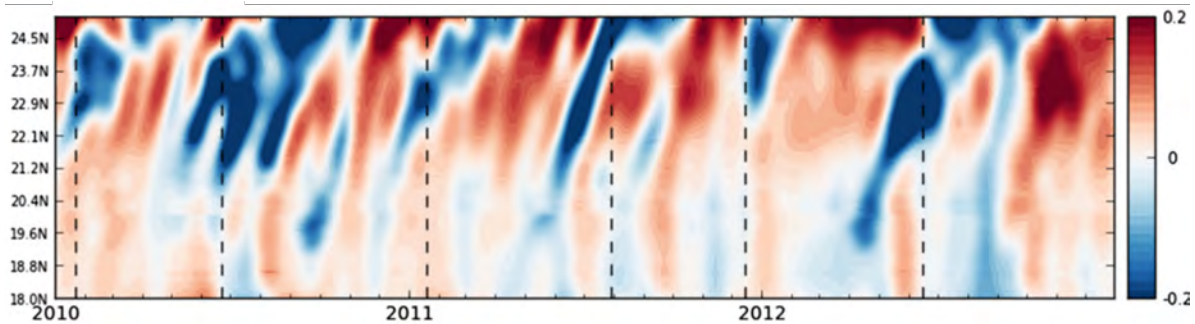


Figure 1.6: Hovmöller diagram of sea surface height anomalies along the western Caribbean Sea and Campeche Bank. Segmented lines indicate LCEs detachments. Figure taken from Jouanno et al. (2016).

So the above-mentioned studies suggest that cyclonic eddies, independently of their origin, could favor the LCEs detachment. But, interestingly, Zavala-Hidalgo et al. (2003, 2006) have shown the occurrence of large cyclonic structures blocking the LC penetration into the GoM over periods larger than 15 months, evidencing that cyclonic eddies can increase the period between LCEs separation. The origin of these large and stationary cyclonic structures at the western side of the LC has not been addressed.

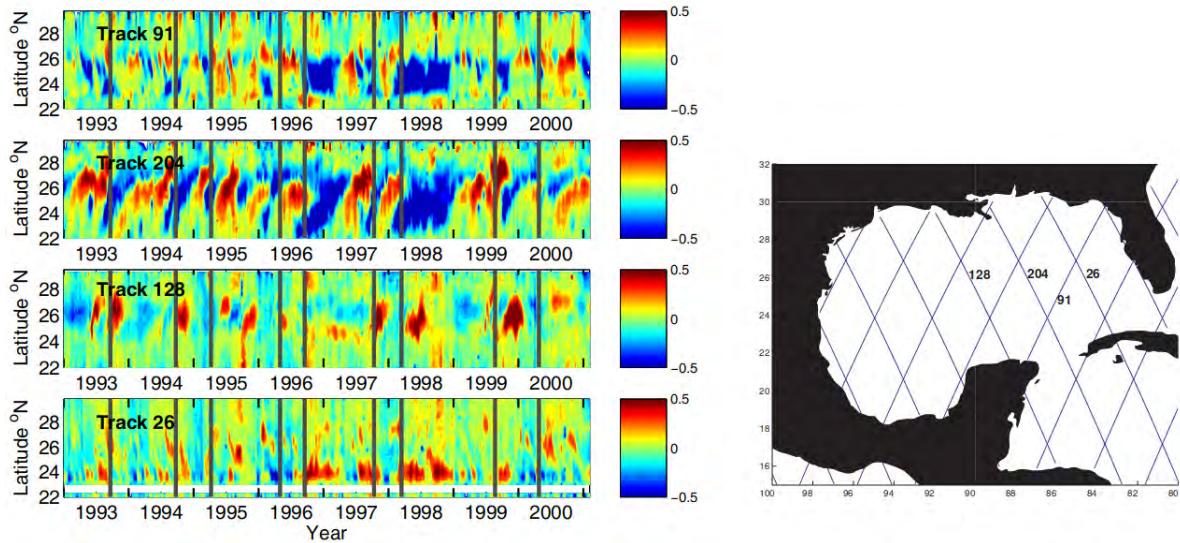


Figure 1.7: Time series of the sea level anomaly from altimeter along-tracks. Positive values depict the LC, whereas negative values represent the presence of cyclonic eddies. The occurrence of LCEs separation is shown with gray lines. Figure taken from [Zavala-Hidalgo et al. \(2006\)](#).

The LCEs detachments are usually accompanied by an intensification of the LC ([Hiron et al., 2020](#)), which are referred to as frontal jets in this work. They can be identified as strong KE pulses in LC regions where frontal eddies occur (Figure 1.8). The authors use satellite observations and a mooring array to show that these jets occur when cyclonic eddies squeeze their boundary against the LC, tilting the cyclonic eddies–LC isotherms and increasing the density gradient and the geostrophic flow (Figure 1.9). Furthermore, it appears that intensified frontal eddies and frontal jets mainly occur in the northwestern and northeastern regions of the LC and near Dry Tortugas, regions characterized by the larger production of eddy kinetic energy through barotropic and baroclinic instabilities ([Garcia-Jove et al., 2016](#); [Donohue et al., 2016](#)). However, the contribution of these jets in the LCEs detachment or in the production of eddy kinetic energy remains unclear.

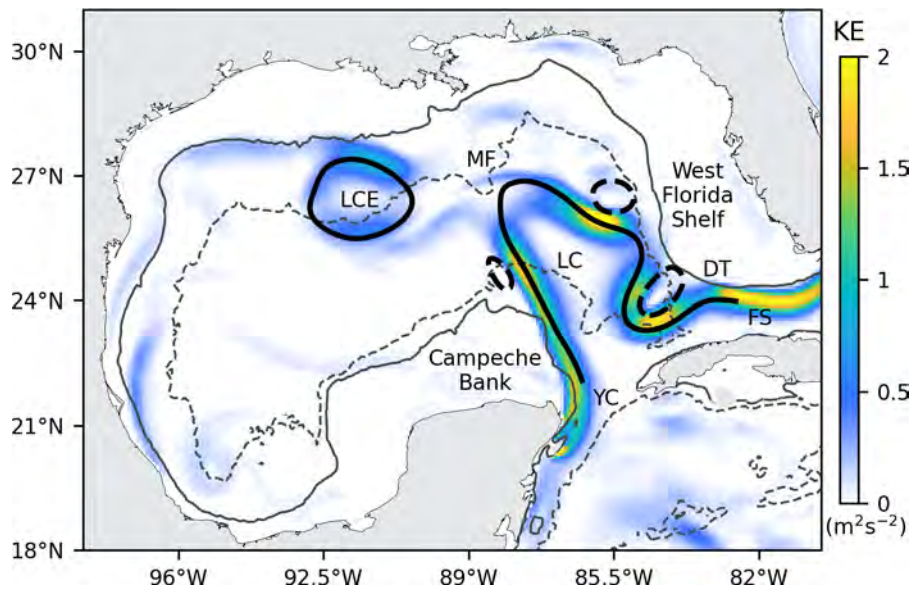


Figure 1.8: Example of frontal jets resulting from the interaction between the LC (black continuous contour) and frontal eddies (black segmented circles).

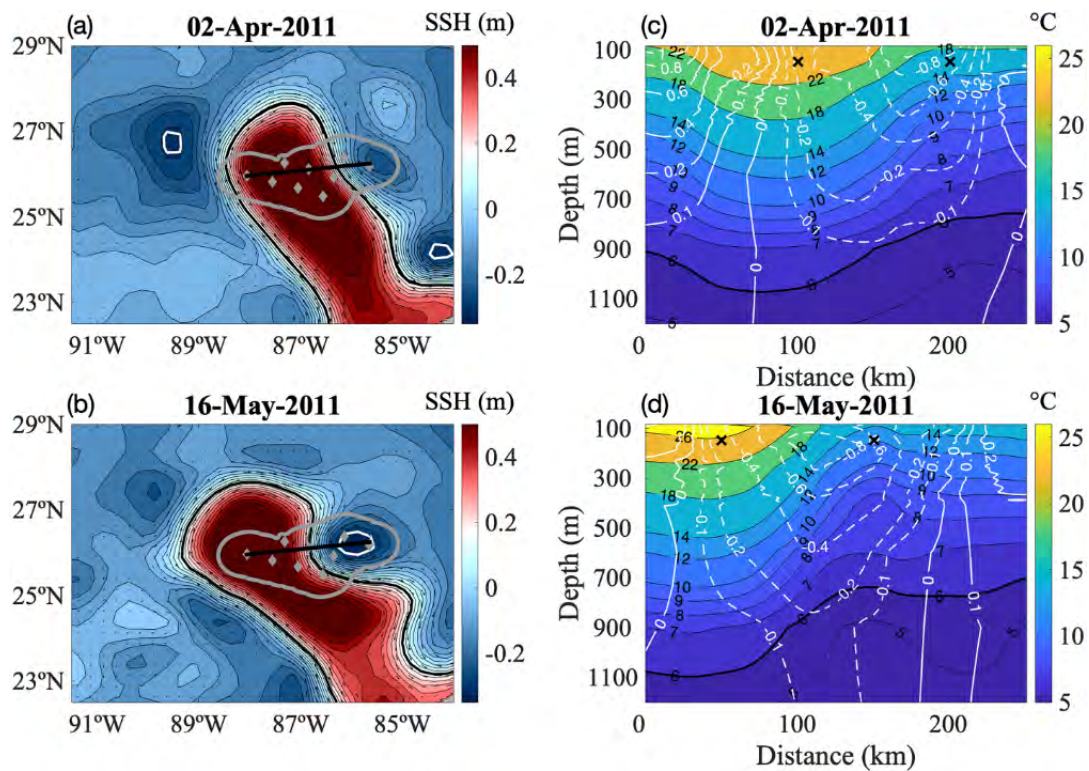


Figure 1.9: The LC in the presence of a weak (a) and intensified frontal eddy (b). The LC is represented by the black contour, a mooring array by the gray dots, and the transect from where the corresponding temperature profiles (c,d) are represented by the black line. Current speeds perpendicular to the transect are displayed by white lines, dotted lines for the southwestward component, and solid lines for the northwestward component. The figure is taken from [Hiron et al. \(2020\)](#).

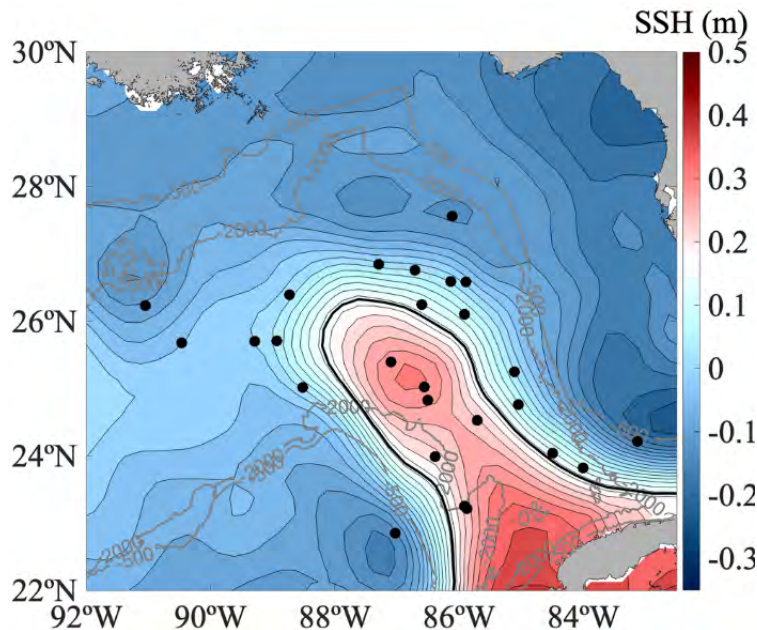


Figure 1.10: Mean sea surface height averaged over the 2009–2011 period. The LC is represented by the black contour and the black exhibit the occurrence of frontal jets and intensified frontal eddies. The figure is taken from [Hiron et al. \(2020\)](#).

Therefore and in conclusion, while the role of cyclonic eddies in the detachment or separation of LCEs has often been suggested or shown for specific events, to our knowledge, there has been no systematic analysis of their relevance in driving the shedding.

#### 1.1.4 Modeling the Gulf of Mexico

Numerical models have been widely used to describe and understand the dynamics of the Gulf of Mexico. However, the modeling community had to face persistent bias, which still makes the representation of the GoM dynamics and its forecast challenging. In particular, models can show very different LC penetration into the GoM and can fail to represent the observed frequency of the LC eddy detachments. This is exemplified in Tables 1.1 and 1.2, which compare LC and LCEs shedding statistics from altimeter observations and forced simulations of [Le Hénaff et al. \(2012\)](#) and [Garcia-Jove et al. \(2016\)](#), and an ocean–atmosphere coupled simulation from [Putrasahan et al. \(2017\)](#).

Altimeter observations have revealed that the mean LC extension is about 1502 km and is commonly extended up to  $\sim 26.30^\circ\text{N}$ . Besides, it has been quantified that around 1.46 LCEs per year separate from the LC, with a mean separation period of about 245 days. Most of the numerical implementations shown in Tables 1.1–1.2 underestimate the LC extension, the number of separated eddies per year, and the period between separations. [Le Hénaff et al. \(2012\)](#) and [Garcia-Jove et al. \(2016\)](#) investigated the role of the incoming Caribbean eddies and show that reducing the energy input from the Caribbean Sea (removing or reducing the

incoming mesoscale variability) increases the LC penetration into the GoM. In fact, [Garcia-Jove et al. \(2016\)](#) found that reducing the mesoscale energy from the Caribbean results in a weaker production of EKE through barotropic and baroclinic instabilities over the LC. [Le Hénaff et al. \(2012\)](#) show that the mean transport over the Yucatan Channel after dampening the mesoscale activity is only reduced by 2.5% (33.3 Sv to 32.5 Sv), which suggests that the LC dynamics are more sensitive to the mesoscale energy input from the Caribbean Sea than for the large scale energy input. [Garcia-Jove et al. \(2016\)](#) obtain similar results. However, they found that the presence or absence of incoming Caribbean eddies does not significantly modify the LCEs separation statistics. [Garcia-Jove et al. \(2016\)](#) remove a canyon over the Campeche Bank to study its impact on the LC variability. The authors do not observe significant modifications in the LC penetration into the GoM, but observe an increase in the period between separations and a reduction in the number of separated eddies over the simulated period. [Garcia-Jove et al. \(2016\)](#) obtain the best statistics related to the LC penetration into the GoM and the period between separation by smoothing the bathymetry. Nevertheless, their simulations still underestimate the number of separated eddies. Additionally, ocean-atmosphere coupled simulations considering the influence of the sea surface temperature on the atmosphere from [Putrasahan et al. \(2017\)](#) do not appear to show improvements in the LC penetration into the GoM or the LCEs separation period. However, authors show that coupled simulations that include mesoscale eddies better represent heat fluxes in the GoM.

In a summary, numerical simulations can reproduce the main characteristics of the GoM, but detailed validations exhibit difficulties in properly reproducing the LC variability and statistics about the detachment of LCEs. The reasons for these underestimations are not clear. However, one conclusion that could be drawn is that less mesoscale activity in the Caribbean seems to favor the LC penetration into the GoM.

Table 1.1: Main characteristic of numerical simulations. Their performance related to the LC penetration into the GoM and separation of LCEs is evaluated in Table 1.2. RIF refers to reduced inflow.

	Oceanic model	Spatial resolution	Forced/coupled simulation	Years
Le Hénaff, 2012 (Reference)	HYCOM	1/25°	Forced	12
Le Hénaff, 2012 (Reduced inflow)	HYCOM	1/25°	Forced	12
García-Jove, 2016 (REF)	NEMO	1/12°	Forced	14
García-Jove, 2016 (VISCO)	NEMO	1/12°	Forced	14
García-Jove, 2016 (SMOOTH)	NEMO	1/12°	Forced	14
Putrasahan, 2017 (HR)	CCSM4	1/10°	OC-ATM	54

Table 1.2: Comparison of statistics related to the LC penetration into the GoM and the separation of LCEs between AVISO and different numerical simulations. AVISO statistics are computed over 24-years of daily data. RIF refers to reduced inflow, NSE to the number of separated eddies, and PBS to the period between separations.

	LC max. lat. ( $^{\circ}$ N)	LC length (km)	NSE	By year	PBS
AVISO	$26.30 \pm 1.21$	$1502.22 \pm 1.38$	35	1.46	$245 \pm 139$
Le Hénaff, 2012 (REF)	$25.40 \pm 1.04$	$1091.00 \pm 373.00$	4	0.33	$390 \pm 213$
Le Hénaff, 2012 (RIF)	$25.80 \pm 1.15$	$1223.00 \pm 417.00$	–	–	–
García-Jove, 2016 (REF)	$26.84 \pm 0.88$	–	22	1.57	$262 \pm 159$
García-Jove, 2016 (SMOOTH)	$26.19 \pm 1.04$	–	19	1.36	$266 \pm 174$
García-Jove, 2016 (VISCO)	$27.16 \pm 0.78$	–	21	1.50	$318 \pm 169$
Putrasahan, 2017 (HR)	$25.61 \pm 0.98$	–	–	–	$334 \pm -$

### 1.1.5 Air-sea interactions in the Gulf of Mexico

The role of the local wind forcing and, more generally, the role of regional air-sea interactions on the LC and LCEs dynamics remain open questions.

The GoM is dominated by a trade wind regime. Although weak (between 2 and 6  $\text{ms}^{-1}$ ) and blowing westward, winds have a notable seasonal variability, with stronger winds during spring and summer over the west of the GoM. The occurrence of the North Atlantic semi-permanent atmospheric high-pressure system over the northeastern region of the GoM is responsible for the larger mean winds in spring and summer (Figure 1.11b-c; Zavala-Hidalgo et al., 2014).

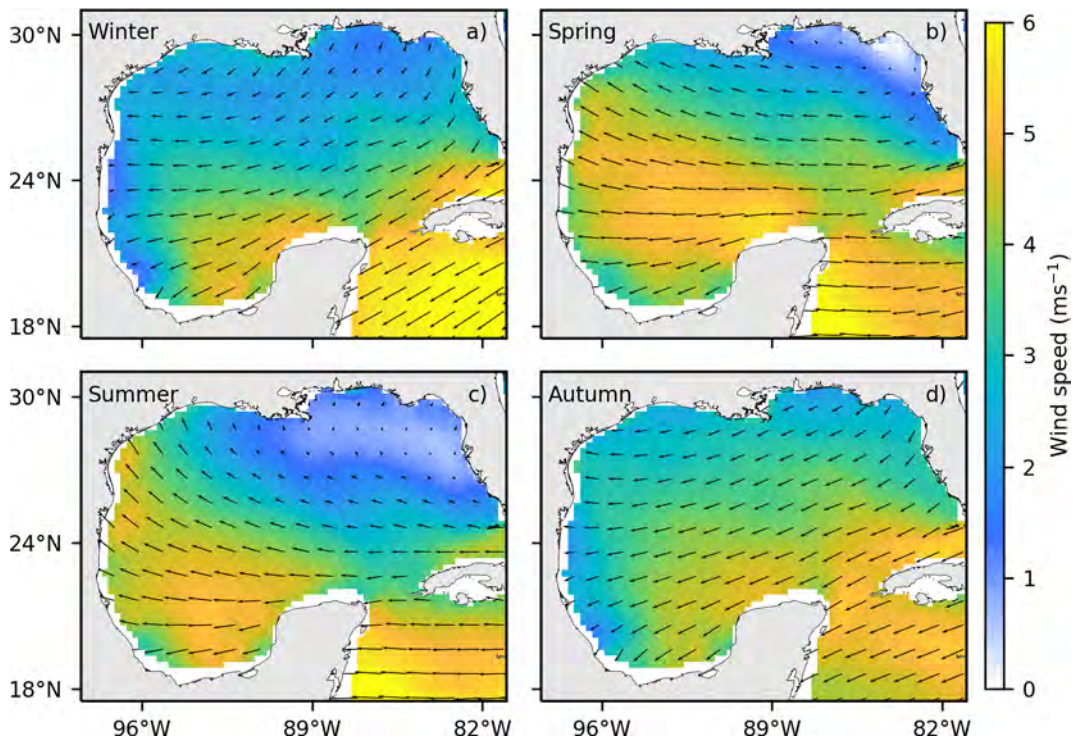


Figure 1.11: Wind speed seasonal climatology (from 1999 to 2009) inferred from SCOW (Scatterometer Climatology of Ocean Winds).

While there are no indications that the seasonality of the eddy shedding is directly related to this seasonal variability, a few studies suggested that the LC variability and the associated eddy shedding could be modulated by the biannually varying trade winds in the Caribbean Sea, which partially control transport in the Yucatan Channel (Chang and Oey, 2010, 2012, 2013; Athié et al., 2020). These studies suggest that strong trade winds in the Caribbean lead to a large transport in the Yucatan Channel, which favors a larger LC penetration into the GoM and the LCEs detachment.

Besides, the GoM is impacted by intense atmospheric events. Around 1.4 Hurricanes per year impact the GoM (Holland et al., 2010), mostly between May and November (Bromirski and Kossin, 2008). From September to May, the Gulf of Mexico is swept by cold fronts or *Northern* (or *Nortes* in Mexico) winds. These events are associated with high-pressure systems originating at the Rocky Mountains that travel to the GoM (Appendini et al., 2014; Kurczyn et al., 2020; Romero-Arteaga et al., 2022). These events generally occur between September to May and vanish between 2 and 4 days after arriving at the GoM. The winds during these events are particularly strong ( $>10 \text{ ms}^{-1}$ ), and combined with dry and cool air, contribute to the cooling and mixing of the surface layers of the Gulf of Mexico (e.g., Sosa-Gutiérrez et al., 2020).

Regarding atmosphere–LCEs interactions, Meunier et al. (2021) use a 25-year satellite–altimeter record and in situ measurements to show that LCEs heat decays exponentially as they travel to the central GoM. The authors show that most of LCEs heat is transferred to

surrounding waters instead of the atmosphere, suggesting that although surface heat fluxes represent an important heat loss for LCEs, surface heat fluxes are more critical for the atmosphere than for LCEs. This is supported by [Potter et al. \(2021\)](#), who examined the rapid dissipation of the LCE Poseidon when interacting with Hurricane Harvey. [Potter et al. \(2021\)](#) show that the LCE only lost about 22% of its heat in the first 100 m depth and about 50% in the first 200 m depth. The authors show that the passage of Hurricane Harvey cooled the waters around Poseidon, thus favoring large heat loss of the eddy through horizontal heat fluxes.

The salinity over the GoM is also strongly structured by the LCEs, which spread high salinity water as they travel west of the Gulf. [Meunier et al. \(2021\)](#) show that the high salinity core in LCEs originates from the Caribbean and can be conserved 7 months after the eddy detachment. Using repeated gliders observations and regional simulations, [Sosa-Gutiérrez et al. \(2020\)](#) show that this salinity maximum tends to dilute or even disappear when the LCEs propagate toward the west. The authors report that it mostly occurs during the late autumn and winter, when cold and dry *Northern* winds blow over the Gulf and induce convective turbulence which mixes the high salinity core with the freshwater above.

Because the GoM is a place of very intense mesoscale dynamics, mesoscale air–sea interactions are expected to play a key role in determining its dynamical equilibrium. To our knowledge, only [Putrasahan et al. \(2017\)](#) addressed this question. For this purpose, they compared LC statistics in global coupled simulations with  $0.1^\circ$  ocean resolution with its low-resolution counterpart ( $1^\circ$  ocean resolution with the same  $0.5^\circ$  atmosphere resolution). This strategy allows inferring the role of mesoscale eddies on the air–sea fluxes. The authors show that coupled eddy-rich simulations better represent heat fluxes in the GoM. Besides, the authors show that mesoscale eddies produce sea surface temperature anomalies through the horizontal advection of heat and that these anomalies partially control the air–sea heat exchanges through latent heat fluxes. Mesoscale eddies are also known to strongly interact with the atmosphere through the so-called Current FeedBack (CFB; Section 1.4), with consequences on the mesoscale eddy energy or western boundary currents ([Renault et al., 2016a,b, 2017b](#); [Seo et al., 2017](#); [Oerder et al., 2018](#)). Nevertheless, the role of the current feedback on the Gulf of Mexico dynamics has never been formally investigated.

Air–sea interactions are also known to be influenced by the sea surface wave field. Sea surface waves in the GoM are dominated mainly by locally generated waves since swell waves are partially blocked by the Yucatan Peninsula, Florida, and the Cuban Island. A 30-year of sea surface wave climatology from forced numerical simulations shows that significant wave heights of about 1.5 m occur at the west of the GoM, while the southwest and east regions are characterized by smaller significant wave height ( $\approx 0.8$  m; [Appendini et al., 2014](#)). Seasonal numerical results from [Appendini et al. \(2014\)](#) and [Abolfazli et al. \(2020; Figure 1.12\)](#) indicate that significant wave heights are larger than 1.5 m in winter, while in summer, significant wave heights oscillate between 0.5 and 1 m. As sea surface waves over the GoM are mostly wind waves, their mean direction is very similar to the mean wind direction (Figures 1.11 and 1.12).

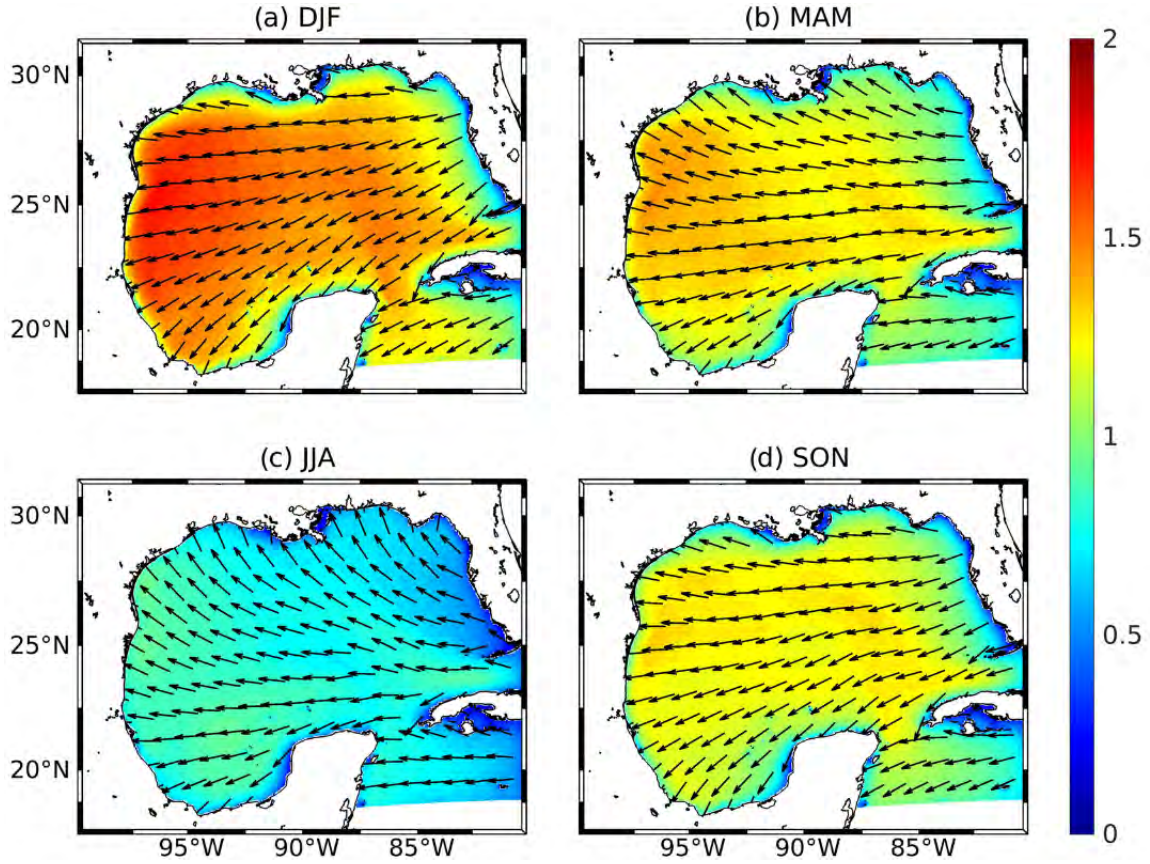


Figure 1.12: Seasonal climatologies (2001 to 2010) of significant wave heights for winter (a), spring (b), summer (c), and autumn (d). The mean wave direction is represented by the black arrows. The figure is taken from Abolfazli et al. (2020).

The potential relevance of these mesoscale air-sea interactions for the Gulf of Mexico, together with that of the sea surface waves on the ocean and the atmosphere, will be discussed in detail in Chapters 4 and 5, and will constitute the core of this thesis work.

## 1.2 Mesoscale Air-Sea Interactions

### 1.2.1 Turbulent air-sea fluxes formulations

The ocean and atmosphere are coupled through radiative fluxes and the turbulent exchange of momentum, heat, and freshwater. To simulate these turbulent exchanges, numerical oceanic and atmospheric models use bulk parametrizations. Formulation for momentum ( $\tau$ ), sensible heat ( $Q_s$ ), and latent heat ( $Q_l$ ) turbulent fluxes, usually read as follows:

$$\tau = \rho_a C_d |\mathbf{U}_r| \mathbf{U}_r, \quad (1.1)$$

$$Q_s = \rho_z c_p C_h |U_r| (\theta_z - T_s), \quad (1.2)$$

$$Q_l = \rho_a L_e C_e |U_r| (q_0 - q_z). \quad (1.3)$$

The wind stress (or momentum flux) is the force per unit area of the ocean surface with which the atmosphere forces ocean currents and is one of the major drivers of ocean circulation. The sensible heat flux is related to the transfer of heat through the thermal conduction between the ocean and the atmosphere and is proportional to the vertical temperature gradient. Latent heat flux, instead, is related to the exchange of heat between the atmosphere and the ocean that occurs when water evaporates or condenses on the surface. All three bulk formulas depend on atmosphere density ( $\rho_a$ ) and the relative wind ( $\mathbf{U}_r = \mathbf{U}_a - \mathbf{U}_o$ ), which consider the effect of surface currents ( $\mathbf{U}_o$ ) on the absolute wind ( $\mathbf{U}_a$ ), commonly referenced at 10 m over the sea surface. An important component of bulk formulations is the coefficient that weighs the transfer of properties between the ocean and the atmosphere ( $C_d$ ,  $C_h$ , and  $C_e$ ), which is the main source of differences between parametrizations. Bulk formulations related to turbulent heat fluxes also consider the specific heat of the air ( $c_p$ ) and the latent heat of water evaporation ( $L_e$ ), as well as the differences in potential temperature ( $\theta_z - T_s$ ) and humidity ( $q_0 - q_z$ ) occurring between the ocean and the atmosphere.

There is a large number of coefficients that need to be defined to compute momentum and heat turbulent fluxes. Specifically for the wind stress, it is commonly parametrized through a drag coefficient linearly related to the wind speed, *e.g.*, [Large and Pond \(1981\)](#):

$$C_d = \begin{cases} 1.2, & 4 \leq U_a < 11 \text{ ms}^{-1}, \\ 0.49 + 0.065U_a, & 11 \leq U_a < 25 \text{ ms}^{-1}. \end{cases} \quad (1.4)$$

These linear relationships are generally inferred from observations but can not be applied everywhere since parametrizations implicitly contain local characteristics related, for example, to the sea state ([Smith et al., 1992](#); [Guan and Xie, 2004](#); [García-Nava et al., 2009](#)).

Theoretical approximations have been proposed for neutral atmospheric conditions, where the drag coefficient can be computed as a function of the roughness scale ( $z_0$ ):

$$C_d = \frac{\kappa^2}{\ln^2(z/z_0)}, \quad (1.5)$$

$$z_0 = \alpha u_*^2 / g, \quad (1.6)$$

where  $\kappa = 0.41$  is the von Kármán constant,  $z$  is the atmospheric reference height (usually 10 m over the sea level),  $\alpha$  the Charnock parameter,  $u_* = \boldsymbol{\tau} / \rho_o$ ,  $g$  the gravitational acceleration, and  $\rho_o$  the ocean density. The roughness scale,  $z_0$ , is related to the roughness of gravity–capillary waves and usually is considered 0.41. However, several studies have suggested that wind stress is also modulated by the roughness of gravitational waves ([Donelan et al., 1993](#); [Smith et al., 1992](#); [Drennan, 2003](#)).

[Janssen \(2004\)](#) proposed a formulation to compute a drag coefficient as a function of the effective roughness ( $z_e = z_{\text{gcw}} + z_{\text{gv}}$ ), which includes the roughness of gravity–capillary ( $z_{\text{gcw}}$ ) and gravity waves ( $z_{\text{gw}}$ ):

$$C_{d_w} = \frac{\kappa^2}{\ln^2(z/z_e)}, \quad (1.7)$$

$$z_e = \alpha_w u_*^2 / g, \quad (1.8)$$

$$\alpha_w = \frac{0.01}{\sqrt{1 - \frac{\tau_w}{\tau}}}, \quad (1.9)$$

where  $\alpha_w$  is the Charnock parameter. The Charnock parameter depends on the net wave-supported stress ( $\tau_w$ ), which is related to the input of energy from the atmosphere to the waves ( $S_{in}$ ):

$$S_{in}(k, \theta) = \frac{\rho_a \beta_{max}}{\rho_o \kappa^2} e^z z^4 \left( \frac{u_*}{C} \right)^2 \times \max[\cos(\theta - \theta_u), 0]^p \sigma F(k, \theta). \quad (1.10)$$

This wind input parametrization corresponds to the [Ardhuin et al. \(2010\)](#) formulations, where  $\rho_o$  is the seawater density,  $\beta_{max} = 1.2$  the wave growth parameter,  $\kappa$  is the von Kármán constant,  $Z$  is the effective wave age,  $C$  is the waves phase speed,  $\theta$  the direction of waves, the power of the cosine ( $p$ ) is equal to 2,  $\sigma$  is the radian frequency, and  $F(k, \theta)$  the directional wave spectrum.

[Janssen \(2004\)](#) also suggests that a realistic formulation of the momentum flux between the atmosphere and the ocean is necessary to adequately represent the ocean surface layer dynamics. To achieve this, [Janssen \(2004\)](#) proposes to compute the stress felt by the ocean  $\tau_o$  by taking into account the stress that ends up in sea surface waves ( $\hat{\tau}_w = \tau_w + \tau_{w_d}$ ):

$$\tau_{o_w} = \tau_{a_w} - \hat{\tau}_w, \quad (1.11)$$

where  $\tau_w$  and  $\tau_{w_d}$  are the net wave-supported stress and the wave-to-ocean momentum flux, respectively.

In practice, sea surface currents are neglected since they are commonly weaker than surface winds. In addition, ocean numerical simulations are mostly forced with prescribed atmospheric datasets, avoiding feedbacks between the ocean and the atmosphere, but also leaving aside sea surface wave feedbacks to the ocean and the atmosphere.

The following subsections describe the main energy pathways between the ocean and the atmosphere, as well as how energy pathways can be modified when using coupled models. In addition, the thermal, current, and wave feedbacks are explained.

### 1.2.2 Main energy pathways

Energy budgets of Lorenz energy cycle terms allow studying the relative importance of energy pathways between mean and anomalous parts of the potential and kinetic energy. Considering a Reynolds decomposition, it is possible to separate the potential and kinetic energy into their

mean ( $\bar{\quad}$ ) and anomalous parts ( $\prime$ ):

$$\text{MPE} = -\frac{1}{2}g \int_V \frac{(\bar{\rho} - \rho_{\text{ref}})^2}{d\rho_{\text{ref}}/dz} dV, \quad (1.12)$$

$$\text{EPE} = -\frac{1}{2}g \int_V \frac{\overline{\rho'^2}}{d\rho_{\text{ref}}/dz} dV, \quad (1.13)$$

$$\text{MKE} = \frac{1}{2}\rho_0 \int_V (\bar{u}^2 + \bar{v}^2) dV, \quad (1.14)$$

$$\text{EKE} = \frac{1}{2}\rho_0 \int_V \overline{(u'^2 + v'^2)} dV, \quad (1.15)$$

where MPE and EPE are the mean and eddy potential energy, whereas MKE and EKE are the mean and eddy kinetic energy. Here,  $\rho_{\text{ref}}$  corresponds to the spatial average of the time-mean density ( $\bar{\rho}$ ) for a certain vertical level. The reference density is represented by  $\rho_0 = 1026 \text{ kg/m}^3$ , the gravitational acceleration by  $g$ , and horizontal components of ocean currents by  $u$  and  $v$  in the  $x$  and  $y$  directions. The main energy conversion terms are the MPE to MKE:

$$P_m K_m = -\frac{g}{\rho_0} \int_V \overline{\rho' w} dV \quad (1.16)$$

EPE to MPE:

$$P_m K_m = -\frac{g}{\rho_0} \int_V \frac{\overline{u' \rho'} \left( \frac{\partial \bar{\rho}}{\partial x} \right) + \overline{v' \rho'} \left( \frac{\partial \bar{\rho}}{\partial y} \right)}{\frac{d\rho_{\text{ref}}}{dz}} dV, \quad (1.17)$$

EPE to EKE:

$$P_e K_e = \int_z^0 -\frac{g}{\rho_0} \overline{\rho' w'} dz, \quad (1.18)$$

and MKE to EKE:

$$K_m K_e = -\int_z^0 \left( \overline{u' u'} \frac{\partial \bar{u}}{\partial x} + \overline{u' v'} \frac{\partial \bar{u}}{\partial y} + \overline{u' w'} \frac{\partial \bar{u}}{\partial z} + \overline{v' u'} \frac{\partial \bar{v}}{\partial x} + \overline{v' v'} \frac{\partial \bar{v}}{\partial y} + \overline{v' w'} \frac{\partial \bar{v}}{\partial z} \right) dz. \quad (1.19)$$

The main energy sources of MPE ( $F_m P_m$ ) and EPE ( $F_e P_e$ ) are related to buoyancy fluxes:

$$F_m P_m = -g \int_S \left( \frac{T_e \overline{J_s} (\bar{\rho} - \rho_{\text{ref}})}{\frac{d\rho_{\text{ref}}}{dz}} + \frac{S_e \overline{G_s} (\bar{\rho} - \rho_{\text{ref}})}{\frac{d\rho_{\text{ref}}}{dz}} \right) dS, \quad (1.20)$$

$$F_e P_e = -g \int_S \left( \frac{T_e \overline{J'_s \rho'}}{\frac{d\rho_{\text{ref}}}{dz}} + \frac{S_e \overline{G'_s \rho'}}{\frac{d\rho_{\text{ref}}}{dz}} \right) dS, \quad (1.21)$$

where  $T_e$  and  $S_e$  are the thermal expansion and haline contraction coefficients. Moreover,  $J_s = Q_{\text{net}}/(\rho_0 c)$  and  $G_s = \bar{S}_0(E - P)$ , where  $Q_{\text{net}}$  is the net heat flux,  $c$  is the specific heat of seawater,  $\bar{S}_0$  the time-mean surface salinity,  $E$  the evaporation, and  $P$  the precipitation.

The main energy sources of MKE and EKE are related to the wind work:

$$F_m K_m = \frac{1}{\rho_0} (\overline{u \tau_x} + \overline{v \tau_y}), \quad (1.22)$$

$$F_e K_e = \frac{1}{\rho_0} (\overline{u' \tau_x'} + \overline{v' \tau_y'}), \quad (1.23)$$

where  $\tau_x$  and  $\tau_y$  are the wind stress components in the  $x$  and  $y$  directions. The derivation of main sources and energy conversion terms can be found in, for example, [Harrison and Robinson \(1978\)](#), [Garcia-Jove et al. \(2016\)](#), and [Jüling et al. \(2018\)](#).

A Lorenz diagram is provided in Figure 1.13 with the purpose of exhibiting the main energy pathways between the ocean and the atmosphere, whereas continuous arrows depict energy pathways in forced simulations and segmented arrows in coupled simulations. Coupled ocean–atmosphere simulations better solve turbulent heat fluxes by considering the feedback of sea surface temperature on the atmosphere ([Putrasahan et al., 2017](#)), but also ocean–waves or ocean–waves–atmosphere simulations ([Breivik et al., 2015](#); [Pianeze et al., 2018](#); [Wu et al., 2019a,b](#); [Couvelard et al., 2020](#)), since using the sea surface waves mixing from a wave model leads to better reproduction of the sea surface temperature. These results evidence that coupled models can modify the sources of MPE and EPE, and therefore, the MKE and EKE. The feedback of surface currents to the atmosphere is also able to modify heat fluxes (Equations 1.2 and 1.3). However, [Renault et al. \(2016a,b, 2017b\)](#) demonstrate that the most important feedbacks occur between the wind stress and geostrophic currents, reducing the geostrophic mean and eddy wind work, and as a consequence, the kinetic and potential energy of the ocean. Geostrophic wind work can be computed by assuming that surface currents can be linearly separated into geostrophic and ageostrophic currents:

$$F_m K_{m_g} = \frac{1}{\rho_0} (\overline{u_g \tau_x} + \overline{v_g \tau_y}), \quad (1.24)$$

$$F_e K_{e_g} = \frac{1}{\rho_0} (\overline{u_g' \tau_x'} + \overline{v_g' \tau_y'}). \quad (1.25)$$

Feedbacks between the ocean, sea surface waves, and the atmosphere can modify the sources and conversion of potential and kinetic energy in the ocean, and the following subsections are intended to explain how the thermal, current, and sea surface wave feedbacks work.

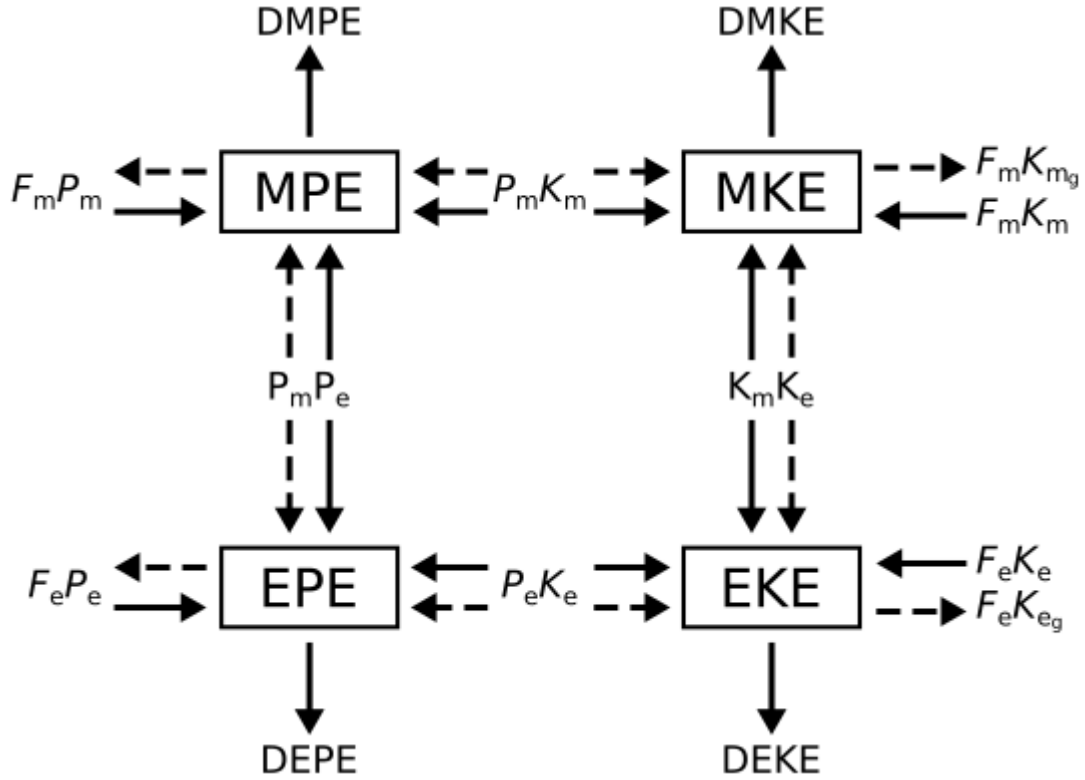


Figure 1.13: Lorenz diagram of main energy sources and conversion terms. Continuous lines represent the classic energy source and conversion terms, while dashed lines represent the energy sources and conversion terms when using coupled models that consider the feedbacks between the ocean, sea surface waves, and the atmosphere. MPE and EPE are the mean and eddy potential energy. MKE and EKE are the mean and eddy potential energy.  $F_m P_m$  and  $F_e P_e$  are the sources of potential energy related to buoyant fluxes, whereas  $F_m K_m$  and  $F_e K_e$  are the sources of kinetic energy related to the wind work.  $P_m K_e$  is the conversion of MPE to MKE,  $P_m P_e$  is the conversion of MPE to EPE,  $K_m K_e$  is the conversion of MKE to EKE, and  $P_e K_e$  is the conversion of EPE to EKE. DMPE, DEPE, DMKE, and DEKE represent the dissipation of MPE, EPE, MKE, and EKE, respectively.

### 1.3 The thermal feedback

The thermal feedback (TFB) is related to the influence of sea surface temperature over the atmosphere. It is well known that this feedback is of great importance for large-scale processes or for driving climate variability such as *El Niño* or *La Niña* (Guilyardi et al., 2009; Bayr and Latif, 2022). This is why climate modeling uses ocean-atmosphere coupled models. However, recent studies have highlighted the importance of TFB at the mesoscale. Earlier evidence of the atmospheric response to the sea surface temperature was identified on winds blowing from cold to warm waters over the Gulf Stream north wall (Sweet et al., 1981). Using satellite observations, Chelton et al. (2001), Chelton (2004), and Chelton et al. (2007) show that strong sea surface temperature fronts can induce fine-scale anomalies in the wind and wind

stress. Additionally, the authors defined linear relationships for different geographical regions between the wind stress divergence and curl to the downwind and crosswind sea surface temperature gradients, respectively (Figure 1.14).

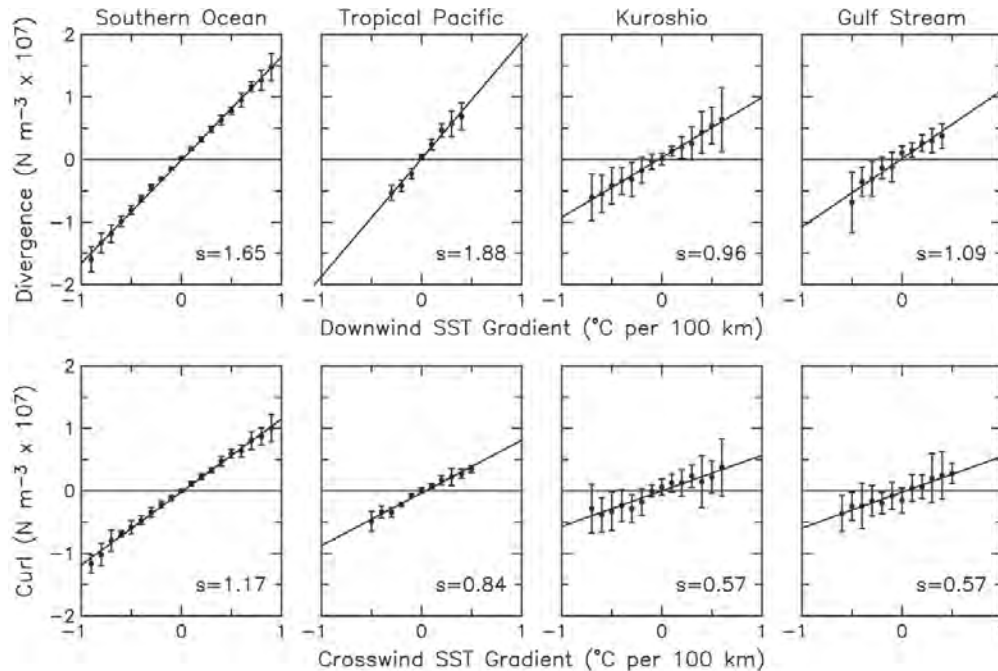


Figure 1.14: Linear relationships between the sea surface temperature and the wind stress divergence and curl.  $s$  corresponds to the linear regression slope. Figure taken from Chelton (2004).

These relationships highlight the occurrence of wind stress anomalies over winds along or crossing strong sea surface temperature fronts (Figure 1.15). As shown by O’Neill et al. (2012), coupling coefficients between the sea surface temperature and wind stress (or speed) anomalies at the mesoscale can also represent these relationships. Small et al. (2008) detail the mechanisms behind these relationships. The authors explain that winds flowing from cold to warm surface waters increase their wind stress by enhancing turbulent mixing. On the contrary, with winds flowing from warm to cold surface waters, the wind stress will depend on the intensity of hydrostatic pressure anomalies, which are induced by changes in the air temperature and moisture over the sea surface temperature front.

Numerical results from, *e.g.*, Oerder et al. (2016) and Putrasahan et al. (2017), have shown that coarse resolution simulations produce negative correlations between anomalies of sea surface temperature and wind stress or latent heat fluxes, which is characteristic of an ocean driven by the atmosphere. In contrast, the authors show that mesoscale resolving simulations exhibit positive correlations, indicating that the feedback of sea surface temperature anomalies related to the mesoscale control air–sea exchanges of heat. In particular, Putrasahan et al. (2017) demonstrate that in the GoM, sea surface temperature anomalies are driven by the horizontal advection of heat, which modulate the latent heat fluxes at the mesoscale.

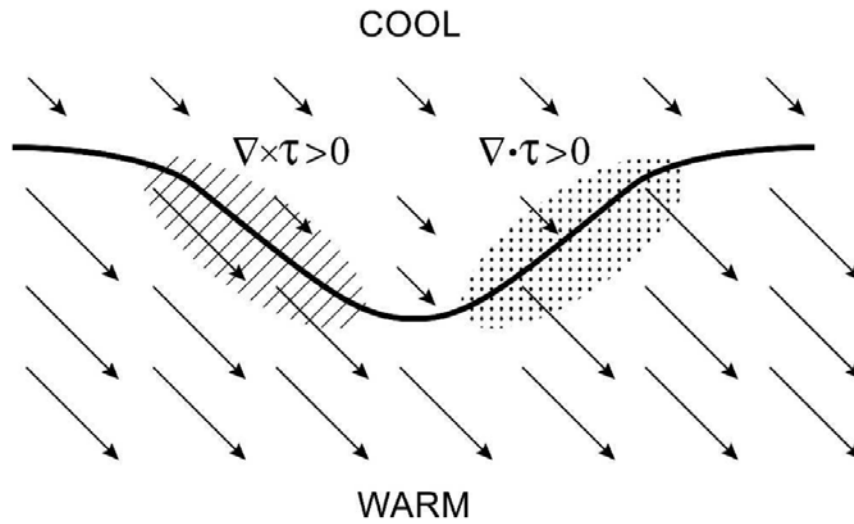


Figure 1.15: Wind stress anomalies resulting from the winds blowing along or crossing sea surface temperature fronts. Figure taken from [Chelton \(2004\)](#).

Similar findings are obtained by [Frenger et al. \(2013\)](#), using satellite observations to demonstrate that local mesoscale eddies affect near-surface winds, cloud properties, and rainfall. The authors found that cyclonic eddies awake near-surface winds and reduce the cloud fraction, water content, and precipitations, and vice versa (Figure 1.16).

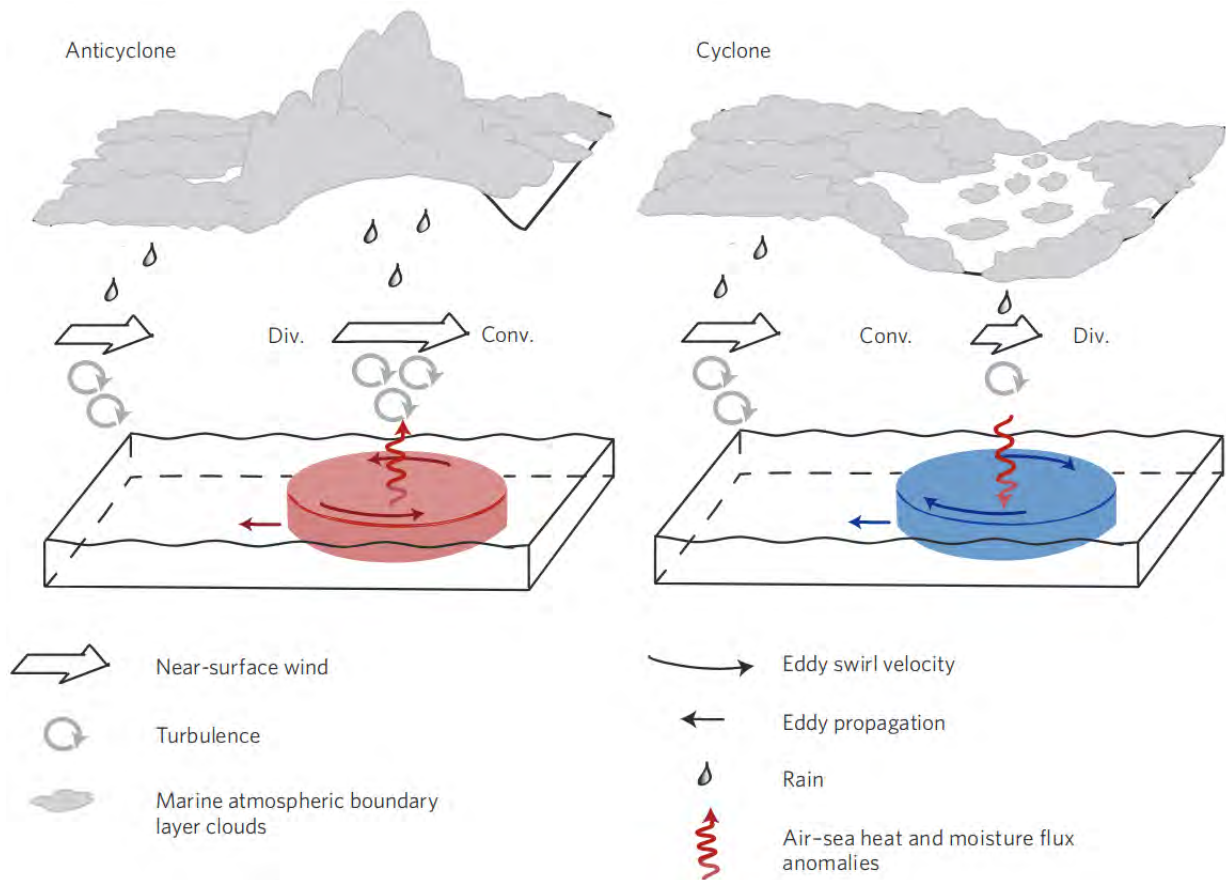


Figure 1.16: Impact of warm-core (left) and cold-core (right) Southern Ocean mesoscale eddies on atmosphere properties. Div. refers to wind divergence and Conv. to wind convergence. Figure taken from [Frenger et al. \(2013\)](#).

As reported by [Bishop et al. \(2020\)](#), mesoscale air-sea interactions between sea surface temperature and surface heat fluxes are responsible for a sink of potential energy from the ocean to the atmosphere. The authors reach this conclusion by comparing the source of potential energy related to buoyant fluxes from 21-years of observations and 35-years from a numerical simulation. As shown in Figure 1.17, the source of potential energy is decomposed into its mean, seasonal, and eddy components. Results evidence that sea surface temperature and surface heat flux anomaly interactions cause a sink of eddy potential energy from the ocean to the atmosphere. This sink is stronger in western boundary currents and regions of large mesoscale activity, as *e.g.*, the Gulf Stream, the Kuroshio Current, and the South African Current System. This sink of potential energy may modulate the conversion of energy by baroclinic instability. Therefore, the potential and kinetic energy could be overestimated in eddy-rich numerical simulations that do not consider the feedback between the ocean and the atmosphere related to the sea surface temperature and surface heat fluxes.

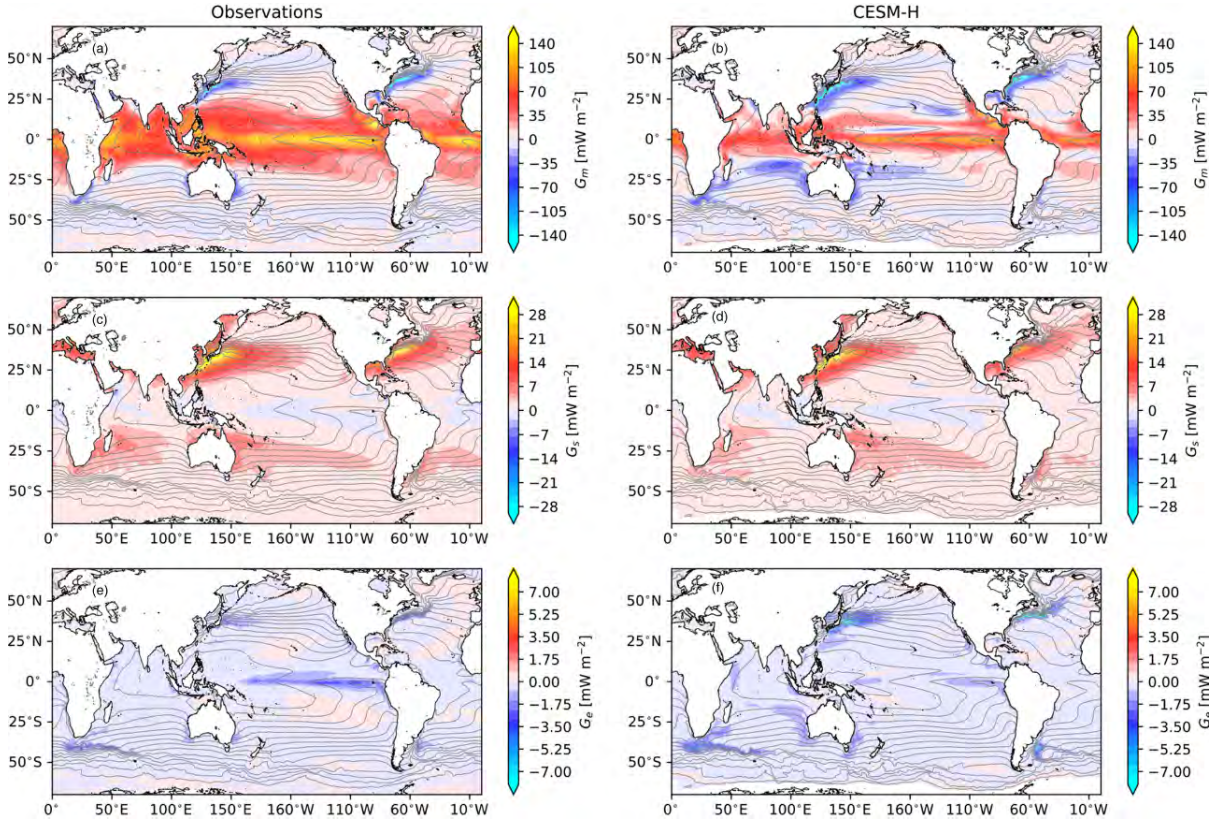


Figure 1.17: Sources of potential energy at the large, seasonal, and turbulent scales. The figure is taken from Bishop et al. (2020).

## 1.4 The current feedback to the atmosphere

The current feedback (CFB) is related to the influence of surface currents on the atmosphere. In numerical models, taking into account CFB leads to a more realistic representation of the energy of the ocean currents. As reported by Renault et al. (2016a), CFB acts at both large scale and at mesoscale, but also at the submesoscale (Renault et al., 2018) and even at tidal scales (Renault and Marchesiello, 2022).

At the large-scale, mean surface currents and winds generally flow in the same direction, causing a positive input of energy from the atmosphere to the ocean (positive mean wind work; Figure 1.18), which is one of the main sources of energy for the ocean (Wunsch, 1998). However, observational and numerical studies have highlighted the signature of mean oceanic currents on the mean surface stress and the mean wind work (Kelly et al., 2001; Scott and Xu, 2009; Renault et al., 2016b, 2017a, 2020). This is related to CFB, which mainly acts through the surface stress by using the relative wind to the oceanic current instead of the absolute wind in the bulk formulae of a coupled ocean-atmosphere model. This weakens (increases) both the surface stress and positive (negative) wind work when surface currents and winds have the same (opposite) directions, as proposed by Bye (1985) and Renault et al.

(2016b; Figure 1.18). As a result, CFB slows down large-scale currents regardless of the wind and currents direction (Figure 1.18). The atmospheric response to CFB tends to re-energize ocean currents by increasing the wind speed when winds and currents have the same direction (Figure 1.18; Renault et al., 2016b), however, the net effect of CFB is still a sink of energy from the ocean to the atmosphere. These findings have been confirmed using *in situ* and satellite observations. For example, using the Tropical Atmosphere–Ocean buoys (TAO) and satellite scatterometer data, Kelly et al. (2001) show that CFB reduces the median wind stress magnitude by 20%. Using scatterometer data, Chelton (2004) reveals that the mean surface currents can induce an imprint of the Gulf Stream in the wind stress curl. This was recently confirmed using numerical models for the Gulf Stream and the Agulhas Current (Renault et al., 2017b, 2020). The reduction of the surface stress causes a weakening of the mean wind work by  $\approx 20\%$ , which consequently slows down the mean circulation and, thereby, the mean kinetic energy (Pacanowski, 1987; Luo et al., 2005; Renault et al., 2016a). Several works assess the influence of surface currents on wind stress and wind work estimation through satellite observations, reporting a 20–30% wind work reduction when surface currents are taken into account (Bye, 1985; Duhaut and Straub, 2006; Scott and Xu, 2009; Hughes and Wilson, 2008; Renault et al., 2017b,a).

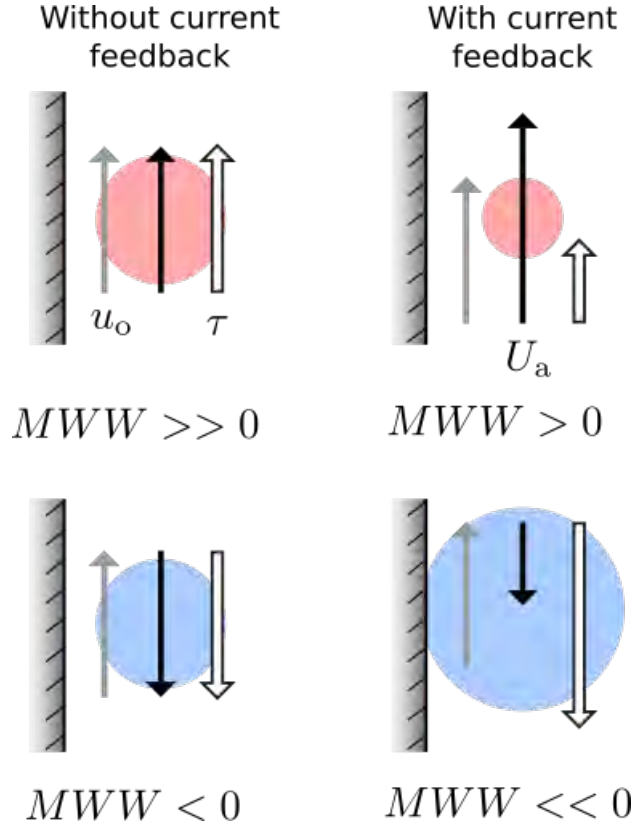


Figure 1.18: Schematic representation of mechanical air-sea interactions when not considering (left) and considering (right) CFB on a uniform northward (upper) and southward (lower) wind blowing over a northward coastal current. MWW refers to the wind work. The red color refers to a positive wind work, *i.e.*, transfer of energy from the atmosphere to the ocean. The blue color refers to a negative wind work, *i.e.*, transfer of energy from the ocean to the atmosphere. Scheme modified from Renault et al. (2016a).

The local or mesoscale effect is stronger than the large-scale one. It was first suggested by Bye (1985) but ignored for decades until recently confirmed by satellite data and eddy-rich coupled models. This mechanism is illustrated in Figure 1.19, which shows the momentum transfer between a southward uniform wind blowing up over an anticyclonic eddy. When CFB is not considered (Figure 1.19a), there is a positive eddy wind work on the eastern branch and a negative eddy wind work on the western branch, resulting in a net eddy wind work near zero. When considering CFB (Figure 1.19a), the eastern branch has currents moving in the same direction as the wind. As a result, the wind stress is reduced since it is computed as a function of the relative wind ( $U_a - U_o$ ). On the contrary, the western branch has currents moving against the wind and increased surface stress. As a result, the positive (negative) part of the geostrophic eddy wind work is reduced (increased), and the net geostrophic eddy wind work becomes negative, deflecting momentum from the ocean to the atmosphere. This process is called *eddy killing*, as it damps the mesoscale activity by  $\approx 30\%$  (Renault et al., 2016a, 2017b). This energy transfer can be observed by satellite data (Renault et al., 2017a) and represents an unambiguous energy sink mechanism. Wind stress anomalies induced by

CFB produce a wind stress curl opposite to the eddy vorticity (Figure 1.19b).

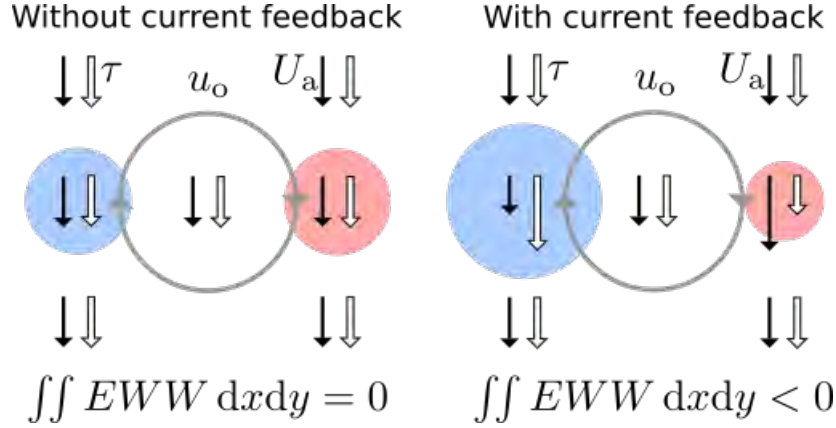


Figure 1.19: Schematic representation of mechanical air-sea interactions when considering (left) and not considering (right) CFB on a uniform southward wind blowing over an anticyclonic eddy. EWW refers to the eddy wind work. The red color refers to a positive wind work, *i.e.*, transfer of energy from the atmosphere to the ocean. The blue color refers to a negative wind work, *i.e.*, transfer of energy from the ocean to the atmosphere. Scheme modified from Renault et al. (2016a).

The degree of coupling between the atmosphere and ocean currents can be estimated over different geographic locations using coupling coefficients. Renault et al. (2016b) define the coupling coefficient ( $s_\tau$ ) defined as the slope between the mesoscale wind stress curl and current vorticity.  $s_\tau$  represents a measure of the CFB efficiency: the more negative the  $s_\tau$ , the more efficient the eddy killing effect (Figure 1.20). As proposed by Renault et al. (2017a),  $s_\tau$  can be predicted from the absolute wind speed referred at 10 m height ( $|U_{a10m}|$ ):

$$s_{\tau_p} = \alpha |U_{a10m}| + \beta, \quad (1.26)$$

where  $\alpha$  and  $\beta$  are derived from a linear regression. This relation shows that the larger the wind, the larger the coupling between the winds and ocean currents.

It results that the eddy wind work is related to  $s_\tau$  and the EKE:

$$F_e K_{ep} = \frac{2}{\rho_0} s_\tau \text{EKE}. \quad (1.27)$$

This explains why the larger coupling is observed in regions with strong mesoscale activity, *e.g.*, the Gulf Stream, the Kuroshio Current, the South African current system, the Caribbean, and the Gulf of Mexico (Figure 1.20), and why the eddy wind work show marked negative value in these regions (Figure 1.21). Besides, this indicates that the CFB strongly contributes to damping of the mesoscale eddies in these high EKE regions.

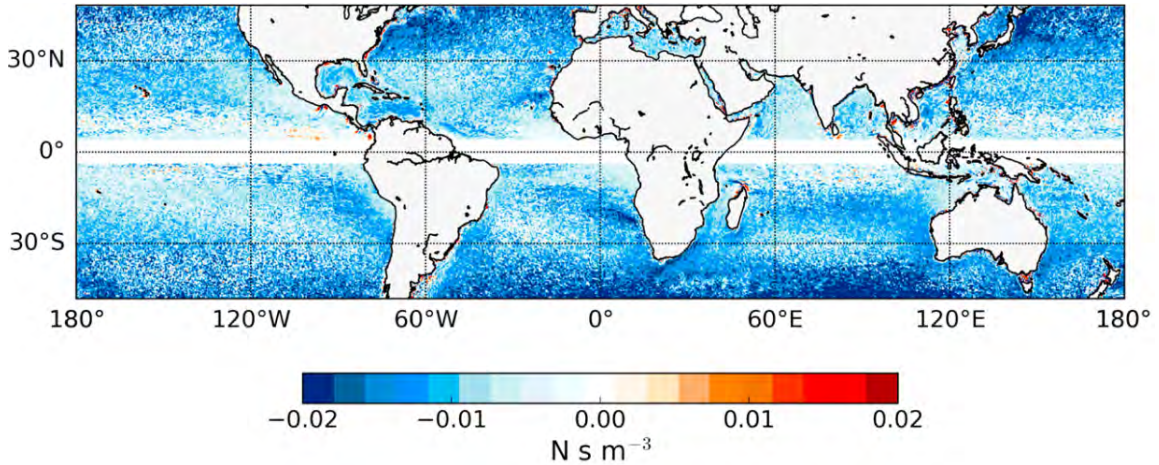


Figure 1.20: Coupling coefficient between the vorticity of surface geostrophic currents and the surface stress curl. Figure taken from Renault et al. (2019b).

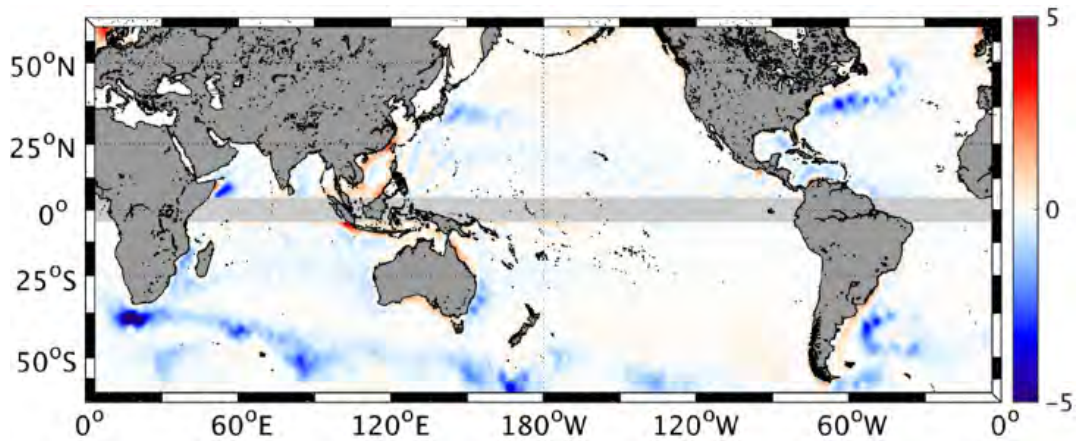


Figure 1.21: Observed eddy wind work ( $1 \times 10^{-6} \text{ m}^3 \text{ s}^{-3}$ ) estimated from 9-year satellite measurements of surface stress and geostrophic currents. The figure is taken from Renault et al. (2017a).

In the same way, the wind response to CFB can be quantified by means of the coupling coefficient  $s_w$  obtained by estimating the slope between the mesoscale wind curl and the current vorticity (Renault et al. (2016b), Figure 1.22).  $s_w$  from a coupled simulation that considers CFB is mainly positive everywhere, indicating an adjustment of low-level winds to mesoscale eddies, which is consistent with the atmospheric response to the *eddy killing* mechanism (1.19). However,  $s_w$  estimated from observations display negative coupling coefficients, as in  $s_\tau$ , which is related to the fact that scatterometers measure the equivalent neutral wind relative to surface currents instead of the absolute wind. This is demonstrated by Renault et al. (2019b), who compare  $s_w$  from equivalent neutral winds relative to surface currents from a coupled simulation and observations.

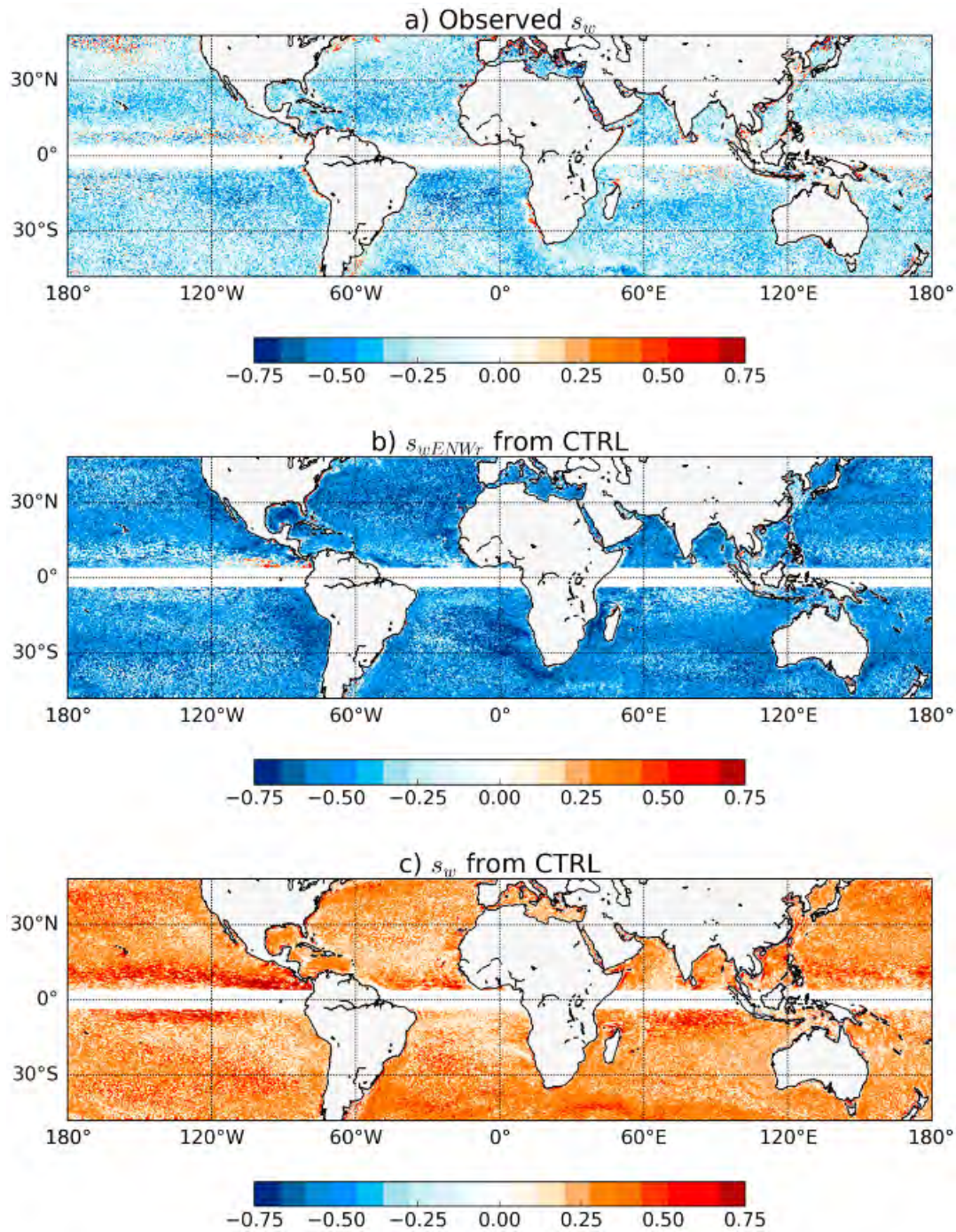


Figure 1.22: Coupling coefficient between the vorticity of surface geostrophic currents and the surface winds from observations (a) and numerical simulations (b,c). The coupling coefficient  $s_w$  in b) is computed using the equivalent neutral winds relative to surface currents, whereas in c) is computed directly from the 10-m winds. Figure taken from Renault et al. (2019b).

The coupling coefficients,  $s_\tau$  and  $s_w$  can also be used to parameterize the CFB effect on the wind stress in forced simulations. Renault et al. (2020) suggest and test two different

approaches: the stress-correction approach and the wind correction approach. With the wind-correction approach, the wind stress ( $\boldsymbol{\tau}$ ) is computed from the absolute wind corrected using the coupling coefficient,  $s_w$ :

$$\boldsymbol{\tau} = \rho_a C_D (\mathbf{U}_a - (1 - s_w) \mathbf{U}_o) |\mathbf{U}_a - (1 - s_w) \mathbf{U}_o|. \quad (1.28)$$

The wind correction approach can also be used to estimate the turbulent heat fluxes. With the stress-correction approach, the wind stress ( $\boldsymbol{\tau}_p$ ) can be prescribed or estimated with a bulk formulae using the absolute 10-m wind. The wind stress is then corrected using the  $s_\tau$  coupling coefficient as:

$$\boldsymbol{\tau} = \boldsymbol{\tau}_p + s_\tau \mathbf{U}_o. \quad (1.29)$$

The stress correction approach allows to reproduce the synoptical and spatial variability of the eddy killing, however, it can not be applied to estimate the heat fluxes response.

## 1.5 The wave feedback to the atmosphere and the ocean

Surface gravity waves participate in the modulation of momentum and heat fluxes, but also in the advection of water properties and tracers. Waves modulate the wind stress by changing the sea surface roughness length (Equations 1.7-1.9; Janssen, 2004) and by altering the wind in the atmospheric boundary layer. Besides, surface waves can also diminish the surface stress felt by the ocean by considering a portion of the surface stress for wind wave development (1.11; Janssen, 2004). Therefore, as wind stress depends on sea surface waves, surface waves could indirectly modulate CFB.

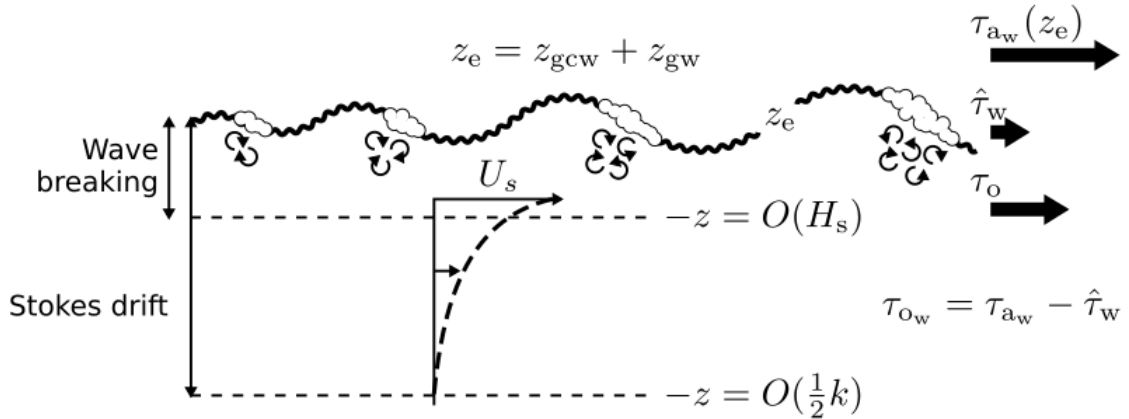


Figure 1.23: Representation of the momentum balance and wave-induced mixing related to the wave breaking and vertical shear of Stokes drift.  $k$  represents the wave number. Foam and curved arrows on the free surface indicate wave breaking and related mixing. Scheme modified from Belcher et al. (2012).

Stokes drift ( $\mathbf{U}_s$ ) is the net drift velocity induced by sea surface waves that exponentially

decay with depth and largely interact with ocean dynamics. The turbulence associated with the Stokes drift vertical shear, as well as that of breaking waves, are important drivers of mixing in the ocean upper layer (Figure 1.23; Belcher et al., 2012; Hamlington et al., 2014). Sea surface wave turbulence decreases the current vertical shear (Rascle et al., 2006), awakening surface current by spreading the wind work along the mixed layer (Rascle and Ardhuin, 2009) and supporting air-sea heat and gas fluxes (Jessup et al., 1997; Melville, 1996; Melville and Matusov, 2002).

Langmuir cells are an important source of vertical mixing in the ocean (Langmuir, 1938; Sullivan et al., 2007). As proposed by Craik and Leibovich (1976) and Leibovich (1983), Langmuir cells are developed through the vortex-force mechanism, which results from the interaction between the Stokes drift and the vorticity related to wind-driven current perturbations ( $\mathbf{U}_s \times \zeta$ ). The force resulting from this interaction horizontally tilts the surface vorticity, giving rise to counter-rotating cells aligned to the wind-generated waves (Figure 1.24).

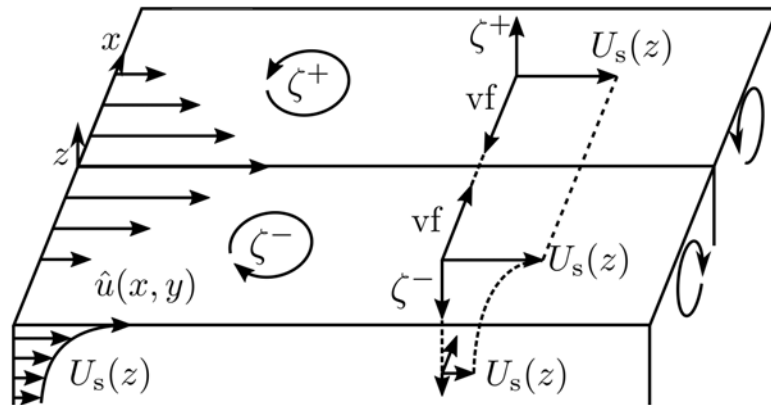


Figure 1.24: Development of Langmuir cells. Wind-driven current perturbations are indicated by  $\hat{u}$ , their vorticity by  $\zeta$ , and the Stokes drift profile by  $U_s$ .  $vf$  is the vortex-force. Scheme modified from Leibovich (1983) and Sullivan et al. (2007).

The Stokes-Coriolis force results from the interaction between the Coriolis force and the Stokes drift. It can significantly deflect mean Ekman current profiles, making this effect more important in upper latitudes (Polton et al., 2005). Lewis and Belcher (2004) and Rio et al. (2014) report that by including the Stokes drift into the Ekman currents estimation, currents deflections from  $10^\circ$  to  $45^\circ$  between surface currents and wind stress are obtained.

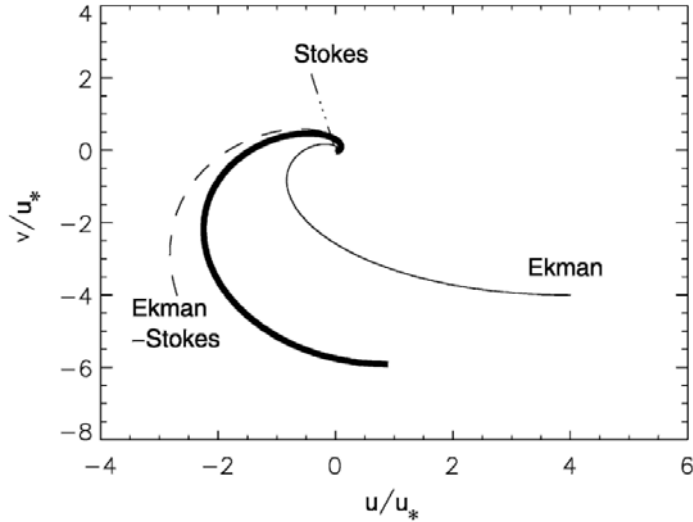


Figure 1.25: Mean flow velocity is related to the full Ekman balance (thick line). Ekman (thin line) and Ekman–Stokes (segmented line) components are depicted with the thin and segmented lines, respectively. Dotted–dashed line is the Stokes drift components. All quantities are normalized with the friction velocity ( $u_*$ ). Scheme modified from Polton et al. (2005).

Several efforts have been made to assess the role of surface waves in global or regional ocean dynamics by using low-resolution ( $1/4^\circ$  or larger spatial resolution) atmosphere–waves or atmosphere–forced simulations, as well as the fully coupled ocean–waves–atmosphere simulations (Breivik et al., 2015; Chune and Aouf, 2018; Couvelard et al., 2020, ; Tables 1.3 and 1.4). The results of these studies show that ocean dynamics are sensitive to the waves, but seems that coupled (full or ocean–wave) simulations lead to colder sea surface temperatures and that waves–atmosphere forced simulations to hotter sea surface temperatures. However, these simulations are not able to solve the full mesoscale activity since there are performed with a spatial resolution equal to or larger than  $1/4^\circ$ , since a higher resolution is necessary to properly reproduce the mesoscale modulation of the air–sea turbulent heat fluxes (Oerder et al., 2016; Putrasahan et al., 2017). High-resolution numerical simulations (about 3.7 km in the ocean) for the Baltic Sea and North Sea that include the ocean–waves (Wu et al., 2019b) and ocean–waves–atmosphere (Wu et al., 2019a) coupling show that waves tend to reduce the sea surface temperature by increasing the vertical mixing.

Table 1.3: Main characteristic of numerical simulations that include surface wave interactions with the ocean or atmosphere. OCE and ATM refer to the ocean and atmosphere models used in the numerical implementations. BS and NS refer to the Baltic Sea and North Sea, respectively.

	Models			Iteration time	Spatial resolution	Region
	OCE	Waves	ATM			
Breivik et al. (2015)	NEMO	ECWAM	IFS	31 years	1/3°	Global
Chune and Aouf (2018)	NEMO	Forced	Forced	3 years	1/4°	Global
Couvelard et al. (2020))	NEMO	WW3	Forced	2 years	1/4°	Global
Wu et al. (2019b)	NEMO	WAM	Forced	1 year	~3.7 km	BS/NS
Wu et al. (2019a)	NEMO	WW3	WRF	2 months	~3.7 km	BS/NS

Table 1.4: Numerical simulations that include surface wave interactions with the ocean or atmosphere and their parametrizations. VF, SC, LT, and TKE refer to vortex–force, Stokes–Coriolis, Langmuir turbulence, and turbulent kinetic energy, respectively. The superscript (\*) indicates that the variable has been computed in the wave model.

	Roughness	Stress	VF/SC	TKE flux	LT	CFB
Breivik et al. (2015)	$z_e = \frac{u_*^2}{g} \frac{0.006}{\sqrt{1-\tau_w/\tau_a}}$	$\tau_o = \tau_a - \hat{\tau}_w$	Yes	Yes	Yes	No
Chune and Aouf (2018)	$z_e^* = z_{10m} e^{-k} \sqrt{C_{dw}}$	$\tau_o = \tau_a - \hat{\tau}_w$	SC	Yes	No	No
Couvelard et al. (2020))	$z_e = \frac{u_*^2}{g} \frac{0.018}{\sqrt{1-\tau_w/\tau_a}}$	$\tau_o = \tau_a (\tau_o^*/\tau_a^*)$	Yes	Yes	Yes	No
Wu et al. (2019b)	$z_e = \frac{u_*^2}{g} \frac{0.006}{\sqrt{1-\tau_w/\tau_a}}$	$\tau_o = \tau_a - \hat{\tau}_w$	Yes	Yes	No	No
Wu et al. (2019a)	$z_e = \frac{u_*^2}{g} \frac{0.0095}{\sqrt{1-\tau_w/\tau_a}}$	$\tau_o = \tau_a - \hat{\tau}_w$	SC	Yes	No	Yes

The WFB can have an impact on wind stress. Forced and low spatial resolution simulations from Chune and Aouf (2018) show that waves increase (decrease) about 10% the momentum flux high–latitudes (above the tropics) and lead to a reduction of the same order in tropical regions (Figure 1.26).

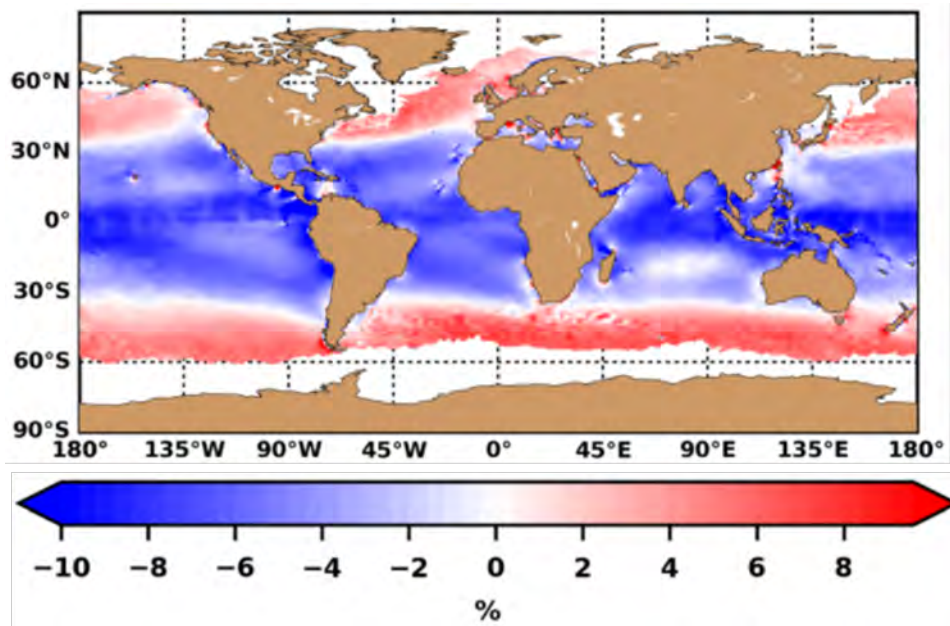


Figure 1.26: Mean differences in the wind stress computed with and without the influence of surface waves over 3-year numerical simulations. Figure taken from [Chune and Aouf \(2018\)](#).

Low spatial resolution simulations of [Couvelard et al. \(2020\)](#) show that the wave-modified wind stress parameterization follows closely significant wave height patterns (Figures 1.27). The authors also found that including a sea surface roughness length with a dependence on the sea state does not significantly modify the drag coefficient over wind speeds lower than  $8 \text{ m s}^{-1}$  (Figure 1.28). In contrast, the authors report a 10% increase in the drag coefficient over wind speeds larger than  $\sim 20 \text{ m s}^{-1}$ . Additionally, the authors show that including a momentum balance with a dependence on the sea state (Equation 1.11) results in a  $\sim 2\%$  reduction in the wind stress and mention that this correction is thus almost negligible. However, their numerical simulations are not able to solve mesoscale eddies, where TFB and CFB effects are more important, and therefore, it is not possible to quantify the impact of surface waves over these feedbacks. [Wu et al. \(2019a\)](#) include CFB in their eddy-solving simulation, however, the authors do not investigate if surface waves can modulate the feedback of surface currents to the atmosphere.

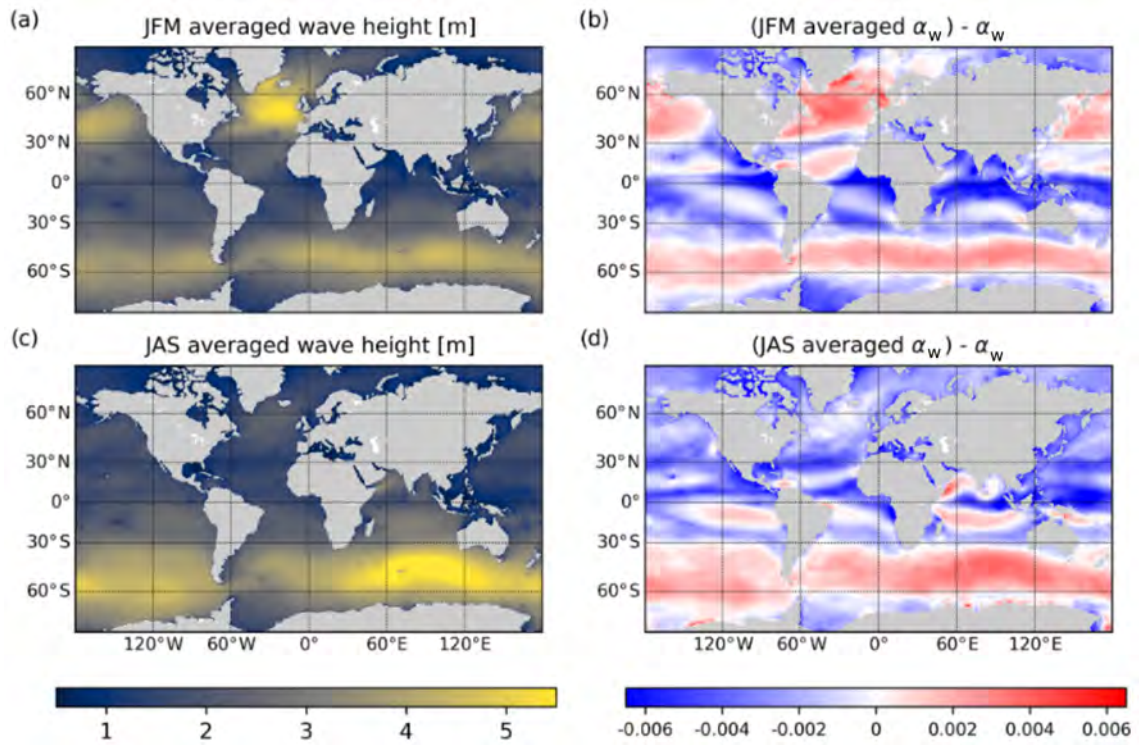


Figure 1.27: Mean differences in the wind stress computed with and without the influence of surface waves over 3-year numerical simulations. The figure is taken from Couvelard et al. (2020).

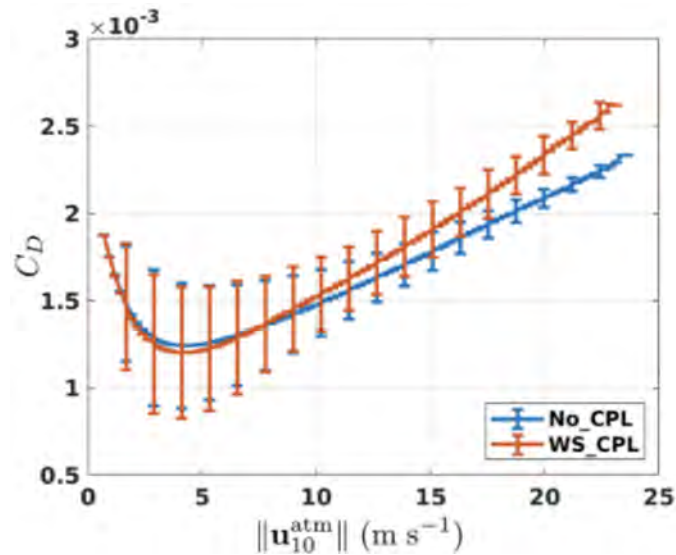


Figure 1.28: Drag coefficient  $C_{d_w}$  as a function of the wind speed ( $|U_a|$ ). WS\_CPL and NO\_CPL refer to the numerical experiments with and without a Charnock parameter dependent on the sea state. The figure is taken from Couvelard et al. (2020).



# Materials and method

---

## Contents

---

<b>2.1</b>	<b>Numerical simulations and observational datasets . . . . .</b>	<b>50</b>
2.1.1	Coupled ocean–atmosphere configurations . . . . .	50
2.1.2	Coupling strategy for ocean–atmosphere coupled simulations . . . . .	51
2.1.3	Coupling strategy for ocean–atmosphere–waves coupled simulations . . . . .	52
2.1.4	Observational datasets . . . . .	52
<b>2.2</b>	<b>Methods . . . . .</b>	<b>53</b>
2.2.1	Energy budget . . . . .	53
2.2.2	Coarse–grained energy flux and geostrophic eddy wind work . . . . .	54
2.2.3	Position of the Loop Current . . . . .	56
2.2.4	Loop Current eddies detection . . . . .	56

---

## 2.1 Numerical simulations and observational datasets

This chapter provides a description of the numerical configurations used in this work and the observational datasets used to validate the numerical simulations. This chapter also describes the methodologies used to analyze or quantify the energy transfers and dynamics of the Loop Current.

### 2.1.1 Coupled ocean–atmosphere configurations

This regional configuration uses the ocean model NEMO (Nucleus for European Modeling of the Ocean) v4.0 (Gurvan et al., 2022) and the atmospheric model WRF (The Weather Research and Forecast) v4.1 to simulate the air–sea interactions over the Intra–Americas Sea and western Tropical Atlantic (Figure 2.1).

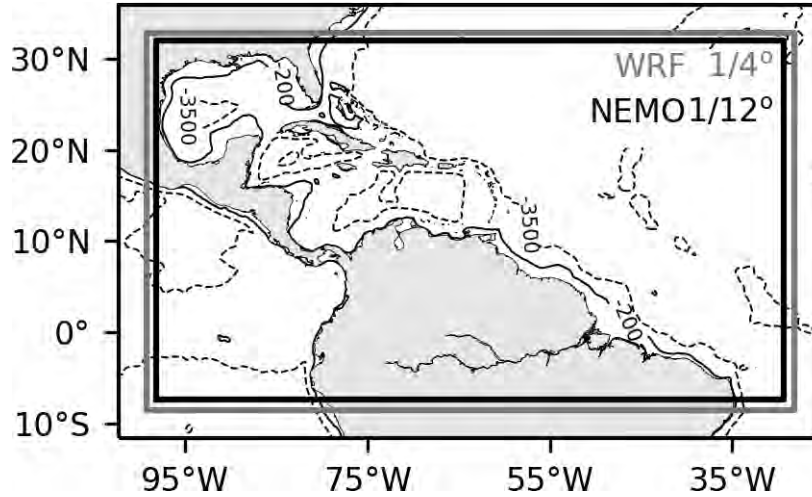


Figure 2.1: Numerical domains of NEMO (black square) and WRF (gray square).

The regional NEMO configuration has a grid which extends from 7.4°S to 31.9°N and from 98.2°W to 29.3°W, with a spatial resolution of 1/12° ( $\sim 8$  km). The grid is composed of 75 fixed vertical levels, with 8 levels in the upper 10 m depth and 38 levels between 10 and 1000 m depth. The model time step is 400 s. At the lateral boundaries, daily averages of temperature, salinity, sea surface elevation, and horizontal velocity are prescribed from the Global Mercator reanalysis (GLORYS2V4; Lellouche et al., 2018). The initial condition is obtained from a previous 3-year simulation initialized with GLORYS2V4 and forced at the surface with the Drakkar Forcing Set (DFS5.2; Dussin et al., 2016), from the year 1990 to 1993. NEMO solves the three-dimensional primitive equations on an Arakawa C-grid, assuming hydrostatic equilibrium and Boussinesq approximation. In NEMO, the advection of tracers is performed with a flux-corrected transport scheme (Zalesak, 1979). The horizontal diffusion of tracers and momentum are parameterized with a bi-Laplacian operator. The vertical turbulent mixing is computed using the Generic Length Scale scheme (GLS, Umlauf

and Burchard, 2003), with a  $k$ - $\epsilon$  turbulent closure model (Reffray et al., 2015; Rodi, 1979). Turbulent heat fluxes are computed through the COARE v3.0 (Coupled Ocean–Atmosphere Response Experiment) bulk formulae (Fairall et al., 2003).

The WRF model is implemented in a one-grid configuration with a spatial resolution of  $1/4^\circ$  (25 km) and 40 terrain-following vertical levels with surface and upper stretch factors of 1.3 and 1.1, respectively. The domain is slightly larger than the NEMO domain to avoid the effect of the WRF sponge (4 points; Renault et al., 2019a). The model time step is 75 s. ERA–Interim data is used to initialize the model and to force the open boundary conditions. The WRF model allows the user to employ a wide range of parameterizations. Following Gévaudan et al. (2021), who performed NEMO–WRF simulations of the Tropical Atlantic at a similar resolution, this implementation includes the WRF–single–moment–microphysics class 6 scheme (WSM6, Hong and Lim, 2006), the rapid radiative transfer model for the longwave flux (RRTM, Mlawer et al., 1997), the RRTMG shortwave flux scheme (Iacono et al., 2008), and the Yonsei University (YSU) scheme to solve the planetary boundary layer physics (Hong et al., 2006; Hong, 2010), the Noah land–surface model and the Monin–Obukhov similarity scheme (Chen and Dudhia, 2001). Cumulus are parameterized by the multi-scale Kain–Fritsch scheme (MSKF, Zheng et al., 2016).

The Ocean Atmosphere Sea Ice Sol (OASIS–MTC) 3.0 (Valcke, 2013) software is used to exchange hourly averaged data between the numerical models NEMO and WRF.

### 2.1.2 Coupling strategy for ocean–atmosphere coupled simulations

The impact of the current feedback on the dynamics of the Gulf of Mexico is analyzed in Chapters 4 and 6 by comparing twin experiments which have been carried out over the period 1993–2016 (24 years): NOCF and CF. In NOCF, which refers to “No Current Feedback”, WRF forces NEMO with hourly momentum, heat, and freshwater fluxes, while NEMO sends SST to WRF. In contrast, in the CF experiment, which refers to “Current Feedback”, WRF includes surface currents from NEMO to compute the turbulent fluxes. The difference between the experiments with and without current feedback lies in how the momentum and turbulent heat fluxes are estimated. In the NOCF experiment, momentum and turbulent heat fluxes are computed by WRF as a function of the 10 m absolute wind ( $\mathbf{U}_a$ ):

$$\boldsymbol{\tau}_a = \rho_a C_d |\mathbf{U}_a| \mathbf{U}_a = \boldsymbol{\tau}_o, \quad (2.1)$$

$$Q_s = \rho_z c_p C_h |U_a| (\theta_z - T_s), \quad (2.2)$$

$$Q_l = \rho_a L_e C_e |U_a| (q_0 - q_z). \quad (2.3)$$

In CF, NEMO also gives hourly averages of surface currents ( $\mathbf{U}_o$ ) to WRF, and the turbulent fluxes are estimated as a function of the relative wind ( $\mathbf{U}_r = \mathbf{U}_a - \mathbf{U}_o$ ; Equations 1.1–1.3). This strategy has been implemented in several studies that have successfully isolated and quantified the effects of CFB on the ocean and atmospheric dynamics (Renault et al., 2016a,b, 2017b; Seo et al., 2017; Oerder et al., 2018; Renault et al., 2019a; Jullien et al., 2020;

Renault et al., 2021a).

### 2.1.3 Coupling strategy for ocean–atmosphere–waves coupled simulations

In order to investigate the role of WFB in regional dynamics, the ocean-atmosphere model has also been coupled with the wave model WW3 (WAVEWATCH III) v6.07.1 (Tolman III). WW3 is used to reproduce the evolution of the ocean wave directional spectra by solving the wave action equation (Komen et al., 1994). The spectral source terms related to the wind energy input and dissipation are parametrized with the Ardhuin et al. (2010) formulations and the nonlinear wave–wave interactions with the discrete interaction approximation (Hasselmann et al., 1985). WW3 has the same domain and spatial resolution as WRF.

The numerical models NEMO and WRF have a similar configuration to the one used in the ocean–atmosphere coupled configuration (Section 2.1.1). In this new configuration WF, which refers to “Wave Feedback”, there is a two–way coupling between atmosphere and waves. WRF has been modified to take into account the Charnock parameter from WW3 to compute the wind stress (estimated using the wave spectrum in WW3) and to force WW3 by means of surface winds. This simulation is developed to analyze whether sea surface waves can modulate CFB through the Charnock parameter and therefore, ocean–sea surface wave interactions are not considered in this simulation. OASIS is used to exchange hourly averaged data between NEMO, WRF, and WW3.

A comparison of the CF and WF experiments will allow us to study whether WFB can modulate CFB and the mechanisms of their interaction by modifying the wind stress.

Table 2.1: Main characteristic of numerical simulations. The Charnock parameter ( $\alpha$ ) in NOCF and CF experiments is equal to 0.0185, whereas in the WF experiment,  $\alpha_w$  is estimated directly by WW3 and sent to WRF.

Experiments	Wind stress	Roughness
NOCF	$\tau_a = \rho_a C_d  \mathbf{U}_a  \mathbf{U}_a$	$z_0 = \alpha \frac{u_*^2}{g}$
CF	$\tau_a = \rho_a C_d  \mathbf{U}_r  \mathbf{U}_r$	$z_0 = \alpha \frac{u_*^2}{g}$
WF	$\tau_a = \rho_a C_d  \mathbf{U}_r  \mathbf{U}_r$	$z_e = \frac{\alpha_w}{\sqrt{1 - \tau_w/\tau_a}} \frac{u_*^2}{g}$

### 2.1.4 Observational datasets

This study makes use of 29–year data of Sea Surface Height and geostrophic currents gridded provided by the Copernicus Marine Environment Monitoring Service CMEMS (2017) from 1993 to 2021, with daily temporal resolution and  $1/4^\circ$  horizontal resolution. This dataset

is referred to as AVISO in this work. AVISO gridded product results from the merge of altimeter along-track data by means of an optimal interpolation over a 10 days window (Taburet et al., 2019). Daily gridded products have allowed the scientific community to identify and track mesoscale eddies and boundary currents, describe the ocean variability by means of frequency/wave number spectra, and also to validate numerical simulations (Traon, 2013). However, the merging of multiple altimeter data sets results in the loss of small-scale signals captured by along-track altimeters. Therefore, only smoothed structures with a radius larger than 40 km and a lifetime larger than a week are captured through this method (Chelton et al., 2011; Amores et al., 2018; Archer et al., 2020). In the Gulf of Mexico, this does not allow, for example, the capture of small and fast propagating frontal eddies (Jouanno et al., 2016).

Sea surface temperature daily data from 1993 to 2016 is obtained from the Optimum Interpolation Sea Surface Temperature (OISST) dataset v2.0 from NOAA (Banzon et al., 2016). This dataset has a spatial resolution of  $1/4^\circ$  and is obtained from the merging of the Advanced Very High Resolution Radiometer (AVHRR) infrared satellite data and in situ observations.

The Scatterometer Climatology of Ocean Winds (SCOW; Risien and Chelton, 2008) dataset is based on the Quick Scatterometer (QuikSCAT) data and provides daily wind stress data from 1999 to 2009 with a spatial resolution of  $1/4^\circ$ . Midlatitudes were usually sampled twice per day by QuikSCAT, with separation periods of about 12 hours. Since the overlapping of measurement swaths from successive orbits, latitudes higher than  $50^\circ$  can be substantially sampled. However, since ground tracks are more widely spaced in low latitudes, these regions are generally sampled less than twice a day. Because of this, SCOW is limited by the fact that the daily estimates only represent a small percentage of the wind variance at most locations. However, an important advantage of SCOW is that the wind stress is in fact the true wind stress on the sea surface since it considers the difference between the wind velocity and surface ocean currents.

The Objectively Analyzed Air–Sea Fluxes (OAFflux) is a project from the Woods Hole Oceanographic Institution which provides  $1^\circ$ -gridded turbulent heat and moisture fluxes (Yu et al., 2008). OAFflux products are constructed from an optimal blending of satellite retrievals and atmospheric reanalyses data and use the COARE formulation to compute the heat and moisture fluxes. The net heat flux is computed by incorporating the radiative fluxes from the International Satellite Cloud Climatology Project.

## 2.2 Methods

### 2.2.1 Energy budget

Following Marchesiello et al. (2003) and Renault et al. (2016b, 2017b), a simplified energy budget is estimated focusing on the following relevant energy sources and eddy–mean conver-

sion terms:

$$F_m K_{m_g} = \frac{1}{\rho_0} (\overline{u_g \tau_x} + \overline{v_g \tau_y}), \quad (2.4)$$

$$F_e K_{e_g} = \frac{1}{\rho_0} (\overline{u'_g \tau'_x} + \overline{v'_g \tau'_y}), \quad (2.5)$$

$$K_m K_e = - \int_z^0 \left( \overline{u' u'} \frac{\partial \bar{u}}{\partial x} + \overline{u' v'} \frac{\partial \bar{u}}{\partial y} + \overline{u' w'} \frac{\partial \bar{u}}{\partial z} + \overline{v' u'} \frac{\partial \bar{v}}{\partial x} + \overline{v' v'} \frac{\partial \bar{v}}{\partial y} + \overline{v' w'} \frac{\partial \bar{v}}{\partial z} \right) dz, \quad (2.6)$$

$$P_e K_e = - \frac{g}{\rho_0} \int_z^0 \overline{\rho' w'} dz. \quad (2.7)$$

All quantities are decomposed into the long-term mean estimated over the 1993–2016 period and indicated with an overbar ( $\bar{\phantom{x}}$ ). Their deviations from this long-term mean are referred to using primes ( $'$ ). Renault et al. (2016b, 2017b) demonstrate that the geostrophic contribution of the wind work (labeled with the sub-index  $_g$ ), and in particular the one related to the eddy wind work, largely sink energy from the ocean to the atmosphere. Additionally, the authors show that this sink of energy can modify the energy budget through barotropic  $K_m K_e$  and baroclinic instabilities  $P_e K_e$ .

## 2.2.2 Coarse-grained energy flux and geostrophic eddy wind work

The coarse-graining method allows estimating the energy flux related to a certain spatial scale (Leonard, 1975; Germano, 1992; Aluie et al., 2018; Schubert et al., 2020). The method is based on the separation between large and small scales around chosen scales,  $L$ . The signal is separated by applying a two-dimensional running mean with diameter  $L$  to a field  $\mathcal{F}(x, y)$ . This filter results from applying a convolution  $\langle \mathcal{F}(x, y) \rangle = \mathcal{C} \times \mathcal{F}(x, y)$  with a top-hat kernel

$$\mathcal{C} = \begin{cases} 1/A, & \text{if } |\mathbf{r}| < L/2, \\ 0, & \text{otherwise.} \end{cases} \quad (2.8)$$

Here,  $A = \pi L^2/4$  is the circular normalization area of diameter  $L$ , and  $\mathbf{r}$  is the radial position vector (Schubert et al., 2020).

Following Aluie et al. (2018), applying the convolution to the equation of motion results in a term that allows us to estimate the energy flux for a certain scale  $L$ :

$$\Pi = - \int_z^0 \left( (\langle u^2 \rangle - \langle u \rangle^2) \frac{\partial \langle u \rangle}{\partial x} + (\langle uv \rangle - \langle u \rangle \langle v \rangle) \left( \frac{\partial \langle u \rangle}{\partial y} + \frac{\partial \langle v \rangle}{\partial x} \right) + (\langle v^2 \rangle - \langle v \rangle^2) \frac{\partial \langle v \rangle}{\partial x} \right) dz. \quad (2.9)$$

As mentioned by Aluie et al. (2018), this term is similar to the barotropic instability (Equation 2.6), which is related to the transfer of energy between the MKE and EKE. Positive values of  $\Pi$  are related to an energy flux to smaller scales (forward cascade), whereas negative values to larger scales (inverse cascade).

Likewise, the baroclinic instability ( $P_e K_{e_{cg}}$ ) and geostrophic eddy wind work ( $F_e K_{e_{cg}}$ ) is

derived from coarse-grained filtered fields:

$$P_e K_{e_{cg}} = -\frac{g}{\rho_0} \int_z^0 (\langle \rho w \rangle - \langle \rho \rangle \langle w \rangle) dz. \quad (2.10)$$

$$F_e K_{e_{cg}} = \frac{1}{\rho_0} ((\langle \tau_x u_g \rangle - \langle \tau_x \rangle \langle u_g \rangle) + (\langle \tau_y v_g \rangle - \langle \tau_y \rangle \langle v_g \rangle)), \quad (2.11)$$

It is worth mentioning that  $P_e K_{e_{cg}}$  and  $F_e K_{e_{cg}}$  represent the production of EKE from EPE and the geostrophic eddy wind work, respectively. Both terms represent the energy flux from  $L$  to smaller scales (Rai et al., 2021).

The coarse-grained KE budget can also be computed from a flow decomposed in a low and high-frequency signal ( $\mathbf{u} = \mathbf{u}_f + \mathbf{u}_{hf}$ ). When applying this decomposition into the coarse-grained EKE budget terms, we will find cross terms associated with non-linear exchanges of energy between the low and high-frequency signals. The barotropic instability reads as:

$$\Pi = \Pi_f + \Pi_{hf} + \Pi_{nl}, \quad (2.12)$$

$$\begin{aligned} \Pi_f = & - \int_z^0 \left( (\langle u_{if}^2 \rangle - \langle u_{if} \rangle^2) \left( \frac{\partial \langle u_{if} + \partial \langle u_{hf} \rangle}{\partial x} \right) + (\langle v_{if}^2 \rangle - \langle v_{if} \rangle^2) \left( \frac{\partial \langle v_{if} + \partial \langle v_{hf} \rangle}{\partial x} \right) \right. \\ & \left. + (\langle u_{if} v_{if} \rangle - \langle u_{if} \rangle \langle v_{if} \rangle) \left( \frac{\partial \langle u_{if} + \partial \langle u_{hf} \rangle}{\partial x} + \frac{\partial \langle v_{if} + \partial \langle v_{hf} \rangle}{\partial y} \right) \right) dz, \end{aligned} \quad (2.13)$$

$$\begin{aligned} \Pi_{hf} = & - \int_z^0 \left( (\langle u_{hf}^2 \rangle - \langle u_{hf} \rangle^2) \left( \frac{\partial \langle u_{hf} + \partial \langle u_{hf} \rangle}{\partial x} \right) + (\langle v_{hf}^2 \rangle - \langle v_{hf} \rangle^2) \left( \frac{\partial \langle v_{hf} + \partial \langle v_{hf} \rangle}{\partial x} \right) \right. \\ & \left. + (\langle u_{hf} v_{hf} \rangle - \langle u_{hf} \rangle \langle v_{hf} \rangle) \left( \frac{\partial \langle u_{hf} + \partial \langle u_{hf} \rangle}{\partial x} + \frac{\partial \langle v_{hf} + \partial \langle v_{hf} \rangle}{\partial y} \right) \right) dz, \end{aligned} \quad (2.14)$$

$$\Pi_{nl} = - \int_z^0 (\langle u_{if} v_{hf} \rangle - \langle u_{if} \rangle \langle v_{hf} \rangle + \langle u_{hf} v_{if} \rangle - \langle u_{hf} \rangle \langle v_{if} \rangle) \left( \frac{\partial \langle u_{if} + \partial \langle u_{hf} \rangle}{\partial x} + \frac{\partial \langle v_{if} + \partial \langle v_{hf} \rangle}{\partial y} \right) dz, \quad (2.15)$$

whereas baroclinic instability ( $P_e K_{e_{cg}}$ ) and geostrophic eddy wind work ( $F_e K_{e_{cg}}$ ):

$$P_e K_{e_{cg}} = P_e K_{e_{if}} + P_e K_{e_{hf}} + P_e K_{e_{nl}}, \quad (2.16)$$

$$P_e K_{e_{if}} = -\frac{g}{\rho_0} \int_z^0 (\langle \rho_{if} w_{if} \rangle - \langle \rho_{if} \rangle \langle w_{if} \rangle) dz, \quad (2.17)$$

$$P_e K_{e_{hf}} = -\frac{g}{\rho_0} \int_z^0 (\langle \rho_{hf} w_{hf} \rangle - \langle \rho_{hf} \rangle \langle w_{hf} \rangle) dz, \quad (2.18)$$

$$P_e K_{e_{nl}} = -\frac{g}{\rho_0} \int_z^0 (\langle \rho_{if} w_{hf} \rangle - \langle \rho_{if} \rangle \langle w_{hf} \rangle + \langle \rho_{hf} w_{if} \rangle - \langle \rho_{hf} \rangle \langle w_{if} \rangle) dz, \quad (2.19)$$

$$F_e K_{e_{cg}} = F_e K_{e_{lf}} + F_e K_{e_{hf}} + F_e K_{e_{nl}}, \quad (2.20)$$

$$F_e K_{e_{lf}} = \frac{1}{\rho_0} ((\langle \tau_{x_{lf}} u_{g_{lf}} \rangle - \langle \tau_{x_{lf}} \rangle \langle u_{g_{lf}} \rangle) + (\langle \tau_{y_{lf}} v_{g_{lf}} \rangle - \langle \tau_{y_{lf}} \rangle \langle v_{g_{lf}} \rangle)), \quad (2.21)$$

$$F_e K_{e_{hf}} = \frac{1}{\rho_0} ((\langle \tau_{x_{hf}} u_{g_{hf}} \rangle - \langle \tau_{x_{hf}} \rangle \langle u_{g_{hf}} \rangle) + (\langle \tau_{y_{hf}} v_{g_{hf}} \rangle - \langle \tau_{y_{hf}} \rangle \langle v_{g_{hf}} \rangle)), \quad (2.22)$$

$$F_e K_{e_{nl}} = \frac{1}{\rho_0} ((\langle \tau_{x_{lf}} u_{g_{hf}} \rangle - \langle \tau_{x_{lf}} \rangle \langle u_{g_{hf}} \rangle) + (\langle \tau_{x_{hf}} u_{g_{lf}} \rangle - \langle \tau_{x_{hf}} \rangle \langle u_{g_{lf}} \rangle) + (\langle \tau_{y_{lf}} v_{g_{hf}} \rangle - \langle \tau_{y_{lf}} \rangle \langle v_{g_{hf}} \rangle) + (\langle \tau_{y_{hf}} v_{g_{lf}} \rangle - \langle \tau_{y_{hf}} \rangle \langle v_{g_{lf}} \rangle)) \quad (2.23)$$

### 2.2.3 Position of the Loop Current

Following [Leben \(2005\)](#), a sea surface height anomaly (SSHa) is first estimated by removing from the sea surface height its long-term temporal mean and its spatial average over the GoM. The daily LC position is then inferred from the 17 cm SSHa contour, starting from the Yucatan Channel and ending at the Florida Straits. Once the LC is detected, the maximum North latitude, minimum East longitude, and LC length are used to infer the LC penetration into the GoM. In addition, as a proxy of the energy stored by the LC, the surface KE is integrated within the 17 cm SSHa contour.

### 2.2.4 Loop Current eddies detection

The eddy tracking detection method developed by [Chaigneau et al. \(2009\)](#) and implemented over the GoM by [Sosa-Gutiérrez et al. \(2020\)](#) is used to detect and track LC eddies. This approach consists of detecting local maxima in daily sea level anomaly maps that are associated with the center of anticyclonic eddies. The detection method identifies the outermost closed contour of sea level anomaly for each eddy center and associates it with the eddy edge. The eddies are tracked by an algorithm developed by [Pegliasco et al. \(2015\)](#), which computes eddy trajectories by the intersection of eddies along with daily maps. In this study, LC eddies are defined as eddies separated from the LC with a lifetime larger than 200 days ([Sosa-Gutiérrez et al., 2020](#); [Chelton et al., 2011](#)).

# Long-term conditions over the Intra-Americas Sea and numerical validations

---

## Contents

---

3.1	Mean and eddy circulation . . . . .	58
3.2	Sea Surface Temperature and air-sea heat fluxes . . . . .	60
3.3	Wind stress and wind stress curl . . . . .	62
3.4	Sensitivity to the Current Feedback . . . . .	63

---

This chapter describes the mean oceanic and atmospheric conditions over the Caribbean Sea and the Gulf of Mexico in terms of surface currents, sea surface temperature, and surface wind properties. Moreover, a validation of the CF experiment is presented, as well as the first insights on the sensitivities of regional conditions to the current feedback.

### 3.1 Mean and eddy circulation

To properly describe the long-term conditions over the Intra-Americas Sea and validate the numerical simulations, the domain is divided into the GoM, Caribbean Sea, and North and South Atlantic regions (Figure 3.1).

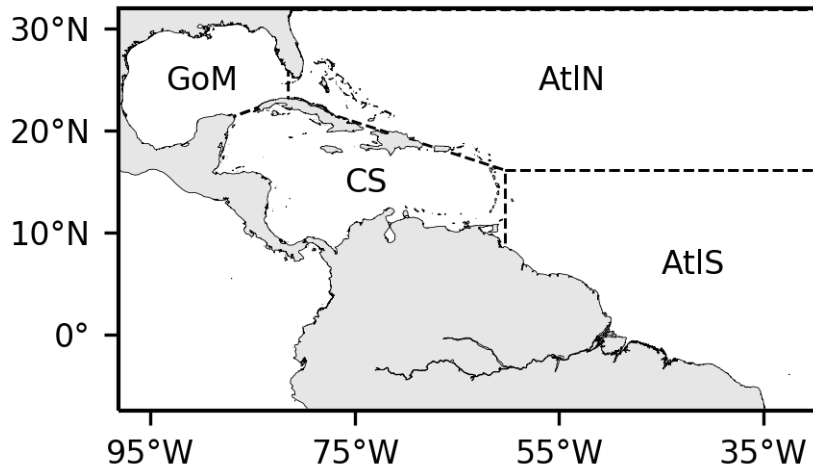


Figure 3.1: Polygons to delimit the Gulf of Mexico (GoM), Caribbean Sea (CS), and the northern and southern Atlantic (AtIN and AtIS) regions.

Long-term geostrophic current patterns from AVISO over 24-years (1993 to 2016) are shown in Figure 3.2. The strongest and permanent current in the GoM is the LC, which is connected to the Caribbean Sea through the Yucatán Current. The Colombia Gyre and the Caribbean and North Caribbean currents are the dominant features in the Caribbean Sea, while in the AtIS are the North Equatorial Counter Current, the Guiana Current, and the North Brazil current. An estimation of the climatological KE from AVISO shows that AtIS and CS are the regions with a larger KE over the IAS, contributing with 46 and 21% of the KE in the IAS (Figure 3.3a,j). Although strong large-scale currents occur in these regions, the total KE is dominated by the EKE (Figure 3.3a-c). This EKE is mainly due to mesoscale eddies embedded in the western boundary current as shown in previous studies, *e.g.*, Jouanno et al. (2012).

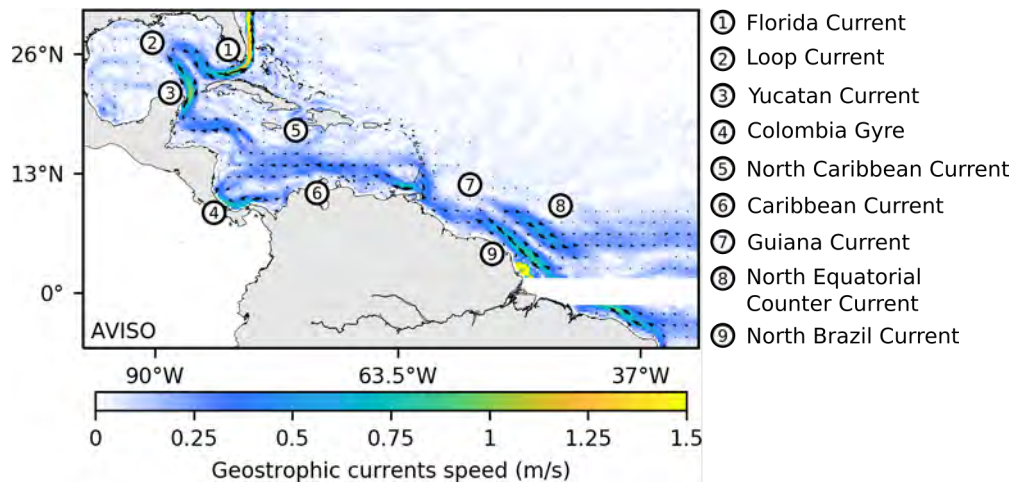


Figure 3.2: Geostrophic currents climatology and main dynamical features over the IAS from 1993 to 2016.

The CF simulation is compared with observations in Figure 3.3. The geostrophic currents that are simulated in CF agree with those inferred from AVISO, evidencing that the numerical simulation can reproduce the main characteristics of the large-scale current system in the IAS (Figure 3.3a,d). Besides, this simulation reproduces nicely the climatological KE over the GoM and the North Atlantic (AtlN) regions (Figure 3.3j). However, the simulation overestimates the KE by 17 and 34% over the Caribbean Sea and South Atlantic (AtlS) regions, respectively (Figure 3.2j). These differences are mainly related to an overestimation in the Eddy Kinetic Energy (Figure 3.2l). This overestimation could be mainly related to model biases. However, previous studies have demonstrated that sampling capabilities of altimetry only allow the detection of large mesoscale eddies signatures (Chelton et al., 2011; Amores et al., 2018; Archer et al., 2020), and therefore, detailed analyses are needed to identify the cause of these biases.

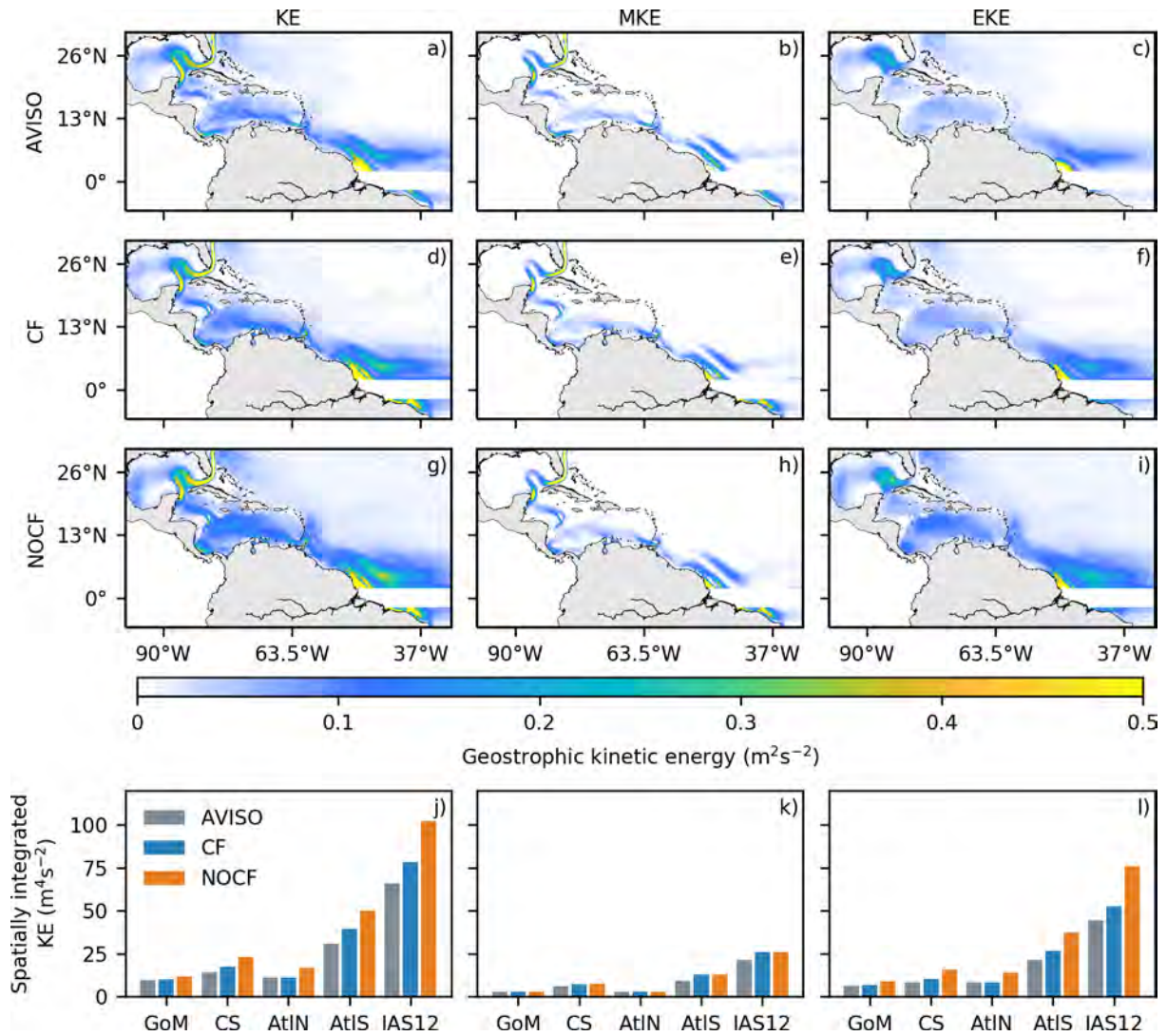


Figure 3.3: KE (first column), MKE (second column), and EKE (third column) climatologies over the IAS for AVISO (first row), CF (second row), and NOCF (third row). j–l) Spatially integrated energy over the regions comprising the IAS is shown in the bottom row.

### 3.2 Sea Surface Temperature and air-sea heat fluxes

The sea surface temperature obtained from AVHRR is shown in Figure 3.4a. Warmer sea surface temperature is found in the northern and western regions of the Caribbean Sea and in the Amazon River mouth, reaching up to 28 °C. The sea surface temperature in the GoM and AtIN ranges between 24 and 27 °C. The signature of recurrent upwelling events can be observed in the Yucatán Peninsula (GoM; Jouanno et al., 2018) and along the southern Caribbean coast, along Colombia and Venezuela (Paramo et al., 2011).

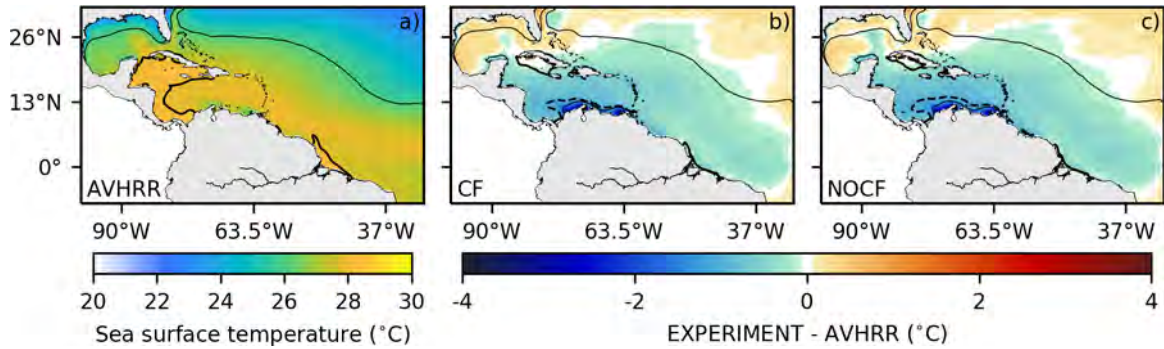


Figure 3.4: Sea surface temperature climatology (1993 to 2016) computed from AVHRR and its difference with respect to CF (b) and NOCF (c). The occurrence of the 26 and 28 °C is delimited by the thin and thick contours, respectively. Differences of  $-1^{\circ}\text{C}$  are shown with the segmented black line (b–c).

The simulation represents averaged sea surface temperature cooler than that observed in the Atlantic and in the Caribbean Sea. These differences are weak ( $<1^{\circ}\text{C}$ ) compared to state-of-the-art climate models that are characterized by a persistent cold bias in the region larger than  $2^{\circ}\text{C}$ , *e.g.*, Jouanno and Sheinbaum (2013); Wang et al. (2014); Li and Misra (2014); Eyring et al. (2019). Differences smaller than  $1^{\circ}$  seem to be related to an overestimation of the turbulent heat fluxes. Radiative heat fluxes are overestimated in the GoM, Caribbean Sea, and North Atlantic region, but are underestimated in the South Atlantic region. However, these differences are smaller than  $25\text{ W/m}^2$ . This can be inferred by comparing the differences between OAFLUX and the CF experiment with respect to the net and turbulent heat fluxes (Figure 3.5b,h). Sea surface temperature biases are exacerbated in the southern Caribbean Sea, where it overcomes  $2^{\circ}\text{C}$  in the upwelling area. This suggests that the CF simulation has too strong southern Caribbean upwelling. There is a direct link between the strength of the Caribbean Low-Level Jet and the southern Caribbean upwelling intensity (Jouanno and Sheinbaum, 2013), so this bias could be associated with the wind stress overestimation of about 10–20% in the numerical simulation (as discussed in the following section). Additionally, because of its relative coarse resolution ( $1/4^{\circ}$ ), the atmospheric simulation does not resolve fine-scale coastal wind that can be induced *e.g.*, by the coastline meandering, the SST front, or local orography and that may modulate the upwelling structure and strength.

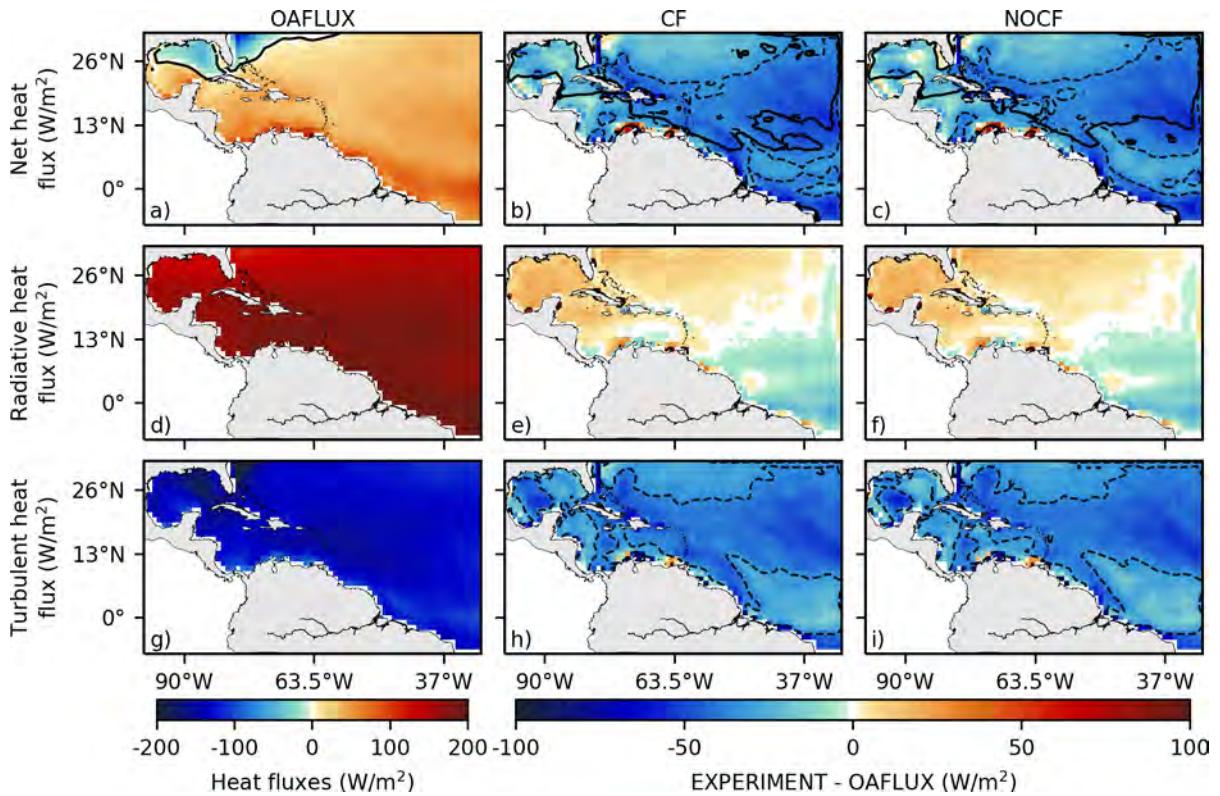


Figure 3.5: Net (first row), radiative (second row), and turbulent (third row) heat fluxes climatologies (1993 to 2016) for OAFUX (first column) and their differences with respect to the numerical simulations CF (second column) and NOCF (third column). The thick and black contour in the first row depicts the  $0 \text{ W/m}^2$  net heat flux. Thin continuous (segmented) contours in the second and third columns depict positive (negative) differences of  $25 \text{ W/m}^2$ .

### 3.3 Wind stress and wind stress curl

As mentioned in Section 1.4, observational and numerical studies have demonstrated that mean surface ocean currents have an imprint on mean surface wind stress (Pacanowski, 1987; Kelly et al., 2001; Scott and Xu, 2009; Renault et al., 2016b) and wind stress curl (Chelton, 2004; Renault et al., 2020). Therefore, mean wind stress and wind stress curl evaluations are important to assess the sensitivity of numerical simulations to CFB.

The wind stress climatology from 1999 to 2019 shows the signature of the northeasterly and southeasterly Trade Winds. In the Caribbean Sea, we can see the signature of the Caribbean Low-Level Jet, which is responsible for upwellings in this region (Figure 3.6a; Rueda-Roa and Muller-Karger, 2013). The wind stress curl exhibits positive values all along the western and south coasts of the IAS, while negative values occur in the northern regions of the GoM and the Caribbean Sea (Figure 3.6d). The strongest values occur over the Colombian and Venezuelan coasts and the region encompassing the Caribbean Islands. Also noteworthy is that signatures of the LC in the GoM and North Brazil Current retroflexion in the AtIS

region can be observed in the wind stress curl climatology, illustrating the influence of the mesoscale currents on the wind stress and wind stress curl.

CF experiment overestimates the wind stress by about 10–20%, with larger biases along the Colombian and Venezuelan coasts. These results are consistent with other regional simulations, *e.g.*, Jouanno and Sheinbaum (2013) and Li and Misra (2014), exhibiting that the acceleration of the trade winds downstream of the peninsula is amplified in numerical simulations. Of course, these differences could be related to model biases. However, as the sampling frequency of SCOW (about two times per day) does not allow it to measure the high-frequency variability of winds, and thus, their wind stress estimation can be underestimated Risien and Chelton (2008). The differences between observations and numerical simulations and their effect on the Caribbean upwelling are beyond the scope of this work, but they should be properly studied.

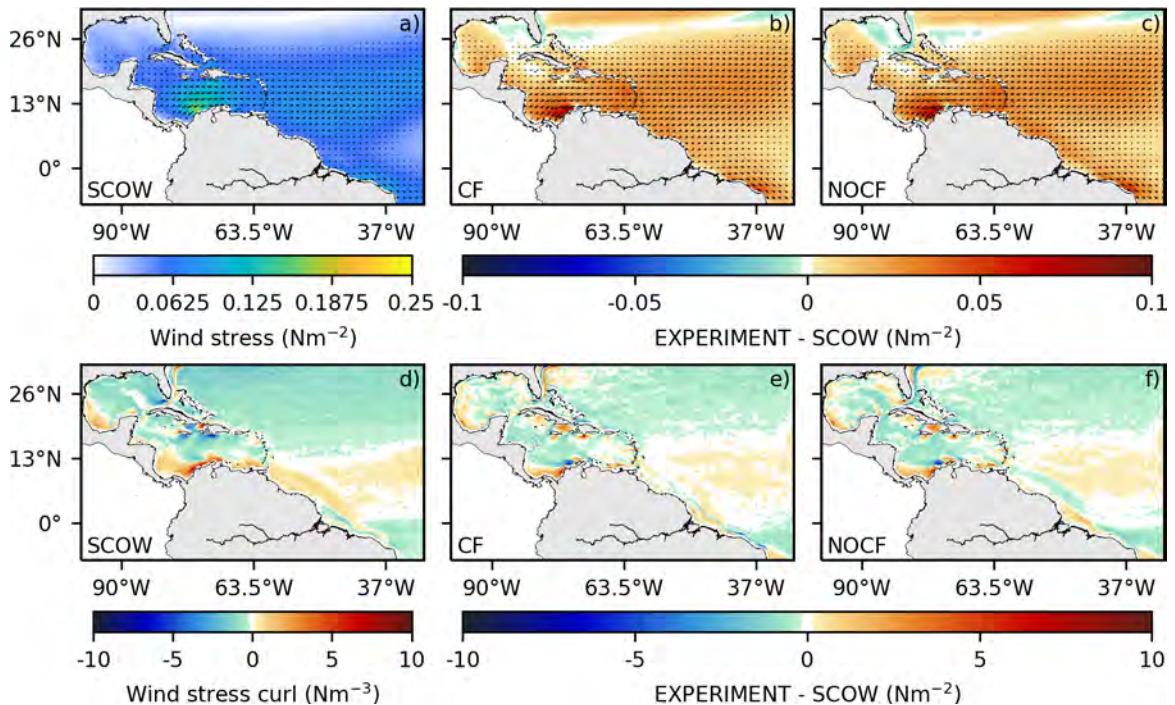


Figure 3.6: Wind stress (first row) and wind stress curl (second row) climatologies from 1993 to 2009. SCOW climatologies are shown in the first row, while climatologies from CF and NOCF experiments are shown in the second and third rows.

### 3.4 Sensitivity to the Current Feedback

Although the sensitivity of the dynamics to the Current Feedback will be discussed in detail for the Gulf of Mexico in the next Chapter, here, we give some first elements concerning this sensitivity for the whole model domain. This is done by comparing the NOCF and CF experiments.

In comparison with CF, NOCF overestimates the KE by about 17% in the GoM and between 20 and 30% in the Caribbean Sea, AtIN, and AtIS regions (Figure 3.3). These energy differences are mainly related to a larger EKE in the NOCF experiment, which in comparison with CF, is about 22% higher in the GoM, about 30% larger in the western regions of the IAS, and up to 28% more intense in the Caribbean Sea.

Besides an overall improvement of the realism of the EKE, mean sea surface temperature over the LC is better represented in the CF experiment than in NOCF, as well as the surface temperature in the southern Caribbean, at the location of the southern Caribbean upwellings (Figure 3.7a). These differences could be related to the feedback of surface currents on the estimation of heat fluxes (Equations 1.3 1.2). However, the improved representation of the mean sea surface temperature related to the Caribbean upwelling could be associated with a 5% reduction of the wind stress in this region by considering CFB. Indeed, from NOCF to CF, the wind stress is reduced in most of the Caribbean Sea and in the south of the GoM (Figure 3.7b). Additionally, as in the observations, imprints of the LC and Gulf Stream are evident in the wind stress and wind stress curl of the CF experiment, evidencing that more realistic results are obtained by considering CFB in coupled numerical simulations (Figure 3.6).

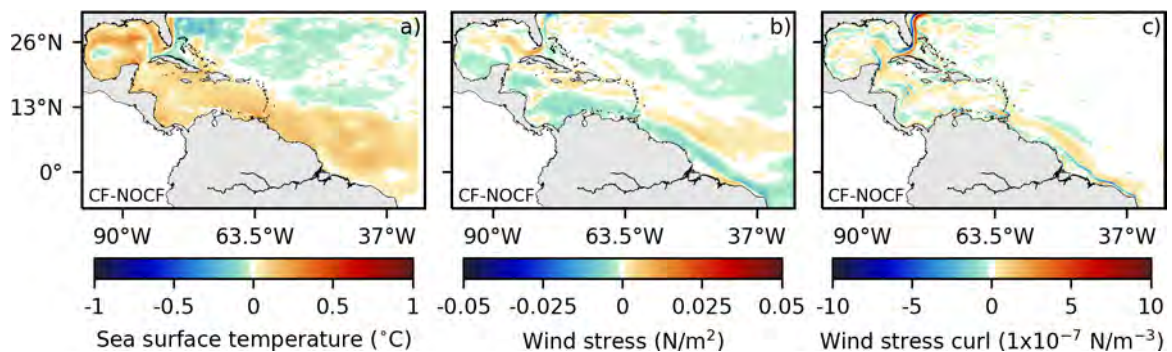


Figure 3.7: Differences between CF and NOCF with respect to the sea surface temperature (a), wind stress (b), and wind stress curl (c) climatologies.

# Partial control of the Gulf of Mexico dynamics by the current feedback to the atmosphere

## Contents

<b>4.1</b>	<b>Introduction . . . . .</b>	<b>66</b>
<b>4.2</b>	<b>Modulation of the kinetic energy and energy conversion by the current feedback . . . . .</b>	<b>66</b>
	4.2.0.1 Mean and eddy kinetic energy . . . . .	66
	4.2.0.2 Energy conversion . . . . .	70
4.2.1	Sensitivity of the Loop Current extension in the Gulf of Mexico . . . . .	73
4.2.2	Sensitivity of the Loop Current eddy shedding statistics and properties by the current feedback . . . . .	74
	4.2.2.1 Number of detachments and separations . . . . .	75
4.2.3	Latitude of the eddy separation . . . . .	76
	4.2.3.1 Loop Current eddy trajectories and properties . . . . .	78
	4.2.3.2 Loop Current eddies vertical structure . . . . .	79
<b>4.3</b>	<b>Discussion and conclusions . . . . .</b>	<b>80</b>

## 4.1 Introduction

This chapter aims at examining and quantifying the extent to which CFB can control the dynamics of the GoM, with a focus on the LC dynamics and eddy shedding statistics. To that end, the twin ocean–atmosphere coupled simulations for the GoM, NOCF, and CF, are analyzed over a period of 24–years. Analyses are focused on assessing the extent to which CFB modulates the Kinetic Energy (KE) and the main energy conversion terms, but also in illustrating the impact of CFB on the LC variability and LCEs detachments and properties. Numerical models, data, and methodology are described in Section 2.

## 4.2 Modulation of the kinetic energy and energy conversion by the current feedback

### 4.2.0.1 Mean and eddy kinetic energy

The first step is to investigate the impact the CFB has on the mean surface circulation. As a proxy of the mean surface circulation, the geostrophic surface Mean Kinetic Energy (MKE, Figure 4.1a) is estimated using the long–term mean geostrophic currents from AVISO. Consistent with [Leben \(2005\)](#), the GoM mean circulation is marked by the presence of the LC that extends up to 26.3°N and 87.8°W, with northwestward and southwestward flows well-defined reaching up to 0.5 m<sup>2</sup> s<sup>-2</sup>. The surface geostrophic Eddy Kinetic Energy (EKE) is furthermore estimated over the 1993–2016 period from AVISO (Figure 4.1d). The EKE is greatest over the LC, in the northern and western regions of the LC, and west of the Florida Shelf with values of about 0.15 m<sup>2</sup> s<sup>-2</sup>. It reaches its maximum values (0.25 m<sup>2</sup> s<sup>-2</sup>) near the Dry Tortugas Islands, where the quasi-stationary Tortugas eddies are generated ([Fratantoni et al., 1998](#)). From the LC region to the west of the GoM, the EKE is also characterized by a zonal band of relatively large energy values (0.06 m<sup>2</sup> s<sup>-2</sup>), which is mainly related to the westward propagation of LCEs.

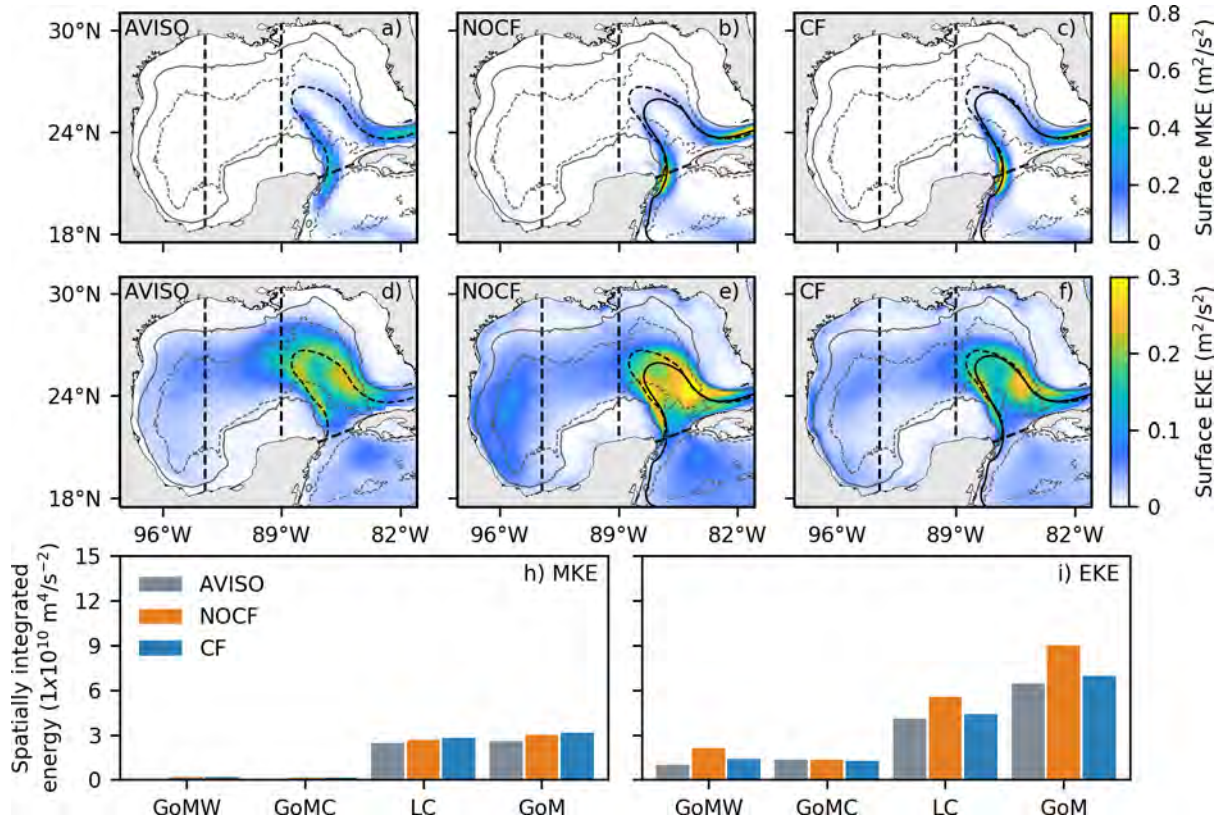


Figure 4.1: Surface mean kinetic energy (first row) and eddy kinetic energy (second row) climatologies (1993–2016) from AVISO (first column), NOCF (second column), and CF (second column). The 17 cm contours of the climatological sea surface height anomaly of AVISO and the numerical experiments are represented by the thin segmented line and the continuous line, respectively. The thick segmented lines delimit the LC (east), center (GoMC), and west (GoMW) regions. GoM makes reference to the whole Gulf of Mexico. The light gray contours refer to the 200 (continuous) and 2500 m (segmented) depths. Spatially integrated values over regions are shown in the last row.

The MKE and EKE are furthermore estimated from NOCF and CF (Figure 4.1). Both experiments have a realistic representation of the mean features of the GoM surface circulation with respect to AVISO. Consistent with previous studies in other regions, CFB improves the realism of the simulations by reducing biases with respect to AVISO, *e.g.*, increasing the mean LC penetration into the GoM. CFB has two main effects on GoM circulation. On the one hand, it causes a damping of the mesoscale activity (Figures 4.1e,f). From NOCF to CF, on average, the EKE in the GoM region is reduced by 22% (Figure 4.1i) while its spatial pattern is improved with respect to AVISO (Figures 4.1d-f). On the other hand, even if at the large-scale CFB slows down the mean circulation (Renault et al., 2016a, 2017b), CFB stabilizes and narrows mean currents in regions with a large mesoscale activity, such as intensified boundary currents (Renault et al., 2019a, 2021a). Similarly, the mean LC has stronger and narrower currents when CFB is considered. Indeed, as shown in Figure 4.2a, the current is concentrated on the coast near Campeche Bank, and outward to the coast near

Tortugas Islands. This is likely explained by a weaker eddy–mean flow interaction in CF with respect to NOCF, and occurs where CFB damps a larger amount of EKE (Figure 4.2b). As a result, from NOCF to CF, the slow–down of the large–scale circulation is counterbalanced by an intensified and more stable LC, resulting in a similar MKE integrated over the LC region (Figures 4.1h–i). Interestingly, the patch of larger EKE values in CF with respect to NOCF (northwestern region of the LC; Figure 4.2b) results from a change of path of the LC extension and of the LCEs detachment statistics and trajectories (see sections 4.2.1 and 4.2.2).

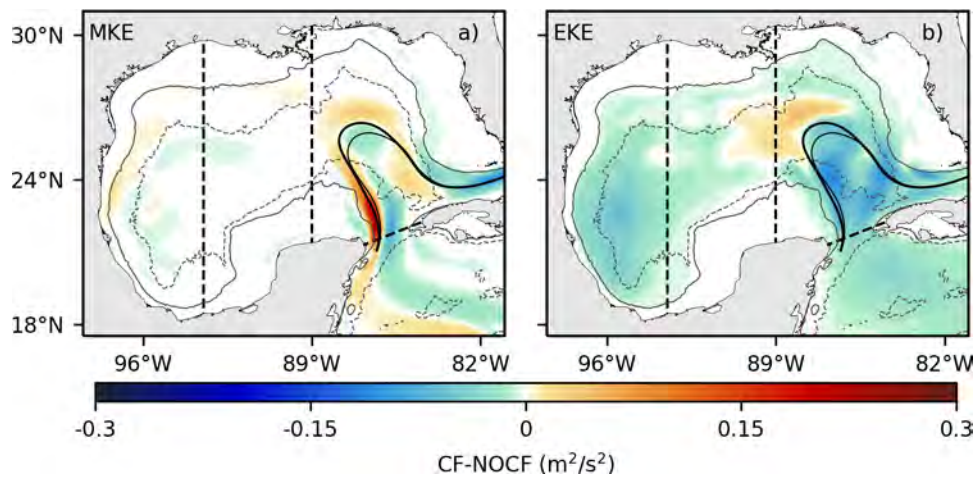


Figure 4.2: Difference between CF (a) and NOCF (b) EKE climatologies (1993–2016). The 17 cm contours of the climatological sea surface height anomaly of NOCF and CF experiments are represented by the black thin line and the black thick line, respectively. The thick segmented lines delimit the LC (east), center (GoMC), and west (GoMW) regions. GoM makes reference to the whole Gulf of Mexico. The light gray contours refer to the 200 (continuous) and 2500 m (segmented) depths.

CF still has some discrepancies with AVISO. The EKE over the LC is overestimated by 7% (*vs.* 28% in NOCF) and the MKE by 40% over the Yucatan Channel. While no doubt some of these are due to model biases, there are important sampling differences between AVISO and model outputs. Indeed, AVISO sea level anomaly can only resolve eddies with a radius larger than about 40 km and a lifetime longer than one week (Chelton et al., 2011; Amores et al., 2018; Archer et al., 2020). In particular, the AVISO data has spatial and temporal resolution issues and only detects the signature of the larger mesoscale eddies (Chelton et al., 2011; Amores et al., 2018; Archer et al., 2020). Additionally, observations from a mooring array over the GoM (Athié et al., 2015) reveal that AVISO underestimates the western current at the Yucatan Channel by about  $\sim 38\%$  (Figure 4.3). This is confirmed by comparing surface current speeds from the simulations to those inferred from a mooring array (Athié et al., 2015) positioned across the Yucatan channel during the period 1992–2001 and 2010–2011 (Figure 4.3). Consistent with the previous results, the mean surface currents in CF are in better agreement with the observations than those in NOCF in terms of velocity and spatial pattern (Figure 4.3).

Table 4.1: Statistics of Yucatan Channel current. The current width is computed as the distance between locations with velocities larger than  $0.6 \text{ ms}^{-1}$  and the current speed rate of change from the maximum speed to the eastern region of the Yucatan Channel.

	Maximum speed ( $\text{ms}^{-1}$ )	Current width (km)	Current speed rate of change along the channel ( $\text{ms}^{-1}/\text{km}$ )
Athié 1999–2001	1.33	–	-0.014
Athié 2010–2011	1.31	81.00	-0.014
CF	1.32	81.00	-0.014
NOCF	1.23	90.00	-0.010
AVISO	0.89	81.00	-0.008

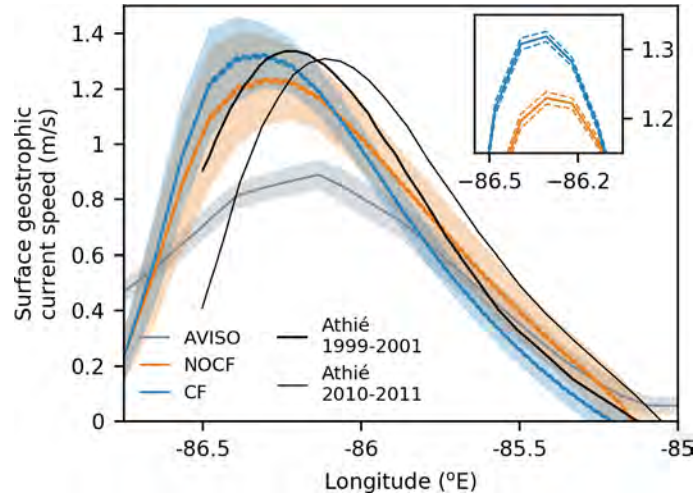


Figure 4.3: Mean (solid lines) and standard deviation (shading area) of geostrophic currents along the Yucatan Channel. Segmented lines in NOCF and CF are associated with an error estimation of the mean current obtained by using a bootstrap method over 50,000 random samples. To more easily appreciate the bootstrap error bars, a zoom of the region with stronger currents in the numerical simulations is included in the upper right corner of the figure.

Noteworthy, the Yucatan Channel current is weaker ( $0.1 \text{ m s}^{-1}$ ) and more spatially spread in NOCF with respect to that in CF and in the observations (Table 4.1), in line with the fact that CFB weakens the eddy–mean flow interactions in regions with a large mesoscale activity (Renault et al., 2019a). As a remaining bias with respect to the observations, the maximum current speed in both NOCF and CF is shifted westward ( $\sim 11 \text{ km}$ ) from the maximum registered by the moorings during 1999–2001 period, and  $40 \text{ km}$  from the one registered during 2010–2011 period. However, extensive time series are needed to better quantify the spatial variability of the Yucatan Channel current and to properly validate long-term numerical simulations.

#### 4.2.0.2 Energy conversion

In order to explain the reduction of EKE from NOCF to CF, energy transfers associated with barotropic and baroclinic instabilities ( $K_m K_e$  and  $P_m K_e$ ), and the mean and eddy geostrophic wind work ( $F_m K_{e_g}$  and  $F_e K_{e_g}$ ) are shown in Figures 4.4 and 4.5. In NOCF, both  $K_m K_e$  and  $P_m K_e$  contribute to the EKE generation over the LC, with  $K_m K_e$  having the larger contribution (about  $6 \times 10^6 \text{ m}^5 \text{ s}^{-3}$ ; Figure 4.4c). The production of EKE is primarily concentrated within the area delimited by the mean LC position inferred from the 17 cm SSHa contour in Figures 4.4a,d. Besides, a large production of EKE by barotropic and baroclinic instabilities is found at the east of the Campeche Bank, the northwestern and northeastern regions of the LC, and the area near Dry Tortugas islands. These regions are characterized by the presence and intensification of cyclonic eddies (Fratantoni et al., 1998; Zavala-Hidalgo et al., 2003; Oey, 2008; Jouanno et al., 2016; Hiron et al., 2020). From NOCF to CF, both  $K_m K_e$  and  $P_e K_e$  are reduced over the mean LC position (Figure 4.4). Over the LC region,  $K_m K_e$  is reduced by 14%, which is mostly compensated by a  $P_e K_e$  increase (11%).

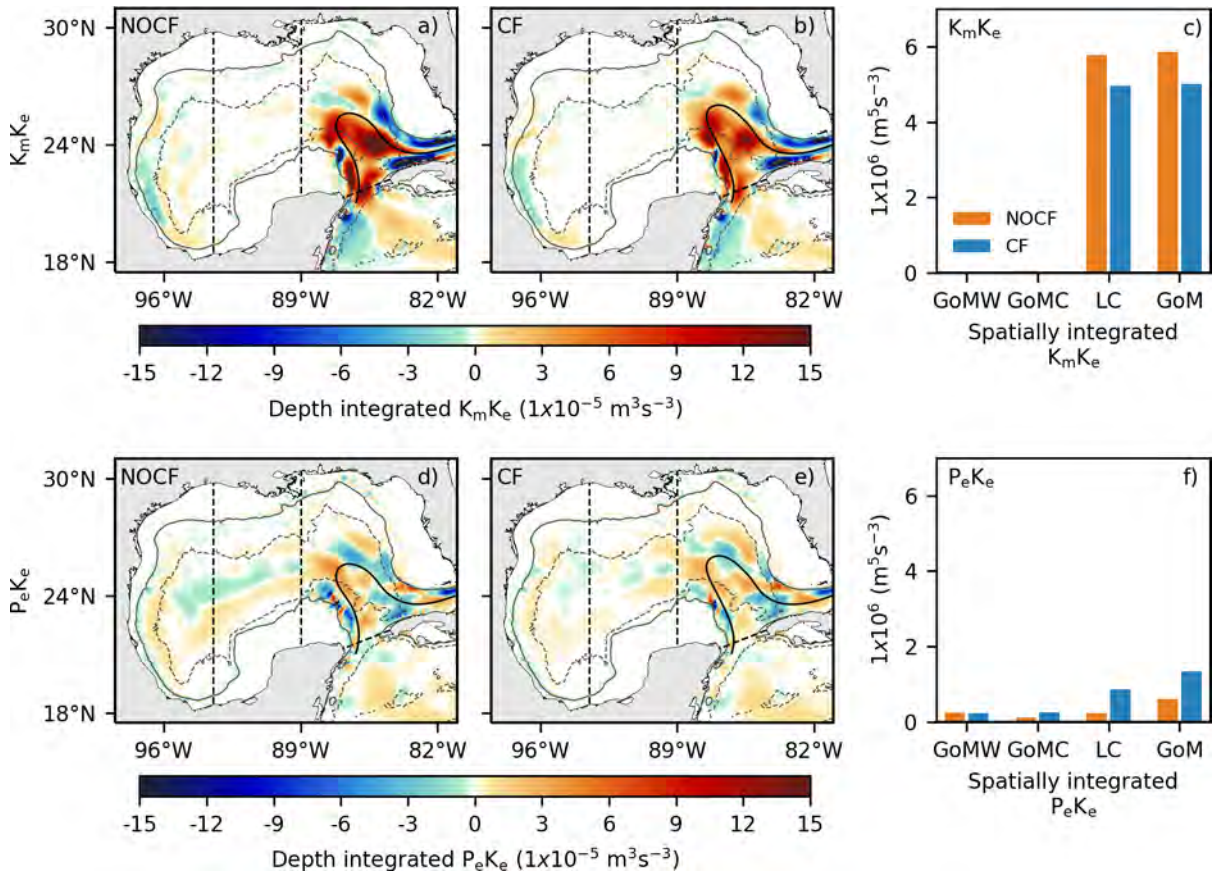


Figure 4.4: Barotropic (top) and baroclinic (bottom) instabilities maps and spatially integrated values over regions (right) for the NOCF and CF experiments for the period 1993–2016. The segmented lines delimit the LC (east), center (GoMC), and west (GoMW) regions. GoM makes reference to the whole Gulf of Mexico. The light gray contours refer to the 200 (continuous) and 2500 m (segmented) depths.

Figure 4.5 shows the geostrophic wind work decomposed into its mean ( $F_m K_{m_g}$ ) and eddy ( $F_e K_{e_g}$ ) components for NOCF and CF (See section 2.2.1).  $F_e K_e$  has positive values on the shelf in both NOCF and CF, which are related to wind-driven current and the resulting geostrophic current anomaly that partially flows in the same direction as the wind (Renault et al., 2016b,a). To better quantify the transfer of energy induced by CFB in the open ocean, the geostrophic eddy wind work ( $F_e K_{e_g}$ ) is spatially integrated over regions deeper than 200 m (Figures 4.5c,f). In NOCF,  $F_e K_{e_g}$  is characterized by alternating positive/negative values (Figure 4.5a) and a weak positive average over the GoM (Figure 4.5c). In contrast,  $F_e K_{e_g}$  in CF is mostly negative over the entire GoM and in particular near Dry Tortugas Islands (up to  $-8 \times 10^{-6} \text{ m}^3 \text{ s}^{-3}$ ). This reveals a sink of energy from mesoscale eddies to the atmosphere that causes the *eddy killing* mechanism and the EKE damping from NOCF to CF (Figure 4.5c). Renault et al. (2016a, 2017b) report similar values for the GoM, although higher ones (about  $-1.5 \times 10^{-5} \text{ m}^3 \text{ s}^{-3}$ ) are found over regions where the EKE and the wind are larger, such as the Gulf Stream and the Agulhas Current retroflection.

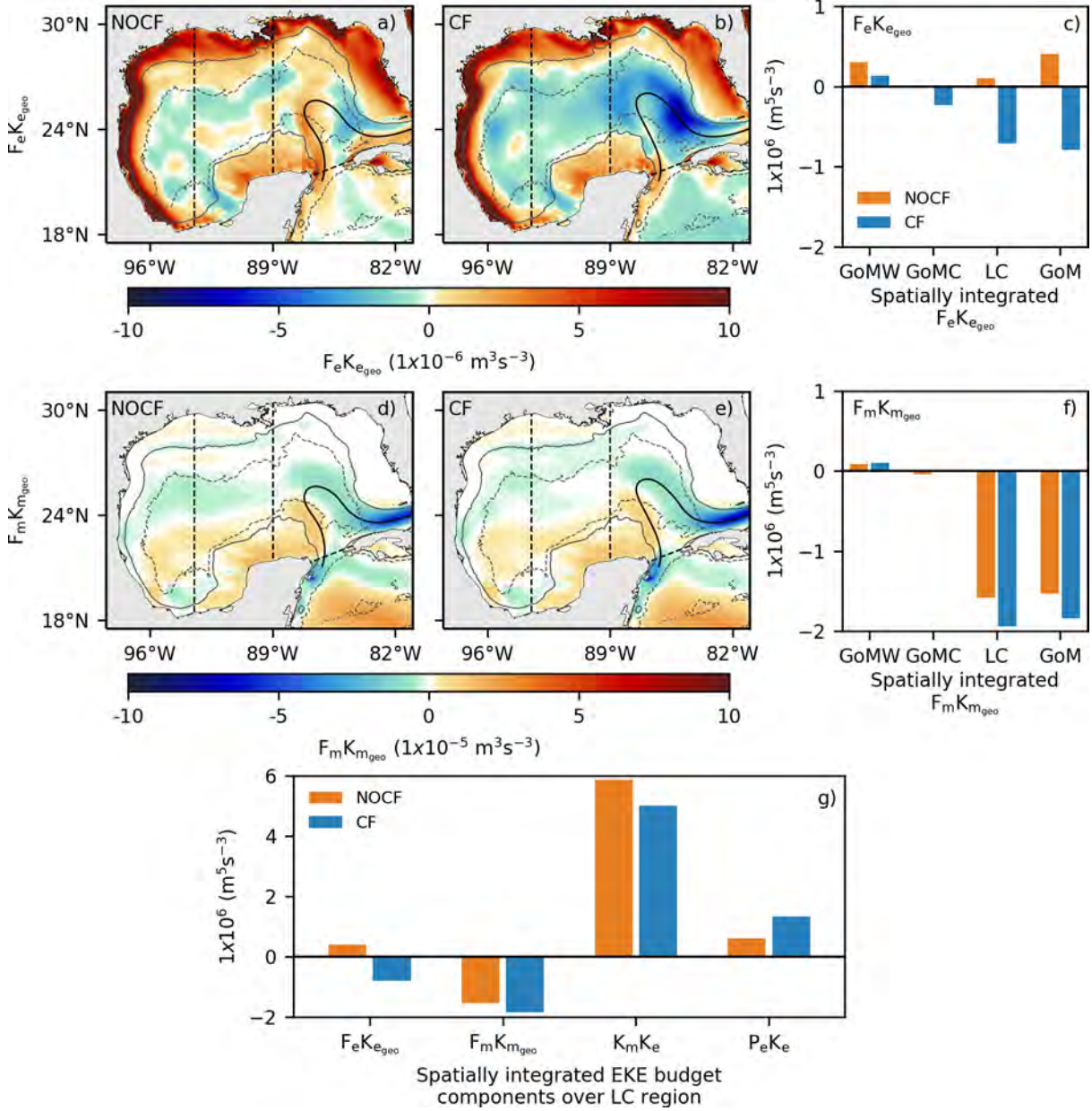


Figure 4.5: Eddy (top) and mean (center) geostrophic wind work maps and spatially integrated values over regions (right) for the NOCF and CF experiments for the period 1993–2016. The segmented lines delimit the LC (east), center (GoMC), and west (GoMW) regions. GoM makes reference to the whole Gulf of Mexico. The light gray contours refer to the 200 (continuous) and 2500 m (segmented) depths. Spatially integrated energy budget terms over the LC region are shown in the last panel (g).

The geostrophic mean wind work ( $F_m K_{m_g}$ ) is slightly larger in CF (Figures 4.5d,e) because the LC mean penetration into the GoM is also larger when the CF is taken into account (Figure 4.1). Notwithstanding, in comparison with NOCF, CFB drives up to 55% more energy to the atmosphere in  $F_e K_{e_g}$  than in  $F_m K_{m_g}$ .

To sum up, for the LC area, CFB reduces the production of EKE related to the horizontal shear of the currents (barotropic instabilities), which is partially compensated by increased baroclinic instabilities. Furthermore, CFB acts as an eddy killer by inducing a negative  $F_e K_{eg}$  that damps the EKE.

### 4.2.1 Sensitivity of the Loop Current extension in the Gulf of Mexico

CFB acts on the circulation through two direct effects: a slowdown of the mean circulation and a damping of the mesoscale activity. This section aims to assess how these changes have impacted the LC characteristics and in particular the LC energetics and its penetration into the GoM.

The LC penetration is generally described as a function of its extension, and has been cataloged into retracted and extended forms (Garcia-Jove et al., 2016; Putrasahan et al., 2017). The retracted form is generally representative of a LC that has shed an eddy shortly before. In contrast, the extended form is representative of a LC that deeply penetrates the GoM and is about to shed an eddy. Figure 4.6 depicts the Probability Density Function (PDF) of the LC penetration into the GoM (binned into  $0.1^\circ$  boxes) from AVISO and the simulations. Three categories of LC penetration can in fact be identified: retracted, canonical, and elongated (Figure 4.6). The extended form found in the literature can be split into canonical and elongated forms. The canonical form, identified as the dominant mode in AVISO, NOCF, and CF (50.4%, 48.5%, and 51.1% of occurrence, respectively), can be located as the relative maximum near the Mississippi Fan (Figures 4.6a-c). In contrast, the elongated form consists of an anomalous westward extension spreading beyond the Mississippi Fan. The elongated form occurs roughly 24% of the time in AVISO. Both simulations underestimate the occurrence of the elongated form. However, its representation is improved from NOCF to CF (from 2.7% in NOCF to 9.5% in CF) with respect to AVISO (24%), consistent with the more extended mean LC extension. They also overestimate the retracted form occurrence despite some improvement from NOCF to CF (25.6% in AVISO *vs.* 49.2% NOCF and 34.4% in CF), which can be identified as the relative maximum located east of the Campeche Bank. In addition, it is worth mentioning that the surface KE integrated over the LC is reduced by about 20% when considering CFB (Figures 4.6d-f).

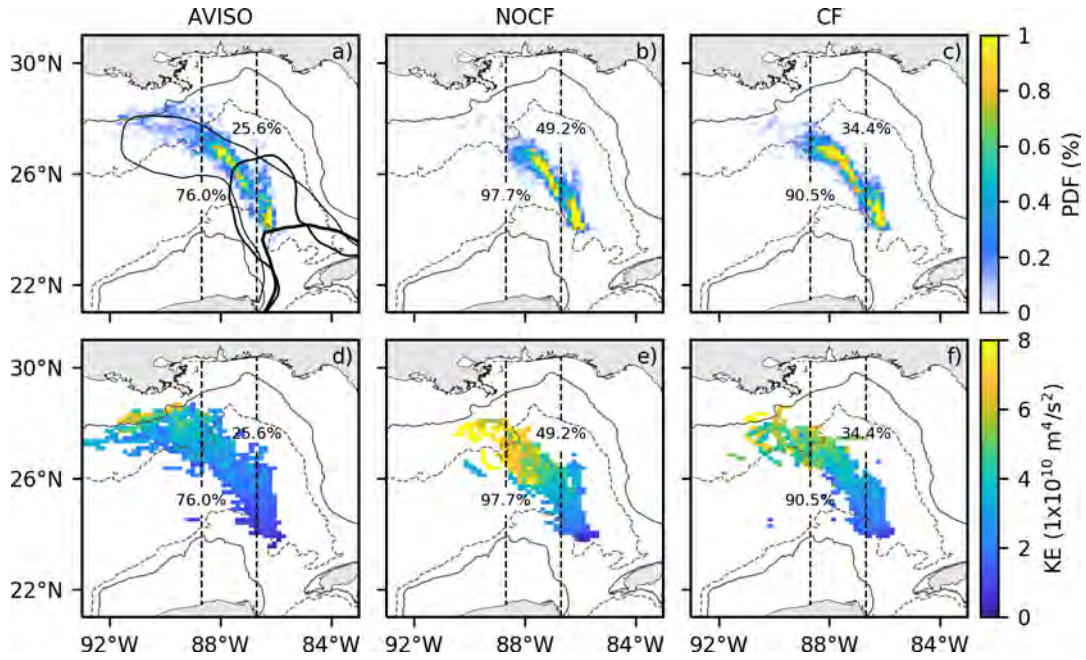


Figure 4.6: Probability density functions related to the occurrence of LC maximum latitudes and longitudes for the period 1993–2016 for AVISO (first column), NOCF (second column) and CF (third column), and associated average of spatially integrated KE. The thick, medium–thick, and thin–black contours represent examples of the retracted, canonical, and elongated LC forms, respectively. The light gray contours refer to the 200 (continuous) and 2500 m (segmented) depths.

The reasons for this sensitivity are difficult to determine but several works propose that the LC extension is related to energy exchange between the GoM and the Caribbean Sea. On the one hand, [Le Hénaff et al. \(2012\)](#) and [Garcia-Jove et al. \(2016\)](#) show a relationship between the mesoscale activity over the Caribbean Sea and the LC penetration into the GoM: the weaker the EKE over the Cayman Sea, the more extended the LC. From NOCF to CF, there is a 27% EKE reduction over the Caribbean Sea (not shown) that would be in line with an increased extension of the LC in CF. However, a more considerable LC penetration into the GoM would be expected given this large EKE reduction. On the other hand, several studies suggest a possible relationship between the LC extension and the transport in the Yucatan Channel ([Lin et al., 2010](#); [Le Hénaff et al., 2012](#); [Mildner et al., 2013](#); [Athié et al., 2015, 2020](#)). No such relationship was found in this study since the mean transport in the Yucatan Channel only reduced by 3% (27.4 Sv in CF and 26.6 Sv in NOCF).

#### 4.2.2 Sensitivity of the Loop Current eddy shedding statistics and properties by the current feedback

LCEs are responsible for transporting warm and salty water to the western region of the GoM. In a numerical simulation, it is, therefore, crucial to properly represent them in order

to obtain realistic air-sea heat fluxes and thermohaline properties of the GoM. The goal of this section is therefore to evaluate the extent to which CFB modulates the LC eddy shedding process and the characteristics of the LCEs during their journey within the GoM. To that end, the LCEs detachment position and trajectory, as well as the properties related to their lifetime, energy, and vertical structure are assessed.

4.2.2.1 Number of detachments and separations

Long-term statistics related to the LC eddy shedding are performed for AVISO, NOCF, and CF for the period 1993–2016. The timing of the eddy shedding is inferred by the inspection of daily SSHa fields and 17 cm SSHa contours length (Leben, 2005; Garcia-Jove et al., 2016; Putrasahan et al., 2017). LC eddy shedding can result both in a reattachment when it is reincorporated to the LC, but also in separation when the eddy travels westward and never reattach. Throughout the period of interest (1993–2016), a total of 61 detached eddies are identified in AVISO, from which 35 become separations (Table 4.2). While the number of detachments is similar in both simulations (55 in NOCF and 48 in CF) and compares relatively well with AVISO, there are large differences in terms of separation events. Indeed, not considering CFB leads to an under-representation of the number of separation events (only 16 in NOCF *vs.* 30 in CF) and to an overestimation of the time between separations (Figure 4.7).

Table 4.2: Statistics related to the LCEs shedding and their detection through the eddy detection method (EDM). A number of detached LCEs (first column). A number of LCEs that are not reabsorbed by the LC and travel to the west of the GoM (second column). A number of separated eddies detected by the eddy detection method (EDM; third column). A number of separated eddies detected by the eddy detection method (EDM) with a lifetime longer than 200 days (fourth column).

	Detachments	Separations	Separated eddies detected by the EDM	Lifetime longer than 200 days
AVISO	61	35	31	21
CF	55	30	30	26
NOCF	48	16	16	14

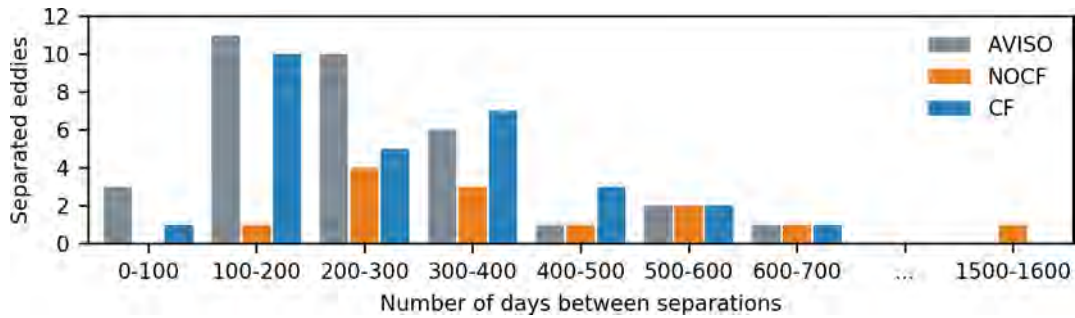


Figure 4.7: Number of separated LCEs as a function of the number of days between separations.

### 4.2.3 Latitude of the eddy separation

The modulation of eddy shedding properties from NOCF to CF may be due to an alteration of the localization of the eddy separation. By ignoring CFB, NOCF favors LCEs liberation farther south (between  $88.6\text{--}87.0^\circ\text{W}$  and  $25.2\text{--}26.5^\circ\text{N}$ ; Figure 4.8c), which is likely related to the over-representation of the LC retracted form in NOCF. In contrast, in CF, CFB causes a higher elongated occurrence of the LC and a weaker EKE in the LC area, and, thus, eddy detachment and statistics are more realistic with respect to AVISO. The impact of CFB on the latitude of detachment is further confirmed by analyzing the outermost position of the LC during separation events (Figure 4.9). For each experiment and AVISO, a meridional PDF is computed by grouping the estimated outermost positions of the LC after a separation event for each degree of latitude (Figures 4.9d,h; note that resizing the boxes between  $0.4$  and  $1.5^\circ$  does not change the results significantly). The  $25\text{--}26^\circ\text{N}$  latitude range remains the preferential latitudes of separation for AVISO and for both simulations. However, in AVISO, more than 77% of the separations (27 cases) occur north of  $25^\circ\text{N}$ , while this ratio falls to 39% (12 cases) in CF and 49% (8 cases) in NOCF. The distributions reveal that in NOCF, both distributions of separations and reattachments are skewed toward the south (Figures 4.9d,h). Including CFB leads to a more realistic LC extension and LC eddy separation events, but also to a decrease in the excessive number of reattachment from the south of the LC.

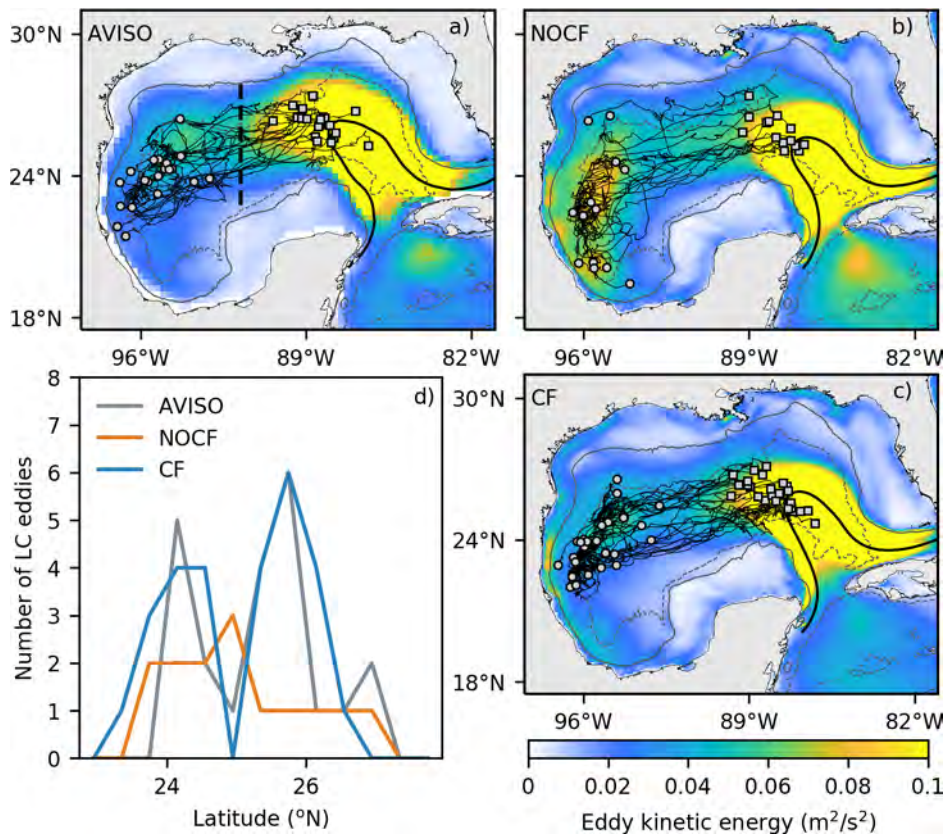


Figure 4.8: Trajectories related to LCEs with a lifetime longer than 200 days for AVISO (a), NOCF (b), and CF (c). Gray squares represent the location of a LC eddy liberation, and gray circles the location where LCEs are no longer detected. The colormap refers to the corresponding climatology of EKE. The 17 cm contours of the climatological sea surface height anomaly of AVISO and the numerical experiments are represented by the black line. The light gray contours refer to the 200 (continuous) and 2500 m (segmented) depths. (d) Number of LCEs that cross the segmented thick line shown in panel a) as a function of the latitude.

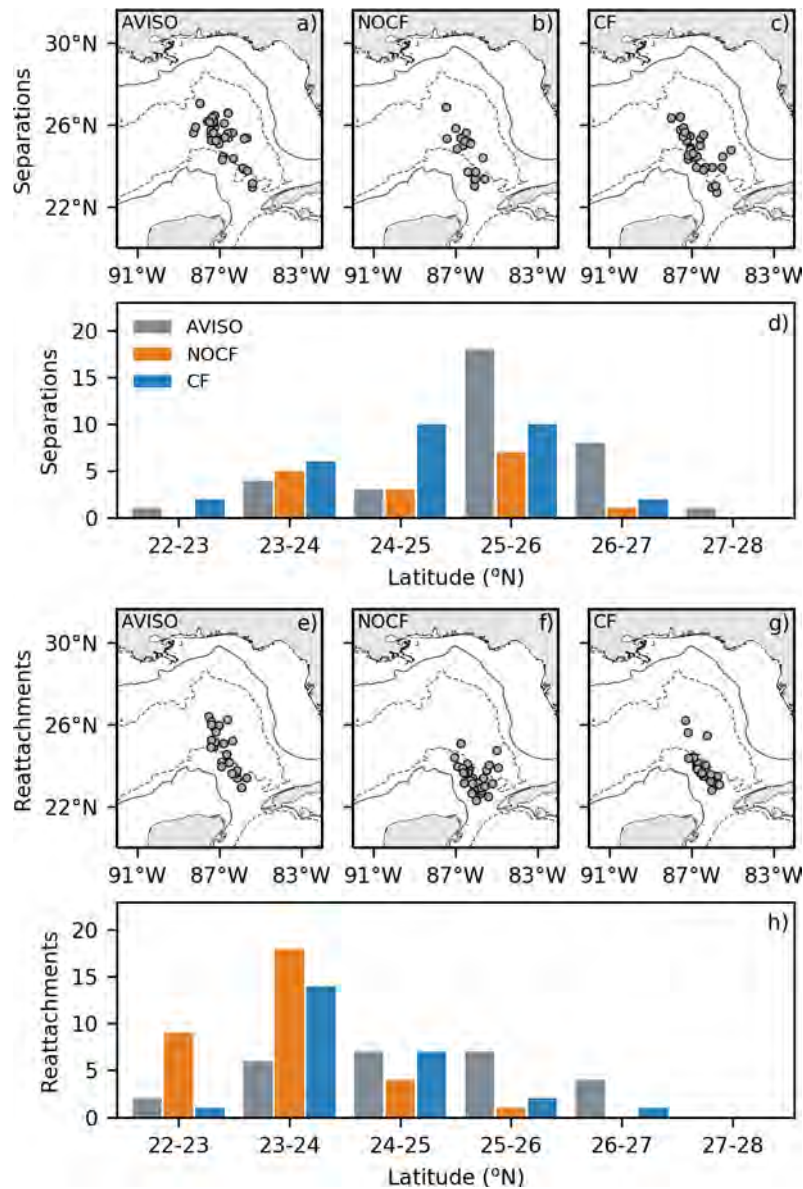


Figure 4.9: LC most extended position (gray dots) after separation (first row) and reattachment (second row) events, for AVISO (first column), NOCF (second column), and CF (third column). The light gray contours refer to the 200 (continuous) and 2500 m (segmented) depths. PDFs related to the latitude of the LC most extended position after separation and reattachment events are shown in g) and h).

#### 4.2.3.1 Loop Current eddy trajectories and properties

To investigate further the impact of CFB on the LCEs, statistics on the long-lived detected eddies (lifetime longer than 3 months as in Sosa-Gutiérrez et al., 2020; Chelton et al., 2011) are assessed in the following.

In both simulations and in AVISO, LCEs preferentially travel southwestward along a vortex street located between 24°N and 26°N (Figure 4.8). CFB clearly alters the LCEs and therefore the vortex street position, improving the realism of the simulations. Two main effects can be distinguished. On the one hand, likely because of the too-south location of the eddy shedding, the vortex street in NOCF is shifted toward the south and mainly restricted between 23–26°N (Figure 4.8d). On the other hand, consistent with the *eddy killing* and the subsequent damping of the EKE, CFB largely impacts the eddy lifetime and fate in the western GoM. Eddy energy is reduced from NOCF to CF by 24% (Table 4.3), and LCEs in NOCF have a larger KE dissipation rate with respect to that in CF. On average, LCEs lifetime is also shortened by about 16% (528 days on average in NOCF *vs.* 445 days in CF and 377 in AVISO). As in Renault et al. (2016b) for the US West coast, the overestimation of the eddy lifetime in NOCF allows the LCEs to travel unrealistically too far in the Bay of Campeche (south of 22°N). Finally, CFB does not have a significant impact on the translation speed of the LCEs (about 4 km/day in both simulations; Table 4.3).

Table 4.3: Statistics of LCEs properties with a lifetime longer than 200 days.

	Lifetime (days)	Translation velocity (km/day)	EKE (m <sup>2</sup> s <sup>-2</sup> )	EKE dissipation rate (1x10 <sup>-4</sup> m <sup>2</sup> s <sup>-2</sup> /day)
AVISO	377 ± 118	4.59 ± 0.71	0.13 ± 0.05	-3.00 ± 1.36
CF	445 ± 126	4.14 ± 0.58	0.25 ± 0.06	-4.00 ± 1.70
NOCF	528 ± 179	4.37 ± 0.53	0.33 ± 0.14	-5.00 ± 2.24

#### 4.2.3.2 Loop Current eddies vertical structure

CFB affects in a profound way LCEs. Indeed, besides the alteration of their lifetime and fate, their 3D structure is also impacted by CFB. The composites of long-lived LCEs thermohaline and vorticity structure from NOCF and CF are shown in Figure 4.10. The vertical structure of the LCEs composite in CF is in good agreement with the observations of Elliott (1982) and Meunier et al. (2018, 2021). LC eddy composite is characterized by a warm and relatively fresh core (between 20 and 25°C and 36.5 PSU) well delimited by a superficial and a deeper thermocline (Figure 4.10d). In NOCF, the eddy composite has a warmer and saltier core and the upper thermocline goes deeper at the center of the eddy (Figure 4.10a,b). The deepening of the surface thermocline in NOCF is likely related to a larger negative vorticity at the eddy core (Figure 4.10c). Additionally, in NOCF, the salinity in the eddy core is uniform and does not exhibit a minimum of salinity between 50 and 100 m, which is present in both the observations (Elliott, 1982; Meunier et al., 2018, 2021) and CF.

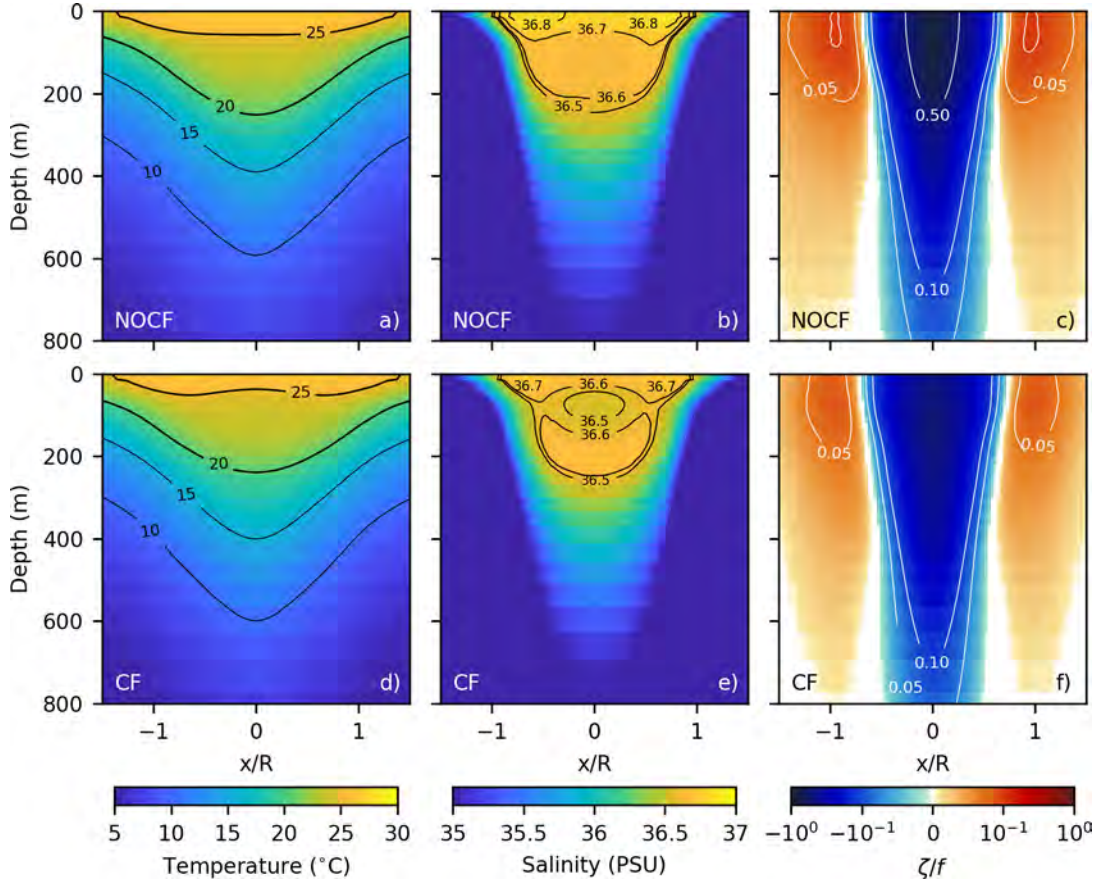


Figure 4.10: LC eddy composite of temperature (first column) and salinity (second column) and the relative vorticity ( $\zeta$ ) normalized with the Coriolis parameter ( $f$ ; third column) for CF (first row) and NOCF (second row). Black and thick contours indicate thermoclines at 26 and 220 m depth. Normalized relative vorticity contours of 0.05, 0.1, and 0.5 are shown using white lines.

### 4.3 Discussion and conclusions

Using long-term regional ocean-atmosphere coupled simulations with and without CFB, we assess to which extent CFB modulates the GoM dynamics. Consistent with previous studies over other regions, as a direct effect, CFB causes a damping of 20% of the mesoscale activity over the GoM. This reduction of mesoscale activity is mainly driven by the *eddy killing* mechanism, *i.e.*, a deflection of momentum from the mesoscale surface current to the atmosphere, and, to a lesser degree, by a reduction of the barotropic conversion of energy that is only partly compensated by an increase of the baroclinic conversion. As an indirect effect, taking into account CFB in a coupled model leads to an improvement in the representation of the LC dynamic. CFB alters the mean LC extension, favoring its western penetration into the GoM. Using satellite observations and simulations, we show that the LC extension can be classified into three categories: retracted, canonical, and elongated. Both simulations underestimate

the elongated form occurrence and over-represent the retracted form, although, consistent with the increase of the mean LC extension, CFB leads to a higher (lower) occurrence of the elongated (retracted) form.

The over-representation of the LC retracted form in NOCF could result in the reattachment of LCEs that are detached from the south of the LC, since their path to the west of the GoM could be blocked by the Campeche Bank. In contrast, CFB favors a larger extension of the LC, allowing eddy shedding in the north and upper north regions of the LC and avoiding numerous reattachments in the south. Besides, by increasing the LC eddy detachments from northern latitudes, LCEs trajectories are not skewed toward the south and become more similar to those observed in AVISO.

CFB also leads to a better representation of LC eddy properties. In particular, the vertical distribution of thermohaline properties of LCEs are in better agreement with hydrographic (Elliott, 1982) and gliders (Meunier et al., 2018, 2021) observations. In a simulation without CFB, LCEs are too energetic, which leads to a deepening of the superficial thermocline, and to an increase in their heat content. The lack of sink of energy from mesoscale currents to the atmosphere also leads to an overestimation of LCEs lifetime and to a poor estimation of their propagation. This may be critical to better represent extreme atmospheric events, as LCEs can participate in an increase in the occurrence of thunderstorms and tornado events in the Southeast U.S., as well as the reinforcement of hurricanes (Molina et al., 2016; Yablonsky and Ginis, 2012).

To conclude, the coupled simulation with CFB used in this study still suffers from biases. For instance, LC penetration into the GoM, although improved, is still underestimated. This could be due to the prescribed oceanic conditions at the open boundary of the simulation, but also to missing physical processes. In particular, wave feedbacks to the ocean and the atmosphere may modulate the ocean energy budget and the transfer of energy between the ocean and the atmosphere. This could modulate the GoM dynamics and the role of CFB in determining it.



# The role of cyclonic eddies in the detachment and separation of Loop Current eddies and clues of their modulation by the current feedback

---

## Contents

---

5.1	Introduction . . . . .	84
5.2	Preferential latitudes of detachments . . . . .	84
5.3	The role of cyclonic eddies in the detachment of Loop Current eddies	85
5.4	Discussion and conclusions . . . . .	89

---

## 5.1 Introduction

The previous chapter demonstrates that GoM dynamics present a large sensitivity to CFB. The regional coupled simulation considering the CFB produces more realistic results. There is a damping of the EKE by 20% over the LC region, which is consistent with previous results obtained over other regions, *e.g.*, 30% over the Caribbean Sea (Chapter 3) and 27% in the Gulf Stream (Renault et al., 2016a). As an indirect and an interesting aspect, CFB drastically modifies and actually improves the shedding properties of the LC. This raises the question of which processes are involved in this sensitivity. Results from the previous Chapter show that the simulation without CFB overestimates the occurrence of reattachments, resulting in fewer LCEs separations. Most of these reattachments occur south of 24°N, and appear to result from a propensity of eddies in NOCF simulation to detach south of this latitude. How CFB alters the LCEs shedding remains an open question. Our hypotheses are that 1) the latitude at which the detachments occur is important for the fate of the Loop Current eddies (reattachment or separation), 2) the cyclonic eddies which surround the LC (and are more energetic in NOCF simulation), are instrumental in this sensitivity.

As discussed in Chapter 1, the LC largely interacts with three main kinds of cyclonic eddies that are suspected to play a crucial role in the shedding process (Cochrane, 1972; Vukovich and Maul, 1985; Chérubin et al., 2006; Le Hénaff et al., 2012): frontal eddies, Tortugas eddies, and Caribbean cyclonic eddies. Frontal eddies are generated East of Campeche Bank and increase their energy and size as they travel along the LC (Jouanno et al., 2016). These eddies can also intensify through merging in the northwestern region of the Florida Straits (Le Hénaff et al., 2012), but also near Dry Tortugas Islands, giving rise to the semi-stationary Tortugas eddies Fratantoni et al. (1998). Finally, as suggested by Candela et al. (2002), Athié et al. (2012) and Jouanno et al. (2016), LCEs separations are often associated with the advection of cyclonic eddies from the Caribbean Sea.

The aim of this chapter is to better understand which conditions favor LCEs to separate or reattach. Here, we will mainly rely on the analysis of AVISO observations, as we will show, it will give some insights to better understand the sensitivity of LCEs detachment between CF and NOCF simulations.

## 5.2 Preferential latitudes of detachments

The first step is to investigate the dependence to the latitude of LCEs detachment in determining the occurrence of reattachments or separations. During the period 1993–2016, a total of 61 detachments were detected in AVISO, from which 26 (43%) reattached to the LC and 35 (57%) separated and traveled westward in the GoM. The latitude of the detachments is estimated as the maximum latitude of the LC at the time of the detachment. Figure 5.1a reveals that the detachments take place over a wide range of latitudes, from 22°N to 27°N.

The fate of detached eddies is largely influenced by the latitude at which detachment

occurs: eddies detached north of 25°N are more likely to separate from the LC (70%), whereas eddies that separate south of 25°N are more prone to reattach (64%, Figure 5.1b). This reveals contrasted shedding dynamics that may depend on the state of the LC (retracted, canonical, or elongated).

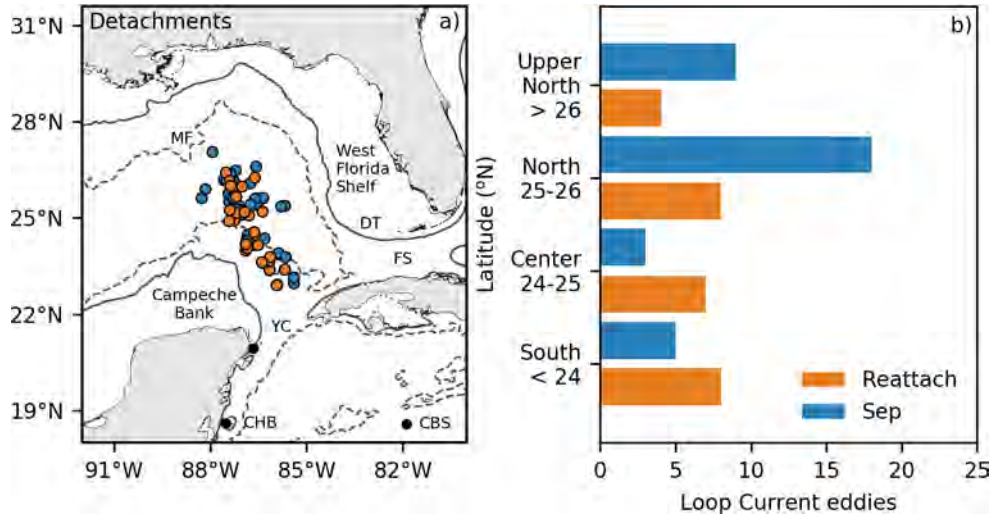


Figure 5.1: a) LC outermost position after reattachment/separation events (orange/blue). b) Histogram related to the number of reattachment (orange) and separation (blue) events as a function of their latitude of occurrence. YC refers to Yucatan Channel, FS to Florida Straits, DT to Dry Tortugas islands, MF to Mississippi Fan, CBS to the Caribbean Sea, and CHB to Chinchorro Bank. Black dots are used to build the transects for the Hovmöller diagrams in figures 3 and 4. The light gray contours refer to the 200 m (continuous) and 2500 m (dashed) depths.

### 5.3 The role of cyclonic eddies in the detachment of Loop Current eddies

The next step is to investigate whether we can find distinct background dynamical conditions that may favor reattachments or separations. This is achieved by estimating a composite of the evolution of the Rossby number ( $R_o$ ) during reattachments and separations.  $R_o$  allows to differentiate cyclonic structures (positive  $R_o$ ) and anticyclonic structures (negative  $R_o$ ). In order to avoid mixing too different LC states, LCEs separation and reattachment are classified within four regions as a function of their latitude of occurrence, and thus,  $R_o$  composites are build for different latitudes of separation. The *south* and *center* regions encompass LCEs detachment occurring at latitudes below 24°N and between 24 and 25°N, respectively, while the *north* and *upper north* regions enclose detachments occurring at latitudes between 25 and 26°, and latitudes above 26°, respectively.

Composites of  $R_o$  at the time of the detachments are shown in Figure 5.2 for the different ranges of latitudes. This reveals that no matter the latitude of detachment, either leading

to a reattachment or to a separation, a positive vorticity bulge related to cyclonic eddies, “cut-off” the LC from the east (Figures 5.2). At first glance, the background conditions of separations or reattachments seem very similar. However, the LC neck in the *south* composite tends to be further away from Campeche Bank in separation cases (Figure 5.2a,e). This is linked to the presence of a large cyclonic circulation between the LC and the Yucatán shelf (Figure 5.2a,e).

At the other latitudes of detachments, the same observation is made in Figure 5.2f-h: the western side of the LC is tilted to the Florida Shelf for separation cases. This appears to be associated with a larger cyclonic circulation on the western side of the LC. In contrast, reattachments are associated with a LC flowing close to Campeche Bank and with a wider LC in the *north* and *upper north* regions.

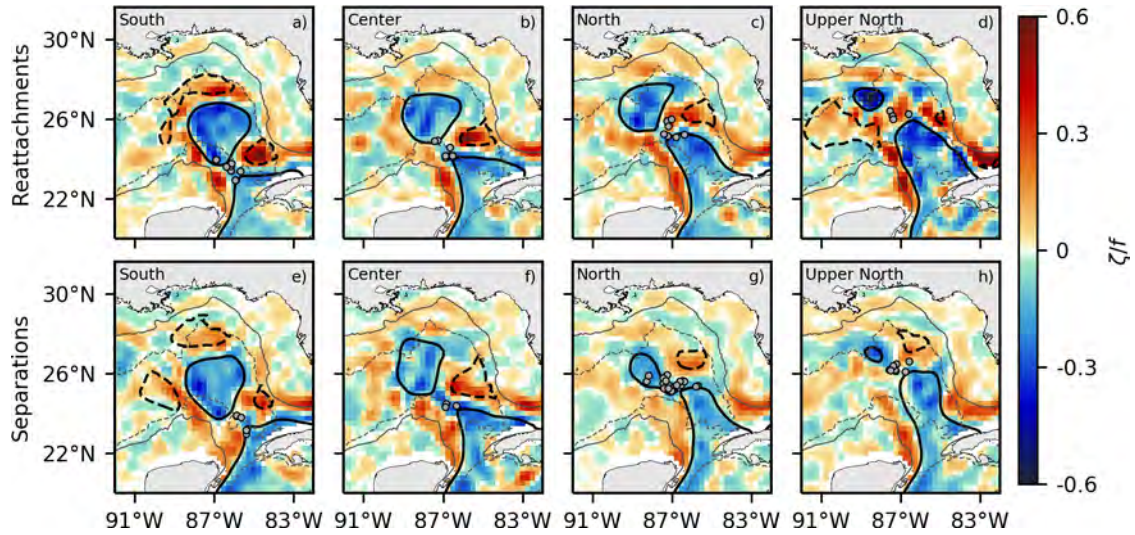


Figure 5.2: Rossby number composites during LCEs detachment that end in reattachments (first row) and separation (second row) for the *south* (first column), *center* (second column), *north* (third column), and *upper north* (fourth column) regions. Continued and discontinued black contours represent the LC (17 cm) and CEs (-18 cm). Gray circles represent the LC outermost position after detachment events used for the composites. The light gray contours refer to the 200 m (continuous) and 2500 m (dashed) depths.

These results suggest that cyclonic eddies or circulation west of the LC contribute to the detachment of LCEs. In order to further investigate the role of cyclonic eddies in LCEs detachment, composite evolution of  $R_o$  related to reattachments and separations are performed from 30 days before to 30 days after the detachments. The *center* and *upper north* cases are very similar to the *south* and *north* cases respectively, therefore we focus on the evolution of the *south* (Figure 5.3) and *north* (Figure 5.4) detachments only.

For both *south* and *north* cases, the time evolution of composites for separations and reattachments reveal that cyclonic eddies west of Florida Straits reduce the LC neck width as they increase in size the days before the detachments (first to third columns in Figures

5.3 and 5.4). This indicates that the intensification of frontal eddies between the LC and the Florida shelf conduct the LC to detach an eddy. This is consistent with Le Hénaff et al. (2012) and Fratantoni et al. (1998) who show that a frontal eddy expands and intensifies when merging with another frontal eddy northwest of the Florida Straits, but also near Dry Tortugas Islands, to produce Tortugas eddies that appear to favor *south* shedding.

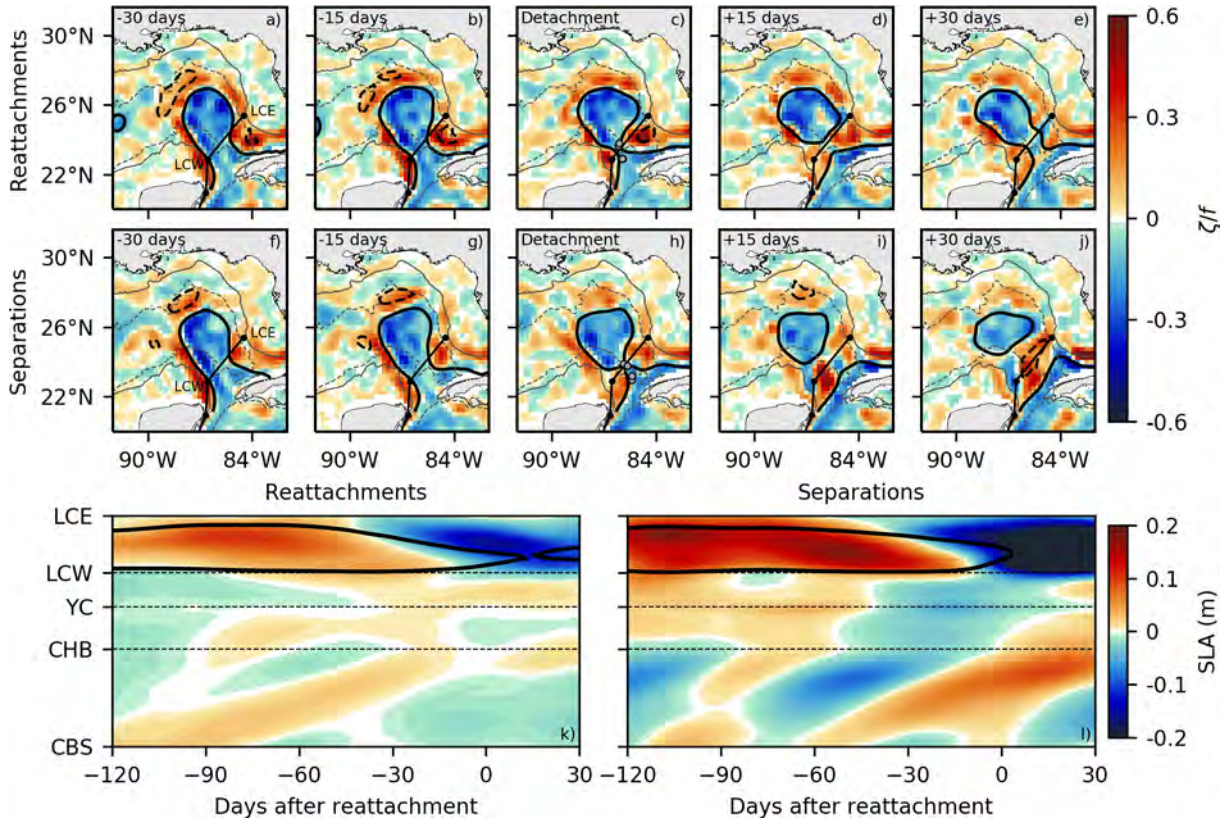


Figure 5.3: Rossby number composites related to the evolution of reattachments (first row), and separations (third row) events for the *south* region. Continued and discontinued black lines represent the LC (17 cm contour of the SSHa) and CEs (-18 cm contour of the SSHa). Gray circles represent the LC outermost position after detachment events used for the composites (c and h). The light gray contours refer to the 200 m (continuous) and 2500 m (dashed) depths. Hovmöller diagrams the low-pass filtered (30 days) SSHa composites of reattachment and separation events are shown in the last column. The LC is represented by the black contour.

We now focus on the  $R_o$  evolution after the detachments in Figures 5.3 and 5.4 (15 and 30 days lag). For separation events, both *south* and *north* cases reveal large cyclonic structures which act as a barrier between the LC and the LCES and prevent the LC from reattaching LCEs (Figures 5.3i,j and Figures 5.4i,j). These large cyclonic structures result from the merging of cyclonic eddies coming from both sides of the LC neck. Therefore, it appears that LCEs separations are favored by the co-occurrence of two cyclonic eddies to “pinch-off” the LC from both sides (Figures 5.3f-j and Figures 5.4f-j). For the *south* cases, cyclonic eddies

west of the LC correspond to intensified Tortugas eddies (Fratantoni et al., 1998; Schmitz, 2005), whereas from the *center* to *north* cases they may correspond to intensified frontal eddies (Le Hénaff et al., 2012).

The origin of the eastern eddies is less clear, but it is most certainly associated either with cyclonic eddies advected from the Caribbean or generated locally. To understand their origin, composite Hovmöeller diagrams built along a transect extending from the Caribbean and Yucatán coasts to the Florida shelf, and using the daily SSHa from 120 days before to 30 days after each detachment (Figures 5.3l and 5.4l) are performed. Composites show that cyclonic eddies east of the Campeche Bank participating in separation events originate from the Caribbean, and after entering the GoM merge with cyclonic structures originating from the east of the LC. A similar influence of the Caribbean cyclonic eddies can be inferred in Figures 5.3a-j and 5.3a-j, although their influence is more clear for *south* separations. The role of Caribbean eddies in *north* separations is a bit more complicated. They are responsible for tilting the LC to the Florida Shelf when entering the GoM, propitiating frontal eddies intensification northwest of the shelf that triggers the LCE detachment. Caribbean eddies continue their journey along the LC to finally merge with the intensified frontal eddy and promote the separation. By contrast, the composite Hovmöeller diagrams for reattachments do not show any clear signature of incoming cyclonic eddies from the Caribbean (Figures 5.3k and 5.4k). This can be explained by the absence of incoming energetic cyclones, or by incoming eddies which are out of phase with the intensification of cyclonic eddies east of the LC.

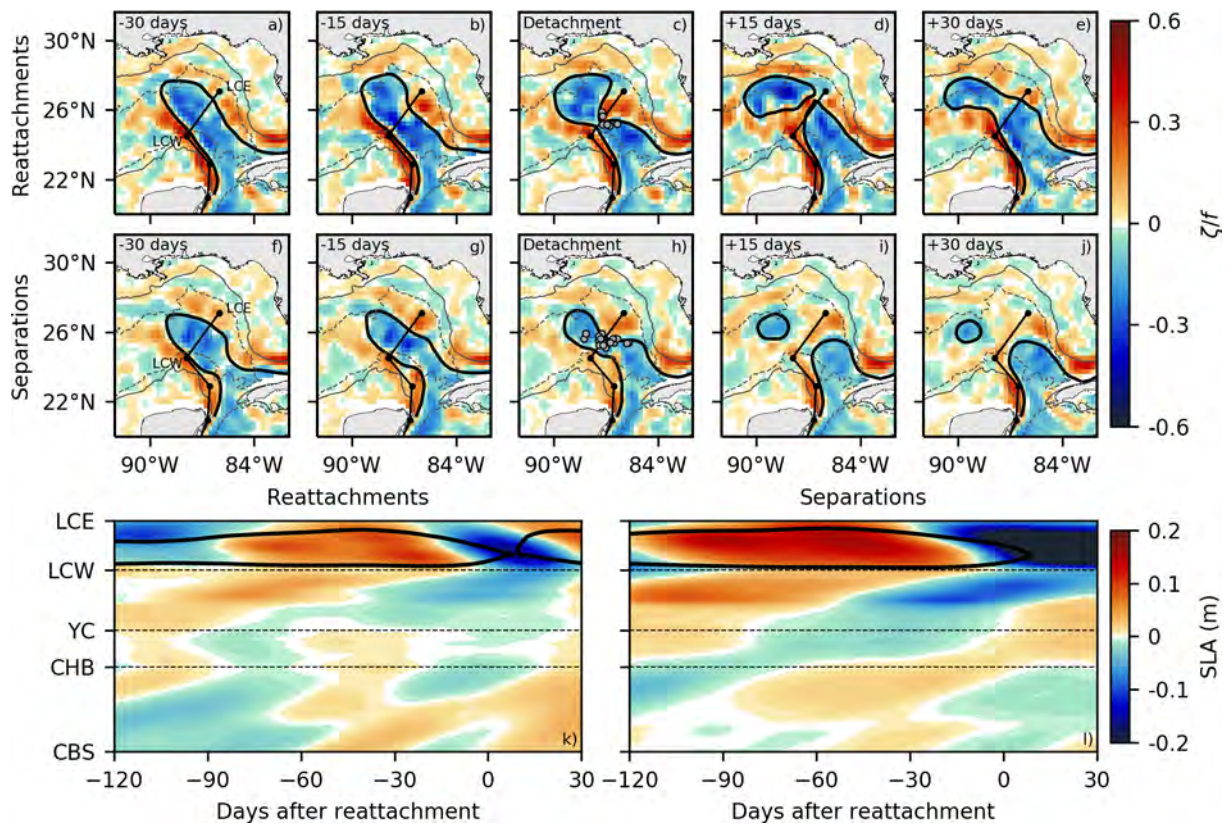


Figure 5.4: Rossby number composites related to the evolution of reattachments (first row), and separations (third row) events for the *north* region. Continued and discontinued black lines represent the LC (17 cm contour of the SSHa) and CEs (-18 cm contour of the SSHa). Gray circles represent the LC outermost position after detachment events used for the composites (c and h). The light gray contours refer to the 200 m (continuous) and 2500 m (dashed) depths. Hovmöller diagrams the low-pass filtered (30 days) SSHa composites of reattachment and separation events are shown in the last column. The LC is represented by the black contour.

## 5.4 Discussion and conclusions

The main goal of this chapter was to identify the possible drivers that control the fate of LCEs upon detachment from the LC: reattachment within a few weeks after the detachment or permanent separation. This issue is of primary interest in the perspective of forecasting the LCE liberation and sheds light on the processes driving the LC variability. The analysis of altimetry records over 24-years has shown the occurrence of 61 LCE detachments, from which 26 (43%) of LCEs reattached 35 (57%) become fully separated. One key aspect of the analysis is to classify and composite the shedding events as a function of latitude. This allows us to take into account contrasted dynamical conditions of shedding occurring, for example, close to the Yucatán Channel (24°N) or in the north of the Gulf of Mexico (6°N).

## Chapter 5. The role of cyclonic eddies in the detachment and separation of 90 Loop Current eddies and clues of their modulation by the current feedback

---

For *south* detachments, Tortuga eddies appear to play a systematic role in the process. Moreover, it has been shown that detachments occurring south of 25°N are more prone to be followed by a reattachment rather than leading to a separation. Separations are related to the simultaneous intensification of Tortugas eddies and the arrival of Caribbean cyclonic eddies. Instead, reattachments are related to the untimely occurrence or lack of one of these cyclonic eddies.

For *north* detachments, Tortugas eddies are not active but instead there is a cyclonic circulation growing between the Loop Current and the West Florida Shelf days before LCEs detachment (Figure 5.4f-j). This is related to the tilt of the LC portion below 25°N toward the West Florida Shelf, which prevents frontal eddies from continuing their journey to the Florida straits and thus favors their intensification by promoting their merging with other frontal eddies traveling behind them. Conditions leading to the tilt of the LC during separations are related to Caribbean Cyclonic eddies pulling the LC to the Florida Shelf as they travel along the Campeche Bank. During reattachments, the conditions leading to this tilt of the LC are unclear.

Several studies have pointed out the role of Tortugas eddies, frontal eddies, or Caribbean cyclonic eddies in the shedding of LCEs, but mainly as an unrelated triggering mechanism. [Athié et al. \(2012\)](#) shows that 76% of detachments between 2005 and 2009 were related to Caribbean cyclonic eddies. Similar results were founded in [Jouanno et al. \(2016\)](#) numerical simulations. However, the authors link the occurrence of Caribbean cyclonic eddies and LCEs detachment in a probabilistic manner, and no explanation of the mechanisms related to LCEs detachments were provided. Through numerical simulations and observations, [Leben and Hall \(2012\)](#) described detailed explanations about particular cases involving LCEs detachments in the presence of intensified frontal eddies. On the other hand, our study points out that a combination of frontal, Tortugas, or Caribbean cyclonic eddies triggers the detachments of LCEs, but also favors eddies separation by merging in large cyclonic structures that prevent the LC from reattaching LCEs.

The AVISO observations also raise the question of why a detachment occurring south of 24°N is more likely to lead to a reattachment. One hypothesis is that the occurrence of out of phase Caribbean cyclonic eddies and intensified Tortugas eddies, which lead to reattachments, is more probable than their simultaneous occurrence.

Based on these results and the one obtained in chapter 4, it is now possible to discuss the effect of CFB on the detachment of LCEs. The main differences between the numerical simulations in terms of LCEs detachment are related to an overestimation (underestimation) of detachment (separation) in the south and center regions by the NOCF experiment. The present chapter shows that separations require the simultaneous occurrence of intensified Tortugas eddies and Caribbean cyclonic eddies. Their delayed occurrence or absence of one of these features results in a reattachment. As mentioned by [Fratantoni et al. \(1998\)](#), Tortugas eddies can last more than four months near Dry Tortugas Islands as long as they continue intensifying by merging with other frontal eddies. The authors also mention that after losing about 55% of their size, Tortugas eddies can continue their journey through the Florida Chanel. Therefore, in the NOCF experiment, the excessive number of reattachments in

the south and center regions may be due to an overestimation in the residence time and intensity of Tortugas eddies near the Dry Tortugas Islands, which increases the probability of their intensification by the merging with other frontal eddies. This hypothesis is reinforced by the larger EKE near the Tortuga dry in NOCF (Figure 4.1). Consequently, excessive reattachments may result in a bias in LC growth. In contrast, Tortugas eddies in the CF experiment can transfer energy into the atmosphere through the eddy killing mechanism, reducing their residence time near Dry Tortugas Islands and the probability of merging with other frontal eddies. The simulation NOCF also results in larger EKE in the Caribbean Sea. This could drive part of the sensitivity of the shedding statistics, although it is not clear at this stage.

The latitude of the detachment, beyond its importance on the tendency to favor separations when it occurs north of  $24^{\circ}\text{N}$ , has important consequences on the properties of the LCEs that are shed. This is revealed in Figure 5.5, which shows that LCEs are larger and more energetic when separated from the *south* and *center* regions. This could also have consequences on the heat and salt transport toward the western Gulf of Mexico, and thus deserves further attention.

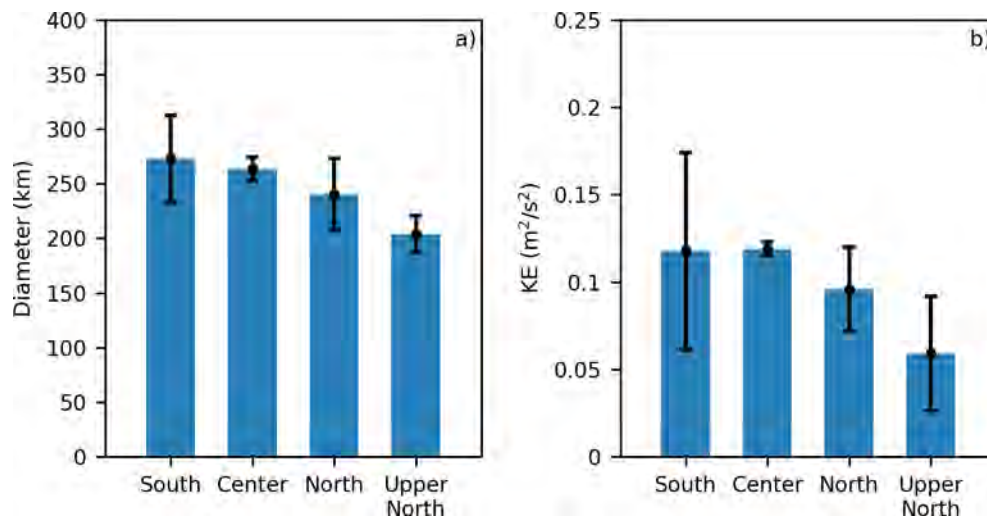


Figure 5.5: Mean diameter (a) and KE (b) of LCEs after separation events. The standard deviation is represented by black lines.



# Spatial scales of the eddy wind work over the Loop Current

---

## Contents

---

6.1	Introduction . . . . .	94
6.2	Methods . . . . .	94
6.3	Energy transfers . . . . .	95
6.4	Impact of the CFB on cyclonic eddies and frontal jets . . . . .	97
6.5	Unraveling the kinetic energy budget over the Loop Current region at 80 km scale . . . . .	102
6.6	Discussion and conclusions . . . . .	104

---

## 6.1 Introduction

In Chapter 4 it has been shown that CFB leads to 20% reduction of EKE over the GoM, with larger impacts over the LC region (Figure 4.1). This reduction of EKE leads to a better representation of the GoM dynamics by increasing the LC extension and producing more realistic LCEs shedding statistics. The reduction of the EKE is mainly explained by two factors: a negative geostrophic eddy wind work in the LC periphery and near Dry Tortugas Islands (Figure 4.5); and a decrease of the EKE production by barotropic instabilities in the same regions (Figure 4.4). However, the LC region dynamics are driven by the occurrence and interaction of oceanic features at different spatial scales, among which are the LC, the LCEs, and the cyclonic eddies traveling around the LC. Note that in the following Chapter, cyclonic eddies will refer to eddies that may have different origins, *i.e.*, Loop Current Frontal Eddies, Tortugas eddies, and Caribbean cyclonic eddies.

This chapter aims to better understand the energy pathways that drive the EKE reduction and to determine at which spatial scales CFB is the most active. To this end, a coarse-graining approach (Aluie et al., 2018; Rai et al., 2021) is used to decompose 10-years (1994 to 2003) of geostrophic eddy wind work ( $F_e K_{e_{cg}}$ ), barotropic and baroclinic conversions of energy.

## 6.2 Methods

The scale-dependent energy transfer terms  $F_e K_{e_{cg}}$ ,  $P_e K_{e_{cg}}$ , and  $\Pi$  are computed using a coarse-graining approach (Aluie et al., 2018). The term  $F_e K_{e_{cg}}$  is the energy flux at scale  $L$  from the ocean to the atmosphere. The term  $P_e K_{e_{cg}}$  is the energy transfer between EPE to EKE at scale  $L$ . Positive values, it is representative of a transfer from EPE to EKE by baroclinic instability, and inversely negative values represent a transfer from EKE to EPE. For a given reference scale  $L$ ,  $\Pi$  represents the energy flux to smaller (if positive, forward cascade) or larger (negative, inverse cascade) scales than the reference scale  $L$ . If positive,  $\Pi$  is related to barotropic instability. The coarse-graining has been applied to 10-years of daily outputs from CF and NOCF simulations (1994-2003). Further details about the coarse-graining method are given in section 2.2.2.

The spatial distribution of the occurrence and averaged KE of cyclonic eddies and frontal jets are performed as a function of their shapes. The shape of the cyclonic eddies is inferred from the 28 cm Sea Surface Height (SSH) anomaly contour, as proposed by Hiron et al. (2020), while the shape of frontal jets is inferred from the  $1 \text{ m}^2 \text{ s}^{-2}$  KE energy contours. Following Leben (2005), SSH anomaly is first estimated by removing from the SSH its long-term temporal mean and its spatial average over the GoM.

### 6.3 Energy transfers

The geostrophic eddy wind work  $F_e K_{e_{cg}}$  is computed for CF and NOCF over scales ranging from 16 km (the smaller scale solved by the oceanic model) to 320 km and spatially integrated over the LC region. Results are shown in Figure 6.1, where one can observe that  $F_e K_{e_{cg}}$  in the CF experiment is negative and is maximum at scales around 80 km. In contrast,  $F_e K_{e_{cg}}$  in the NOCF experiment is almost null at scales below 110 km, which is consistent with the literature (see *e.g.*, Renault et al. (2016b)). At scales larger than 110 km,  $F_e K_{e_{cg}}$  is positive, indicating that the atmosphere injects energy into the ocean at these scales.

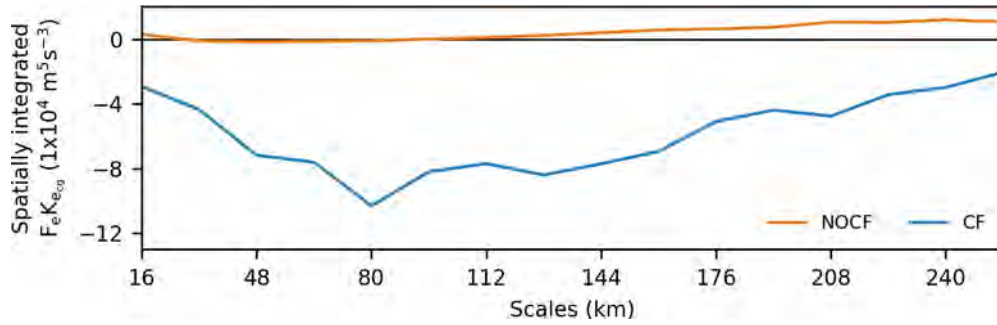


Figure 6.1: Geostrophic eddy wind work  $F_e K_{e_{cg}}$  for scales ranging from 16 km to 256 km and spatially integrated over the polygon delimited by the black segmented contours in Figure 6.2 and out of the shelf delimited by the 200 m depth contour.

In order to better understand where the 80–km eddy wind work is active and its consequences of the baroclinic and barotropic energy transfers at the same scale, the coarse–grained EKE budget terms at a scale of 80 km for NOCF and CF are shown in Figure 6.2.

In NOCF,  $F_e K_{e_{cg}}$  is mainly dominated by positive values, revealing that the atmosphere is forcing the ocean dynamics on the 80 km scale (Figure 6.2a). Negative wind work, corresponding to a sink of energy from the ocean to the atmosphere, is found on the eastern side of the mean LC path where surface currents are flowing eastward, *i.e.*, in the opposite direction of the mean winds (Figure 1.11).

The baroclinic conversion term  $P_e K_{e_{cg}}$  is positive over the LC region, which indicates a transfer of potential energy to kinetic energy at the 80–km scale (Figure 6.2b). Negative baroclinic conversion is found between the Western Florida Shelf and northwest of the LC, but also southwest of the Florida Shelf, where Tortugas eddies occur, indicating kinetic energy transfer to potential energy and, thus, damping of the eddies.

The energy fluxes for  $\Pi$  are one order of magnitude more intense than the other EKE budget terms (Figure 6.2a–c). Besides, it displays more negative values, which are associated with an energy flux from smaller to larger scales (inverse cascade). However, a strip of positive values indicative of a forward cascade energy flux is found on the north and eastern side of the LC, from the Mississippi Fan to the south of the West Florida Shelf (Figure 6.2c).

6.3).

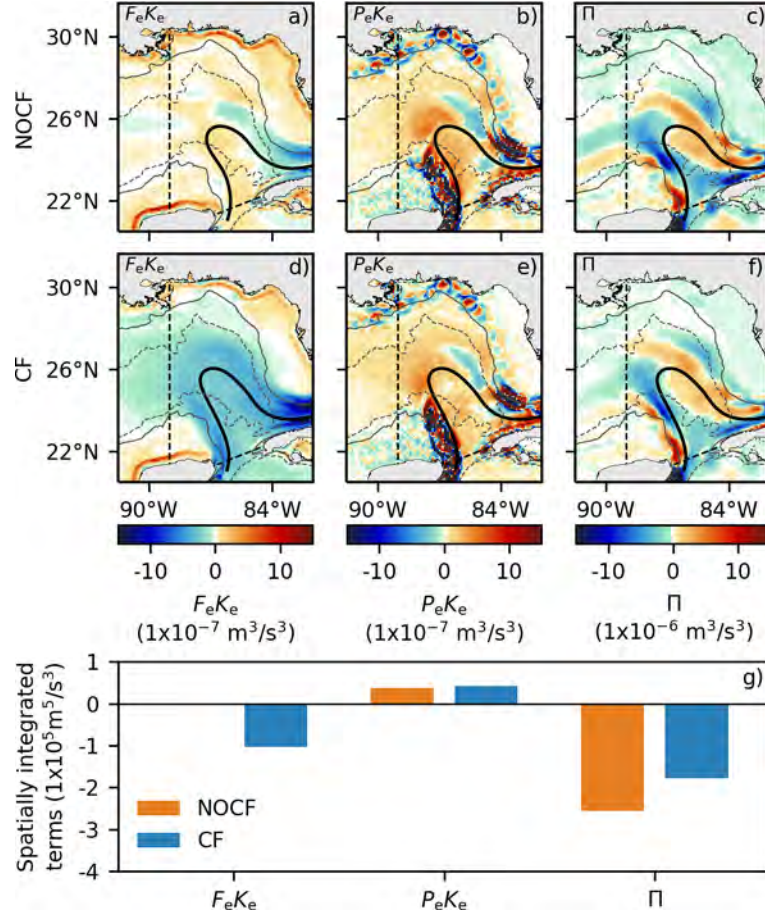


Figure 6.2: 10–years of averaged coarse–grained geostrophic eddy wind work (first column), baroclinic instability (second column), and barotropic instability (third column) for the NOCF (first row) and CF (second row) experiments. The 10–year LC mean position is represented by the 17 cm contour of the sea surface height anomaly. The thick segmented black lines delimit the LC region. The light gray contours refer to the 200 (continuous) and 2500 m (segmented) depths. Spatially integrated values over the LC region are shown in the last row.

Not surprisingly, from NOCF to CF,  $F_e K_{eg}$  becomes negative in the regions out of the shelf delimited by the 200 m depth contour, revealing a sink of energy from the ocean to the atmosphere at 80 km scale (Figures 6.2a,d). As mentioned in Section 4.2.0.2,  $F_e K_{eg}$  over the shelf is related to wind–driven current anomalies that partially flow in the same direction as the wind (Renault et al., 2016a,b), and therefore exhibit positive values. Spatial patterns of baroclinic and barotropic instabilities do not show major differences between the numerical simulations.

To infer the impact of the CFB over the whole LC region,  $F_e K_{eg}$  and energy conversions are spatially integrated east of 89°W without considering the values over the shelf (Figure 6.2g). It shows that CFB induces a sink of energy from the ocean to the atmosphere but also

indirectly results in a 30% reduction of the inverse cascade energy flux. Baroclinic conversion at this scale remains the same. However, a comparison of spatial maps of  $\Pi$  also reveals that the forward cascade (positive  $\Pi$  in Figure 6.2c,g) occurring from the Mississippi Fan to the south of the West Florida Shelf is decreased in CF. This suggests that the barotropic instability over this region is indirectly reduced by the CFB.

There are still important questions regarding the spatial distribution of the energy transfer terms. It is evident that  $FeK_{eg}$  largely sinks energy from the ocean to the atmosphere all around the LC. However, it is not clear which processes drive barotropic instabilities to produce forward cascade energy fluxes on the eastern portion of the LC, and why barotropic and baroclinic energy transfers are negative northwest of the Florida Shelf. In the following, the main features that dominate the LC region dynamics are analyzed in order to answer this question.

## 6.4 Impact of the CFB on cyclonic eddies and frontal jets

The previous section highlights the importance of fine-scale dynamics in driving the ocean energy sink through eddy wind work. This raises the question of which ocean dynamical processes are participating in (and are affected by) this sink. A sequence of weekly KE maps over a month and a half (Figure 6.3) illustrate that the LC and cyclonic eddies are the more recurrent features over the LC region that apparently occur at scales around 80 km. Figure 6.3 shows that the interaction between the cyclonic eddies and the LC gives rise to intense jets that can reach KE values up to  $2 \text{ m}^2 \text{ s}^{-2}$ . These jets embedded in the LC are referred to as frontal jets and occur from the LC–cyclonic eddies interaction, which horizontally tilts the isopycnals between these two features and produces these strong geostrophic currents (Hiron et al., 2020). The KE pulses associated with these jets can strongly contribute to the EKE budget over the LC region and are associated with strong horizontal shear. Another important pattern that can be distinguished from Figure 6.3 is that the LC modifies its shape by squeezing cyclonic eddies over the boundary outlined by the 2500 m depth contour, but also that frontal jets are more intense in these situations. This is more evident northeast the LC in Figures 6.3d-f.

Figure 6.3 also illustrates the occurrence of standing and intense frontal jets around standing Tortugas eddy, which can be observed over the 6 weeks southwest of the Florida Shelf. This eddy is most probably energized by its fusion with incoming cyclonic eddies. Indeed, Figure 6.3a shows a cyclonic eddy northwest of the Florida Shelf traveling to the Tortugas eddy. When the cyclonic eddy reaches the Tortugas eddy and merges with it (Figure 6.3c), the merged cyclonic eddy increases its size and produces intense frontal jets by largely deforming the LC (Figures 6.3d-f).

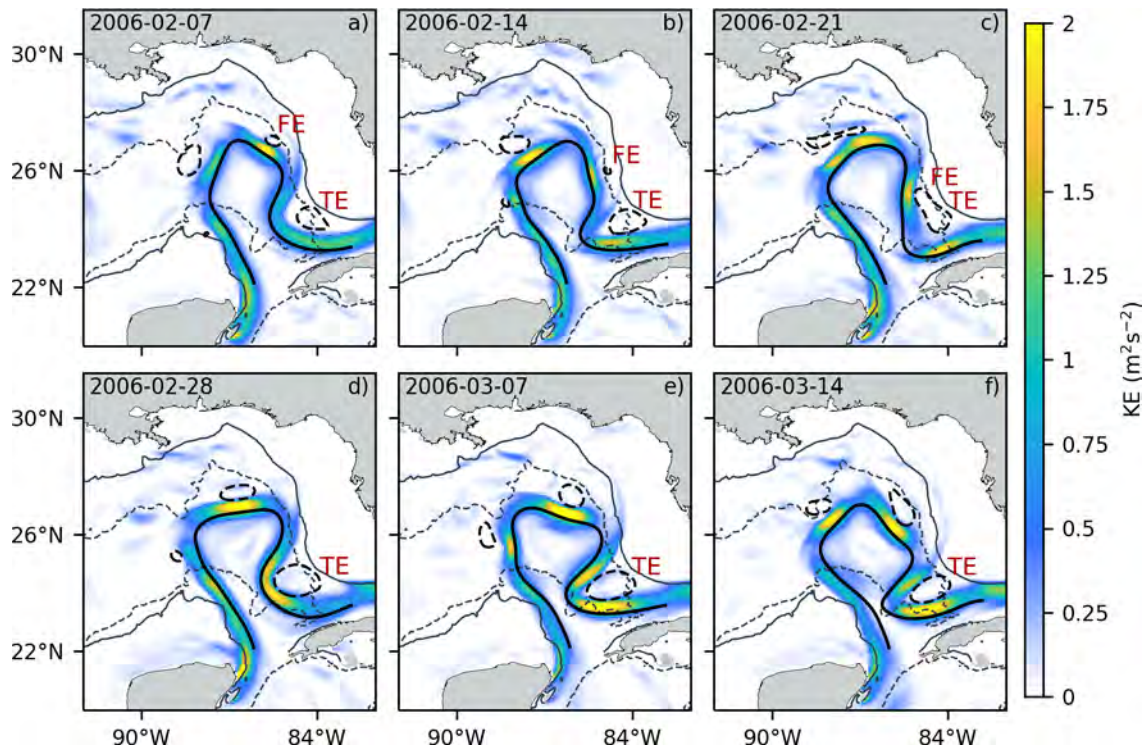


Figure 6.3: Kinetic energy snapshots from CF every 7 days from February 7, 2006, to March 14, 2006. Black continuous contours denoted the LC and black segmented contours represent the cyclonic eddies. FE refers to frontal eddy and TE to Tortugas eddy. The light gray contours refer to the 200 m (continuous) and 2500 m (dashed) depths.

The impact of the CFB on the size and energy of cyclonic eddies and frontal jets is now investigated. The distribution of their diameter and spatially averaged energy is shown in Figure 6.4 for both CF and NOCF simulations. In both simulations, cyclonic eddies in NOCF and CF are predominantly less than 60 km in diameter and are not very energetic (less than  $0.1 \text{ m}^2 \text{ s}^{-2}$ ; Figures 6.4a,c). The CFB limits the occurrence of the largest and most energetic cyclonic eddies. From NOCF to CF, the occurrence of cyclonic eddies of diameters between 60 and 120 km is reduced by 36.4%, and the occurrence of cyclonic eddies of KE between 0.1 and  $0.4 \text{ m}^2 \text{ s}^{-2}$  is reduced by 31.8%.

Regarding frontal jets, they are mostly between 30 and 80 km in diameter, displaying a spatially averaged KE between  $1.2$  and  $1.4 \text{ m}^2 \text{ s}^{-2}$  (Figures 6.4b,d). As for cyclonic eddies, CF promotes smaller and less energetic frontal jets. There is a 27.9% larger occurrence of jets with diameters up to 100 km and a 50.1% lower occurrence of larger ones. Additionally, weaker frontal jets (spatially averaged KE up to  $1.2 \text{ m}^2 \text{ s}^{-2}$ ) are about 22.2% more prone to occur when CF is taken into account. As can be seen in Figure 6.4, there is a larger occurrence of frontal jets than of cyclonic eddies, when they should have a similar occurrence. The reason is associated with their detection method. On the one hand, frontal jets are high-energy features that can be easily detected through an energy level contour. On the other hand, cyclonic eddies are much less energetic in comparison with the LC or frontal jets,

so it was decided to detect the cyclonic eddies using sea surface height anomalies. However, small eddies are difficult to detect. Therefore, cyclonic eddies and frontal jets are sampled over 24-years in order to obtain accurate statistics on their properties.

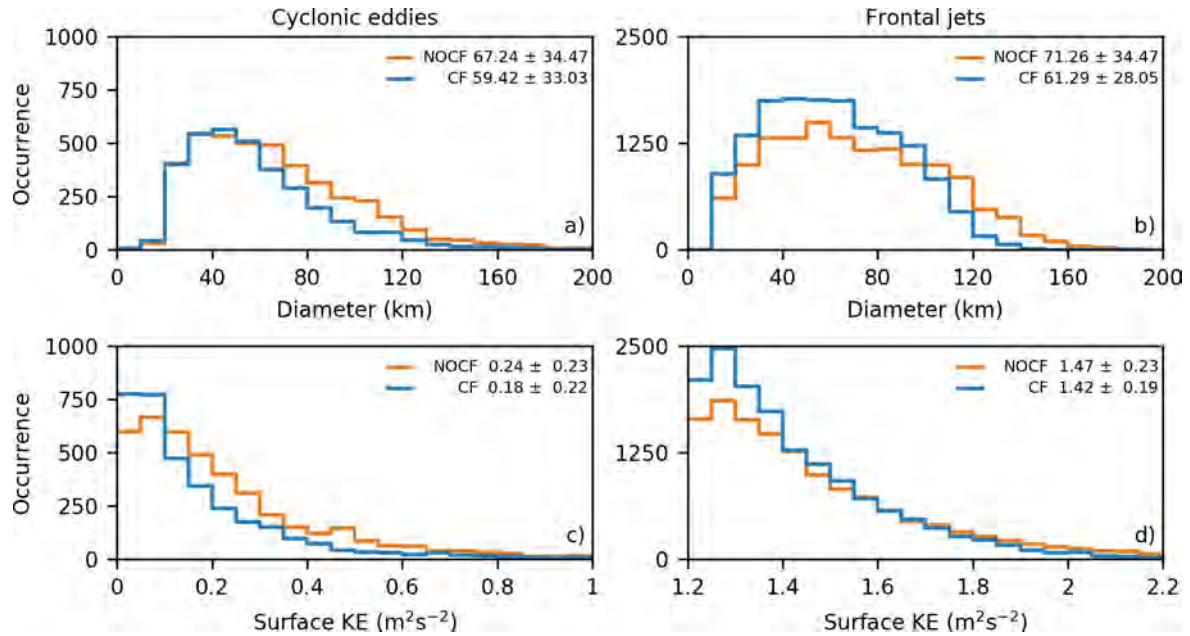


Figure 6.4: 24-year statistics about the diameter (first row) and KE (second row) of cyclonic eddies (first column) and frontal jets (second column). The mean and standard deviation of cyclonic eddies and frontal jets properties are included on the top right corner.

Scatter plots relating the diameter and KE help us to better characterize cyclonic eddies and frontal jets, and more specifically, the ones with diameters around 80 km (Figure 6.4). Most of the cyclonic eddies have diameters and KE up to 60 km and  $0.2 m^2 s^{-2}$ , respectively. Anomalous cyclonic eddies can be classified into two categories: the small and high energetic ones and the large and low energetic ones (Figure 6.4a,c). Although both kinds of cyclonic eddies are not very recurrent, these eddies could be responsible for modulating the LC penetration into the GoM and the detachment and separation of the LCEs. Regarding frontal eddies with diameters between 60 and 100 km have a spatially averaged KE up to  $0.2 m^2 s^{-2}$ . At these scales, CFB drastically reduces the occurrence of both low (up to  $0.2 m^2 s^{-2}$ ) and high (larger than  $0.2 m^2 s^{-2}$ ) by 29.1% and 57.8%, respectively.

Frontal jets exhibited a linear relationship between their diameter and averaged KE: the larger the diameter, the stronger the eddies. The most recurrent frontal jets have diameters up to 60 km and an averaged KE smaller than  $1.4 m^2 s^{-2}$  and their occurrence is increased in 9.6% when considering CF. The occurrence of these frontal jets and the high-energetic ones with diameters between 60 and 100 km is increased by 23.3% 31.6% when CF is taken into account, while the occurrence of large and intense jets is reduced by 65.5%. This increment in the occurrence of these frontal jets could be related to CFB in two main ways. On one side, CFB reduced the occurrence of intense frontal jets due to the sink of energy into the

atmosphere. On the other side, CFB promotes the occurrence of smaller and less energetic cyclonic eddies, leading to weaker cyclonic eddies–LC interactions and, therefore, weaker frontal jets. Additionally, the net occurrence of frontal jets is increased by roughly 9% when CFB is considered by promoting a larger LC penetration into the GoM.

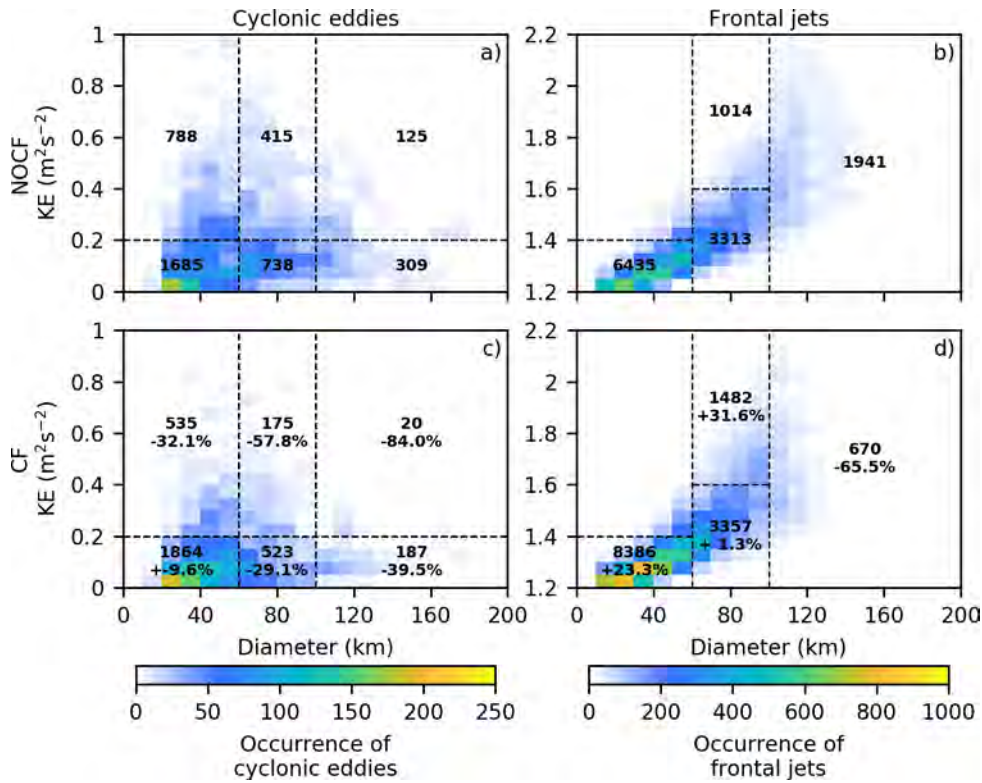


Figure 6.5: Two-dimensional probability density function relating the diameter and KE of cyclonic eddies (first column) and frontal jets (second column) for the numerical simulations NOCF (first row) and CF (second row). The figures show the number of eddies and jets for the different classifications delimited by the segmented lines. The second line shows the percentage increase/decrease in the number of eddies and jets from NOCF to CF.

An analysis of the spatial variability related to the occurrence and energy of cyclonic eddies and frontal jets is presented below. The purpose is to investigate whether these features are related to regions with higher forward cascade energy fluxes and a larger sink of ocean energy to the atmosphere via the geostrophic eddy wind work. It is clear that the energy of cyclonic eddies is low compared to the LC and frontal jets; therefore, their contribution in terms of energy sink to the atmosphere is small. However, their ubiquitous presence around the LC could make them an important contribution to the regional EKE budget.

Both numerical simulations, CF and NOCF, show that the occurrence of cyclonic eddies is well delimited by the 2500 m depth contour, suggesting that these eddies have a deep structure (Figure 6.6a,e). Three main locations with a larger occurrence of cyclonic eddies can be identified: northeast, center, and southeast of the LC. These regions are also characterized by strong cyclonic eddies (Figures 6.6b,f) and coincide with the regions where the merging

of cyclonic eddies results in the detachment of LCEs (Figure 5.2). However, important differences can be distinguished from the cyclonic eddies in the numerical simulations. From NOCF to CF the occurrence of cyclonic eddies is reduced by about 25% east of the LC, and about 35% within the LC mean position contour. Besides, their energy levels are reduced by roughly 15% east of the LC.

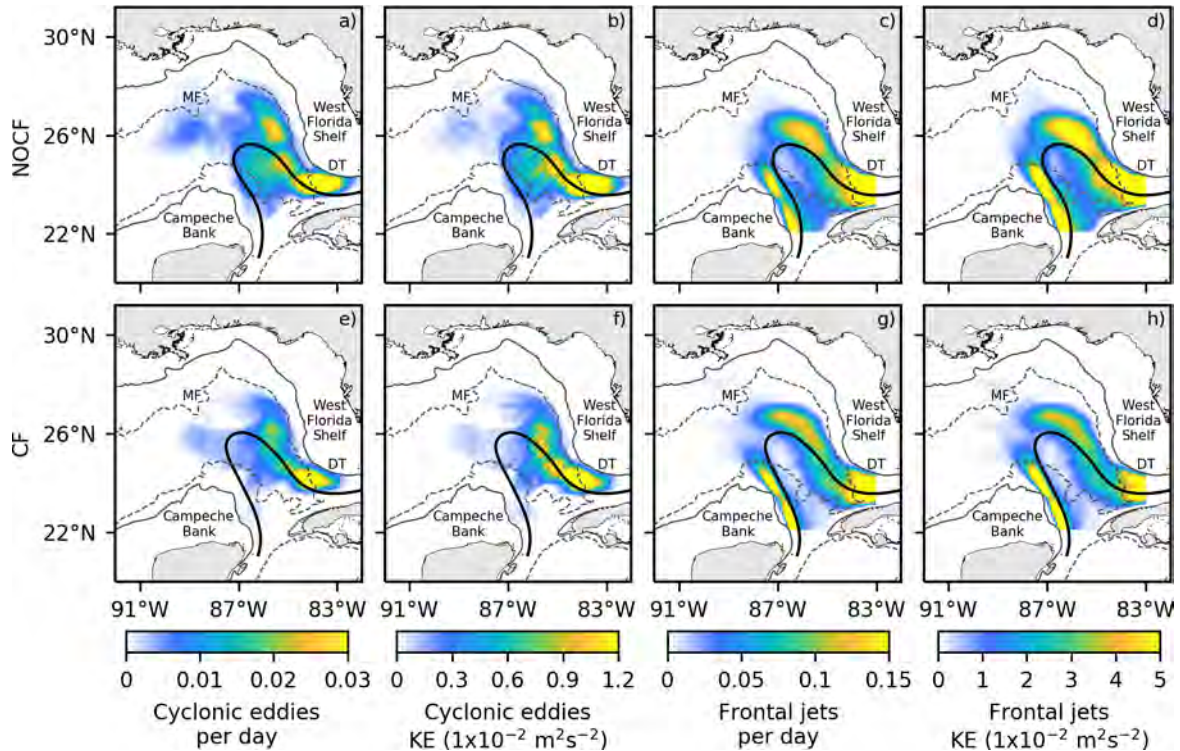


Figure 6.6: Probability of cyclonic eddies (first column) and frontal jets (third column) occurrence over the GoM over 24-years and associated kinetic energy (second and fourth columns) for AVISO (first row) and the numerical simulations NOCF (second row) and CF (third row). A thick contour represents the mean LC penetration into the GoM. The light gray contours refer to the 200 m (continuous) and 2500 m (dashed) depths. MF represents the Mississippi Fan and DT Dry Tortugas Islands.

Frontal jets occur almost all along the LC in both numerical simulations, only exhibiting a minor presence in the northwest of the LC (Figures 6.6c,g). These features largely occur northeast and southeast of the LC, where they are also more energetic. From NOCF to CF, frontal jets northeast of the LC are more widely distributed in this region, and their energy is reduced by about 20% (Figures 6.6c,d,g,h). Nevertheless, the larger differences occur west Dry Tortugas Islands, where frontal eddies reduce their energy by about 40% when CF is considered (Figures 6.6d,h).

Both simulations display a larger occurrence of KE pulses between Campeche Bank and the LC. Still, there is no significant number of detected frontal eddies in this region to relate their occurrence with the presence of frontal jets. However, numerical simulations of  $1/36^\circ$

from Jouanno et al. (2016) show the occurrence of cyclonic eddies with diameters between 20 and 60 km in this region. Therefore, this may indicate that these energy pulses do correspond to frontal jets generated by small cyclonic eddies that are not captured by our detection method or not fully resolved at  $1/12^\circ$  resolution.

## 6.5 Unraveling the kinetic energy budget over the Loop Current region at 80 km scale

A comparison between the 10-year coarse-grained barotropic conversions (Figure 6.2c,f) and the spatial distribution of cyclonic eddies and frontal jets (Figure 6.6) confirm that the spatial occurrence of these features is consistent with regions exhibiting forward cascade energy fluxes. Instead, inverse cascade energy fluxes occurring east of the Campeche Bank LC could be related to the strength of the LC. In comparison with  $\Pi_{cg}$ , spatial patterns of  $P_e K_{e_{cg}}$  and  $K_e K_{e_{cg}}$  (Figures 6.2a,b,d,e) do not appear to be strongly related to the occurrence of frontal jets (Figure 6.6). As the role of the LC and frontal jets in the EKE budget is unclear, a temporal filter with a 91-day cutoff period is used to separate the frontal jets (high-frequency component) from the LC (low-frequency component). It is worth noting that the LC has a similar diameter to frontal jets and that its energy is higher than that of FEs but lower than that of frontal jets (Figure 6.3). The coarse-grained EKE budget is then applied to both low and high-frequency components, but also a non-linear term resulting from the signal decomposition. This non-linear term is related to the interaction between the LC and the frontal jets (see section 2.2.2 for details).

Results for the CF experiment are shown in Figure 6.7. As NOCF exhibits similar spatial patterns, its figure is not shown.  $\Pi_{lf}$  drives energy to the background LC east Campeche Bank through inverse cascade energy fluxes. Besides,  $\Pi_{lf}$  exhibit forward cascade energy fluxes all along the Florida Straits. The latter are associated with persistent frontal jets occurring when long-standing cyclonic eddies interact with the LC (Figures 6.7g and 6.6e,g). These results suggest that the temporal filter can not completely separate the low-frequency signal of frontal jets from the LC, but also that persistent frontal jets east of the LC are fed through barotropic instabilities.  $\Pi_{hf}$  exhibit forward cascade energy fluxes all long the LC (Figure 6.7h). These energy fluxes can be associated with the occurrence of high-frequency frontal jets, such as those freely traveling around the LC in Figure 6.3, showing that barotropic instabilities also fed high-frequency frontal jets. However, the main role of  $\Pi_{hf}$  is to drive inverse cascade energy flux all around the LC (Figures 6.7h and 6.8b,c). Moreover,  $\Pi_{nl}$  results in two main energy pathways. On the one hand, this strengthens the LC by counteracting forward cascade energy fluxes from  $\Pi_{hf}$  (Figure 6.7i). On the other hand,  $\Pi_{nl}$  largely increases forward cascade energy fluxes southwest Florida Shelf, where long-standing Tortugas eddies lead to persistent frontal jets (Figures 6.3c-f). Baroclinic instabilities are mainly high-frequency and the domain of forward cascade energy fluxes could be interpreted as a tendency to re-stratification (Figure 6.7d-f). The geostrophic eddy wind work shows the same order energy fluxes in both low and high-frequency signals, with a small non-linear contribution (Figure 6.7a-c and 6.8).

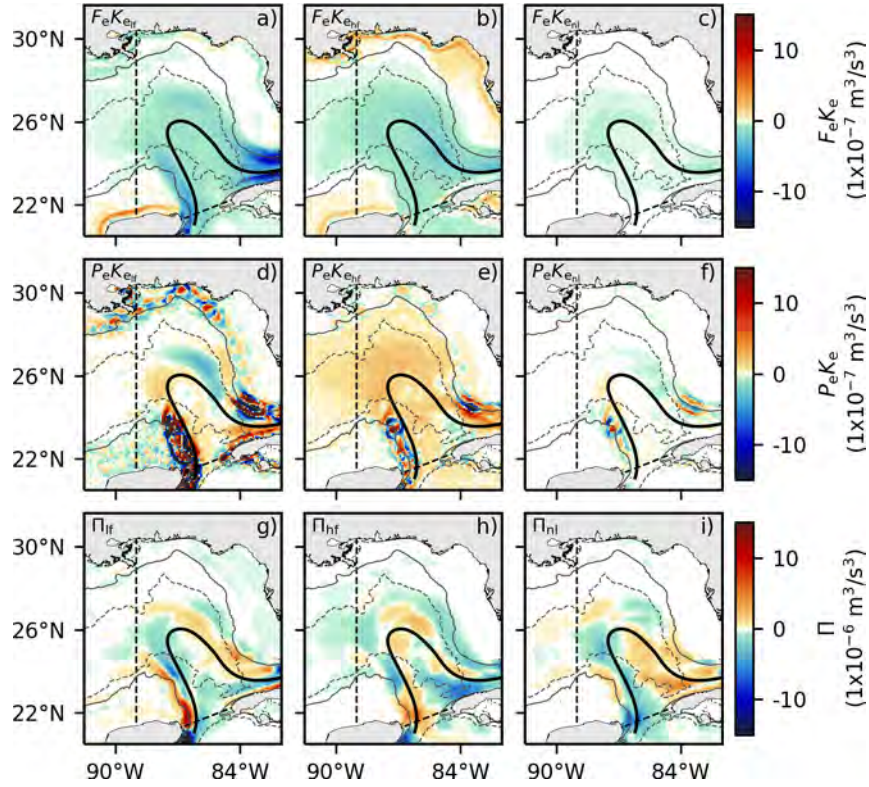


Figure 6.7: Coarse-grained geostrophic eddy wind work (first row) and baroclinic (second row) and barotropic (third row) energy conversions decomposed into their low-frequency (first column), high-frequency (second column), and non-linear interaction components (third column). The thick segmented black lines delimit the LC region. The light gray contours refer to the 200 (continuous) and 2500 m (segmented) depths.

To sum up,  $\Pi_{nl}$  and  $\Pi_{lf}$  are the main drivers of forward energy fluxes west of the Florida Shelf, but also produce important inverse cascade energy fluxes east of Campeche Bank that strengthens LC (Figure 6.8).  $F_e K_{ehf}$  seems to compensate  $P_e K_{ehf}$  (Figure 6.8a). Nevertheless, results exhibit that the most important contribution of CFB regarding the EKE balance is the reduction of forward cascade energy fluxes from  $\Pi_{lf}$  (27.1%) and  $\Pi_{nl}$  (34.9%), and the reduction of inverse cascade energy fluxes in  $\Pi_{hf}$  (35.9%; Figure 6.8b,c).

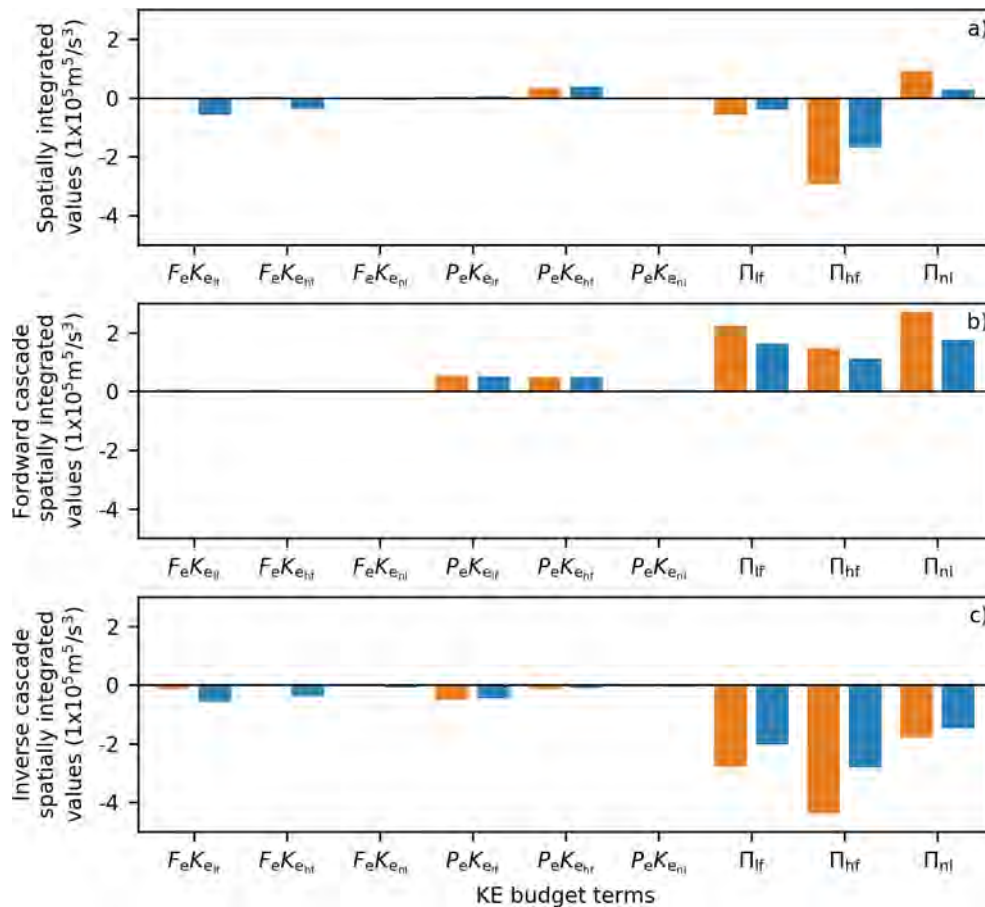


Figure 6.8: Spatially integrated coarse-grained EKE budget terms over 10-years for NOCF (orange) and CF (blue). Forward and inverse cascade energy fluxes are spatially integrated in a), whereas only Forward cascade energy fluxes are considered in b) and only inverse cascade energy fluxes in c).

## 6.6 Discussion and conclusions

The purpose of this chapter is to better understand how CFB performs and modulates the EKE budget in the GoM. The geostrophic eddy wind work largely sinks energy from the ocean to the atmosphere at a scale of 80 km. Over this scale, the larger patch of forward cascade barotropic conversions occurs east of the LC, where cyclonic eddies and frontal jets generally occur. This result suggests that frontal jets could be mainly fed through barotropic instabilities. In contrast, barotropic conversions west of the LC are characterized by inverse cascade energy fluxes (Figures 6.2c,f), being this the predominant energy pathway of barotropic instabilities over the LC region (Figure 6.2g). Geostrophic eddy wind work, on the contrary, largely acts all around the LC and does not seem to display spatial patterns associated with the occurrence of frontal jets (Figure 6.2d).

In an attempt to separate the contributions to the EKE budget by the LC and frontal

jets, components of the energy budget are computed from the low and high-frequency variability (cut-off period of 91 days). Baroclinic instabilities seem to feed two kinds of frontal jets: the high-frequency ones that occur all around the LC, and the low-frequency ones that occur all over the Florida Shelf. The latter are generated from the interaction between the LC and long-standing cyclonic eddies occurring east of the LC. However, non-linear interactions between low and high-frequency signals are also important for barotropic conversions. These counteract the positive and high-frequency energy fluxes by producing inverse cascade energy fluxes that strengthen the background LC. In addition, this non-linear interactions increase forward cascade energy fluxes near Dry Tortugas Islands, were large and long-standing cyclonic eddies promote LCEs detachments (Chapter 5).

This study shows that frontal jets are important features powered by barotropic instabilities that mainly drive KE anomalies all along the LC, which can even intensify the background LC through inverse cascade energy fluxes. CFB leads to more realistic energy estimations over the region by directly weakening the LC, cyclonic eddies, and frontal jets through the geostrophic eddy wind work, but also by reducing barotropic energy conversions. This reduction of barotropic energy conversions could be related to an indirect effect of CFB: by weakening the cyclonic eddies, weaker horizontal current shears result from LC-cyclonic eddies interactions.

Previous studies which investigated the EKE budget over the GoM (Chérubin et al., 2006; Oey, 2008; Garcia-Jove et al., 2016), were performed using a classic Reynolds decomposition, which is based on a temporal eddy-mean decomposition. However, results from this method are difficult to interpret since length-scales are not considered. In contrast, the coarse-graining approach (Aluie et al., 2018; Schubert et al., 2020; Contreras et al., 2022) allows us a length-scale point of view. In this work, we implement a time-space EKE budget decomposition, allowing us to further understand the processes behind the energy flows over the LC region.



# Conclusion and perspectives

## Conclusion

The Gulf of Mexico (GoM) is a region characterized by complex ocean dynamics, which is dominated by the emblematic Loop Current (LC) and large anticyclonic eddies that detach episodically from the LC: the Loop Current Eddies (LCEs). Numerous economic and commercial activities are developed both in coastal regions and in the open waters of the GoM, *i.e.*, oil extraction and fisheries, which are continuously affected by the detachment of LCEs or by the occurrence of intense atmospheric features such as storms, cold fronts, or hurricanes. As a complement to *in situ* or satellite observations, numerical models are important tools that help us to better understand the ocean dynamics and its interaction with the atmosphere. However, so far, most of the high-resolution numerical implementations of the GoM dynamics are characterized by over-energized (sub)mesoscale features. This overweight energy is reflected in persistent biases in the GoM dynamics simulated by numerical simulations, *e.g.*, a limited LC penetration into the GoM, anomalous statistics about LCEs detachments, and too energetic and long-lived LCEs. This work aims to investigate whether these biases can be reduced by including in eddy-rich ocean-atmosphere coupled simulations, the mechanical interaction between the surface current and the atmosphere, the so-called current feedback (CFB) to the atmosphere.

To this end, a set of eddy-rich ocean-atmosphere coupled simulations considering or not CFB have been carried out over a time period of 24-year (1993 to 2016): NOCF, which refers to “No Current FeedBack”, and “CF”, which takes into account CFB. The numerical strategy consists in reproducing the ocean dynamics with a spatial resolution of  $1/12^\circ$  using the ocean model NEMO and the atmosphere dynamics with a spatial resolution of  $1/4^\circ$  using WRF. Previous studies have shown that the dynamics in the Caribbean Sea have an important influence on that of the GoM, so the numerical domain extends from the GoM to North Brazil Current retroreflection region in order to properly resolve this western boundary dynamical continuum. A first evaluation of the numerical simulations with respect to the observations (Chapter 3) shows that the reference simulation (CF) can properly reproduce the main large-scale currents over the numerical domain. We furthermore show that considering CFB in the model leads to a reduction of the mesoscale activity by about 22% over the GoM and about 34% over the Caribbean Sea. The wind stress and wind stress curl are also better reproduced in the CF experiment with respect to the NOCF experiment. In CF, consistent with the observations, the surface oceanic currents have an imprint on these variables over the North Brazil Current retroreflection, the LC, and the Gulf Stream.

Numerical simulations were furthermore compared to altimeter and *in situ* observations over the GoM in Chapter 4. Results show that the eddy kinetic energy (EKE) is largely reduced and actually better reproduced over the LC region, principally on both sides of the LC. This energy reduction is related to the *eddy killing* mechanism, which induces sink

energy from the ocean mesoscale currents to the atmosphere. Besides, it is also demonstrated that CFB modifies the conversion of energy that drives the eddy generation over the GoM. While the production through barotropic instability is reduced by about 14%, it is partially compensated by an increase of conversion by baroclinic instability. As an indirect effect, the EKE modulation caused by CFB leads to a spatial increase of 11% in the mean LC extension, better reproducing the occurrence of its retracted, canonical, and elongated states. LCEs detachment statistics are also largely improved by considering CFB, reducing/increasing the occurrence of reattachments/separations below/above 25°N. The larger LC penetration into the GoM in the CF experiment also had an effect on LCEs trajectories. As in observations, LCEs from CF preferentially travel along a vortex street between 24°N and 26°N. In contrast, LCEs in NOCF tend to travel a more southerly path. Regarding LCEs properties, CFB promotes eddies with more realistic KE, energy decay rate, and lifetimes. In agreement with observations (Elliott, 1982; Meunier et al., 2018, 2021), a composite of LCEs characterized by a lifetime longer than 200 days reveals that eddies are characterized by a warm core between 50 and 250 m depth that is well delimited by the 25°C and 20°C isotherms. As in observations, the warm core displays a pancake shape, shallower at the eddy center and deeper at the edges. The composite also reveals that salinity exhibit two cores: a fresher (about 36.5 PSU) and superficial one between 50 and 100 m depth, and a saltier (about 36.6 PSU) and deeper one between 100 and 150 m depth. By contrast, NOCF composite is characterized by a deeper surface thermocline, which may result in an over-intensification of atmospheric features such as storms and hurricanes due to the larger heat content. Additionally, the salinity core in this composite is well-mixed and saltier (36.6 PSU), and therefore lacks the fresher and superficial core.

To further investigate how CFB modulates the LCEs detachment, we try to identify the mechanisms that trigger LCEs detachments, but also the conditions that lead to the occurrence of reattachments or separations (Chapter 5). Using 24-year (1993-2016) of altimeter observations, both reattachment and separation events are classified according to their latitude of occurrence. Results show that LCEs detached below 24°N have a probability of 64% of reattaching, whereas eddies detached over 24°N are more prone to separate (70%). Results also reinforce the hypothesis that cyclonic eddies located between the LC and the Florida Shelf play a key and systematic role in the detachment of LCEs. Moreover, results indicate that Caribbean cyclonic eddies west of the LC are instrumental in leading to a final separation. The co-occurrence of eastern and western cyclonic eddies, which merge and grow below 24°N, limits the ability of the LC to capture newly formed LCEs. Therefore, the fate of LCEs detached during the unphased arrival or lack of one of these cyclonic eddies is generally to be reattached by the LC.

A comparison between the LC outermost position after LCEs reattachment and separation from observations and the numerical simulations show that not considering CFB leads to overestimating/underestimating the number of reattachments south/north of the LC. Results point out that this unrealistic statistic about LCEs reattachment is associated with the occurrence of highly energetic cyclonic eddies southwest of the LC and incoming cyclonic eddies from the Caribbean. The larger number of reattachments south of the LC could be also the reason for a shorter mean LC penetration into the GoM and fewer LCE separations north of

the LC.

As described in Chapter 4, there are considerable improvements in reproducing the GoM dynamics when including the CFB in eddy-rich air-sea coupled simulations through the reduction of the ocean KE at the mesoscale. The question of the energetic pathways by which the CFB leads to such KE reduction in the LC area is addressed in Chapter 6. A spatial decomposition of the geostrophic eddy wind work allows us to identify that the largest sink of energy happens at the scale of 80 km, which corresponds to the scale where the LC, cyclonic eddies, and frontal jets occur. The frontal jets result from the interaction between frontal eddies and the LC and contribute to a substantial fraction of the surface EKE in the LC. By comparing the zones of occurrence of these features and a KE balance at 80 km, we show that frontal jets occurring east of the LC are associated with a larger forward cascade, *i.e.*, a more intense transfer of energy from larger scales to smaller scales.

Frontal jets are important features over the LC region that are mainly powered by barotropic instabilities. These features mainly drive the EKE over the LC, and its recurrent presence strengthens the LC by means of inverse cascade energy fluxes. CFB leads to more realistic EKE estimations by directly weakening the LC and frontal jets, but mainly by reducing barotropic energy conversions over the LC region.

To sum up, this Ph.D. work highlights the importance of considering air-sea interactions related to CFB in numerical simulations of the GoM dynamics, exhibiting significant improvements in the reproduction of the KE, LC extension, and the detachment and fate of LCEs.

## Perspectives

### Current feedback in forced numerical simulations of the Gulf of Mexico

This thesis is based on coupled ocean-atmosphere simulations. It demonstrates the extent to which CFB modulates the GoM dynamics, the LC, and the associated eddy shedding. The question that arises is whether the uncoupled approach is still suitable, and are we doomed to use a coupled model to simulate the GoM oceanic circulation, or can we rely on a parameterization of CFB? Following Renault et al. (2020), CFB can be parameterized in a bulk formula using a wind or a stress correction approach. This has been done successfully at an almost global scale by Renault et al. (2020) and for the U.S. West coast by Renault et al. (2021b), but should be tested for the GoM. In fact, Renault et al. (2020) demonstrate that a parametrization based on  $s_w$  is able to reproduce the momentum flux response to CFB but also the response of heat and freshwater fluxes. In contrast, a parametrization based on a predicted  $s_\tau$  cannot represent CFB effects on heat and freshwater fluxes, but better represent the energy at the mesoscale.

Therefore, parameterizations based on  $s_w$  and  $s_\tau$  should be tested by considering or not their seasonal and spatial variability to properly evaluate the sensitivity of GoM dynamics in

terms of the KE, LC extension, and LCEs detachments.

### Importance of the current feedback on heat transfer in the Gulf of Mexico

It is now well known that LCEs contribute to the transport of heat toward the GoM (Meunier et al., 2020; Potter et al., 2021) and that this heat can be transferred to atmospheric events such as storms and hurricanes (Molina et al., 2016; Yablonsky and Ginis, 2012). This thesis demonstrated that numerical simulations that do not take into account the CFB produce over-energized and very long-lived LCEs, and alter the thermal properties of these eddies. This raises the question of the net impact of this mechanical coupling on the thermal equilibrium of the GoM, which most certainly combines local effects (via turbulent heat fluxes), and non-local effects (via heat transport by the LCEs). This question could be addressed by comparing, from NOCF and CF observations and numerical experiments, the different contributions to the GoM heat balance.

### Sensitivity of high-resolution numerical simulations of the GoM dynamics to the current feedback

High-resolution numerical simulations, *i.e.*,  $1/36^\circ$ , can solve a wider range of oceanic features over the GoM, including small mesoscale features such as high-frequency frontal eddies (6 to 10-day period; Jouanno et al., 2016), but also some of the submesoscale turbulence generated by and ageostrophic fronts, filaments, and eddies (Barkan et al., 2019), which are characterized by strong vertical velocities (Capet et al., 2008; MOLEMAKER et al., 2010). Even though resolving these features could result in an important energy dissipation pathway, Renault et al. (2018) have shown that increasing the resolution of forced simulations results in a larger production of EKE through baroclinic energy conversions which is partially compensated when including CFB.

Chapter 4 shows that not including CFB in numerical simulations of GoM dynamics results in excessive reattachments south of the LC. This appears to be related to an over-occurrence of long-standing Tortugas eddies near Dry Tortugas Islands. Without the energy sink related to CFB, the longer lifetime of Tortugas eddies favors their merging with other cyclonic eddies, resulting in a sudden increase in their size and the detachment of LCEs by cutting the LC. CFB leads to more realistic LCEs shedding statistics. However, to a lesser extent, the overestimation of reattachment events persists south of the LC. Therefore, high-resolution simulations considering CFB could help us to better reproduce the lifetime of Tortugas eddies by propitiating more realistic forward cascade energy fluxes, reducing Tortugas eddies intensification and the uncommon occurrence of LCEs reattachment.

## Mesoscale activity over the North Brazil Current retroflection and the Caribbean Sea

Similarly to the LC, the North Brazil Current sheds large anticyclonic eddies from its retroflection into the North Equatorial Counter current (Huang et al., 2021). As demonstrated by Huang et al. (2021), these anticyclonic eddies can enter the Caribbean Sea by crossing the Lesser Antilles. The analysis of altimeter observations over a 10-year period shows that between 5 and 6 anticyclonic eddies are detached by year (Goni and Johns, 2003). Our set of 24-year simulations and altimeter observations can help to investigate if North Brazil Current eddies detachment are sensible to CFB, and if so, how these eddies can modify the mesoscale activity over the Caribbean Sea.

## Evidence of current feedback in new satellite missions

Existing satellite products do not accurately characterize the surface current, the surface stress response to CFB, and the wind work (Renault et al., 2017a). Future satellite missions such as SWOT (Morrow et al., 2019) will allow measuring the geostrophic currents with a better spatial resolution than the current observations. This will allow us to better understand the geostrophic contribution of, for example, cyclonic eddies–LC interactions associated with the LCEs detachment and the production of frontal jets.

However, coherent measurements of total current and surface stress will still be missing. Future Satellite missions projects such as Odysea (Ocean Dynamical Surface Exchange with the Atmosphere; Bourassa et al., 2016; Rodríguez et al., 2019) should overcome this issue, helping to better characterize the wind work, the air-sea interactions, the energy pathway in the ocean and more generally to better constrain and validate numerical models.

## The Role of Wave Feedbacks in determining the GoM Dynamics

As mentioned in Chapter 1, surface gravity waves could modulate CFB by altering the wind stress. Waves are linked to the computation of wind stress in two principal ways: they modify the ocean surface roughness (controlled through the Charnock parameter) and alter the stress felt by the ocean by accounting for the portion of the stress consumed to generate waves. In order to understand how the wave modulation of surface roughness influences the regional ocean dynamics, we carried out a 22-year ocean–waves–atmosphere coupled simulation considering only one loop of coupling: the modification of the roughness estimated by the Charnock parameter from a wave model.

As a preliminary result, a comparison of the EKE over the Intra–Americas Sea between AVISO, CF, and this last experiment that includes the WFB (WF) is shown in Figure 6.9. Surprisingly, the comparison does not show any significant difference between CF and WF. We plan to analyze the EKE budget, LC extension, and detachments of LCEs to evaluate the extent to which the sinks of energy induced by CFB and the GoM dynamics are sensitive to

WFB.

The next step will be to perform additional simulations considering, *e.g.*, the portion of the stress consumed by the generation of the wave, the Stokes drift in the momentum equation, and waves-induced turbulence in the mixing layer.

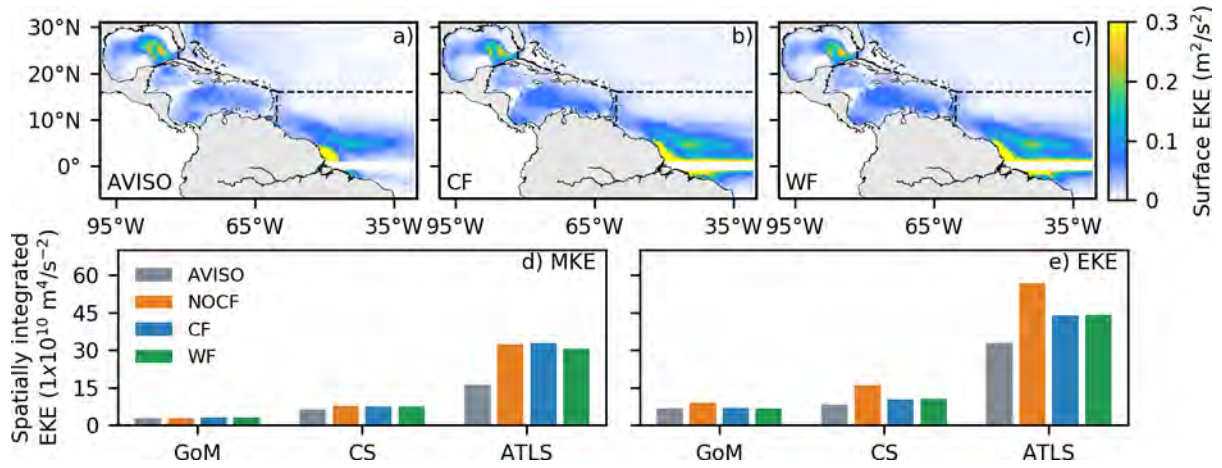


Figure 6.9: EKE climatologies over the Intra-Americas Sea for AVISO (a), CF (b), and NOCF (c). Spatially integrated MKE (d) and EKE (e) over the regions comprising the IAS are shown in the bottom row. GoM refers to the Gulf of Mexico, CS to the Caribbean Sea, and ATLS to the south Atlantic region.

# Conclusion et perspectives

## Conclusion

Le Golfe du Mexique (GdM) est une région caractérisée par une dynamique océanique complexe, dominée par l'emblématique Loop Current (LC) et de grands tourbillons anticycloniques qui se détachent épisodiquement du LC : les Loop Current Eddies (LCEs). De nombreuses activités économiques et commerciales sont développées à la fois dans les régions côtières et dans les eaux hauturières du GdM, à savoir l'extraction pétrolière et la pêche, qui sont continuellement affectées par le détachement des LCEs ou par l'apparition de phénomènes atmosphériques intenses telles que les tempêtes ou les ouragans. En complément des observations *in situ* ou satellite, les modèles numériques sont des outils importants qui nous aident à mieux comprendre la dynamique de l'océan et son interaction avec l'atmosphère. Cependant, jusqu'à présent, la plupart des implémentations numériques à haute-résolution de la dynamique du GdM sont caractérisées par une dynamique (sous-)mésoscale sur-énergétisée. Cette surestimation de l'énergie se reflète dans des biais persistants dans la dynamique du GdM simulée par les modèles numériques, comme par exemple une pénétration limitée du LC dans le GdM, des statistiques anormales sur les détachements de LCEs, et des LCEs trop énergiques et qui persistent trop longtemps dans le GdM. Cette thèse a pour but d'étudier si ces biais peuvent être réduits en incluant dans les simulations couplées océan-atmosphère riches en tourbillons, l'interaction mécanique entre le courant de surface et l'atmosphère, le "current feedback" (CFB) en anglais.

Pour ce faire, un jeu de simulations couplées océan-atmosphère riches en tourbillons, considérant ou non le CFB a été réalisé sur une période de 24 ans (de 1993 à 2016) : NOCF, qui fait référence à "No Current FeedBack", et "CF", qui prend en compte le CFB. La stratégie numérique consiste à reproduire la dynamique de l'océan avec une résolution spatiale de  $1/12^\circ$  en utilisant le modèle océanique NEMO et la dynamique de l'atmosphère avec une résolution spatiale de  $1/4^\circ$  à l'aide du modèle atmosphérique WRF. Des études antérieures ont montré que la dynamique de la mer des Caraïbes a une influence importante sur celle du GdM. Ainsi, le domaine numérique s'étend du GdM à la région de réflexion du courant nord-brésilien, ce afin de résoudre correctement ce continuum dynamique de courants de bord-ouest.

Le Chapitre 3 propose une évaluation des simulations par rapport aux observations satellites sur tout le domaine simulé, ce qui inclut donc non seulement le GdM mais aussi le Courant du Brésil et la Mer des Caraïbes. Nous montrons ainsi que la simulation de référence (CF) reproduit de manière réaliste les principaux courants à grande échelle sur le domaine simulé. Nous illustrons en outre que la prise en compte du CFB dans le modèle conduit à une réduction de l'énergie cinétique tourbillonnaire (EKE) d'environ 22% sur le GdM et d'environ 34% sur la mer des Caraïbes. La tension de vent ainsi que son rotationnel sont également mieux reproduits dans l'expérience CF par rapport à l'expérience NOCF. Dans CF, en accord avec les observations, les courants océaniques de surface ont une signature sur la tension de

vent notamment au-dessus de la réflexion du courant Nord du Brésil et du LC.

Le Chapitre 4 se concentre sur l'impact du CFB sur la dynamique du GdM. Dans un premier temps, les simulations numériques ont été comparées en détails aux observations altimétriques et *in situ* sur cette région. Nous confirmons une réduction de l'EKE d'environ 20% sur cette région, ce qui améliore grandement son réalisme. Cette réduction d'énergie est liée au mécanisme de destruction des tourbillons, l'eddy killing en anglais. L'eddy killing induit des puits d'énergie des courants océaniques de mésoéchelle vers l'atmosphère. En outre, il est également démontré que le CFB altère la conversion d'énergie barocline et barotrope qui conduit à la génération de tourbillons sur le GdM: une réduction d'environ 14% de la production par conversion est partiellement compensée par une augmentation de la conversion barocline.

Le CFB a de plus de nombreux effets indirects sur la dynamique du GdM. La réduction de l'EKE conduit à une augmentation spatiale de 11% de l'extension moyenne du LC, reproduisant mieux l'occurrence de ses différents états (rétracté, canonique et allongé). Les statistiques de détachements des LCEs sont aussi largement améliorées par la prise en compte du CFB, réduisant/augmentant l'occurrence des rattachements/séparations au-dessous/au-dessus de 25°N. La plus grande pénétration du LC dans le GdM dans l'expérience CF a également un effet sur les trajectoires des LCEs. En accord avec les observations, les LCEs dans la simulation CF se déplacent préférentiellement le long d'une trajectoire comprise entre 24°N et 26°N. En revanche, les LCEs de NOCF ont tendance à parcourir une trajectoire plus au sud. Les propriétés générales des LCEs, comme par exemple leur durée de vie et leur intensité, sont aussi plus réalistes dans la simulation CF.

En accord avec les observations (Elliott, 1982; Meunier et al., 2018, 2021), un composite des LCEs révèle que les tourbillons sont caractérisés par un noyau chaud entre 50 et 250 m de profondeur qui est bien délimité par les isothermes 25°C et 20°C. En accord avec les observations, le noyau chaud présente une forme de "pancake", moins profond au centre du tourbillon et plus profond sur les bords. Le composite révèle également que la salinité présente deux noyaux : un moins salé (environ 36,5 PSU) et superficiel entre 50 et 100 m de profondeur, et un plus salé (environ 36,6 PSU) et plus profond entre 100 et 150 m de profondeur. En revanche, le composite NOCF est caractérisé par une thermocline de surface plus profonde, ce qui peut entraîner une surintensification des caractéristiques atmosphériques telles que les tempêtes et les ouragans en raison du contenu thermique plus important.

Afin d'étudier plus en profondeur la façon dont le CFB module le détachement des LCEs, une étude vise à identifier les mécanismes qui déclenchent le détachement des LCEs ainsi que les conditions qui conduisent à l'apparition de rattachements ou de séparations (Chapitre 4). En utilisant 24 ans d'observations altimétriques (1993-2016), les événements de rattachement et de séparation sont classés en fonction de leur latitude d'occurrence. Les résultats montrent que les LCEs détachés en dessous de 24°N ont une probabilité de 64% de se rattacher, alors que les tourbillons détachés au-dessus de 24°N sont plus enclins à se séparer (70%). Les résultats renforcent également l'hypothèse selon laquelle les tourbillons cycloniques situés entre la LC et le plateau de la Floride jouent un rôle clé et systématique dans le processus de séparation. De plus, les résultats indiquent que les tourbillons cycloniques des Caraïbes

à l'ouest du LC jouent un rôle déterminant dans la séparation finale. La cooccurrence des tourbillons cycloniques orientaux et occidentaux, qui fusionnent et se développent sous  $24^{\circ}\text{N}$ , limite la capacité du LC à re-fusionner avec les LCEs nouvellement formés. Par conséquent, les LCEs qui se détachent en l'absence d'un de ces tourbillons cycloniques est généralement rattaché par le LC.

Une comparaison entre la position la plus externe du LC après le rattachement et la séparation des LCEs à partir des observations et des simulations numériques montre que le fait de ne pas considérer le CFB conduit à surestimer le nombre de rattachements près du canal du Yucatan, et à les surestimer plus au nord. Les résultats suggèrent que cette statistique irréaliste sur le rattachement des LCEs pourraient être associée à la présence de tourbillons cycloniques trop énergétiques au sud-ouest du LC et de tourbillons cycloniques en provenance des Caraïbes également trop énergétiques. Le plus grand nombre de rattachements au sud du LC pourrait également être la raison pour laquelle la pénétration moyenne du LC est plus courte dans le GdM et la raison du plus faible nombre de séparations de LCE au nord.

Comme décrit au Chapitre 4, il y a des améliorations considérables dans la reproduction de la dynamique du GdM lorsqu'on inclut le CFB dans les simulations couplées air-mer riches en tourbillons, ce grâce à la réduction de l'énergie océanique à la mésoéchelle. La question des voies énergétiques par lesquelles le CFB conduit à une telle réduction de l'énergie cinétique dans la zone du LC est abordée de manière préliminaire dans le Chapitre 6. Une décomposition spatiale du travail du vents sur les courants géostrophiques (le "geostrophic eddy windwork") nous permet d'identifier que le plus grand puits d'énergie se produit à l'échelle de 80 km, ce qui correspond à l'échelle caractéristique du LC, des tourbillons cycloniques et des jets frontaux. Les jets frontaux résultent de l'interaction entre les tourbillons frontaux et le LC et contribuent à une fraction substantielle de l'EKE de surface dans le LC. En comparant les zones d'occurrence de ces caractéristiques et les principaux termes de conversions d'énergie à 80 km, nous montrons que les jets frontaux se produisant à l'est du LC sont associés à une plus grande cascade directe, c'est-à-dire à un transfert d'énergie plus intense des grandes échelles aux petites échelles.

En résumé, ce travail de doctorat souligne l'importance de considérer l'interaction mécanique entre l'océan et l'atmosphère dans des simulations numériques de la dynamique du GdM. Cette dernière permet de réduire significativement des biais jusqu'alors persistants dans les modèles comme par exemple une surestimation de l'énergie tourbillonnaire, un LC trop retractoré et des détachements de LCEs trop peu fréquents.

## Perspectives

### Rétroaction de courant dans les simulations numériques forcées du Golfe du Mexique

Certains résultats de cette thèse demandent à être plus poussés. Cependant, une des questions qui se pose est de savoir si l'approche non couplée est toujours appropriée, et si nous sommes condamnés à utiliser un modèle couplé pour simuler la dynamique du GdM. Sommes-nous condamnés à utiliser un modèle couplé pour simuler la circulation océanique du GdM, ou pouvons-nous nous appuyer sur une paramétrisation du CFB ? Renault et al. (2020) propose deux paramétrisations du CFB qui se basent sur une correction du vent ou de la tension de vent. Ces paramétrisations ont été testées avec succès à une échelle presque globale par Renault et al. (2020) et pour la côte ouest des États-Unis par Renault et al. (2021b), mais devrait être testée pour le GdM. En particulier Renault et al. (2020) démontrent qu'une paramétrisation basée sur le coefficient de couplage entre vent et courants ( $s_w$ ) est capable de reproduire la réponse du flux de moment au CFB mais aussi la réponse des flux de chaleur et d'eau douce. En revanche, une paramétrisation basée sur une prédiction de  $s_\tau$  ne peut pas représenter les effets du CFB sur les flux de chaleur et d'eau douce, mais représente de manière plus réaliste le flux de moment en considérant notamment son possible ajustement à l'échelle synoptique et saisonnière.

### Importance du le “current feedback” sur les transferts de chaleur dans le Golfe du Mexique

Il est désormais bien connu que les LCEs apportent de la chaleur au GdM (Meunier et al., 2020; Potter et al., 2021) et que cette chaleur peut être transférée vers des phénomènes atmosphériques tels que les tempêtes et les ouragans (Molina et al., 2016; Yablonsky and Ginis, 2012). Cette thèse a démontré que les simulations numériques qui ne prennent pas en compte le CFB produisent des LCE sur-énergisés et à très longue durée de vie, et modifient les propriétés thermiques de ces tourbillons. Ce pose ainsi la question de l'impact net de ce couplage mécanique sur l'équilibre thermique du GdM, qui combine très certainement des effets locaux (via les flux de chaleurs turbulents), et des effets non locaux (transport de chaleur par les LCEs). Cette question pourrait être abordée en comparant, à partir des observations et des expériences numériques NOCF et CF, les différentes contributions au bilan de chaleur du GdM.

### Apport de futures données satellites

Les produits satellitaires existants ne permettent pas de caractériser avec précision les courants de surface, la réponse de la tension de vent au CFB et le travail du vent (Renault et al., 2017a). Les futures missions satellitaires telles que SWOT (Morrow et al., 2019) permettront de mesurer les courants géostrophiques avec une meilleure résolution spatiale que les observations

actuelles. Cela nous permettra de mieux comprendre la contribution géostrophique, par exemple, des interactions tourbillons cycloniques-LC associées au détachement des LCEs et à la production de jets frontaux.

Cependant, des mesures cohérentes du courant total et de la contrainte de surface feront toujours défaut. Les futurs projets de missions satellitaires tels que Odysea (Ocean Dynamical Surface Exchange with Atmosphere; Bourassa et al., 2016; Rodríguez et al., 2019) devraient permettre de surmonter ce problème, en aidant à mieux caractériser le travail du vent, les interactions air-mer, les chemins d'énergie dans l'océan et, plus généralement, à mieux contraindre et valider les modèles numériques.

### **Activité mésoéchelle sur la rétroflexion du courant Nord Brésilien et sur la Mer des Caraïbes**

Comme le LC, le courant Nord Brésilien libère de grands tourbillons anticycloniques depuis sa rétroflexion dans le Contre-Courant Nord Equatorial (Huang et al., 2021). Comme l'a démontré Huang et al. (2021), ces tourbillons anticycloniques peuvent pénétrer dans la mer des Caraïbes en traversant les Petites Antilles. L'analyse des observations altimétriques sur une période de 10 ans montre qu'entre 5 et 6 tourbillons anticycloniques sont détachés chaque année (Goni and Johns, 2003). Notre ensemble de simulations sur 24 ans et les observations altimétriques peuvent aider à étudier si le détachement des tourbillons du courant Nord Brésilien est sensible au CFB, et si oui, comment ces tourbillons peuvent modifier l'activité mésoéchelle dans la Mer des Caraïbes.

### **Le rôle des rétroactions des vagues dans la détermination de la dynamique du GdM**

Comme mentionné dans le chapitre 1, les vagues pourraient moduler le CFB en modifiant la tension du vent. Les vagues sont reliées au calcul de la tension du vent de deux manières principales : elles modifient la rugosité de la surface de l'océan (contrôlée par le paramètre de Charnock) et modifient la tension de vent ressentie par l'océan en tenant compte de la partie consommée pour générer des vagues. Afin de comprendre comment la modulation de la rugosité de surface par les vagues influence la dynamique océanique régionale, nous avons réalisé une simulation couplée océan-vagues-atmosphère sur 22 ans en ne considérant qu'une seule boucle de couplage : la modification de la rugosité estimée par le paramètre de Charnock à partir d'un modèle de vagues.

Comme résultat préliminaire, une comparaison de l'EKE sur la Mer Intra-Américaine entre AVISO, CF, et cette dernière expérience qui inclut le WFB (WF) est montrée dans la Figure 6.9. De manière surprenante, la comparaison ne montre pas de différence significative entre CF et WF. Nous prévoyons d'analyser le budget EKE, l'extension LC et les détachements de LCE pour évaluer dans quelle mesure les puits d'énergie induits par la CFB et la dynamique du GoM sont sensibles au WFB.

L'étape suivante consistera à effectuer des simulations supplémentaires en considérant, *e.g.*, la partie de la contrainte consommée par la génération de la vague, la dérive de Stokes dans l'équation de la quantité de mouvement, et la turbulence induite par les vagues dans la couche de mélange.

# Bibliography

- Abolfazli, E., Liang, J.H., Fan, Y., Chen, Q.J., Walker, N.D., Liu, J., 2020. Surface gravity waves and their role in ocean-atmosphere coupling in the gulf of mexico. *Journal of Geophysical Research: Oceans* 125. URL: <https://doi.org/10.1029/2018jc014820>, doi:10.1029/2018jc014820.
- Aluie, H., Hecht, M., Vallis, G.K., 2018. Mapping the energy cascade in the north atlantic ocean: The coarse-graining approach. *Journal of Physical Oceanography* 48, 225–244. URL: <https://doi.org/10.1175/jpo-d-17-0100.1>, doi:10.1175/jpo-d-17-0100.1.
- Amores, A., Jordà, G., Arsouze, T., Le Sommer, J., 2018. Up to what extent can we characterize ocean eddies using present-day gridded altimetric products? *Journal of Geophysical Research: Oceans* 123, 7220–7236.
- Andrade-Canto, F., Beron-Vera, F.J., Goni, G.J., Karrasch, D., Olascoaga, M.J., Triñanes, J., 2022. Carriers of isargassum/i and mechanism for coastal inundation in the caribbean sea. *Physics of Fluids* 34, 016602. URL: <https://doi.org/10.1063/5.0079055>, doi:10.1063/5.0079055.
- Appendini, C.M., Torres-Freyermuth, A., Salles, P., López-González, J., Mendoza, E.T., 2014. Wave climate and trends for the gulf of mexico: A 30-yr wave hindcast. *Journal of Climate* 27, 1619–1632. URL: <https://doi.org/10.1175/jcli-d-13-00206.1>, doi:10.1175/jcli-d-13-00206.1.
- Archer, M.R., Li, Z., Fu, L.L., 2020. Increasing the space–time resolution of mapped sea surface height from altimetry. *Journal of Geophysical Research: Oceans* 125. URL: <https://doi.org/10.1029/2019jc015878>, doi:10.1029/2019jc015878.
- Ardhuin, F., Rogers, E., Babanin, A.V., Filipot, J.F., Magne, R., Roland, A., Van Der Westhuysen, A., Queffeuilou, P., Lefevre, J.M., Aouf, L., et al., 2010. Semiempirical dissipation source functions for ocean waves. part i: Definition, calibration, and validation. *Journal of Physical Oceanography* 40, 1917–1941.
- Athié, G., Candela, J., Ochoa, J., Sheinbaum, J., 2012. Impact of caribbean cyclones on the detachment of loop current anticyclones. *Journal of Geophysical Research: Oceans* 117, n/a–n/a. URL: <https://doi.org/10.1029/2011jc007090>, doi:10.1029/2011jc007090.
- Athié, G., Sheinbaum, J., Candela, J., Ochoa, J., Pérez-Brunius, P., Romero-Arteaga, A., 2020. Seasonal variability of the transport through the yucatan channel from observations. *Journal of Physical Oceanography* 50, 343–360. URL: <https://doi.org/10.1175/jpo-d-18-0269.1>, doi:10.1175/jpo-d-18-0269.1.
- Athié, G., Sheinbaum, J., Leben, R., Ochoa, J., Shannon, M.R., Candela, J., 2015. Interannual variability in the yucatan channel flow. *Geophysical Research Letters* 42, 1496–1503. URL: <https://doi.org/10.1002/2014gl062674>, doi:10.1002/2014gl062674.

- Banzon, V., Smith, T.M., Chin, T.M., Liu, C., Hankins, W., 2016. A long-term record of blended satellite and in situ sea-surface temperature for climate monitoring, modeling and environmental studies. *Earth System Science Data* 8, 165–176. URL: <https://essd.copernicus.org/articles/8/165/2016/>, doi:10.5194/essd-8-165-2016.
- Barkan, R., Molemaker, M.J., Srinivasan, K., McWilliams, J.C., D’Asaro, E.A., 2019. The role of horizontal divergence in submesoscale frontogenesis. *Journal of Physical Oceanography* 49, 1593–1618. URL: <https://doi.org/10.1175/jpo-d-18-0162.1>, doi:10.1175/jpo-d-18-0162.1.
- Bayr, T., Latif, M., 2022. ENSO atmospheric feedbacks under global warming and their relation to mean-state changes. *Climate Dynamics* URL: <https://doi.org/10.1007/s00382-022-06454-3>, doi:10.1007/s00382-022-06454-3.
- Belcher, S.E., Grant, A.L.M., Hanley, K.E., Fox-Kemper, B., Van Roekel, L., Sullivan, P.P., Large, W.G., Brown, A., Hines, A., Calvert, D., Rutgersson, A., Pettersson, H., Bidlot, J.R., Janssen, P.A.E.M., Polton, J.A., 2012. A global perspective on Langmuir turbulence in the ocean surface boundary layer. *Geophysical Research Letters* 39.
- Bishop, S.P., Small, R.J., Bryan, F.O., 2020. The global sink of available potential energy by mesoscale air-sea interaction. *Journal of Advances in Modeling Earth Systems* 12. URL: <https://doi.org/10.1029/2020ms002118>, doi:10.1029/2020ms002118.
- Bourassa, M.A., Rodriguez, E., Chelton, D., 2016. Winds and currents mission: Ability to observe mesoscale AIR/SEA coupling, in: 2016 IEEE International Geoscience and Remote Sensing Symposium (IGARSS), IEEE. URL: <https://doi.org/10.1109/igarss.2016.7730928>, doi:10.1109/igarss.2016.7730928.
- Breivik, Ø., Mogensen, K., Bidlot, J.R., Balmaseda, M.A., Janssen, P.A.E.M., 2015. Surface wave effects in the NEMO ocean model: Forced and coupled experiments. *Journal of Geophysical Research: Oceans* 120, 2973–2992. URL: <https://doi.org/10.1002/2014jc010565>, doi:10.1002/2014jc010565.
- Bromirski, P.D., Kossin, J.P., 2008. Increasing hurricane wave power along the u.s. atlantic and gulf coasts. *Journal of Geophysical Research* 113. URL: <https://doi.org/10.1029/2007jc004706>, doi:10.1029/2007jc004706.
- Bye, J.A., 1985. Chapter 6 large-scale momentum exchange in the coupled atmosphere-ocean, in: Elsevier oceanography series. Elsevier, pp. 51–61. URL: [https://doi.org/10.1016/s0422-9894\(08\)70702-5](https://doi.org/10.1016/s0422-9894(08)70702-5), doi:10.1016/s0422-9894(08)70702-5.
- Candela, J., Ochoa, J., Sheinbaum, J., López, M., Pérez-Brunius, P., Tenreiro, M., Pallàs-Sanz, E., Athié, G., Arriaza-Oliveros, L., 2019. The flow through the gulf of mexico. *Journal of Physical Oceanography* 49, 1381–1401. URL: <https://doi.org/10.1175/jpo-d-18-0189.1>, doi:10.1175/jpo-d-18-0189.1.
- Candela, J., Sheinbaum, J., Ochoa, J., Badan, A., Leben, R., 2002. The potential vorticity flux through the yucatan channel and the loop current in the gulf of mexico. *Geophysical*

- Research Letters 29, 16–1–16–4. URL: <https://doi.org/10.1029/2002gl015587>, doi:10.1029/2002gl015587.
- Capet, X., McWilliams, J.C., Molemaker, M.J., Shchepetkin, A.F., 2008. Mesoscale to sub-mesoscale transition in the california current system. part II: Frontal processes. *Journal of Physical Oceanography* 38, 44–64. URL: <https://doi.org/10.1175/2007jpo3672.1>, doi:10.1175/2007jpo3672.1.
- Chaigneau, A., Eldin, G., Dewitte, B., 2009. Eddy activity in the four major upwelling systems from satellite altimetry (1992–2007). *Progress in Oceanography* 83, 117–123.
- Chang, Y.L., Oey, L.Y., 2010. Why can wind delay the shedding of loop current eddies? *Journal of Physical Oceanography* 40, 2481–2495.
- Chang, Y.L., Oey, L.Y., 2012. Why does the loop current tend to shed more eddies in summer and winter? *Geophysical Research Letters* 39.
- Chang, Y.L., Oey, L.Y., 2013. Loop current growth and eddy shedding using models and observations: Numerical process experiments and satellite altimetry data. *Journal of Physical Oceanography* 43, 669–689. URL: <https://doi.org/10.1175/jpo-d-12-0139.1>, doi:10.1175/jpo-d-12-0139.1.
- Chassignet, E.P., Xu, X., 2017. Impact of horizontal resolution ( $1/12^\circ$  to  $1/50^\circ$ ) on gulf stream separation, penetration, and variability. *Journal of Physical Oceanography* 47, 1999–2021. URL: <https://doi.org/10.1175/jpo-d-17-0031.1>, doi:10.1175/jpo-d-17-0031.1.
- Chelton, D.B., 2004. Satellite measurements reveal persistent small-scale features in ocean winds. *Science* 303, 978–983. URL: <https://doi.org/10.1126/science.1091901>, doi:10.1126/science.1091901.
- Chelton, D.B., Esbensen, S.K., Schlax, M.G., Thum, N., Freilich, M.H., Wentz, F.J., Gentemann, C.L., McPhaden, M.J., Schopf, P.S., 2001. Observations of coupling between surface wind stress and sea surface temperature in the eastern tropical pacific. *Journal of Climate* 14, 1479–1498. URL: [https://doi.org/10.1175/1520-0442\(2001\)014<1479:ooCBSW>2.0.CO;2](https://doi.org/10.1175/1520-0442(2001)014<1479:ooCBSW>2.0.CO;2), doi:10.1175/1520-0442(2001)014<1479:ooCBSW>2.0.CO;2.
- Chelton, D.B., Schlax, M.G., Samelson, R.M., 2007. Summertime coupling between sea surface temperature and wind stress in the california current system. *Journal of Physical Oceanography* 37, 495–517. URL: <https://doi.org/10.1175/jpo3025.1>, doi:10.1175/jpo3025.1.
- Chelton, D.B., Schlax, M.G., Samelson, R.M., 2011. Global observations of nonlinear mesoscale eddies. *Progress in Oceanography* 91, 167–216. URL: <https://www.sciencedirect.com/science/article/pii/S0079661111000036>, doi:<https://doi.org/10.1016/j.pocean.2011.01.002>.
- Chen, F., Dudhia, J., 2001. Coupling an advanced land surface–hydrology model with the penn state–near mm5 modeling system. part i: Model implementation and sensitivity. *Monthly weather review* 129, 569–585.

- Chérubin, L.M., Morel, Y., Chassignet, E.P., 2006. Loop current ring shedding: The formation of cyclones and the effect of topography. *Journal of Physical Oceanography* 36, 569–591. URL: <https://doi.org/10.1175/jpo2871.1>, doi:10.1175/jpo2871.1.
- Chune, S.L., Aouf, L., 2018. Wave effects in global ocean modeling: parametrizations vs. forcing from a wave model. *Ocean Dynamics* 68, 1739–1758. URL: <https://doi.org/10.1007/s10236-018-1220-2>, doi:10.1007/s10236-018-1220-2.
- CMEMS, 2017. The ssalto/duacs altimeter products were produced and distributed by the copernicus marine and environment monitoring service. URL: <https://www.avisio.altimetry.fr/>, doi:<https://www.avisio.altimetry.fr/>.
- Cochrane, J., 1972. Separation of an anticyclone and subsequent developments in the loop current (1969). *Contributions on the Physical Oceanography of the Gulf of Mexico* 2, 91–106.
- Contreras, M., Renault, L., Marchesiello, P., 2022. Understanding energy pathways in the gulf stream. *Journal of Physical Oceanography* URL: <https://doi.org/10.1175/jpo-d-22-0146.1>, doi:10.1175/jpo-d-22-0146.1.
- Cooper, C., Forristall, G.Z., Joyce, T.M., 1990. Velocity and hydrographic structure of two gulf of mexico warm-core rings. *Journal of Geophysical Research* 95, 1663. URL: <https://doi.org/10.1029/jc095ic02p01663>, doi:10.1029/jc095ic02p01663.
- Coronado, C., Candela, J., Iglesias-Prieto, R., Sheinbaum, J., López, M., Ocampo-Torres, F.J., 2007. On the circulation in the puerto morelos fringing reef lagoon. *Coral Reefs* 26, 149–163. URL: <https://doi.org/10.1007/s00338-006-0175-9>, doi:10.1007/s00338-006-0175-9.
- Couvelard, X., Lemarié, F., Samson, G., Redelsperger, J.L., Arduin, F., Benshila, R., Madec, G., 2020. Development of a two-way-coupled ocean–wave model: assessment on a global nemo(v3.6)–ww3(v6.02) coupled configuration. *Geoscientific Model Development* 13, 3067–3090. URL: <https://gmd.copernicus.org/articles/13/3067/2020/>, doi:10.5194/gmd-13-3067-2020.
- Craik, A.D.D., Leibovich, S., 1976. A rational model for langmuir circulations. *Journal of Fluid Mechanics* 73, 401. URL: <https://doi.org/10.1017/s0022112076001420>, doi:10.1017/s0022112076001420.
- Damien, P., Sheinbaum, J., Pasqueron de Fommervault, O., Jouanno, J., Linacre, L., Duteil, O., 2021. Do loop current eddies stimulate productivity in the gulf of mexico? *Biogeosciences Discussions* , 1–52.
- Donelan, M.A., Dobson, F.W., Smith, S.D., Anderson, R.J., 1993. On the dependence of sea surface roughness on wave development. *Journal of Physical Oceanography* 23, 2143–2149. URL: [https://doi.org/10.1175/1520-0485\(1993\)023<2143:otdoss>2.0.co;2](https://doi.org/10.1175/1520-0485(1993)023<2143:otdoss>2.0.co;2), doi:10.1175/1520-0485(1993)023<2143:otdoss>2.0.co;2.

- Donohue, K., Watts, D., Hamilton, P., Leben, R., Kennelly, M., 2016. Loop current eddy formation and baroclinic instability. *Dynamics of Atmospheres and Oceans* 76, 195–216. URL: <https://doi.org/10.1016/j.dynatmoce.2016.01.004>, doi:10.1016/j.dynatmoce.2016.01.004.
- Drennan, W.M., 2003. On the wave age dependence of wind stress over pure wind seas. *Journal of Geophysical Research* 108. URL: <https://doi.org/10.1029/2000jc000715>, doi:10.1029/2000jc000715.
- Duhaut, T.H.A., Straub, D.N., 2006. Wind stress dependence on ocean surface velocity: Implications for mechanical energy input to ocean circulation. *Journal of Physical Oceanography* 36, 202 – 211. URL: <https://journals.ametsoc.org/view/journals/phoc/36/2/jpo2842.1.xml>, doi:10.1175/JP02842.1.
- Dussin, R., Barnier, B., Brodeau, L., Molines, J.M., 2016. The making of the drakkar forcing set dfs5. *DRAKKAR/MyOcean Rep* 104, 16.
- Elliott, B.A., 1982. Anticyclonic rings in the gulf of mexico. *Journal of Physical Oceanography* 12, 1292–1309. URL: [https://doi.org/10.1175/1520-0485\(1982\)012<1292:aritgo>2.0.co;2](https://doi.org/10.1175/1520-0485(1982)012<1292:aritgo>2.0.co;2), doi:10.1175/1520-0485(1982)012<1292:aritgo>2.0.co;2.
- Eyring, V., Cox, P.M., Flato, G.M., Gleckler, P.J., Abramowitz, G., Caldwell, P., Collins, W.D., Gier, B.K., Hall, A.D., Hoffman, F.M., Hurtt, G.C., Jahn, A., Jones, C.D., Klein, S.A., Krasting, J.P., Kwiatkowski, L., Lorenz, R., Maloney, E., Meehl, G.A., Pendergrass, A.G., Pincus, R., Ruane, A.C., Russell, J.L., Sanderson, B.M., Santer, B.D., Sherwood, S.C., Simpson, I.R., Stouffer, R.J., Williamson, M.S., 2019. Taking climate model evaluation to the next level. *Nature Climate Change* 9, 102–110. URL: <https://doi.org/10.1038/s41558-018-0355-y>, doi:10.1038/s41558-018-0355-y.
- Fairall, C.W., Bradley, E.F., Hare, J.E., Grachev, A.A., Edson, J.B., 2003. Bulk parameterization of air–sea fluxes: Updates and verification for the COARE algorithm. *Journal of Climate* 16, 571–591. URL: [https://doi.org/10.1175/1520-0442\(2003\)016<0571:bpoasf>2.0.co;2](https://doi.org/10.1175/1520-0442(2003)016<0571:bpoasf>2.0.co;2), doi:10.1175/1520-0442(2003)016<0571:bpoasf>2.0.co;2.
- Forristall, G.Z., Schaudt, K.J., Cooper, C.K., 1992. Evolution and kinematics of a loop current eddy in the gulf of mexico during 1985. *Journal of Geophysical Research* 97, 2173. URL: <https://doi.org/10.1029/91jc02905>, doi:10.1029/91jc02905.
- Fratantoni, P.S., Lee, T.N., Podesta, G.P., Muller-Karger, F., 1998. The influence of loop current perturbations on the formation and evolution of tortugas eddies in the southern straits of florida. *Journal of Geophysical Research: Oceans* 103, 24759–24779. URL: <https://doi.org/10.1029/98jc02147>, doi:10.1029/98jc02147.
- Frenger, I., Gruber, N., Knutti, R., Münnich, M., 2013. Imprint of southern ocean eddies on winds, clouds and rainfall. *Nature geoscience* 6, 608–612.
- Garcia-Jove, M., , Sheinbaum, J., Jouanno, J., and, 2016. Sensitivity of loop current metrics and eddy detachments to different model configurations: The impact of topography and

- caribbean perturbations. *Atmósfera* 29, 235–265. URL: <https://doi.org/10.20937/atm.2016.29.03.05>, doi:10.20937/atm.2016.29.03.05.
- García-Jove, M., 2016. Origen de las perturbaciones y caracterización de la variabilidad de mesoescala de la Corriente de Lazo en el Golfo de México. Ph.D. thesis. Centro de Investigación Científica y de Educación Superior de Ensenada, Baja California.
- García-Nava, H., Ocampo-Torres, F.J., Osuna, P., Donelan, M.A., 2009. Wind stress in the presence of swell under moderate to strong wind conditions. *Journal of Geophysical Research* 114. URL: <https://doi.org/10.1029/2009jc005389>, doi:10.1029/2009jc005389.
- Germano, M., 1992. Turbulence: the filtering approach. *Journal of Fluid Mechanics* 238, 325–336. URL: <https://doi.org/10.1017/s0022112092001733>, doi:10.1017/s0022112092001733.
- Gévaudan, M., Jouanno, J., Durand, F., Morvan, G., Renault, L., Samson, G., 2021. Influence of ocean salinity stratification on the tropical atlantic ocean surface. *Climate Dynamics* URL: <https://doi.org/10.1007/s00382-021-05713-z>, doi:10.1007/s00382-021-05713-z.
- Goni, G.J., Johns, W.E., 2003. Synoptic study of warm rings in the north brazil current retroflection region using satellite altimetry, in: *Interhemispheric Water Exchange in the Atlantic Ocean*. Elsevier, pp. 335–356. URL: [https://doi.org/10.1016/s0422-9894\(03\)80153-8](https://doi.org/10.1016/s0422-9894(03)80153-8), doi:10.1016/s0422-9894(03)80153-8.
- González-Ramírez, J., , and, A.P.S., 2019. Streamflow modeling of five major rivers that flow into the gulf of mexico using SWAT. *Atmósfera* 32, 261–272. URL: <https://doi.org/10.20937/atm.2019.32.04.01>, doi:10.20937/atm.2019.32.04.01.
- Goolsby, D.A., Battaglin, W.A., Lawrence, G.B., Artz, R.S., Aulenbach, B.T., Hooper, R.P., Keeney, D.R., Stensland, G.J., 1999. Flux and sources of nutrients in the Mississippi-Atchafalaya River Basin. Technical Report. National Oceanic and Atmospheric Administration National Ocean Service . . . .
- Gower, J., Hu, C., Borstad, G., King, S., 2006. Ocean color satellites show extensive lines of floating sargassum in the gulf of mexico. *IEEE Transactions on Geoscience and Remote Sensing* 44, 3619–3625. URL: <https://doi.org/10.1109/tgrs.2006.882258>, doi:10.1109/tgrs.2006.882258.
- Guan, C., Xie, L., 2004. On the linear parameterization of drag coefficient over sea surface. *Journal of Physical Oceanography* 34, 2847–2851. URL: <https://doi.org/10.1175/jpo2664.1>, doi:10.1175/jpo2664.1.
- Guilyardi, E., Wittenberg, A., Fedorov, A., Collins, M., Wang, C., Capotondi, A., van Oldenborgh, G.J., Stockdale, T., 2009. Understanding el niño in ocean–atmosphere general circulation models: Progress and challenges. *Bulletin of the American Meteorological Society* 90, 325–340. URL: <https://doi.org/10.1175/2008bams2387.1>, doi:10.1175/2008bams2387.1.

- Gurvan, M., Bourdallé-Badie, R., Chanut, J., Clementi, E., Coward, A., Ethé, C., Iovino, D., Lea, D., Lévy, C., Lovato, T., Martin, N., Masson, S., Mocavero, S., Rousset, C., Storkey, D., Müeller, S., Nurser, G., Bell, M., Samson, G., Mathiot, P., Mele, F., Moulin, A., 2022. Nemo ocean engine. URL: <https://doi.org/10.5281/zenodo.6334656>, doi:10.5281/zenodo.6334656.
- Hall, C.A., Leben, R.R., 2016. Observational evidence of seasonality in the timing of loop current eddy separation. *Dynamics of Atmospheres and Oceans* 76, 240–267. URL: <https://doi.org/10.1016/j.dynatmoce.2016.06.002>, doi:10.1016/j.dynatmoce.2016.06.002.
- Hamlington, P.E., Roedel, L.P.V., Fox-Kemper, B., Julien, K., Chini, G.P., 2014. Langmuir–submesoscale interactions: Descriptive analysis of multiscale frontal spindown simulations. *Journal of Physical Oceanography* 44, 2249–2272. URL: <https://doi.org/10.1175/jpo-d-13-0139.1>, doi:10.1175/jpo-d-13-0139.1.
- Harrison, D., Robinson, A., 1978. Energy analysis of open regions of turbulent flows — mean eddy energetics of a numerical ocean circulation experiment. *Dynamics of Atmospheres and Oceans* 2, 185–211. URL: [https://doi.org/10.1016/0377-0265\(78\)90009-x](https://doi.org/10.1016/0377-0265(78)90009-x), doi:10.1016/0377-0265(78)90009-x.
- Hasselmann, S., Hasselmann, K., Allender, J., Barnett, T., 1985. Computations and parameterizations of the nonlinear energy transfer in a gravity-wave spectrum. part ii: Parameterizations of the nonlinear energy transfer for application in wave models. *Journal of Physical Oceanography* 15, 1378–1391.
- Hauser, D., Tourain, C., Hermozo, L., Alraddawi, D., Aouf, L., Chapron, B., Dalphiné, A., Delaye, L., Dalila, M., Dormy, E., Gouillon, F., Gressani, V., Grouazel, A., Guitton, G., Husson, R., Mironov, A., Mouche, A., Ollivier, A., Oruba, L., Piras, F., Suquet, R.R., Schippers, P., Tison, C., Tran, N., 2021. New observations from the SWIM radar onboard CFOSAT: Instrument validation and ocean wave measurement assessment. *IEEE Transactions on Geoscience and Remote Sensing* 59, 5–26. URL: <https://doi.org/10.1109/tgrs.2020.2994372>, doi:10.1109/tgrs.2020.2994372.
- Hénaff, M.L., Kourafalou, V.H., Dussurget, R., Lumpkin, R., 2014. Cyclonic activity in the eastern gulf of mexico: Characterization from along-track altimetry and in situ drifter trajectories. *Progress in Oceanography* 120, 120–138. URL: <https://doi.org/10.1016/j.pocean.2013.08.002>, doi:10.1016/j.pocean.2013.08.002.
- Hiron, L., Cruz, B.J., Shay, L.K., 2020. Evidence of loop current frontal eddy intensification through local linear and nonlinear interactions with the loop current. *Journal of Geophysical Research: Oceans* 125. URL: <https://doi.org/10.1029/2019jc015533>, doi:10.1029/2019jc015533.
- Holland, G., Done, J., Bruyere, C., Cooper, C.K., Suzuki, A., 2010. Model investigations of the effects of climate variability and change on future gulf of mexico tropical cyclone activity, in: *All Days, OTC*. URL: <https://doi.org/10.4043/20690-ms>, doi:10.4043/20690-ms.

- Hong, S.Y., 2010. A new stable boundary-layer mixing scheme and its impact on the simulated east asian summer monsoon. *Quarterly Journal of the Royal Meteorological Society* 136, 1481–1496.
- Hong, S.Y., Lim, J.O.J., 2006. The wrf single-moment 6-class microphysics scheme (wsm6). *J. Korean Meteor. Soc.* 42, 129–151.
- Hong, S.Y., Noh, Y., Dudhia, J., 2006. A new vertical diffusion package with an explicit treatment of entrainment processes. *Monthly weather review* 134, 2318–2341.
- Huang, M., Liang, X., Zhu, Y., Liu, Y., Weisberg, R.H., 2021. Eddies connect the tropical atlantic ocean and the gulf of mexico. *Geophysical Research Letters* 48. URL: <https://doi.org/10.1029/2020gl091277>, doi:10.1029/2020gl091277.
- Hughes, C.W., Wilson, C., 2008. Wind work on the geostrophic ocean circulation: An observational study of the effect of small scales in the wind stress. *Journal of Geophysical Research* 113. URL: <https://doi.org/10.1029/2007jc004371>, doi:10.1029/2007jc004371.
- Hurlburt, H.E., 1986. Dynamic transfer of simulated altimeter data into subsurface information by a numerical ocean model. *Journal of Geophysical Research* 91, 2372. URL: <https://doi.org/10.1029/jc091ic02p02372>, doi:10.1029/jc091ic02p02372.
- Hurlburt, H.E., Thompson, J.D., 1980. A numerical study of loop current intrusions and eddy shedding. *Journal of Physical Oceanography* 10, 1611–1651. URL: [https://doi.org/10.1175/1520-0485\(1980\)010<1611:ansolc>2.0.co;2](https://doi.org/10.1175/1520-0485(1980)010<1611:ansolc>2.0.co;2), doi:10.1175/1520-0485(1980)010<1611:ansolc>2.0.co;2.
- Iacono, M.J., Delamere, J.S., Mlawer, E.J., Shephard, M.W., Clough, S.A., Collins, W.D., 2008. Radiative forcing by long-lived greenhouse gases: Calculations with the aer radiative transfer models. *Journal of Geophysical Research: Atmospheres* 113.
- Ichiye, T., 1959. Circulation and water-mass distribution in the gulf of mexico, in: *Journal of Geophysical Research*, AMER GEOPHYSICAL UNION 2000 FLORIDA AVE NW, WASHINGTON, DC 20009. pp. 1109–1110.
- Jaimes, B., Shay, L.K., 2009. Mixed layer cooling in mesoscale oceanic eddies during hurricanes katrina and rita. *Monthly Weather Review* 137, 4188–4207. URL: <https://doi.org/10.1175/2009mwr2849.1>, doi:10.1175/2009mwr2849.1.
- Janssen, P., 2004. *The Interaction of Ocean Waves and Wind*. Cambridge University Press. URL: <https://doi.org/10.1017/cbo9780511525018>, doi:10.1017/cbo9780511525018.
- Jessup, A.T., Zappa, C.J., Loewen, M.R., Hesany, V., 1997. Infrared remote sensing of breaking waves. *Nature* 385, 52–55. URL: <https://doi.org/10.1038/385052a0>, doi:10.1038/385052a0.
- Jouanno, J., Ochoa, J., Pallàs-Sanz, E., Sheinbaum, J., Andrade-Canto, F., Candela, J., Molines, J.M., 2016. Loop current frontal eddies: Formation along the campeche bank and impact of coastally trapped waves. *Journal of Physical Oceanography* 46, 3339–3363. URL: <https://doi.org/10.1175/jpo-d-16-0052.1>, doi:10.1175/jpo-d-16-0052.1.

- Jouanno, J., Pallàs-Sanz, E., Sheinbaum, J., 2018. Variability and dynamics of the yucatan upwelling: High-resolution simulations. *Journal of Geophysical Research: Oceans* 123, 1251–1262. URL: <https://doi.org/10.1002/2017jc013535>, doi:10.1002/2017jc013535.
- Jouanno, J., Sheinbaum, J., 2013. Heat balance and eddies in the caribbean upwelling system. *Journal of Physical Oceanography* 43, 1004–1014. URL: <https://doi.org/10.1175/jpo-d-12-0140.1>, doi:10.1175/jpo-d-12-0140.1.
- Jouanno, J., Sheinbaum, J., Barnier, B., Molines, J.M., Candela, J., 2012. Seasonal and interannual modulation of the eddy kinetic energy in the caribbean sea. *Journal of Physical Oceanography* 42, 2041–2055. URL: <https://doi.org/10.1175/jpo-d-12-048.1>, doi:10.1175/jpo-d-12-048.1.
- Jüling, A., Viebahn, J.P., Drijfhout, S.S., Dijkstra, H.A., 2018. Energetics of the southern ocean mode. *Journal of Geophysical Research: Oceans* 123, 9283–9304. URL: <https://doi.org/10.1029/2018jc014191>, doi:10.1029/2018jc014191.
- Jullien, S., Masson, S., Oerder, V., Samson, G., Colas, F., Renault, L., 2020. Impact of ocean–atmosphere current feedback on ocean mesoscale activity: Regional variations and sensitivity to model resolution. *Journal of Climate* 33, 2585–2602. URL: <https://doi.org/10.1175/jcli-d-19-0484.1>, doi:10.1175/jcli-d-19-0484.1.
- Kantha, L., 2014. Empirical models of the loop current eddy detachment/separation time in the gulf of mexico. *Journal of Waterway, Port, Coastal, and Ocean Engineering* 140. URL: [https://doi.org/10.1061/\(asce\)ww.1943-5460.0000220](https://doi.org/10.1061/(asce)ww.1943-5460.0000220), doi:10.1061/(asce)ww.1943-5460.0000220.
- Kelly, K.A., Dickinson, S., McPhaden, M.J., Johnson, G.C., 2001. Ocean currents evident in satellite wind data. *Geophysical Research Letters* 28, 2469–2472. URL: <https://doi.org/10.1029/2000g1012610>, doi:10.1029/2000g1012610.
- Komen, G.J., Cavaleri, L., Donelan, M., Hasselmann, K., Hasselmann, S., Janssen, P., 1994. Dynamics and modelling of ocean waves. Cambridge University Press, Cambridge.
- Kostka, J.E., Prakash, O., Overholt, W.A., Green, S.J., Freyer, G., Canion, A., Delgardio, J., Norton, N., Hazen, T.C., Huettel, M., 2011. Hydrocarbon-degrading bacteria and the bacterial community response in gulf of mexico beach sands impacted by the deepwater horizon oil spill. *Applied and Environmental Microbiology* 77, 7962–7974. URL: <https://doi.org/10.1128/aem.05402-11>, doi:10.1128/aem.05402-11.
- Kurczyn, J.A., Appendini, C.M., Beier, E., Sosa-López, A., López-González, J., Posada-Vanegas, G., 2020. Oceanic and atmospheric impact of central american cold surges ( inortes/i ) in the gulf of mexico. *International Journal of Climatology* 41. URL: <https://doi.org/10.1002/joc.6779>, doi:10.1002/joc.6779.
- Langmuir, I., 1938. Surface motion of water induced by wind. *Science* 87, 119–123. URL: <https://doi.org/10.1126/science.87.2250.119>, doi:10.1126/science.87.2250.119.

- Large, W.G., Pond, S., 1981. Open ocean momentum flux measurements in moderate to strong winds. *Journal of Physical Oceanography* 11, 324–336. URL: [https://doi.org/10.1175/1520-0485\(1981\)011<0324:oomfmi>2.0.co;2](https://doi.org/10.1175/1520-0485(1981)011<0324:oomfmi>2.0.co;2), doi:10.1175/1520-0485(1981)011<0324:oomfmi>2.0.co;2.
- Le Hénaff, M., Kourafalou, V.H., Morel, Y., Srinivasan, A., 2012. Simulating the dynamics and intensification of cyclonic loop current frontal eddies in the gulf of mexico. *Journal of Geophysical Research: Oceans* 117, n/a–n/a. URL: <https://doi.org/10.1029/2011jc007279>, doi:10.1029/2011jc007279.
- Leben, R.R., 2005. Altimeter-derived loop current metrics. *Geophysical Monograph-American Geophysical Union* 161, 181.
- Leben, R.R., Hall, C.A., 2012. Poster: A 34-year record of loop current eddy separation events, in: OSTST, Venice.
- Leibovich, S., 1983. The form and dynamics of langmuir circulations. *Annual Review of Fluid Mechanics* 15, 391–427. URL: <https://doi.org/10.1146/annurev.fl.15.010183.002135>, doi:10.1146/annurev.fl.15.010183.002135.
- Lellouche, J.M., Greiner, E., Galloudec, O.L., Garric, G., Regnier, C., Drevillon, M., Benkiran, M., Testut, C.E., Bourdalle-Badie, R., Gasparin, F., Hernandez, O., Levier, B., Drillet, Y., Remy, E., Traon, P.Y.L., 2018. Recent updates to the copernicus marine service global ocean monitoring and forecasting real-time 1/12° high-resolution system. *Ocean Science* 14, 1093–1126. URL: <https://doi.org/10.5194/os-14-1093-2018>, doi:10.5194/os-14-1093-2018.
- Leonard, A., 1975. Energy cascade in large-eddy simulations of turbulent fluid flows, in: *Turbulent Diffusion in Environmental Pollution, Proceedings of a Symposium held at Charlottesville*. Elsevier, pp. 237–248. URL: [https://doi.org/10.1016/s0065-2687\(08\)60464-1](https://doi.org/10.1016/s0065-2687(08)60464-1), doi:10.1016/s0065-2687(08)60464-1.
- Lewis, D., Belcher, S., 2004. Time-dependent, coupled, ekman boundary layer solutions incorporating stokes drift. *Dynamics of Atmospheres and Oceans* 37, 313–351. URL: <https://doi.org/10.1016/j.dynatmoce.2003.11.001>, doi:10.1016/j.dynatmoce.2003.11.001.
- Li, H., Misra, V., 2014. Thirty-two-year ocean–atmosphere coupled downscaling of global reanalysis over the intra-american seas. *Climate Dynamics* 43, 2471–2489. URL: <https://doi.org/10.1007/s00382-014-2069-9>, doi:10.1007/s00382-014-2069-9.
- Lin, Y., Greatbatch, R.J., Sheng, J., 2010. The influence of gulf of mexico loop current intrusion on the transport of the florida current. *Ocean Dynamics* 60, 1075–1084. URL: <https://doi.org/10.1007/s10236-010-0308-0>, doi:10.1007/s10236-010-0308-0.
- López-Álzate, M.E., Sayol, J.M., Hernández-Carrasco, I., Osorio, A.F., Mason, E., Orfila, A., 2022. Mesoscale eddy variability in the caribbean sea. *Ocean Dynamics* URL: <https://doi.org/10.1007/s10236-022-01525-9>, doi:10.1007/s10236-022-01525-9.

- Luo, J.J., Masson, S., Roeckner, E., Madec, G., Yamagata, T., 2005. Reducing climatology bias in an ocean–atmosphere cgm with improved coupling physics. *Journal of Climate* 18, 2344 – 2360. URL: <https://journals.ametsoc.org/view/journals/clim/18/13/jcli3404.1.xml>, doi:10.1175/JCLI3404.1.
- Madec, G., Delecluse, P., Imbard, M., Levy, C., 1997. Ocean general circulation model reference manual. Note du Pôle de modélisation .
- Marchesiello, P., McWilliams, J.C., Shchepetkin, A., 2003. Equilibrium structure and dynamics of the california current system. *Journal of physical Oceanography* 33, 753–783.
- McClean, J.L., Bader, D.C., Bryan, F.O., Maltrud, M.E., Dennis, J.M., Mirin, A.A., Jones, P.W., Kim, Y.Y., Ivanova, D.P., Vertenstein, M., Boyle, J.S., Jacob, R.L., Norton, N., Craig, A., Worley, P.H., 2011. A prototype two-decade fully-coupled fine-resolution CCSM simulation. *Ocean Modelling* 39, 10–30. URL: <https://doi.org/10.1016/j.ocemod.2011.02.011>, doi:10.1016/j.ocemod.2011.02.011.
- McKinney, L.D., Shepherd, J.G., Wilson, C.A., Hogarth, W.T., Chanton, J., Murawski, S.A., Sandifer, P.A., Sutton, T., Yoskowitz, D., Wowk, K., et al., 2021. The gulf of mexico. *Oceanography* 34, 30–43.
- Melville, W.K., 1996. The role of surface-wave breaking in air-sea interaction. *Annual Review of Fluid Mechanics* 28, 279–321. URL: <https://doi.org/10.1146/annurev.fl.28.010196.001431>, doi:10.1146/annurev.fl.28.010196.001431.
- Melville, W.K., Matusov, P., 2002. Distribution of breaking waves at the ocean surface. *Nature* 417, 58–63. URL: <https://doi.org/10.1038/417058a>, doi:10.1038/417058a.
- Meunier, T., Pallás-Sanz, E., Tenreiro, M., Portela, E., Ochoa, J., Ruiz-Angulo, A., Cusí, S., 2018. The vertical structure of a loop current eddy. *Journal of Geophysical Research: Oceans* 123, 6070–6090. URL: <https://doi.org/10.1029/2018jc013801>, doi:10.1029/2018jc013801.
- Meunier, T., Pérez-Brunius, P., Bower, A., 2022. Reconstructing the three-dimensional structure of loop current rings from satellite altimetry and in situ data using the gravest empirical modes method. *Remote Sensing* 14, 4174. URL: <https://doi.org/10.3390/rs14174174>, doi:10.3390/rs14174174.
- Meunier, T., Sanz, E.P., de Marez, C., Pérez, J., Tenreiro, M., Angulo, A.R., Bower, A., 2021. The dynamical structure of a warm core ring as inferred from glider observations and along-track altimetry. *Remote Sensing* 13, 2456. URL: <https://doi.org/10.3390/rs13132456>, doi:10.3390/rs13132456.
- Meunier, T., Sheinbaum, J., Pallàs-Sanz, E., Tenreiro, M., Ochoa, J., Ruiz-Angulo, A., Carton, X., de Marez, C., 2020. Heat content anomaly and decay of warm-core rings: the case of the gulf of mexico. *Geophysical Research Letters* 47. URL: <https://doi.org/10.1029/2019g1085600>, doi:10.1029/2019g1085600.

- Michel, J., Owens, E.H., Zengel, S., Graham, A., Nixon, Z., Allard, T., Holton, W., Reimer, P.D., Lamarche, A., White, M., Rutherford, N., Childs, C., Mauseth, G., Challenger, G., Taylor, E., 2013. Extent and degree of shoreline oiling: Deepwater horizon oil spill, gulf of mexico, USA. *PLoS ONE* 8, e65087. URL: <https://doi.org/10.1371/journal.pone.0065087>, doi:10.1371/journal.pone.0065087.
- Mildner, T.C., Eden, C., Czeschel, L., 2013. Revisiting the relationship between loop current rings and florida current transport variability. *Journal of Geophysical Research: Oceans* 118, 6648–6657. URL: <https://doi.org/10.1002/2013jc009109>, doi:10.1002/2013jc009109.
- Mlawer, E.J., Taubman, S.J., Brown, P.D., Iacono, M.J., Clough, S.A., 1997. Radiative transfer for inhomogeneous atmospheres: Rrtm, a validated correlated-k model for the longwave. *Journal of Geophysical Research: Atmospheres* 102, 16663–16682.
- MOLEMAKER, M.J., MCWILLIAMS, J.C., CAPET, X., 2010. Balanced and unbalanced routes to dissipation in an equilibrated eady flow. *Journal of Fluid Mechanics* 654, 35–63. URL: <https://doi.org/10.1017/s0022112009993272>, doi:10.1017/s0022112009993272.
- Molina, M.J., Timmer, R.P., Allen, J.T., 2016. Importance of the gulf of mexico as a climate driver for u.s. severe thunderstorm activity. *Geophysical Research Letters* 43. URL: <https://doi.org/10.1002/2016gl071603>, doi:10.1002/2016gl071603.
- Morrow, R., Fu, L.L., Arduin, F., Benkiran, M., Chapron, B., Cosme, E., d’Ovidio, F., Farrar, J.T., Gille, S.T., Lapeyre, G., et al., 2019. Global observations of fine-scale ocean surface topography with the surface water and ocean topography (swot) mission. *Frontiers in Marine Science* 6, 1–19.
- Oerder, V., Colas, F., Echevin, V., Masson, S., Hourdin, C., Jullien, S., Madec, G., Lemarié, F., 2016. Mesoscale SST–wind stress coupling in the peru–chile current system: Which mechanisms drive its seasonal variability? *Climate Dynamics* 47, 2309–2330. URL: <https://doi.org/10.1007/s00382-015-2965-7>, doi:10.1007/s00382-015-2965-7.
- Oerder, V., Colas, F., Echevin, V., Masson, S., Lemarié, F., 2018. Impacts of the mesoscale ocean-atmosphere coupling on the peru-chile ocean dynamics: The current-induced wind stress modulation. *Journal of Geophysical Research: Oceans* 123, 812–833. URL: <https://doi.org/10.1002/2017jc013294>, doi:10.1002/2017jc013294.
- Oey, L.Y., 2008. Loop current and deep eddies. *Journal of Physical Oceanography* 38, 1426–1449. URL: <https://doi.org/10.1175/2007jpo3818.1>, doi:10.1175/2007jpo3818.1.
- Oey, L.Y., Ezer, T., Lee, H.C., 2005. Loop current, rings and related circulation in the gulf of mexico: A review of numerical models and future challenges. *Geophysical Monograph-American Geophysical Union* , 31–56URL: <https://doi.org/10.1029/161gm04>, doi:10.1029/161gm04.

- O'Neill, L.W., Chelton, D.B., Esbensen, S.K., 2012. Covariability of surface wind and stress responses to sea surface temperature fronts. *Journal of Climate* 25, 5916–5942. URL: <https://doi.org/10.1175/jcli-d-11-00230.1>, doi:10.1175/jcli-d-11-00230.1.
- Pacanowski, R.C., 1987. Effect of equatorial currents on surface stress. *Journal of physical oceanography* 17, 833–838. URL: [https://doi.org/10.1175/1520-0485\(1987\)017<0833:eoecos>2.0.co;2](https://doi.org/10.1175/1520-0485(1987)017<0833:eoecos>2.0.co;2), doi:10.1175/1520-0485(1987)017<0833:eoecos>2.0.co;2.
- Paramo, J., Correa, M., Núñez, S., 2011. Evidencias de desacople físico-biológico en el sistema de surgencia en la guajira, caribe colombiano. *Revista de biología marina y oceanografía* 46, 421–430. URL: <https://doi.org/10.4067/s0718-19572011000300011>, doi:10.4067/s0718-19572011000300011.
- Pegliasco, C., Chaigneau, A., Morrow, R., 2015. Main eddy vertical structures observed in the four major eastern boundary upwelling systems. *Journal of Geophysical Research: Oceans* 120, 6008–6033.
- Pérez-Brunius, P., García-Carrillo, P., Dubranna, J., Sheinbaum, J., Candela, J., 2013. Direct observations of the upper layer circulation in the southern gulf of mexico. *Deep Sea Research Part II: Topical Studies in Oceanography* 85, 182–194. URL: <https://doi.org/10.1016/j.dsr2.2012.07.020>, doi:10.1016/j.dsr2.2012.07.020.
- Phillips, M.B., Bonner, T.H., 2015. Occurrence and amount of microplastic ingested by fishes in watersheds of the gulf of mexico. *Marine Pollution Bulletin* 100, 264–269. URL: <https://doi.org/10.1016/j.marpolbul.2015.08.041>, doi:10.1016/j.marpolbul.2015.08.041.
- Pianezze, J., Barthe, C., Bielli, S., Tulet, P., Jullien, S., Cambon, G., Bousquet, O., Claeys, M., Cordier, E., 2018. A new coupled ocean-waves-atmosphere model designed for tropical storm studies: Example of tropical cyclone bejisa (2013-2014) in the south-west indian ocean. *Journal of Advances in Modeling Earth Systems* 10, 801–825. URL: <https://doi.org/10.1002/2017ms001177>, doi:10.1002/2017ms001177.
- Pichevin, T., Nof, D., 1997. The momentum imbalance paradox. *Tellus A* 49, 298–319. URL: <https://doi.org/10.1034/j.1600-0870.1997.t01-1-00009.x>, doi:10.1034/j.1600-0870.1997.t01-1-00009.x.
- Polton, J.A., Lewis, D.M., Belcher, S.E., 2005. The role of wave-induced coriolis–stokes forcing on the wind-driven mixed layer. *Journal of Physical Oceanography* 35, 444–457. URL: <https://doi.org/10.1175/jpo2701.1>, doi:10.1175/jpo2701.1.
- Potter, H., Hsu, C.Y., DiMarco, S.F., 2021. Rapid dissipation of a loop current eddy due to interaction with a severe gulf of mexico hurricane. *Ocean Dynamics* 71, 911–922. URL: <https://doi.org/10.1007/s10236-021-01471-y>, doi:10.1007/s10236-021-01471-y.
- Putrasahan, D.A., Kamenkovich, I., Hénaff, M.L., Kirtman, B.P., 2017. Importance of ocean mesoscale variability for air-sea interactions in the gulf of mexico. *Geophysical Research Letters* 44, 6352–6362. URL: <https://doi.org/10.1002/2017g1072884>, doi:10.1002/2017g1072884.

- Rai, S., Hecht, M., Maltrud, M., Aluie, H., 2021. Scale of oceanic eddy killing by wind from global satellite observations. *Science Advances* 7. URL: <https://doi.org/10.1126/sciadv.abf4920>, doi:10.1126/sciadv.abf4920.
- Raschle, N., Arduin, F., 2009. Drift and mixing under the ocean surface revisited: Stratified conditions and model-data comparisons. *Journal of Geophysical Research* 114. URL: <https://doi.org/10.1029/2007jc004466>, doi:10.1029/2007jc004466.
- Raschle, N., Arduin, F., Terray, E.A., 2006. Drift and mixing under the ocean surface: A coherent one-dimensional description with application to unstratified conditions. *Journal of Geophysical Research* 111.
- Reffray, G., Bourdalle-Badie, R., Calone, C., 2015. Modelling turbulent vertical mixing sensitivity using a 1-d version of nemo. *Geoscientific Model Development* 8, 69–86. URL: <https://gmd.copernicus.org/articles/8/69/2015/>, doi:10.5194/gmd-8-69-2015.
- Renault, L., Arsouze, T., Ballabrera-Poy, J., 2021a. On the influence of the current feedback to the atmosphere on the western mediterranean sea dynamics. *Journal of Geophysical Research: Oceans* 126. URL: <https://doi.org/10.1029/2020jc016664>, doi:10.1029/2020jc016664.
- Renault, L., Marchesiello, P., 2022. Ocean tides can drag the atmosphere and cause tidal winds over broad continental shelves. *Communications Earth & Environment* 3. URL: <https://doi.org/10.1038/s43247-022-00403-y>, doi:10.1038/s43247-022-00403-y.
- Renault, L., Marchesiello, P., Masson, S., McWilliams, J.C., 2019a. Remarkable control of western boundary currents by eddy killing, a mechanical air-sea coupling process. *Geophysical Research Letters* 46, 2743–2751.
- Renault, L., Masson, S., Arsouze, T., Madec, G., McWilliams, J.C., 2020. Recipes for how to force oceanic model dynamics. *Journal of Advances in Modeling Earth Systems* 12. URL: <https://doi.org/10.1029/2019ms001715>, doi:10.1029/2019ms001715.
- Renault, L., Masson, S., Oerder, V., Jullien, S., Colas, F., 2019b. Disentangling the mesoscale ocean-atmosphere interactions. *Journal of Geophysical Research: Oceans* 124, 2164–2178.
- Renault, L., McWilliams, J.C., Gula, J., 2018. Dampening of submesoscale currents by air-sea stress coupling in the californian upwelling system. *Scientific reports* 8, 1–8.
- Renault, L., McWilliams, J.C., Kessouri, F., Jousse, A., Frenzel, H., Chen, R., Deutsch, C., 2021b. Evaluation of high-resolution atmospheric and oceanic simulations of the california current system. *Progress in Oceanography* 195, 102564. URL: <https://doi.org/10.1016/j.pocean.2021.102564>, doi:10.1016/j.pocean.2021.102564.
- Renault, L., McWilliams, J.C., Masson, S., 2017a. Satellite observations of imprint of oceanic current on wind stress by air-sea coupling. *Scientific Reports* 7. URL: <https://doi.org/10.1038/s41598-017-17939-1>, doi:10.1038/s41598-017-17939-1.

- Renault, L., McWilliams, J.C., Penven, P., 2017b. Modulation of the agulhas current retroflection and leakage by oceanic current interaction with the atmosphere in coupled simulations. *Journal of Physical Oceanography* 47, 2077–2100.
- Renault, L., Molemaker, M.J., Gula, J., Masson, S., McWilliams, J.C., 2016a. Control and stabilization of the gulf stream by oceanic current interaction with the atmosphere. *Journal of Physical Oceanography* 46, 3439–3453.
- Renault, L., Molemaker, M.J., McWilliams, J.C., Shchepetkin, A.F., Lemarié, F., Chelton, D., Illig, S., Hall, A., 2016b. Modulation of wind work by oceanic current interaction with the atmosphere. *Journal of Physical Oceanography* 46, 1685–1704.
- Rio, M.H., Mulet, S., Picot, N., 2014. Beyond GOCE for the ocean circulation estimate: Synergetic use of altimetry, gravimetry, and in situ data provides new insight into geostrophic and ekman currents. *Geophysical Research Letters* 41, 8918–8925. URL: <https://doi.org/10.1002/2014gl1061773>, doi:10.1002/2014gl1061773.
- Risien, C.M., Chelton, D.B., 2008. A global climatology of surface wind and wind stress fields from eight years of quikscat scatterometer data. *Journal of Physical Oceanography* 38, 2379–2413.
- Rodi, W., 1979. Turbulence models for environmental problems. Von Karman Inst. for Fluid Dynamics: Prediction Methods for Turbulent Flows .
- Rodríguez, E., Bourassa, M., Chelton, D., Farrar, J.T., Long, D., Perkovic-Martin, D., Samelson, R., 2019. The winds and currents mission concept. *Frontiers in Marine Science* 6. URL: <https://doi.org/10.3389/fmars.2019.00438>, doi:10.3389/fmars.2019.00438.
- Romero-Arteaga, A., de Alegría-Arzaburu, A.R., Rivas, D., Juarez, B., 2022. Nearshore current variations during the passage of cold fronts in NW gulf of mexico. *Continental Shelf Research* 238, 104697. URL: <https://doi.org/10.1016/j.csr.2022.104697>, doi:10.1016/j.csr.2022.104697.
- Rudnick, D.L., Gopalakrishnan, G., Cornuelle, B.D., 2015. Cyclonic eddies in the gulf of mexico: Observations by underwater gliders and simulations by numerical model. *Journal of Physical Oceanography* 45, 313–326. URL: <https://doi.org/10.1175/jpo-d-14-0138.1>, doi:10.1175/jpo-d-14-0138.1.
- Rueda-Roa, D.T., Muller-Karger, F.E., 2013. The southern caribbean upwelling system: Sea surface temperature, wind forcing and chlorophyll concentration patterns. *Deep Sea Research Part I: Oceanographic Research Papers* 78, 102–114. URL: <https://doi.org/10.1016/j.dsr.2013.04.008>, doi:10.1016/j.dsr.2013.04.008.
- Schmitz, W.J., 2005. Cyclones and westward propagation in the shedding of anticyclonic rings from the loop current, in: *Circulation in the Gulf of Mexico: Observations and Models*. American Geophysical Union, pp. 241–261. doi:10.1029/161gm18.
- Schmitz, W.J., McCartney, M.S., 1993. On the north atlantic circulation. *Reviews of Geophysics* 31, 29–49. URL: <https://doi.org/10.1029/92rg02583>, doi:10.1029/92rg02583.

- Schubert, R., Gula, J., Greatbatch, R.J., Baschek, B., Biastoch, A., 2020. The submesoscale kinetic energy cascade: Mesoscale absorption of submesoscale mixed layer eddies and frontal downscale fluxes. *Journal of Physical Oceanography* 50, 2573–2589. URL: <https://doi.org/10.1175/jpo-d-19-0311.1>, doi:10.1175/jpo-d-19-0311.1.
- Scott, R.B., Xu, Y., 2009. An update on the wind power input to the surface geostrophic flow of the world ocean. *Deep Sea Research Part I: Oceanographic Research Papers* 56, 295–304. URL: <https://doi.org/10.1016/j.dsr.2008.09.010>, doi:10.1016/j.dsr.2008.09.010.
- Seo, H., Kwon, Y.O., Joyce, T.M., Ummenhofer, C.C., 2017. On the predominant nonlinear response of the extratropical atmosphere to meridional shifts of the gulf stream. *Journal of Climate* 30, 9679–9702. URL: <https://doi.org/10.1175/jcli-d-16-0707.1>, doi:10.1175/jcli-d-16-0707.1.
- Skamarock, W.C., Klemp, J.B., Dudhia, J., Gill, D.O., Liu, Z., Berner, J., Wang, W., Powers, J.G., Duda, M.G., Barker, D.M., et al., 2019. A description of the advanced research wrf model version 4. National Center for Atmospheric Research: Boulder, CO, USA , 145.
- Small, R., deSzoeko, S., Xie, S., O’Neill, L., Seo, H., Song, Q., Cornillon, P., Spall, M., Minobe, S., 2008. Air–sea interaction over ocean fronts and eddies. *Dynamics of Atmospheres and Oceans* 45, 274–319. URL: <https://doi.org/10.1016/j.dynatmoce.2008.01.001>, doi:10.1016/j.dynatmoce.2008.01.001.
- Smith, S.D., Anderson, R.J., Oost, W.A., Kraan, C., Maat, N., Cosmo, J.D., Katsaros, K.B., Davidson, K.L., Bumke, K., Hasse, L., Chadwick, H.M., 1992. Sea surface wind stress and drag coefficients: The hexos results. *Boundary-Layer Meteorology* 60, 109–142. URL: <https://doi.org/10.1007/bf00122064>, doi:10.1007/bf00122064.
- Sosa-Gutiérrez, R., Pallàs-Sanz, E., Jouanno, J., Chaigneau, A., Candela, J., Tenreiro, M., 2020. Erosion of the subsurface salinity maximum of the loop current eddies from glider observations and a numerical model. *Journal of Geophysical Research: Oceans* 125, e2019JC015397.
- Sturges, W., Blaha, J.P., 1976. A western boundary current in the gulf of mexico. *Science* 192, 367–369. URL: <https://doi.org/10.1126/science.192.4237.367>, doi:10.1126/science.192.4237.367.
- Sturges, W., Leben, R., 2000. Frequency of ring separations from the loop current in the gulf of mexico: A revised estimate. *Journal of Physical Oceanography* 30, 1814–1819. URL: [https://doi.org/10.1175/1520-0485\(2000\)030<1814:forsft>2.0.co;2](https://doi.org/10.1175/1520-0485(2000)030<1814:forsft>2.0.co;2), doi:10.1175/1520-0485(2000)030<1814:forsft>2.0.co;2.
- Sullivan, P.P., McWilliams, J.C., Melville, W.K., 2007. Surface gravity wave effects in the oceanic boundary layer: large-eddy simulation with vortex force and stochastic breakers. *Journal of Fluid Mechanics* 593, 405–452. URL: <https://doi.org/10.1017/s002211200700897x>, doi:10.1017/s002211200700897x.

- Sweet, W., Fett, R., Kerling, J., Violette, P.L., 1981. Air-sea interaction effects in the lower troposphere across the north wall of the gulf stream. *Monthly Weather Review* 109, 1042–1052. URL: [https://doi.org/10.1175/1520-0493\(1981\)109<1042:asieit>2.0.co;2](https://doi.org/10.1175/1520-0493(1981)109<1042:asieit>2.0.co;2), doi:10.1175/1520-0493(1981)109<1042:asieit>2.0.co;2.
- Taburet, G., Sanchez-Roman, A., Ballarotta, M., Pujol, M.I., Legeais, J.F., Fournier, F., Faugere, Y., Dibarboue, G., 2019. DUACS DT2018: 25 years of reprocessed sea level altimetry products. *Ocean Science* 15, 1207–1224. URL: <https://doi.org/10.5194/os-15-1207-2019>, doi:10.5194/os-15-1207-2019.
- Tolman III, H., . The WAVEWATCH III Development Group (WW3DG),(2019): User Manual and System Documentation of WAVEWATCH III R Version 6.07, Tech. Technical Report. Note 333.
- Traon, P.Y.L., 2013. From satellite altimetry to argo and operational oceanography: three revolutions in oceanography. *Ocean Science* 9, 901–915. URL: <https://doi.org/10.5194/os-9-901-2013>, doi:10.5194/os-9-901-2013.
- Umlauf, L., Burchard, H., 2003. A generic length-scale equation for geophysical turbulence models. *Journal of Marine Research* 61, 235–265. URL: <https://www.ingentaconnect.com/content/jmr/jmr/2003/00000061/00000002/art00004>, doi:doi:10.1357/002224003322005087.
- Valcke, S., 2013. The oasis3 coupler: A european climate modelling community software. *Geoscientific Model Development* 6, 373–388.
- Vukovich, F.M., Crissman, B.W., 1986. Aspects of warm rings in the gulf of mexico. *Journal of Geophysical Research* 91, 2645. URL: <https://doi.org/10.1029/jc091ic02p02645>, doi:10.1029/jc091ic02p02645.
- Vukovich, F.M., Crissman, B.W., Bushnell, M., King, W.J., 1979. Some aspects of the oceanography of the gulf of mexico using satellite and in situ data. *Journal of Geophysical Research* 84, 7749. URL: <https://doi.org/10.1029/jc084ic12p07749>, doi:10.1029/jc084ic12p07749.
- Vukovich, F.M., Maul, G.A., 1985. Cyclonic eddies in the eastern gulf of mexico. *Journal of Physical Oceanography* 15, 105–117. URL: [https://doi.org/10.1175/1520-0485\(1985\)015<0105:ceiteg>2.0.co;2](https://doi.org/10.1175/1520-0485(1985)015<0105:ceiteg>2.0.co;2), doi:10.1175/1520-0485(1985)015<0105:ceiteg>2.0.co;2.
- Wang, C., Zhang, L., Lee, S.K., Wu, L., Mechoso, C.R., 2014. A global perspective on CMIP5 climate model biases. *Nature Climate Change* 4, 201–205. URL: <https://doi.org/10.1038/nclimate2118>, doi:10.1038/nclimate2118.
- White, H.K., Hsing, P.Y., Cho, W., Shank, T.M., Cordes, E.E., Quattrini, A.M., Nelson, R.K., Camilli, R., Demopoulos, A.W.J., German, C.R., Brooks, J.M., Roberts, H.H., Shedd, W., Reddy, C.M., Fisher, C.R., 2012. Impact of the deepwater horizon oil spill on a deep-water coral community in the gulf of mexico. *Proceedings of the National Academy of Sciences* 109, 1042–1047.

- Sciences 109, 20303–20308. URL: <https://doi.org/10.1073/pnas.1118029109>, doi:10.1073/pnas.1118029109.
- Wu, L., Breivik, Ø., Rutgersson, A., 2019a. Ocean-wave-atmosphere interaction processes in a fully coupled modeling system. *Journal of Advances in Modeling Earth Systems* 11, 3852–3874. URL: <https://doi.org/10.1029/2019ms001761>, doi:10.1029/2019ms001761.
- Wu, L., Staneva, J., Breivik, Ø., Rutgersson, A., Nurser, A.G., Clementi, E., Madec, G., 2019b. Wave effects on coastal upwelling and water level. *Ocean Modelling* 140, 101405. URL: <https://doi.org/10.1016/j.ocemod.2019.101405>, doi:10.1016/j.ocemod.2019.101405.
- Wunsch, C., 1998. The work done by the wind on the oceanic general circulation. *Journal of Physical Oceanography* 28, 2332–2340. URL: [https://doi.org/10.1175/1520-0485\(1998\)028<2332:twdbtw>2.0.co;2](https://doi.org/10.1175/1520-0485(1998)028<2332:twdbtw>2.0.co;2), doi:10.1175/1520-0485(1998)028<2332:twdbtw>2.0.co;2.
- Yablonsky, R.M., Ginis, I., 2012. Impact of a warm ocean eddy's circulation on hurricane-induced sea surface cooling with implications for hurricane intensity. *Monthly Weather Review* 141, 997–1021. URL: <https://doi.org/10.1175/mwr-d-12-00248.1>, doi:10.1175/mwr-d-12-00248.1.
- Yu, L., Jin, X., Weller, R.A., 2008. 2008: Multidecade global flux datasets from the objectively analyzed air-sea fluxes (oafux) project: Latent and sensible heat fluxes, ocean evaporation, and related surface meteorological variables. woods hole oceanographic institution oafux project tec, in: Rep, Citeseer.
- Zalesak, S.T., 1979. Fully multidimensional flux-corrected transport algorithms for fluids. *Journal of Computational Physics* 31, 335–362. URL: [https://doi.org/10.1016/0021-9991\(79\)90051-2](https://doi.org/10.1016/0021-9991(79)90051-2), doi:10.1016/0021-9991(79)90051-2.
- Zavala-Hidalgo, J., Morey, S., O'Brien, J., Zamudio, L., 2006. On the loop current eddy shedding variability. *Atmósfera* 19, 41–48.
- Zavala-Hidalgo, J., Morey, S.L., O'Brien, J.J., 2003. Cyclonic eddies northeast of the campeche bank from altimetry data. *Journal of Physical Oceanography* 33, 623–629. URL: [https://doi.org/10.1175/1520-0485\(2003\)033<0623:cenotc>2.0.co;2](https://doi.org/10.1175/1520-0485(2003)033<0623:cenotc>2.0.co;2), doi:10.1175/1520-0485(2003)033<0623:cenotc>2.0.co;2.
- Zavala-Hidalgo, J., Romero-Centeno, R., Mateos-Jasso, A., Morey, S.L., Martínez-López, B., 2014. The response of the gulf of mexico to wind and heat flux forcing: What has been learned in recent years? *Atmósfera* 27, 317–334. URL: [https://doi.org/10.1016/s0187-6236\(14\)71119-1](https://doi.org/10.1016/s0187-6236(14)71119-1), doi:10.1016/s0187-6236(14)71119-1.
- Zheng, Y., Alapaty, K., Herwehe, J.A., Del Genio, A.D., Niyogi, D., 2016. Improving high-resolution weather forecasts using the weather research and forecasting (wrf) model with an updated kain–fritsch scheme. *Monthly Weather Review* 144, 833–860.

